Model-based analysis of respiratory mechanics for diagnosis of cardiopulmonary diseases

Von der Fakultät für Elektrotechnik und Informationstechnik der Rheinisch-Westfälischen Technischen Hochschule Aachen zur Erlangung des akademischen Grades eines Doktors der Ingenieurwissenschaften genehmigte Dissertation

vorgelegt von

Diplom-Ingenieur Hoang Chuong Ngo Nguyen aus Ho Chi Minh City, Vietnam

Berichter: 1) Univ.-Prof. Dr.-Ing. Dr. med. Steffen Leonhardt, Aachen

2) Assistant Prof. Dr.Ir. F.H.C. de Jongh, Twente

3) Prof. Dr. med. Klaus Tenbrock, Aachen

Tag der mündlichen Prüfung: 18.01.2019

Diese Dissertation ist auf den Internetseiten der Universitätsbibliothek online verfügbar.

Acknowledgment

This dissertation was conducted during my work as a research assistant at the Chair of Medical Information Technology (MedIT), Helmholtz Institute for Biomedical Engineering at RWTH Aachen between 2013 and 2018. I would like to express my sincere gratitude to my doctor father, Professor Steffen Leonhardt, the holder of the Chair for Medical Information Technology, for the great opportunity to carry out such an interesting research. His scientific competence and ambition have constantly guided and encouraged me for the competition of this thesis. His willingness to give his time so generously has been very much appreciated. I also thank Professor Frans de Jongh and Professor Klaus Tenbrock for serving as co-examiner, as well as Professor Gerd Ascheid and Professor Albert Moser for serving on the examination committee.

Furthermore, I would also like to thank to my group leader, Dr. Berno Misgeld for his advice and assistance in keeping my progress on schedule. I also would like to express my very great appreciation to Dr. Lehman for her advice and her help in acquisition and analysis of the EIT data.

My gratitude is specifically given to Philips Research for the financial support during my whole dissertation period. My grateful thanks are also extended to Mr. Thomas Vollmer and Mr. Stefan Winter from Philips for their useful and constructive recommendations on this work.

I wish to thank various students for their contribution to this thesis: Stephan Dahlmanns, Carlos Munoz, Falk Dippel, Philip Ackermann, Sarah Spagnesi, Karl Krüger, Alexander Kube, Rober Schlözer, Ai Bahram, and Tony Zhang. I also thank my former and current colleagues Stephan Dahlmanns, Philip von Platen, Markus Lüken, Bernhard Penzlin, Christian Brendle, Christoph Weiss, Daniel Rüschen, and others for the great time at MedIT.

In addition, I would like to extend my thanks to all my proof-readers and further friends and colleagues who were involved in the correction process of the thesis.

Finally, I wish to thank my parents and my sister for their unconditional love, consistent care, support and encouragement throughout my study and phD time.

Contents

Αc	Acknowledgment		
1	Intr	oduction	1
	1.1	Motivation	1
		1.1.1 Obstructive pulmonary diseases	1
		1.1.2 Restrictive pulmonary diseases	2
	1.2	History of respiratory researches	3
	1.3	Methodology of mathematical modeling of biomedical systems .	5
		1.3.1 Forward modeling	5
		1.3.2 Inverse modeling	6
	1.4	Objectives of the research	7
	1.5	Organization of this book	8
2	Fun	damentals	9
	2.1	Physiological background	9
		2.1.1 Physiology of the respiratory tract	9
		2.1.2 Respiratory mechanics	13
		2.1.3 Physiology of heart, circulation, and lymphatics	16
	2.2	Pulmonary function diagnostics	20
		2.2.1 Spirometry	22
		2.2.2 Helium dilution and nitrogen washout methods	24
		2.2.3 Body plethysmography	24
		2.2.4 Rapid interrupter technique	26
		2.2.5 Esophageal catheter	27
		2.2.6 Forced Oscillation Technique	28
	2.3	Mechanical ventilation	30
		2.3.1 Continuous positive airway pressure (CPAP)	30
		2.3.2 Pressure- and volume-controlled ventilation	30
	2.4	Electrical Impedance Tomography	31
	2.5	Object-oriented modeling language for biophysical modeling $$.	33
3	Res	piratory modeling	37
	3.1	Non-linear model components	37
		3.1.1 Airways and airspaces	37
		3.1.2 Tissue and chest wall	45
	3.2	The two-degree-of-freedom model	49
		3.2.1 Parametrization and implementation	50

		3.2.2 3.2.3	Simulation results	52 54
	3.3		-based analysis of the interrupter technique	54 57
	5.5	3.3.1	Model behavior during an interruption	58
		3.3.2	Simulation-based analysis of the interrupter technique .	59
		3.3.3	Pendelluft and the Otis parallel model structure	63
	3.4		ary	64
	9.4	Summ	ату	04
4			ed parameter estimation with the forced oscillation tech	
		e (FOT		67
	4.1		rement of respiratory impedance	67
	4.2		ing and parameter identification	70
		4.2.1	A survey of lung models used in Forced Oscillation Tech-	70
		400	nique	70
		4.2.2 $4.2.3$	Model-based analysis	72 77
	4.9	_	Model hierarchy and recommendations	79
	4.3	4.3.1	olume-dependent FOT	79 79
		4.3.1		80
		4.3.3	The reduced non-linear model	83
	4.4			85
	$4.4 \\ 4.5$		asal FOT	89
	4.0	Summ	ary	09
5	Mod	leling o	f cardiopulmonary interactions and cardiogenic congestion	ı 91
	5.1	Model	ing of heart and circulation	91
		5.1.1	Atria, ventricles and heart valves	91
		5.1.2	Septum and pericardium	93
		5.1.3	Vascular arteries and veins	94
		5.1.4	Baseline simulation of the cardiovascular system \dots	96
	5.2	Cardio	opulmonary hemodynamic interactions	99
		5.2.1	Simulation results	100
	5.3	The fl	uid balance and the lymphatic system	106
		5.3.1	Model development	106
		5.3.2	Model extension for cardiogenic pulmonary congestion $.$	112
	5.4		ation results	116
		5.4.1	Fluid filtration through the capillary walls	116
		5.4.2	Lymphatic absorption	118
		5.4.3	Cardiogenic pulmonary congestion and CPAP treatment	118
	5.5	Discus	ssion and summary	199

6	Asse	essment of global and regional ventilation using EIT	123
	6.1	Diagnosis of pulmonary function with EIT during forced expi-	
		ratory maneuvers	124
		6.1.1 Study design	124
		6.1.2 Linearity between EIT and spirometry in healthy adults	127
		6.1.3 Linearity between EIT and spirometry in pediatric pa-	
		tients with asthma	128
		6.1.4 Regional EIT-derived flow volume (FV) loop	133
	6.2	Introduction of oscillatory Electrical Impedance Tomography	
		(oEIT)	137
		6.2.1 Visibility of FOT frequencies in EIT signal	137
		6.2.2 The band-pass filtered oEIT signal	138
	6.3	Summary	141
7	Disc	cussion and outlook	143
Α	Арр	pendix	147
В	Pub	lications	159
Bil	oliogi	raphy	163

Abbreviation

Symbol	Meaning
ARDS	Acute respiratory distress syndrome
ASB	Assisted spontaneous breathing
ATS	American Thoracic Society
BiPAP	Bilevel positive airway pressure
BSL	Bronchospasmolysis
CHF	Congestive heart failure
COPD	Chronic obstructive disease
CPAP	Continuous positive airway pressure
CPS	Cardiopulmonary system
CVS	Cardiovascular system
ECG	Electrocardiogram
EDPVR	End-diastole pressure-volume relationship
EIT	Electrical impedance tomography
ERS	European Respiratory Society
ESPVR	End-systole pressure-volume relationship
FEV_{05}	Forced expiratory volume in 0.5 second
FEV_1	Forced expiratory volume in 1 second
FOT	Forced oscillation technique
FRC	Functional residual capacity
FV	Flow-volume
FVC	Forced vital capacity
GOLD	Global Initiative for Chronic Obstructive Lung Disease
IGV	Intra-thoracic gas volume
ITBV	Intra-thoracic blood volume
LV	Left ventricle
MEF_{25}	Maximum expiratory flow at 25% of FVC
MEF_{50}	Maximum expiratory flow at 50% of FVC
MEF_{75}	Maximum expiratory flow at 75% of FVC
MRI	Magnet resonance imaging
ODE	Ordinary differential equation
oEIT	Oscillatory electrical impedance tomography
OOML	Object-oriented modeling language
OSA	Obstructive sleep apnea
PCV	Pressure-controlled ventilation
PCW	Pulmonary capillary wedge (pressure)

n

Symbol	Meaning
PEEP	Positive end-expiratory pressure
PEF	Peak expiratory flow
PFT	Pulmonary function test
PIP	Positive inspiratory pressure
PV	Pressure-volume
RLD	Restrictive pulmonary disease
RV	Right ventricle
SD	Standard deviation
SV	Stroke volume
TI	Tiffeneau index
TLC	Total lung capacity
TOP	Threshold opening pressure
TPR	Total peripheral resistance (circulation)
VC	Vital capacity
VCV	Volume-controlled ventilation
$ m V_{ m T}$	Tidal volume
WHO	World Health Organization
WOB	Work of breathing

Physical parameters

Symbol	Meaning	Unit
p, P	Pressure	$cmH_2O, mmHg$
t	Time	S
V	Volumen	L
Ċ	Flow	L/s
R	Resistance	${ m cmH_2O/L/s}$
C	Compliance	L/cmH_2O
I	Inertance	$cmH_2O/L/s^2$
f	Frequency	$_{ m Hz}$
Z	Impedance	$\mathrm{cmH_2O/L/s}$
G	Conductance	$L/(cmH_2Os)$
sG	Specific conductance	$1/(\text{cmH}_2\text{Os})$
sR	Specific resistance	$\mathrm{cmH_2Os}$
au	Time constant	S
φ	Phase	radian
G	Tissue damping (constant-phase)	undefined
H	Tissue elastance (constant-phase)	undefined
$Z_{ m R}$	Resistive impedance	$\rm cmH_2O/L/s$
$Z_{ m R}$	Reactive impedance	$\mathrm{cmH_2O/L/s}$

Indexes

Symbol	Meaning
a, art	arterial
alv	alveolar
ao	airway opening
ao	aortic (circulation)
av	aortic valve
aw	airway
b	bronchial
$^{\mathrm{c}}$	central
c+cw	central and chest wall
cap	capillary
cw	chest wall
ed	diastolic
es	systolic
es	esophageal
f	filtration
int	interrupter (for resistance)
int	interstitial
\mathbf{L}	lung
la	left atrial
le	left (lung)
leak	leakage
liq	liquid
lrs	lower respiratory system
lv	left ventricular
$_{ m lym}$	lymphatic
meas	measured
mus	respiratory muscles
naw	nasal airway
os	oscillation, oscillatory
osm	osmotic
p	peripheral
pa	pulmonary arterial
PE	pleural extended
pl	pleural
pul	pulmonary

Indexes

Symbol	Meaning
pv	pulmonary venous
pvc	pulmonary venous capillary
ra	right atrial
$_{\rm res,R}$	resistive
ri	right (lung)
rs	respiratory
rv	right ventricular
sa	systemic arterial
safe	safety factor
stat	static
sys	systemic
tc	tricuspid valve
ti	tissue
tr	transmural
v,ven	venous
vc	vena cava
X	reactive

1 Introduction

Breathing in, there is only the present moment.

Breathing out, it is a wonderful moment.

Thich Nhat Hanh

1.1 Motivation

Breathing is fundamental for the survival of living beings by delivering oxygen and removing carbon dioxide. Disturbances caused by diseases or injuries can lead to serious physiological damages. Respiratory failures in humans are classified into obstructive and restrictive pulmonary diseases.

1.1.1 Obstructive pulmonary diseases

People with obstructive pulmonary disease often face shortness of breath. An obstruction, flow limitation, or air "trapped" inside the lungs occurs if an abnormally high amount of air remains in the lungs at the end of a full exhalation. The obstruction becomes worse during activity or exertion, when the rate of breathing is higher than normal. The main reason for obstruction is damage or narrowing of the airways. Common obstructive pulmonary diseases are chronic obstructive pulmonary disease (COPD), asthma, sleep apnea, bronchiectasis, and cystic fibrosis.

COPD is the most common obstructive pulmonary disease. According to the World Health Organization (WHO) and the Global Initiative for Chronic Obstructive Lung Disease, COPD is the cause of about 3 million deaths per year (2015) and will rank third in the causes of death in 2020 [25,211]. COPD's symptoms are coughing and secretion that are usually associated with chronic bronchitis and pulmonary emphysema [139]. Main causes of airway obstruction are air contaminants (for example, cigarette smoke or fine dust) that are located in the lungs and trigger inflammatory processes. COPD worsens with aging. Lifelong smokers have a 50% probability of developing COPD developed during their lifetime [106].

Asthma (or bronchial asthma) is the most common chronic disease among children. It is a chronic, incurable disease caused by hypersensitivity, e.g. by allergies, which leads to a long-term inflammation and narrowing of the airways. Typical symptoms are wheezing, coughing, shortness of breath, and increased work of breathing (WOB). While the WHO estimates 334 million people worldwide to suffer from asthma [1,141], the International Study of Asthma and Allergies in Childhood reported that about 14% of the world's

children are likely to have asthmatic symptoms (2014). Since uncontrolled asthma can damage the airways permanently, it's crucial to get asthma diagnosed and receive treatment as soon as possible.

The common diagnostic tool for COPD and asthma is spirometry [1,211]. Spirometry is a non-invasive pulmonary function test (PFT) which is helpful in assessing breathing patterns in the form of flow-volume (FV) loops that identify abnormal conditions. Results of spirometry tests are volume parameters, such as forced vital capacity (FVC), or forced expiratory volume in one second (FEV₁). These indicies are indirect parameters, which means they do not provide physical characteristics of lung mechanics such as resistance or compliance, but rather give an indicator for the exhaling time and the related flow limitation. Other pulmonary function tools such as whole-body plethysmography, interruption technique, or oscillometry, which measure directly mechanical parameters of the lungs, have proven their discriminative power in assessing lung mechanics in clinical studies. However, they are not listed as standardized PFTs in assessing COPD and asthma.

Also, there are several limitations in standard spirometry. First, it requires strong patients' cooperation during the forced expiration maneuver, hence, is not suited for infants, young children, sleeping patients, or patients with severe diseases. Second, spirometry and other PFTs are limited to global function of the lungs, while regional information can be beneficial to assess heterogeneous changes in diseased lungs and to improve treatment. Both aspects will be discussed later in this work.

1.1.2 Restrictive pulmonary diseases

Restrictive pulmonary diseases (RLDs) are conditions in which the lungs cannot be fully filled with air. It is defined as a reduction of total lung capacity (TLC) below the 5th percentile of the predicted value, while the ratio FEV_1/FCV is preserved [181]. Restrictive diseases are often caused by an increased stiffness in the lungs, with the restricted area in the lung parenchyma, in the pleural space, or in the chest wall. Interstitial lung diseases, sarcoidosis, cardiogenic congestion and edema, acute lung injury and acute respiratory distress syndrome (ARDS) are typical RLDs. The symptoms vary from cardiogenic congestion, atelectasis, reduction of lung compliance, impaired gas exchange, ventilation-perfusion inequality, to severe hypoxia.

The focus of this work is on cardiogenic congestion. It is a condition where fluid accumulates in the interstitial tissue and alveolar spaces of the lungs as a result of left ventricular congestive heart failure (CHF). CHF often occurs in patients with coronary artery diseases, including a previous heart attack and a left ventricular dysfunction. The reduced pumping capacity of the left

ventricle leads to an elevation of blood pressure in the pulmonary circulation, a cardiogenic congestion. Severely elevated blood pressure can have serious consequences in the lungs, including interstitial and alveolar flooding, reduced compliance, and insufficient gas exchange. Beside pharmacologic treatment (including nitroglycerin, morphine sulfate, loop diuretics [125]), ventilation support such as noninvasive positive pressure ventilation (continuous positive airway pressure CPAP, bilevel positive airway pressure BiPAP) or mechanical ventilation with or without endotracheal intubation [124, 125] are typical therapies of pulmonary congestion.

From a physiological and technical point of view, the development of cardiogenic congestion is an interesting phenomenon caused by the interactions between different processes, namely the respiration, the circulation, and the fluid balance including lymphatic absorption. Mathematical models describing functionality of each process have been investigated by many researchers. However, there is a lack on a mathematical model which focuses on physiological interactions among these processes, especially during edema development and the treatment with a positive end-expiratory pressure (PEEP). Development of such a model is one major issue of this work.

1.2 History of respiratory researches

The first attempt to measure lung volume can be tracked to the Greek physician Galen (Claudius Gelenus of Pergamo, A.D. 129 – circa 200), as he had a child breathe in and out a bladder and found that the tidal volume did not change [208]. Sixteen centuries later, in 1846, an English physician named John Hutchinson invented the first modern spirometer by turning a gasometer into an instrument to measure the exhaled volume in humans [196]. After Hutchinson, many versions of spirometer have been introduced, from the first "pneumotachograph" by Gad J. in 1879, to the "peak flow meter" by Wright B.M. and McKerrow in 1959. The first standardized guidelines for spirometry were released by the European Community for Coal and Steel in 1960.

Besides the attempt to measure lung volume, researchers have searched for mathematical descriptions of the respiratory system since the beginning of the last century. In 1915, the Rohrer equation was introduced for laminar and turbulent flow patterns in the respiratory system [178]. Geometrical models of the bronchial tree were first introduced by Fineisen in 1935 [52], where he divided the airways into 9 compartments from trachea to alveolar sacs and investigated three mechanisms of gas transport: inertial impaction, gravity, and diffusion [216]. In 1963, Weibel introduced a mathematical model of the bronchial tree with 23 generations of bifurcation [219, 220], which was later

modified by Yeh and Schum [226]. The use of body plethysmography to measure residual lung volume and airway resistance was introduced by Dubois, Comroe Jr., and their colleagues in 1956 [41, 42]. The methods described in their two papers are still used today in clinical pulmonary function laboratories. In the same year, Dubois published another paper on oscillation mechanics on lungs and chest in human [43], which made him the inventor of the forced oscillation technique (FOT). Other important contributions are from Mead and his coworkers who investigated mathematical models of flow limitation during forced expiratory maneuvers and interruption technique [127,128,130,131]; and from Otis [156,157] on frequency dependency of lung parameters.

The rapid development of computer science has brought new possibilities to model complex biophysical systems. In 1972, Guyton published a comprehensive mathematical model of fluid, electrolyte, and circulatory regulation which is capable of simulating a variety of experimental conditions [67]. Guyton's model demonstrated the use of compartment modeling with lumped parameters to simulate complex physical and physiological interactions between systems. Later, Rideout's work on computer modeling of physiological systems produced a sophisticated model of human physiology implemented in Fortran [174], where he included a model of lung mechanics to describe the pulmonary gas exchange in humans. In 2001, Lu et al. introduced a comprehensive model of cardiopulmonary interactions applied to analysis of the Valsalva maneuver [117]. Jallon et al. introduced a model of the cardiopulmonary system (CPS) in which the respiratory muscles were modeled by a central respiratory pattern generator [89]. Recently in 2016, the group of Chbat et al. developed a comprehensive model of the CPS that emphasized on the interaction between the respiratory and cardiovascular systems via thorax pressure and gas exchange [3, 29]. The mentioned models were implemented in the signal-based or text-based programming languages (Matlab Simulink, Fortran, C++).

1997, Elmqvist introduced the object-oriented modeling language (OOML) ModelicaTM to model physical systems [46]. Later in the same year, the commercial version Dymola was released. Eleven years later, Mathworks introduced the first SimscapeTM version in their R2008a+ product. These modeling languages have widely found applications in mechanical, electrical, hydraulic, and thermal domains. However, while OOMLs have gained increasing attention in modeling complex, interconnected biophysical systems, the number of publications in this field are moderate. Few existing object-oriented biophysical models focus on the cardiovascular system [7,24,36,77]. The use of OOML for the investigation of respiratory mechanics and cardiopulmonary interactions is a novel scientific contribution of this research.

1.3 Methodology of mathematical modeling of biomedical systems

Mathematical models have been developed to formalize existing knowledge of complex natural processes in medicine and physiology. With the help of modern computers, mathematical and computing models are used more and more in biomedical research. They provide several advantages: (1) system abstraction for explaining and understanding, (2) system simplification by focusing on certain aspects, (3) testing possibilities via computer simulations [9]. The third has been becoming more important regarding the rapid development of computer technology and simulation tools. Instead of setting up complex biomedical experiments or animal trials, various scenarios can be tested with a computer model.

Biologists and medical doctors are familiar with a-priori knowledge of complex biomedical systems, even to the certain degree of precision. However, since their conceptual models do not often contain much mathematics, they may face difficulties in abstracting the problem into a mathematical / biophysical model. This is the job of the system engineer to connect the problem with his knowledge in physics, system dynamics, and control theory. In most of the cases, he will soon find that the available knowledges are incomplete, many interrelationships are unknown, and a large number of parameters are not assessable. Regarding the a-priori knowledge he has and the complexity of the problem, he may choose the forward or the inverse modeling approach [9, 16].

1.3.1 Forward modeling

The creation of a forward, or "white box" model, requires the entire knowledge of the process, which means high certainty of the model structure, and high accessibility of the model parameters. Often, a-priori information comes in the form of mathematical/physical relations between the variables, such as first principles like conservation of mass, electrical charge, or motion equations. In industrial production, white box models are common, since parameters of a designed product (such as a batch process, a robot arm, or a vehicle) are often known and constant.

Biomedical systems are especially complex and often require individualization, as parameters vary. The parameters of such a complex system like the human lungs differ strongly with respect to age, height, weight, health status, temporal stress level or sport activities. Even the applied measurement techniques can have an impact on the parameter values. Hence, forward modeling of such systems does not focus on any individual, but rather on a "standard" subject or object to demonstrate the systematical coherence among the com-

ponents. Forward models usually use as much as a-priori knowledge as possible to make the model more accurate, hence, can include many details. For example, the Weibel's model [219] calculates the length, diameter, and volume of 23 generations of airways in the human bronchial tree. His model provides a physiological understanding of the system dimension, but cannot be applied to any individual treatment, since the parameters are not measurable for a living human. For that reason, a biophysical forward model may not be used for an individual, but rather as a tool for investigation of biomedical hypotheses which are difficult or impossible to be tested experimentally.

Forward models are often implemented in a computer programming language. Its validation is the computer simulation, where dynamical responses of the system on a certain set of inputs and model parameters are estimated via a simulation environment. Comparing these simulation results with a-priori knowledge, the assumptions on the structures and dynamics of the model components can be validated.

1.3.2 Inverse modeling

Inverse modeling, or system identification, is the process of constructing a model and identifying its parameters from experimental data. The term "black box" model is used if no a-priori knowledge about the system is available. Identification methods applied for input and output data can provide characteristics of the system such as impulse or frequency responses. However, black box modeling requires strong simplification and is limited to the input-output behavior of small systems. For biomedical processes, another approach, so called "grey box" model, appears to be more useful. Grey box modeling combines the advantages of white and black box modeling. It applies model structures, whose propriety has been proven in a forward model, on a set of measurement data. The parameters are tuned and evaluated by making the model to predict the outputs as precisely as possible. This procedure, called "parameter estimation", is especially useful for monitoring physiological parameters that are not directly measurable in praxis [9].

Inverse models often present a reduction of more complicated forward models. During the modeling process, since the amount of identifiable parameters is limited regarding the applied measurement techniques, the modeler has to decide which model components are important and which can be ignored. For the respiratory system, on the one hand, it is obvious that the identification of all parameters of the 23-generation Weibel model is not possible; on the other hand, the widely used two-element RC lung model seems to be too simple to describe advanced respiratory mechanics and pathological conditions. An increase from 2 to 4-9 model components requires careful consideration regard-

ing parameter identifiability and physiological interpretation of the estimated values.

The validation of the estimated parameters appears to be a problem in lung mechanics research. Validation of an inverse model contains two tasks, which can be called a forward validation (error of estimation) and a backward validation (physiological interpretation). The first task computes the error of estimation by comparing model and experimental data. If the error is small enough, the model can be judged "acceptable". If the model fails to follow the measurement data, a better (often more complicated) structure is needed [9]. By including more parameters in the model, we also increase the degree of freedom of the identification algorithm, i.e. allow the model to fit the data easier. The more parameters are used, the smaller the error becomes. However, the uncertainty of parameter interpretation increases, since non-linear relations between model components can lead to unphysiological extrema. The second task, called physiological interpretation or backward validation, judges the consistency of the estimated results against a priori knowledge. In other words, it examines if the estimated values lie in physiological ranges. If this is not the case, the estimated extrema should be considered as mathematical, but not physiological extrema. Problems occur if there is no measurement technique or literature report for certain parameters. For such parameters, a combination of forward model simulation and system identification for various testing scenarios (change of model input or diseases-related alteration, influences of other parameters, etc...) can provide more validity of the model assumptions.

1.4 Objectives of the research

The ultimate goals of this research are

- to develop a biophysical forward model of the respiratory system. The models should consider, as much as possible, all significant non-linear behaviors of lung mechanics,
- to apply the forward model for reevaluation of existing theories and measurement techniques in lung mechanics. If possible, model's behavior should give adequate, quantitative explanations for current controversial discussion in this field.
- to perform inverse modeling with parameter estimation algorithms. Modelbased analysis should clarify the identifiability of model components regarding the use of different measurement techniques,

- 4. to extend the forward lung model to a comprehensive cardiopulmonary model for analysis of cardiopulmonary interactions and cardiogenic congestion. The model should be validated by comparing simulation results with clinical data and animal experiments in literature, and
- 5. to introduce new measurement modalities for assessing global and regional respiratory mechanics with respects to cardiopulmonary diseases.

1.5 Organization of this book

Chapter 2 introduces the backgrounds of this research. First, it provides the anatomical and physiological background of the respiratory and cardiovascular systems. Second, it gives an overview on the state-of-the-art methods in pulmonary function testing. Third, three technologies related to this research: the mechanical ventilation, the electrical impedance tomography, and the object-oriented modeling are briefly discussed.

Chapter 3 introduces a novel non-linear object-oriented respiratory model. Model development consists of compartmentalization, characterization of model components, and validation. The model is demonstrated to be useful in the reevaluation of the interrupter technique.

Parameter identification in the frequency domain with data obtained via forced oscillation technique (FOT) is the topic of Chapter 4. Model-based analysis aims to provide an explanation of controversial theories regarding the physiological interpretation of the respiratory impedance and to abstract a model hierarchy. This chapter also discusses the possibility to extend FOT for additional diagnostic information.

Chapter 5 focuses on the modeling of the cardiovascular system, cardiopulmonary interaction, and cardiogenic congestion. The novel models of cardiopulmonary interaction are validated by comparing model's responses with clinical and animal data.

In chapter 6, new measurement modalities for assessing global and regional pulmonary function by combining electrical impedance tomography with existing testing methods are introduced. The new techniques are tested in studies involving healthy and diseased patients.

The main findings of this research are summarized in chapter 7, followed by an outlook on future scientific contributions and applications of the work.

2 Fundamentals

As you breathe in, cherish yourself. As you breathe out, cherish all Beings. Dalai Lama XIV

This chapter is intended to convey the knowledge necessary to conveniently follow the upcoming chapters. Therefore, it provides the physiological and technical fundamentals related to the research. First, it gives an overview of the anatomy and physiology of the cardiorespiratory system. Second, diverse techniques for pulmonary function diagnostics are introduced. In addition, technical basics of mechanical ventilation, electrical impedance tomography, and the object-oriented programming language SimscapeTM are explained.

2.1 Physiological background

2.1.1 Physiology of the respiratory tract

The structure of the human respiratory system has evolved to suit uniquely its functionality. The system consists of the upper respiratory tract, the bronchial tree, the alveolar and tissue compartment, the pleural space, the chest wall, and the respiratory muscles (Fig. 2.1). Each component plays an essential role in maintaining the transport of gas from the airway opening to the alveolar–capillary barrier.

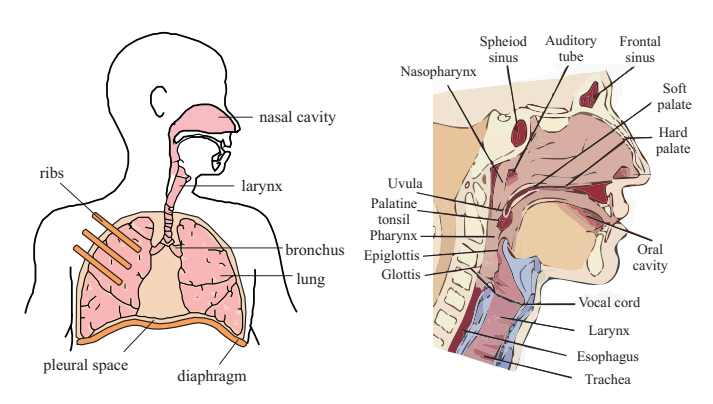


Figure 2.1: Anatomy of the respiratory system (left) and the upper airways (right).

The upper respiratory tract

In nasal breathing, air flows from the environment through the nostrils to the nasal cavities, where it later passes the internal nasal valves. The valves open up into the main cavity, where three curled bony structures, the nasal conchae, are located on its lateral wall. The curved structure of the conchae increases the surface area of the nasal walls, thus aiding in heating, humidifying, and filtering of the air. Tiny particles in the air are trapped in nasal mucus, which covers the surface of the nasal cavities. The olfactory cells are situated above the conchae in the main cavity and serve as the sensory organ responsible for smelling. Two nasal cavities join at the nasopharynx, which merges with the oral cavity at the pharynx (Fig. 2.1).

In mouth breathing, air enters the oropharynx directly through the mouth and bypasses the nasal cavities. Further downstream, air reaches the laryngopharynx which is the junction of the trachea and the esophagus. The glottis and the larynx, situated at the entrance of the trachea, mark the border between the upper respiratory tract and the bronchial tree.

The bronchial tree

The human bronchi network has an anatomic structure with branches resembling a tree. Each bifurcation level is called a generation. The bronchial tree has approximately 23-26 generations [38,71,220]. Generation 0, the trachea, is a thin-walled tube, about 10cm in length and 2.5cm in diameter, extends from the larynx into the thorax and divides into the left and right principal (primary) bronchi at the level of the sternal angle (Fig. 2.2). The right principal bronchus divides into two lobar (secondary) bronchi corresponding to two right lung lobes, while three left lobar bronchi connect to three left lung lobes.

The lobar bronchi, in turn, divide into tertiary and quaternary bronchi, then bronchioles and terminal bronchioles. The trachea and the large bronchi (generation 1-4) have the same wall structure of three layers: mucosa, submucosa, and adventitia. The submucosa contains cartilage rings, which stabilize their diameters for large changes of transmural pressures. In contrast, the bronchioles (generation 5-16) are intralobular airways with a diameter of $0.5-5\,\mathrm{mm}$ which are lined by respiratory epithelium without any cartilage wall structure. Each terminal bronchiole is connected to two or three respiratory bronchioles, which are rich in elastic fibers. The walls of the respiratory bronchioles are interrupted by the alveolar sacs and alveolar ducts.

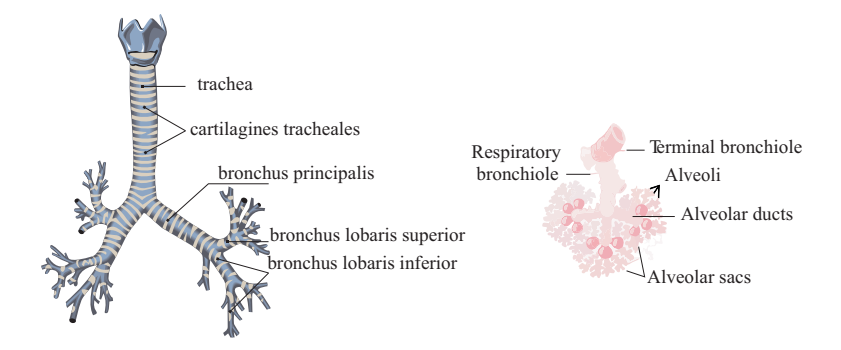


Figure 2.2: The bronchial tree (left) and the alveoli (right).

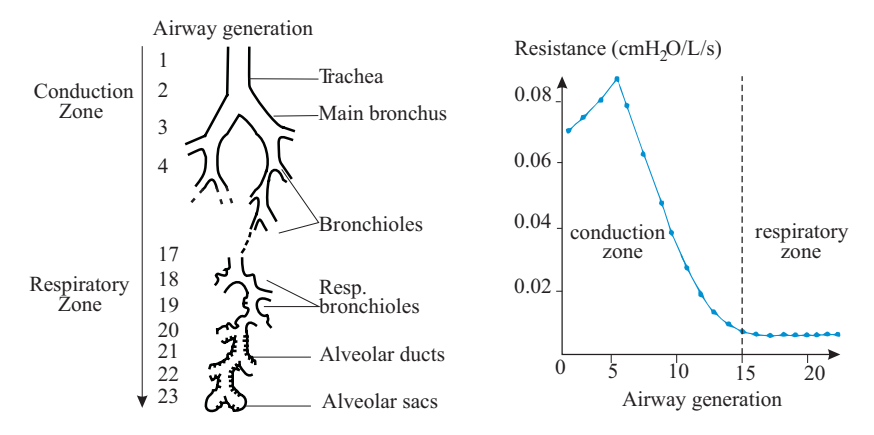


Figure 2.3: Left: Generations of the bronchial tree. Right: Airway resistance regarding the generation number, modified from [219] and [205].

Alveoli and the blood-gas-barrier

The last generations of the bronchial tree form the respiratory zone of the lungs. Generations 17, 18, and 19 constitute the respiratory bronchioles. Generations 20-23, comprising of alveolar ducts and sacs, are the main region where gas exchange occurs. Alveoli are minimal hollow cavities branching from either alveolar ducts or sacs. There are approximately 300-500 million alveoli inside of human lungs. They are found in the lung parenchyma, surrounded by connective tissue and a high number of blood capillaries. Most of the air-facing

surfaces of the alveoli are lined by one-cell-thick layer of type I alveolar cells. Located between these cells are type II cells that produce a substance called "surfactant" necessary for reduction of alveolar surface tension [225].

The gas exchange takes place in the alveolar wall through the blood-gas barrier. The alveolar walls, less than a third of a micron thin in some places, are surrounded by many thin blood capillaries. The oxygen-depleted blood arriving through these capillaries is refilled with $\rm O_2$ and discharged of $\rm CO_2$ via diffusion through the thin tissue layer. The driving force for this diffusion is given by the gas concentration gradients. The volume of gas passing through a tissue sheet by diffusion follows Fick's law:

$$\overrightarrow{\dot{V}} = \frac{AK}{d} \cdot \overrightarrow{\Delta P}, \tag{2.1}$$

where A is the sectional area, d the sheet thickness, ΔP the pressure gradient, \dot{V} the gas flow and K the diffusion coefficient depending on the element considered (O_2, CO_2, N_2) .

The gas exchange is optimized for an important area and a small thickness layer. The 300-500 millions of alveoli represents a total gas exchange area of about $50\,\mathrm{m}^2$ [222]. The gas exchange area and the alveolar wall thickness are two key parameters which maintain the efficiency of the gas exchange.

Chest wall, pleural, and respiratory muscles

Ventilation is a mechanical process which includes the inhalation and exhalation of air in and out of the lungs, respectively. Breathing is driven by the respiratory muscles, namely the diaphragm, the rib muscles as well as the abdominal muscles. In daily life, ventilation is spontaneous and almost unconscious. The muscles contract and release instinctively with a frequency

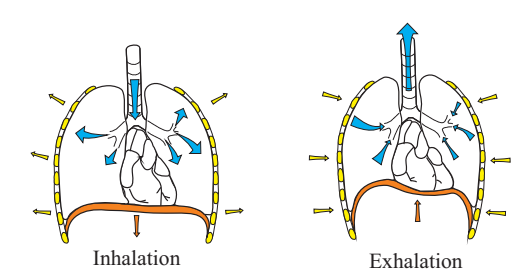


Figure 2.4: Location of the diaphragm and the ribs during inhalation and exhalation.

depending on individuals age and physical condition, about 16 respiratory cycles per minute on average [206]. During exercise, this rate accelerates to balance the increasing energy consumption of the cells. Although respiration

is mostly spontaneous, it is possible to control the driving muscles and thus our breathing rate and amplitude with some effort.

The diaphragm is located under the pulmonary compartments and closes the thorax cage in a convex shape with its highest point at rest position (Fig. 2.4). The rib muscles resting position corresponds to the functional residual capacity (FRC) of the lungs. During inspiration, the respiratory muscles contract. The diaphragm flattens and stretches, while the ribs move out and open the chest leading to an increased volume available for the lungs. A forced expiration can be achieved by an additional contraction of the abdominal muscles.

The lungs are located in the thorax cavity. The pleural space is the potential space located between the parietal and the vis-It functions as a mechaniceral pleural. cal coupling which transfers and regulates the pressure inside and outside of the lungs (Fig. 2.5). Since the lungs are only suspended at the hilum from the mediastinum without any other attachment to the chest wall, the lungs float in a waterbed created by the pleural fluid, which is $8-12\,\mathrm{mL}$ or $0.3\,\mathrm{mL\,kg^{-1}}$ in volume [135]. The process of fluid filtration from from the pulmonary capillaries to lung interstitium is normally kept in equilibrium regarding the Starling equation [197]. The heart, in turn, is embedded in the pleural space via the pericardium, a relatively stiff covering. From the heart, the pulmonary artery and the aorta lead blood to the pulmonary and body circulation. Refluxing blood passes back into the heart via the pulmonary vein and the superior vena cava.

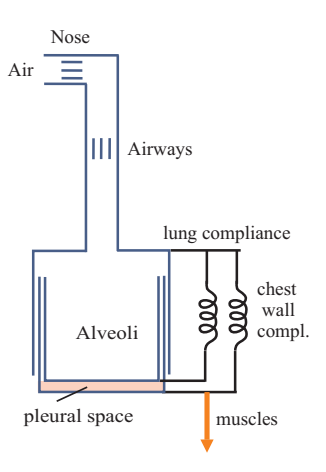


Figure 2.5: Technical abstraction of lungs, chest wall, and pleural space.

2.1.2 Respiratory mechanics

The contraction of the respiratory muscles causes a decrease in the pleural pressure (approximately equal to $-7.5 \,\mathrm{cmH_2O^1}$ during spontaneous inspiration [68]). As a result, the alveolar pressure decreases and air is driven into the lungs through the upper airways. During passive expiration, the respiratory muscles relax, and the elastic recoil pressure of the lung presses the air out of

 $^{^{1}1 \, \}text{cmH}_{2} \text{O} = 98.0665 \, \text{N/m}^{2}$

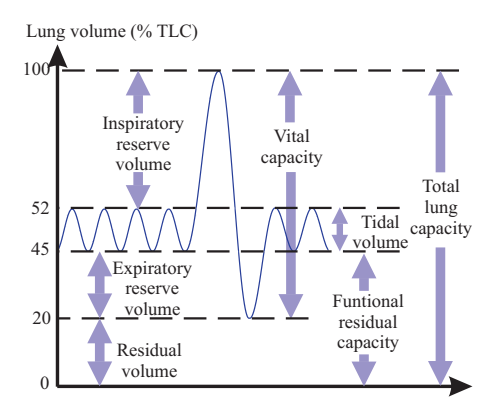


Figure 2.6: Anatomy and technical abstraction of respiratory mechanics.

the lungs. At functional residual capacity (FRC), the pleural pressure $P_{\rm pl}$ is slightly negative (about $-5\,{\rm cmH_2O}$). This pressure is generated by the opposing elastic forces of the chest wall and lung between the visceral and parietal pleura.

Lung volumina

Lung volumes and lung capacities refer to the air volume associated with different phases of the respiratory cycle. The total lung capacity (TLC) is defined as the gas volume in the lungs after a maximal inspiration. The residual volume is the volume remaining in the lungs after a maximal expiration. The difference between TLC and the residual volume is called the vital capacity (VC). For a standard adult male, VC is about 80% of TLC. The functional residual capacity (FRC) is the gas volume in the lungs after a normal expiration (Fig. 2.6).

Forces involved in breathing and respiratory parameters

Forces involved in breathing were first described by Otis et al. in 1950 [156] and completed by Mead in 1961 [127]. The respiratory system can be modeled by three different parts: the thorax, the lungs shaped by the pulmonary tissues and the gas inside the alveoli and airways. These three components form a mechanical system whose equilibrium point corresponds to the full respiratory muscle release and the absence of gas flow at the functional residual capacity (FRC). The respiratory cycle is driven by the muscles, which overcome opposing elastic forces of lung parenchyma to create the displacement from the

equilibrium position. Otis, Fenn and Rahn have detailed the forces involved in the respiratory mechanism in [156]:

• Elasticity: The respiratory system has elastic properties characterized by the respiratory compliance $C_{\rm rs}$, defined as the quotient of a volume change $\Delta V(t)$ over the overall transmural pressure change $\Delta P_{\rm tr}(t)$:

$$C_{\rm rs} = \frac{\Delta V(t)}{\Delta P_{\rm tr}(t)} \ . \tag{2.2}$$

• Airflow resistance: energy dissipation in the system can be represented by a resistive component. Airflow in the respiratory tract is defined as a transition flow with a laminar and turbulent component. More details on flow patterns are given in Appendix A.2. The restrictive pressure drop P_{res} can be expressed as:

$$P_{\text{res}} = K_1 \dot{V}(t) + K_2 \dot{V}^2(t), \tag{2.3}$$

where the constants K_1 and K_2 are the laminar and turbulent component, respectively [178]. The flow can be assumed to be laminar during spontaneous breathing (below a flow rate of 1 L/s) and in the lower airways. In this case, the resistive force can be simplified as

$$P_{\rm res} = R_{\rm rs} \cdot \dot{V}(t). \tag{2.4}$$

Typical values for the respiratory resistance and compliance are given in Table 2.1 as a function of age.

Table 2.1: Typical value of respiratory resistance and compliance [110].

Age	$R_{\rm rs}~({\rm cmH_2O/L/s})$	$C_{\rm rs}~({\rm L/cmH_2O})$
Neonate	30 - 50	0.003 - 0.005
Infant	20 - 30	0.01 - 0.02
Small children	20	0.02 - 0.04
Adult	2 - 4	0.07 - 0.1

 Inertia: The inertial force P_{in} is proportional to the volume acceleration and is equivalent to a mass in a mechanical or an inductor in an electrical system:

$$P_{\rm in} = I\ddot{V}(t). \tag{2.5}$$

The inertial components have been estimated during high frequency breathing [127]. Typical values for I lie between 0.004 and 0.01 cmH₂O/L/s².

Pressure-Volume Diagrams

Mechanical properties of the respiratory system can be characterized by the pressure-volume (PV) diagrams. We distinguish the static PV curve from the dynamic PV curve due to the dynamics of the measurement conditions (Fig. 2.7).

The static PV diagram is reconstructed under quasi-static conditions. Static states, approximated by negligible airflow resistance and convection effects can be measured when airflow is slow or during short apnea time. The static diagram can be obtained by different methods such as the super syringe, the constant flow, or the ventilator method [74]. The PV static curve of the respiratory system, characterized by an S-shape with a linear domain in the normal breathing range and concavity at the extremities, is a combination of the chest wall and lung reaction. The downward concavity for high pressure and volume represents the limits of the lung tissue elasticity while the chest wall confers the non-linearity in the low-pressure range. The static compliance $C_{\rm stat}$ determines the lung volume variation for an unit change in pressure.

The dynamic PV loop describes the behavior of pressure and volume during breathing. It is characterized by an hysteresis between inspiration and expiration phase. The diagram extremities correspond to the tidal volume for the higher point and the functional residual volume as the origin.

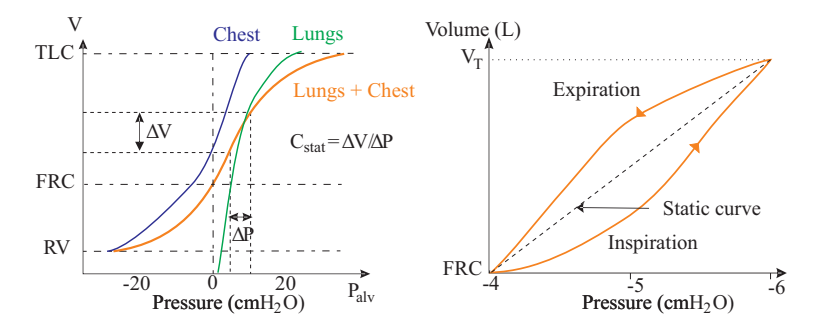


Figure 2.7: Left: Static pressure-volume (PV) relationship of the respiratory system, adapted from [221]. Right: dynamic PV diagram, modified from [68]. $V_T = \text{tidal volume}$.

2.1.3 Physiology of heart, circulation, and lymphatics

The respiratory system coordinates with the cardiovascular system to maintain the transport of oxygenated blood to the organs. The cardiovascular system consists of the heart, the pulmonary and systemic circulation, and the lymphatic system.

Heart

The heart consists of four chambers: two atria and two ventricles. The atria produce low pressures and serve the ventricles mainly as blood stores. The right (RV) and left ventricle (LV) volumes are encircled by cardiac muscle tissue, the "myocardium". Their coordinated contractions pump blood out of the chambers to the blood vessels. The dividing wall between the left and right ventricles of the heart is called the (ventricular) septum, which also consists of cardiac muscles. The entire heart is surrounded by a passive, relatively stiff pericardium, which gives the heart stability and protection from overstretching. There are four heart valves that separate the ventricles from the atria and from the arteries and arrange the direction of blood flow in the body. The tricuspid valve separates the right atrium from the right ventricle and prevents reflux of blood from the ventricle into the atrium. The right ventricle is connected to the pulmonary artery via the pulmonary valve. Similarly, the left ventricle is connected to the left atrium via the mitral valve and to the aorta via the aortic valve. The pressure arising during the systole is dependent on the filling volume of the ventricles (Frank-starling mechanism).

The heart cycle is described by a loop bounded by the end-diastole pressure-volume relationship (EDPVR) and the end-systole pressure-volume relationship (ESPVR). While EDPVR represents the elasticity of the ventricles, ESPVR describes the ventricular contractility. A heart cycle is divided into four cardiac action phases: a) isovolumetric contraction, b) ventricular ejection, c) isovolumetric relaxation, and d) ventricular filling. The first two phases are summarized as systole and the second two ones as diastole. The individual phases are presented in the pressure-volume diagram of the heart (Fig. 2.8).

During the isovolumetric contraction, the sinus node stimulates the contraction of cardiac muscles that produce a high ventricular pressure, while four heart valves are closed. As soon as this ventricular pressure exceeds the corresponding arterial pressure, the pulmonary and aortic valves are opened, causing a large blood flow to the arteries (ejection phase). During the isovolumetric relaxation, the heart muscle relaxes and the ventricular pressures decrease (relaxation phase). When the ventricular pressures underlie the venous pressures, the tricuspid and mitral valves open and the ventricles fill again with blood from the atria (filling phase) [68,96]. The volume difference between the contraction and the relaxation phase is the cardiac stroke volume (SV) of the ventricles and typically ranges between 70 and 100 mL in the adult humans [68]. The product of pulse and SV defines the cardiac output (amount of blood flowing

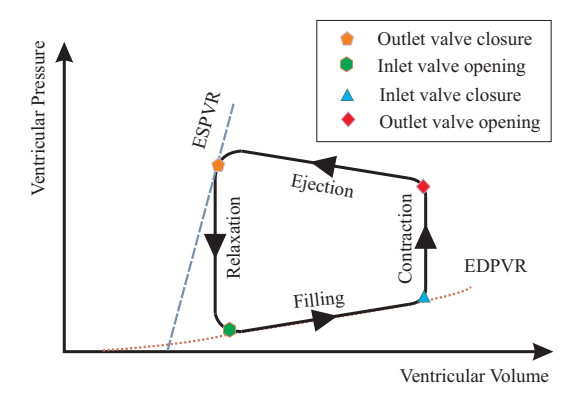


Figure 2.8: PV-diagram of the heart, modified from [76].

through the blood circuits per minute). An SV of 75 mL and a pulse of 80 beats per minute (bpm) results in a cardiac output of 6 L/min.

Systemic and pulmonary circulation

The human circulation system consists of the systemic and pulmonary circulation. Each is, in turn, divided into arteries, capillaries and veins according to the functionality of the blood vessels (Fig. 2.10 left panel). The systemic circuit describes the transport of oxygenated blood from the left ventricle to the organs. For a rapid transport, the arterial pressure is high, typically 163 cmH₂O (120 mmHg) systolic and 109 cmH₂O (80 mmHg) diastolic in the aorta [68]. The arteries are characterized by a thick elastic wall with a thickness of up to 2.5 mm [96]. Systemic arteries branch to smaller arteries and to arterioles, before opening into capillaries. The capillary wall is extremely thin, consisting of only an endothelial layer to allow for an effective gas exchange. After delivering oxygen and absorbing carbon dioxide, blood flows though the veins back to the right atrium. The veins are a thin-walled and low-pressure system. Their compliance is high so that a large amount of blood can be stored. The systemic veins stores approximately 60% of the total blood volume in the human body [68, 96, 184].

While the pulmonary circulation has a similar structure to that of the systemic one, the pulmonary blood pressure is significantly less. Pulmonary arterial pressure is about $34 \, \text{cmH}_2\text{O}$ (25 mmHg) in systole and $11 \, \text{cmH}_2\text{O}$ (8 mmHg) in diastole. The mean capillary pressure in the lungs is about $10 \, \text{cmH}_2\text{O}$. The median pressure drop in the pulmonary circulation is about $19 \, \text{cmH}_2\text{O}$. This

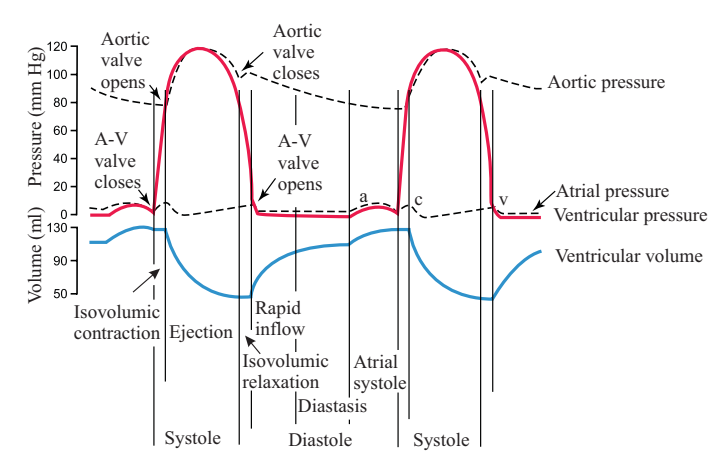


Figure 2.9: Events of the cardiac cycle for left ventricular function pressure, left ventricular pressure, aortic pressure and ventricular volume. Adapted from [68].

value results in a pulmonary flow resistance of $R_{\rm pul} = 190\,{\rm cmH_2OL^{-1}}\,s$, for a cardiac output of 6 L/min. Analogously, the flow resistance of the systemic circulation can also be determined to be around $R_{\rm sys} = 1330\,{\rm cmH_2OL^{-1}}\,s$ [68,96].

Lymphatic system

The human circulatory system processes an average of 20 L of plasma per day through capillary filtration. While 17 L are reabsorbed directly back to the vessels, the other 3 L remain in interstitial space and are later returned to the blood by the lymphatic system (Fig. 2.10, right top figure). The lymphatics comprise a network of lymphatic capillaries, collectors, nodes, and larger strains that carries fluid from interstitial spaces towards the vena cava superior. In the lungs, a lymphatic capillary network of about $50 \cdot 10^{-6}$ m in diameter crosses the interstitial space. Unlike the cardiovascular system, the lymphatic system has no central pump. Lymph movement occurs due to contraction and relaxation of the lymphatic collectors, valves, and compression during adjacent skeletal muscles' contraction [187]. Lymphatic collectors have a similar structure to the systemic veins: They consist of smooth muscles which contract as a forward fluid pump; and they are separated by lymphatic valves which allow a unidirectional flow of fluid [138, 184]. From lymphatics collectors, fluid is transported to lymph nodes and large lymphatic strains, before returning to

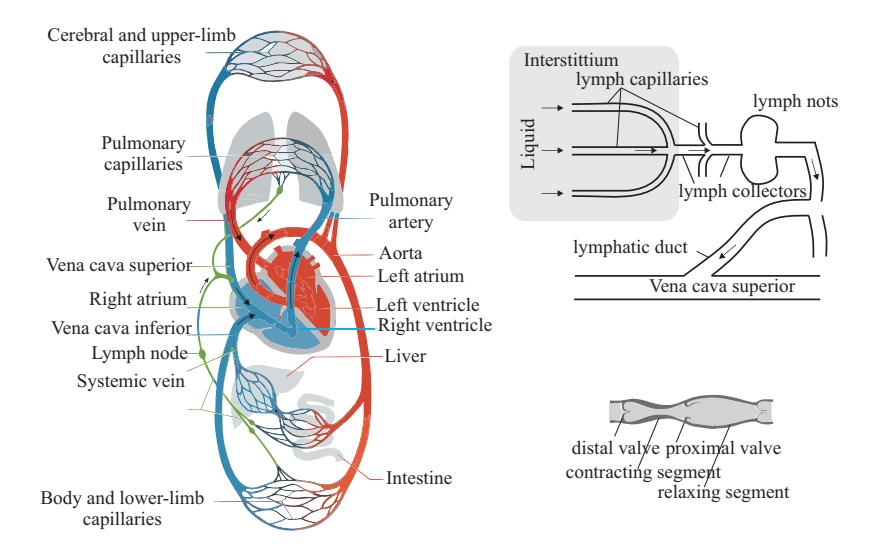


Figure 2.10: Left: The circulation system. Right top: fluid transport in the lymphatic system. Right bottom: a lymphatic collector, modified from [184].

the vena cava superior. Figure 2.10 right figures illustrate the components of the lymphatic system and the structure of a lymph collector.

2.2 Pulmonary function diagnostics

Pulmonary function tests are elementary diagnostic tools in pneumology. A pulmonary function test (PFT) is ordered by a doctor as a part of a routine physical check-up to examine the presence of lung pathologies or to assess the status of the lungs prior to medical treatment or surgery. In general, PFTs can be divided into direct and indirect measurement techniques [110], as illustrated in Fig. 2.11. Direct PFTs, comprising of the esophageal catheter, the interrupter and the forced oscillation technique, measure mechanical parameters such as resistance, compliance, or impedance. Indirect PFTs provides information about subdivisions of lung volumes via spirometry, helium dilution, nitrogen washout, or diagnostic images via radiography, computer tomography, or magnetic resonance imaging. The body plethysmography provides both lung volumes and airway resistance, thus, belongs to both categories.

With exception of the imaging techniques, PFTs generally involve uncovering relationship between pressure, flow, and volume measured at the airway open-

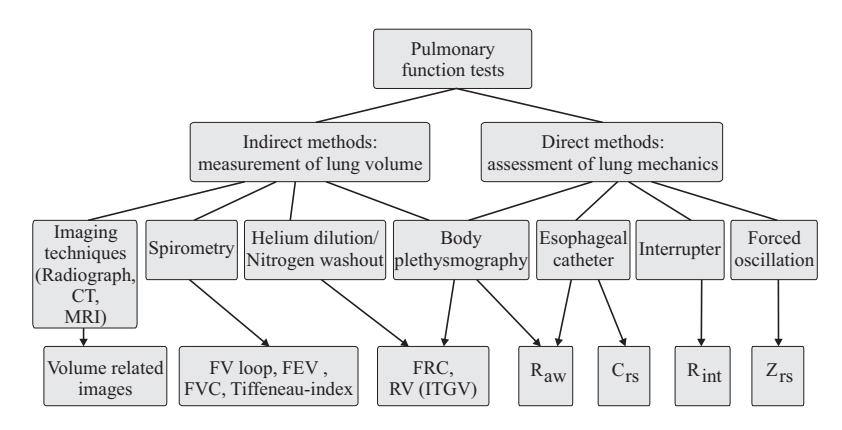


Figure 2.11: Pulmonary function testing (modified from [110]).

ing. Spirometry, FOT and interrupter are noninvasive techniques with simple measurement setup where data are captured only at the airway opening of the test subjects. In contrast, the esophageal catheter requires that the subjects swallow a balloon catheter during the test, which makes this technique invasive and unpratical in use. Body plethysmography, helium dilution, and nitrogen washout are more complex and expensive in installation, thus are often only available in clinics or pulmonary laboratories.

Standard guidelines of pulmonary function testing in adults and children are given by the European Respiratory Society (ERS) and American Thoracic Society (ATS) with the latest series of papers for adults and children published in 2005 [132, 133, 162, 218]. For infants, a series of seven articles have been carried out by the ATS/ERS Task Force in 2000 [13,59–61,137,190,198]. In 2007, an ATS/ERS consensus statement on pulmonary function testing in preschool children, mostly based on personal experiences [19], was published. ATS and ERS recommend the measurement of lung volumes during a spirometry test (forced vital capacity (FVC), forced expiration volume (FEV), and Tiffeneau-index), in combination with a bronchodilator or bronchial challenge test as the standard method to assess lung function in adults and children. Advanced PFTs require a higher level of system understanding and instrumentation [183]. Body plethysmography efficiently combines the measurement of residual lung volume and airway resistance and is considered as the gold standard for measurement of airway resistance. However, it should be noted that there is no standardization recommended by ERS/ATS for the use of direct parameters such as resistance or compliance to assess lung pathologies. Major

difficulties are the strong variation between measurement values among methods and devices, the invasiveness (in esophageal catheter technique), or the difficult interpretation of the measurement results (in FOT).

2.2.1 Spirometry

Spirometry is the most widely used method for the determination of lung volume in pulmonary function diagnostics because of the low expenditure on equipment and the simple handling. Modern spirometry is based on the continuous measurement of airflow at the airway opening over time via a pneumotachograph. Figure 2.12 shows a pneumotachograph of type Fleisch, which works with the principle of pressure gradient over a pre-defined flow resistance. The air flow is proportional to the pressure difference before and after the capillaries due to multiple capillary tubes with small diameters that ensure a laminar flow of air through the tube [133,139]. Pressures are captured by sensors and transduced to a computing unit. A subsequent integration of the flow over time allows the determination of the lung volumes. The resistance element is heated up to 37 °C to prevent water vapor condensation and droplet formation, and fit to the body moisture conditions.

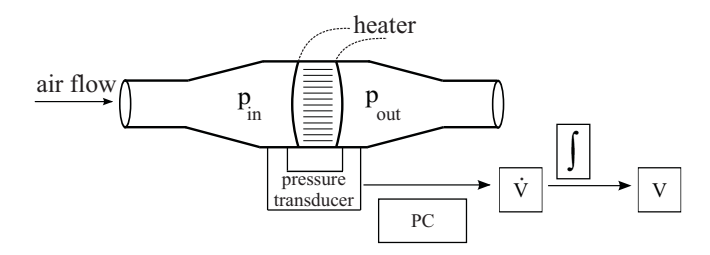


Figure 2.12: Schematic construction of a Fleisch-pneumotachograph.

The execution form of a spirometry test is called the Tiffeneau or forced expiratory maneuver. At the beginning of the test, subjects breath quietly through the spirometer while wearing a nose clips for nasal closing. After a few spontaneous breaths, subjects are asked to perform three consecutive forced expiration maneuvers, e.g. a fast exhalation from total lung capacity to residual volume with maximum effort. The forced expiratory volume can be determined after the first half second (FEV $_{05}$), after the first second (FEV $_{1}$), or over the whole lung vital capacity (FVC). Plotting flow over volume will generate the flow-volume (FV) loop (Fig. 2.13). The flow during expiration locates in the positive half-plane of the loop, the inspiratory flow in the negative half-plan.

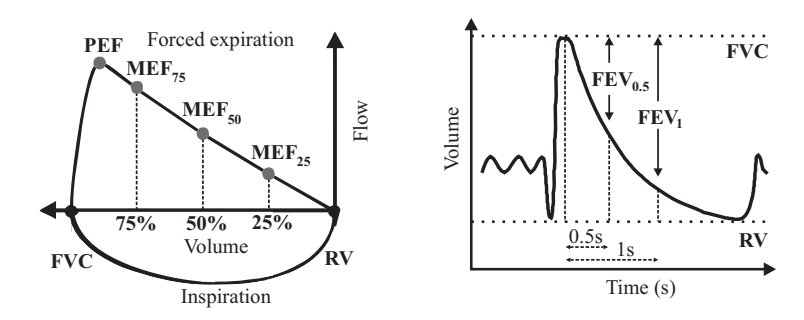


Figure 2.13: The flow-volume loop and the spirometric parameters.

Lung pathologies hide in the form of FV loops, as shown in Fig. 2.14.

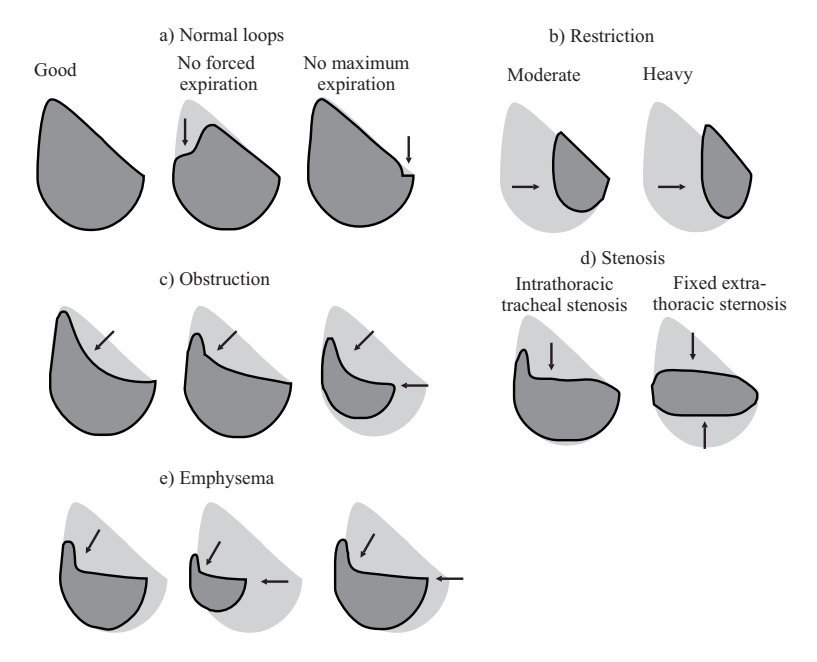


Figure 2.14: Illustration of different ventilation disorders in the flow-volume loop, redrawn from [183].

The Tiffeneau index (TI), calculated as the ratio FEV₁/FVC, serves as

a means of diagnosing lung diseases. According to the Global Initiative for Chronic Obstructive Lung Disease (GOLD), a TI of less than 0.7 is already an indication for COPD [160]. A second indicator for lung pathologies is the value of FEV₁ in percentage of the predicted reference value. This value is determined by means of regression equations regarding age, body height, and weight of the patient. Other diagnostic parameters are peak expiratory flow (PEF), as well as maximum expiratory flow at 75%, 50%, and 25% of FVC (MEF₇₅, MEF₅₀, and MEF₂₅, respectively). While the expiratory part of the healthy patient's loop shows a linear gradient, the asthmatic one has a concave drop (Fig. 2.14) [139]. This concavity becomes more pronounced depending on the severity of the obstruction.

The bronchodilator test utilizes spirometry to assess possible reversibility of bronchoconstriction in diseases such as asthma. Spirometry measurements are performed before and after the patients taking a dose of bronchodilator medication (such as 400 μg of salbutamol). An increase in FEV₁ of > 12% is considered a positive result.

2.2.2 Helium dilution and nitrogen washout methods

Helium dilution and nitrogen washout methods are pulmonary function tests which determine the functional residual capacity (FRC) of the lungs. Both have been standardized by the ATS/ERS [218]. The helium dilution technique is based on the idea that helium does not diffuse from the alveoli into the blood and thus is not affected by the gas exchange. During the test, the patient inhales a predefined helium volume in addition to the inhaled air. FRC is computed from the proportion of helium concentration before and after inhalation in the lungs [110, 218]:

$$FRC = V_{container} \frac{[He]_{before} - [He]_{after}}{[He]_{after}}$$
(2.6)

The second technique is based on washing out N_2 from the lungs, while patients inhale 100% O_2 . Lung volume at the start of washout can be calculated by the amount of N_2 washed out and the initial alveolar N_2 concentration [218].

2.2.3 Body plethysmography

The (whole) body plethysmography was introduced by DuBois in 1956 [42]. Besides the measurement of spirometric parameters, it provides the effective airway resistance ($R_{\rm aw}$), the specific respiratory resistance (sRaw), and the thoracic gas volume (TGV) [62,110]. While the measurements require trained medical personal, the patients' effort is reduced compared to spirometry.

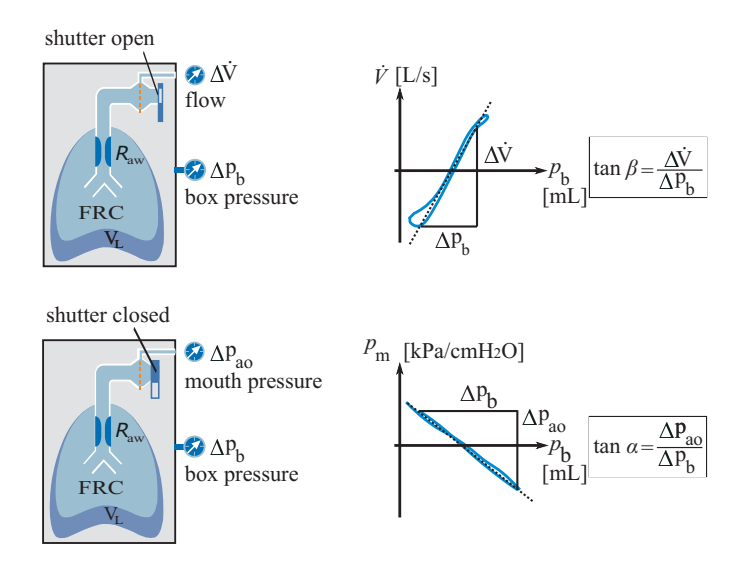


Figure 2.15: Determination of the airway resistance $R_{\rm aw}$ with the body plethysmography, modified from [35]. Top: shutter open, respiratory loop of airway flow against cabin pressure. Bottom: shutter closed, shutter-maneuver loop of airway pressure $p_{\rm ao}$ against cabin pressure $p_{\rm b}$.

The plethysmograph is a hermetically sealed cabin with an integrated pneumotachograph and a shutter. The box has a defined volume of air and a minimal leakage for pressure compensation caused by patient's body heat. During the test, the patient breathes quietly through a pneumotachograph, while flow, airway and cabin pressures are recorded. During inhalation, the patient's ribcage rises, the cabin volume falls and the box pressure increases. The intrathoracic gas volume (IGV) can be determined by the law of Boyle-Mariotte for isothermal gas $(P \cdot V = \text{const})$ [62, 110]. Considering the water vapor partial pressure in the lungs, $p_{\rm H_2O} = 6.27\,\mathrm{kPa}$, IGV can be computed as:

$$IGV = \frac{\Delta V_{\text{lung}}}{\Delta p_{\text{ao}}} \cdot (p_{\text{atm}} - 6.27 \,\text{kPa})$$
 (2.7)

The change in lung volume $\Delta V_{\rm lung}$ is not directly measurable and can be replaced by the product of the box pressure drop $\Delta p_{\rm b}$ and a calibration constant $K_{\rm body}$:

$$IGV = \frac{\Delta p_{\rm b}}{\Delta p_{\rm ao}} \cdot K_{\rm body} \cdot (p_{\rm atm} - 6.27 \,\text{kPa})$$
 (2.8)

During spontaneous breathing, an installed shutter is activated. The subject continues his normal breathing against the shutting valve. Since there is no pressure drop along the resistance element at that time, the alveolar pressure is equal to the mouth pressure. Plotting the flow and the airway pressure against the box pressure gives us the respiratory loops of the body plethysmography (Fig. 2.15). The airway resistance $R_{\rm aw}$ is computed as

$$R_{\rm aw} = \frac{\tan \alpha}{\tan \beta} \tag{2.9}$$

where α and β are obtained from the two respiratory diagrams. The specific airway resistance sRaw is the product of the airway resistance and the functional residual capacity (FRC) of the lungs:

$$sRaw = R_{aw} \cdot FRC. \tag{2.10}$$

An alternative body plethysmography introduced by Mead in 1960, measures lung volume change directly by having subjects breath in and out across the wall of the box [126]. Although Mead's body plethysmography provides the lung compliance as an additional parameter, calibration and execution of the measurements are more difficult compared to the DuBois's version. Mead's method is not widely used in the praxis nowadays.

2.2.4 Rapid interrupter technique

The rapid interrupter technique (or occlusion technique) was first introduced by Von Neergaard and Wirz in 1927 [215]. This technique relies on the fact that during a sudden airflow interruption at the airway opening, alveolar and mouth pressure will rapidly equilibrate. Figure 2.16 shows the pressure and flow obtained at the airway opening of a healthy subject. The interrupter was activated during a spontaneous inspiration. Two rises in $P_{\rm ao}$ can be observed. The respiratory resistance is computed as the quotient between the pressure drop immediately before and after closing the valve, and the flow at airway opening immediately before closing:

$$R_{\rm int} = \frac{\Delta P_{\rm ao}}{\dot{V}_{\rm ao}} \tag{2.11}$$

In the ATS/ERS statement on pulmonary testing in preschool children [19], the authors commented on the first rise $P_{\rm init}$ and the second rise $P_{\rm diff}$ of the pressure as follow: "During tidal breathing, $P_{\rm init}$, and thus $R_{\rm init}$, will include a component of both lung tissue and chest wall resistance, not only airway resistance. $P_{\rm diff}$ is due to the viscoelastic properties of the respiratory tissue

and reflects stress adaption (relaxation or recovery) within the tissues of the lung and chest wall, plus any gas redistribution (pendelluft) between pulmonary units with different pressures at the time of interruption [12, 88, 188]". This statement gives a rough explanation for the two rises in $P_{\rm ao}$ during occlusion. However, there is a lack of a mathematical explanation and a computer model, which is able to reconstruct those rises. In Chapter 3, we perform a model-based analysis to reevaluate the method and clarify the cause of the rises in $P_{\rm ao}$.

In infants and very young children, the execution of the occlusion technique is different due to the invoked Hering-Breuer Inflation Reflex (HBIR) during occlusion. In adults, HBIR is normally triggered to prevent over-inflation of the lungs. In infants, it occurs as soon as the airways are occluded at a positive endexpiratory lung level. The ATS/ERS standardization for infants recommends an occlusion at the end of inspiration [61]. The recommended calculation of the respiratory compliance C_{rs} and resistance R_{rs} assumes that (1) pressure at airway opening equals alveolar pressure during occlusion and (2) compliance is constant during spontaneous breathing. The second assumption can become problematic under pathological con-

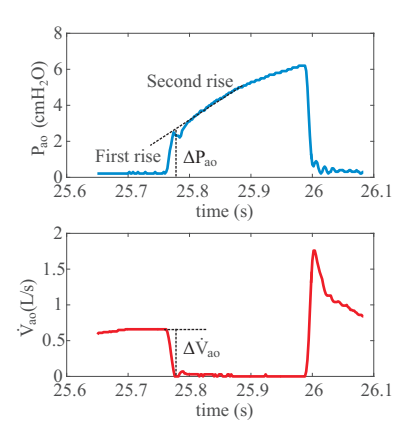


Figure 2.16: Pressure and flow measured at the airway opening during an interruption. Data obtained on a healthy subject with the Jaeger Masterscreen system.

ditions [47]. Instead of the single interrupter method, the multiple interrupter technique is recommended by many authors [47, 55, 154].

2.2.5 Esophageal catheter

The esophageal catheter method is based on the insertion of a pressure balloon catheter into the patient's esophagus. It is well accepted that the changes in the esophageal pressure are representative of changes in the pleural pressure $p_{\rm pl}$ applied to the lungs. In combination with a pneumotachograph, resistances

of the lungs and thorax are given as follow:

$$R_{\text{aw}} = \frac{p_{\text{pl}}(t) - p_{\text{mouth}}(t)}{\dot{V}(t)}$$

$$R_{\text{cw}} = \frac{p_{\text{mus}}(t) - p_{\text{pl}}(t)}{\dot{V}(t)}$$
(2.12)

$$R_{\rm cw} = \frac{p_{\rm mus}(t) - p_{\rm pl}(t)}{\dot{V}(t)}$$
(2.13)

Dependent on the breathing mode, either eq. (2.12) or eq. (2.13) can be applied. During spontaneous breathing, the pressure at airway opening is equal to the atmospheric one $p_{\text{mouth}} = p_{\text{atm}}$ while p_{mus} remains unknown. Hence, the airway resistance $R_{\rm aw}$ can be computed regarding eq. (2.12). During mechanical ventilation, the respiratory muscles are inactive $p_{\text{mus}} = 0$, eq.(2.13) can be applied to calculate the chest wall damping R_{cw} . Note that the tissue resistance $R_{\rm ti}$ is included in the airway resistance $R_{\rm aw}$ in eq.(2.12).

The accuracy of the esophageal catheter technique depends strongly on the correct localization of the balloon. Furthermore, the method is invasive, since either the patient needs to swallow the balloon or it is inserted through his nose. Although this technique

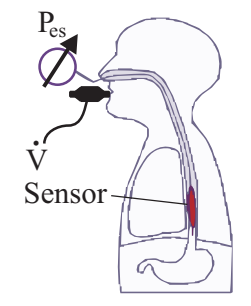


Figure 2.17: Measurement principle of the esophageal method.

can be useful for monitoring the intra-thoracic pressure during mechanical ventilation, the practical use of the esophageal catheter is limited. It has been used mostly in former clinical studies and animal trials.

2.2.6 Forced Oscillation Technique

The Forced Oscillation Technique (FOT) was first introduced by DuBois et al. in 1956 [43]. This noninvasive method is based on external small-amplitude oscillatory signals applied at the patient's mouth and superimposed on the spontaneous breathing. The oscillation signals can be sinusoidal (FOT), impulse (Impulse Oscillometry), or noise (Pseudo Random Noise). The absence of patient's cooperation necessity makes FOT attractive for examination during sleep, in infants or when breathing is difficult to control. Technical recommendations and clinical practice of this method is given in the ERS guidelines published in 2003 [155].

In FOT, the sinusoidal signals can include single or multiple frequencies. Measurements are conducted simultaneously to spontaneous breathing because the frequencies used are mostly more than 10 times higher than the respiration

rate and thus, can be easily separated from the respiratory rate. Due to linearity requirement of spectral analysis, FOT signals should remain in a relatively small amplitude range [119, 155].

Respiratory mechanical parameters are then assessed by spectral analysis of the resulting flow and pressure recorded at the patient's airway opening. The respiratory impedance $Z_{\rm rs}$ defined as the spectral ratio of the measured pressure and flow signals is divided into a resistance and reactance part:

$$Z_{\rm rs}(j\omega) = \frac{P_{\rm ao}(j\omega)}{\dot{V}_{\rm ao}(j\omega)} = Z_{\rm rs,R}(\omega) + jZ_{\rm rs,X}(\omega), \tag{2.14}$$

where ω is the oscillatory frequency. The resistance $Z_{\rm rs,R}$ describes the pressure-flow fraction of the part of the pressure signal in phase with the flow. The reactance $Z_{\rm rs,X}$ represents effects of both elastic and inertial forces which create a phase shift between pressure and flow signal [63]. At lower frequencies, $Z_{\rm rs,X}$ is dominated by elastic components. Above the resonance frequency $f_{\rm res}$, inertia has a stronger impact on the impedance [54].

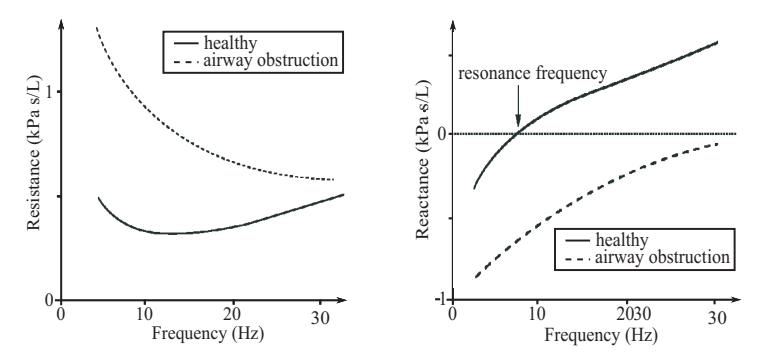


Figure 2.18: Resistance (left) and reactance (right) with respect to frequency measured with FOT, redrawn from [155].

Different studies have established impedance resistance disparities between healthy subject and individuals suffering from obstructive lungs diseases [73, 209] (Fig 2.18). In acute asthma, FOT may prove to be useful for assessing bronchodilator response [44,155]. However, a study in preschool children reported only a marginal correlation between the resistive impedance at 8 Hz and the asthma severity ratings [26]. FOT measurements also exhibit a poor correlation with the spirometric indices in children with cystic fibrosis [79, 195]. Hence, for FOT, the systematic relationship between the impedance $Z(j\omega)$ measured with FOT and other lung function parameters such as FEV₁ and

 $R_{\rm int}$ has not been understood. There is a lack on the physiological interpretation of the respiratory impedance $Z(j\omega)$.

2.3 Mechanical ventilation

Mechanical ventilation is the medical treatment where a technical machine is used to assist or replace spontaneous breathing. Mechanical ventilation has four main goals: (1) delivering oxygen to the alveoli, (2) removing carbon dioxide from the lungs, (3) providing mechanical work of breathing, and (4) maintaining pressure and volume in patients' lungs. Ventilators are most often used during surgery with general anesthesia, or for patients with impaired lung function (Pneumonia, COPD, ARDS, etc). In the 19th and 20th centuries, negative pressure ventilators or the iron lungs were widely used. The iron lung is a hermetically scaled metal chamber surrounding the patient's body with subatmospheric pressure for lung expansion [92,113,121]. Since the development of positive pressure ventilation and the intensive care unit in the 1960s, more than 174 different ventilation modes have been developed [134]. They can be classified in two main categories: assisted spontaneous breathing (ASB) and controlled-ventilation.

2.3.1 Continuous positive airway pressure (CPAP)

A typical form of ASB is the Continuous Positive Airway Pressure (CPAP), which applies a mild pressure on top of spontaneous breathing to keep the airways continuously open. CPAP is typically used for patients with obstructive sleep apnea and/or heart failure during sleep, usually through a nasal mask. Another form of CPAP with a pre-defined level of inspiration is the Biphasic Positive Airway Pressure (BiPAP) mode, as illustrated in Fig. 2.19.

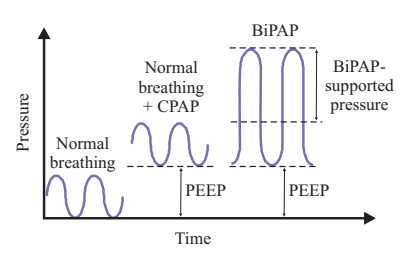


Figure 2.19: Spontaneous breathing, CPAP, and BiPAP.

2.3.2 Pressure- and volume-controlled ventilation

Pressure- and volume-controlled ventilation (PCV and VCV) are different control variables within a mode. In VCV, tidal volume is pre-set manually, while PCP allows the adjustment of ventilation pressure (positive inspiratory

pressure PIP and positive end-expiratory pressure PEEP). A mixed form is the pressure-regulated volume control, which applies VCV with an additional pressure-limited control. This form ensures a consistent tidal volume for dynamic alteration of lung mechanics during mechanical ventilation, and monitors the maximal pressure to reduce the risk of ventilation-induced lung injury.

2.4 Electrical Impedance Tomography

Electrical Impedance Tomography (EIT) is a noninvasive, radiation-free imaging technique which is based on the measurement of cross sectional impedance distribution of biological tissues. The response of a material exposed to external electric field depends on its electrical properties such as conductivity σ and permittivity ϵ :

$$\gamma(x,\omega) = \frac{1}{z(x,\omega)} = \sigma(x) + j\omega\epsilon(x), \qquad (2.15)$$

where γ is the admittivity, the inverse of the impedivity z,x is the position considered in the material and ω the excitation pulsation. Impedance tomography determines the impedance distribution inside the material using information measured at the element boundaries. Electrodes placed at the object circumference repeatedly send small alternating electrical currents while measuring the resulting surface voltages. The transfer impedances obtained are used to resolve the inverse problem of the distribution using to numerical reconstruction methods [22].

The first transmission image of the chest based on the impedance was introduced by Henderson and Webster in 1976. The measurement system had a 100-electrode matrix coupled with a single large electrode on the back and the front of the thorax, respectively [80]. In 1983, Brown *et al.* published the first tomographic images using current injection between adjacent electrodes with only 16 electrodes [6]. Since then, his method has been continuously studied and developed to enlarge the application fields and enhance the performance. EIT has become a very promising tool in bedside monitoring of lungs ventilation and perfusion [57, 73, 102, 112].

In 2011, Dräger Medical GmbH, Lübeck, Germany released the first EIT device for daily clinical use, the PulmoVista® 500, utilized for patient monitoring in intensive care settings. The PulmoVista 500 sequentially applies small alternating electrical currents (IEC 60601-1, $80-130\,\mathrm{kHz}$, automatically adjusted amplitude at approximately $5\,\mathrm{mA}$) through a pair of the 16 electrodes attached to a belt on the circumference of the patient's chest, and measures the difference of voltage between the remaining electrode pairs (Fig. 2.20 left). For each frame, 208 differential voltages are recorded, of which 104 are linearly

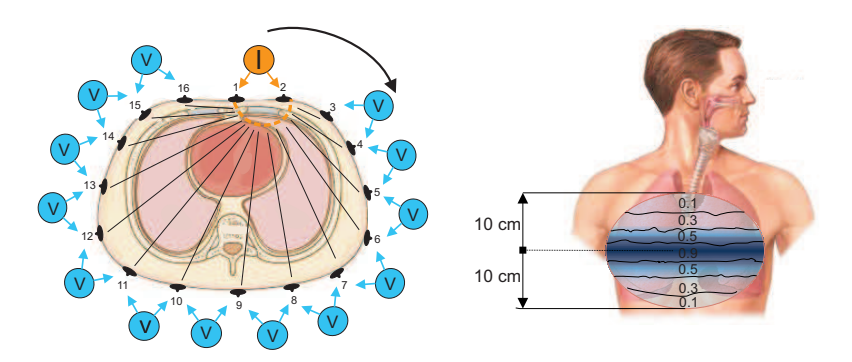


Figure 2.20: Left: Sequence of current injection and voltage measurement. Right: Effect of distance in impedance calculation.

independent due to reciprocity. The electrical impedance Z is obtained as the measured voltage V over the injected current I $(Z(t) = \frac{V(t)}{I(t)})$.

An integrated finite-element-method based on the linearized Newton-Raphson reconstruction algorithm can be used to reconstruct EIT images from the raw voltage signals (Fig 2.21). One image is obtained when all electrode pairs have been used to inject current. In general, around 10 cm over and below the electrode plane can be detected with EIT devices (Fig. 2.20, right panel) [203].

Once EIT images have been reconstructed, each pixel value of the 32x32 images is equal to the impedivity variation at this point with respect to a reference, which is the relative impedance value for each pixel (called impedance index or relative image pixel):

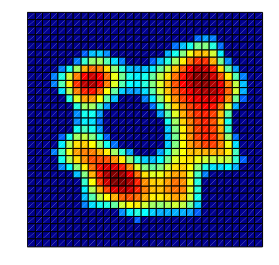


Figure 2.21: A reconstructed EIT image (32x32 pixel).

$$p(x,t) = \Delta z(x,t) = \frac{z(x,t) - z_{\text{ref}}(x)}{z_{\text{ref}}(x)}.$$
 (2.16)

The sum over all pixel is called the *global impedance index*:

$$\Delta Z(t) = \sum_{32\times32} \Delta z(x,t). \tag{2.17}$$

Many studies have investigated the relation between impedance values and pulmonary ventilation. In the 80s, Harris *et al.* showed that the global impedance index was highly correlated with the volume of air contained inside the lungs [73], which was confirmed later by different research groups [57,82]. In other words, the global impedance index can be linearly interpolated by the spirometry measurement obtained at the airway opening. Thanks to this relationship, it is possible to assess the airflow inside the lungs with EIT data.

Other researchers have also highlighted the local information given by EIT through the comparison of the right and left lung behavior [57,58]. Serrano et al. identified a volume difference between the compartments consistent with physiological data (47% to 53% for respectively the left and right lung) [186]. Kunst et al. compared EIT left-to-right ratio with radionuclide scanning and attested the reproducibility and reliability of EIT measurements for both perfusion and ventilation division [102].

2.5 Object-oriented modeling language for biophysical modeling

In this thesis, biophysical forward models are programmed in the object-oriented modeling language (OOML) Matlab SimscapeTM. OOML considers energy flow among the compartments in four-terminal representation [86]. It uses lumped elements to model physical quantities such as energy sources, storages, transformers, converters, and sinks. There are three types of equations in the four-terminal representation: balance, constitutive, and phenomenological equations [86]. The energy inflow, outflow, and storage of a system are described by balance equations. Constitutive equations characterize the energy flow between two potentials, or in other words, represent the mathematical relation between a through-variable (fluid flow, electrical current, chemical concentration changes) and an across-variable (potential, voltage, pressure) [86]. Phenomenological equations describe the sinks and losses of energy by dissipative elements, e.g. due to Ohm's law or Fick's law of diffusion.

In OOML, each model component is modeled by one or more constitutive equations (pressure-volume characteristics for compliances) or phenomenological equations (pressure-flow characteristics for resistance). A representative example is the Windkessel model of the vascular system [56] (Fig. 2.22). Blood from the arterial compartment $C_{\rm a}$ flows through the total peripheral resistance of the vascular bed $R_{\rm TPR}$ to the venous compartment $C_{\rm v}$. $P_{\rm a}$, $P_{\rm v}$, $P_{\rm sur}$ are the arterial, venous, and surrounding pressures, respectively. The balance

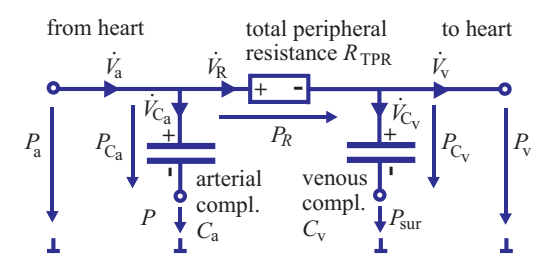


Figure 2.22: A simple model of a vascular system.

equations are given as:

The pressure-volume relation of the compliances $C_{\rm a}$ and $C_{\rm v}$ are described by the constitutive equations:

$$\Delta P_{\mathbf{C}_{\mathbf{a},\mathbf{v}}}(t) = \frac{1}{C_{\mathbf{a},\mathbf{v}}} \cdot \Delta V_{\mathbf{C}_{\mathbf{a},\mathbf{v}}}(t), \quad \text{or} \quad \dot{V}_{\mathbf{C}_{\mathbf{a},\mathbf{v}}}(t) = C_{\mathbf{a}} \cdot \frac{dP_{\mathbf{C}_{\mathbf{a},\mathbf{v}}}(t)}{dt}.$$

The phenomenological equation for the flow resistance R_{TPR} is given as

$$P_{\rm R}(t) = R_{\rm TPR} \cdot \dot{V}_{\rm R}(t) \tag{2.19}$$

In signal-based or text-based programming languages such as Simulink or C++, we need an explicit implementation of the balance equations. In SimscapeTM, these equations can be realized implicitly in the graphical structure of the model, thus no explicit implementation is required. In this case, the balance equations (2.18) are implicitly derived from Fig. 2.22. Electrical equivalent representation can be applied by replacing hydraulic elements by electrical ones, since pressure, volume, and flow correspond to voltage, charge, and current in the hydraulic-electrical analogy, respectively (Table 2.2). This simplification assumes a perfect Newtonian fluid, e.g. constant density and viscoelasticity, within a medium.

 $\textbf{Table 2.2:} \ \ \text{Correspondence between electrical and hydraulic (cardiorespiratory)} \\ \text{units.}$

Electrical	Unit	Hydraulic	Unit
Voltage U	V	Pressure gradient Δp	cmH ₂ O or mmHg
Current I	A	Flow \dot{V}	L/s
Charge Q	С	Volume V	L
Resistance R	Ω	Flow resistance R	$\rm cmH_2O/L/s$
Capacitor C	F	Compliance C	L/cmH ₂ O
Inductance L	Н	Inertance I	$\rm cm H_2 O/L/s^2$

3 Respiratory modeling

I'm an adventurer, looking for treasure.
Paulo Coelho

This chapter introduces a mathematical multi-compartment model of the respiratory system. The model is developed in order to gain better understanding of respiratory mechanics and lung pathologies. The development of the model comprises compartmentalization, non-linear characterization of the components, parametrization, and validation. At the end of the chapter, a model-based analysis for reevaluation of the interrupter technique is presented to exemplarily demonstrate the use of the model.

Parts of the chapter were previously published in a peer-reviewed journals [146].

3.1 Non-linear model components

A lumped model of the respiratory system is a set of ordinary differential equations (ODEs) that describe precisely the behavior of the lungs. With respect to system complexity, a compartmentalization of the respiratory tract ensures a lumped structure. Figure 3.1 illustrates the abstraction of lung mechanics from the physiological view (left) to the physical compartment structure (right).

3.1.1 Airways and airspaces

The human airways are divided into the upper airways and the bronchial tree separated by the larynx. The bronchi tree is subdivided into central bronchi (first 5 generations, N=0-4) and peripheral bronchi (next 11 generations, N=5-15). Generations 16-23 (or 16-26 in the Hansen-Ampaya model [71]) shape the respiratory bronchioles and alveoli. Regarding their mechanical properties and physiological functionalities, it is adequate to subdivide the airways and airspaces into three compartments: the central compartment (including upper airways and central bronchi), the peripheral compartment, and the alveoli (Fig. 3.2).

Volume of the airway/airspace compartments.

The upper airways are small in volume (approx. 70 mL including a nasal volume of 31 mL [207]). Bronchial volume for each generation can be estimated by the morphometric data of Weibel [219], Hansen [71], or Yeh and Schum [226].

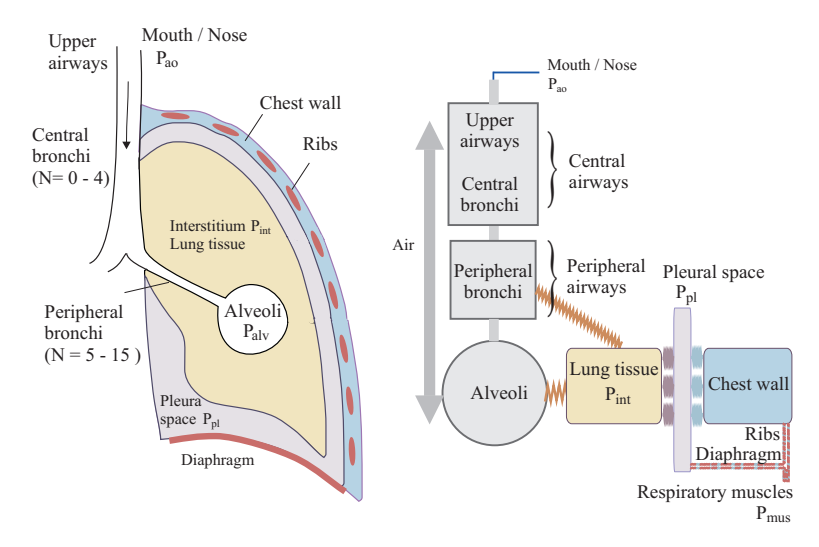


Figure 3.1: Compartmentalization of the respiratory system. N = generation number.

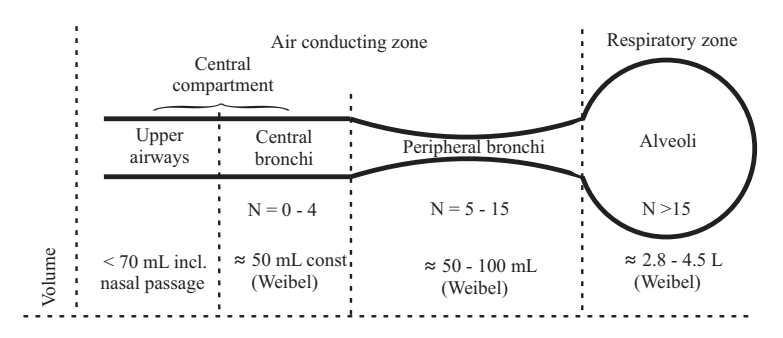


Figure 3.2: Airway compartments with generation number and volume.

Table 3.1 displays the resulting volume for central and peripheral bronchi as well as alveoli.

The Weibel model proposes a volume of approx. $V_{\rm c}=49$ mL (1.6 %) for the central bronchi, $V_{\rm b}=59$ mL (2 %) for the peripheral airways, and $V_{\rm alv}=2864$ (95 %) mL for the alveoli at a total lung gas volume of $V_{\rm lung}=3$ L. Increasing $V_{\rm lung}$ from 3 L to 4.76 L, the central bronchial volume remains constant, while

1135.8

5336.67

49.4

32.9

$V_{\text{lung}} = \text{total lung volume}, V_{\text{c}} = \text{volume of the central bronchi}, V_{\text{b}} = \text{volume of the peripheral bronchi}, and V_{\text{alv}} = \text{alveolar volume}.$						
		$V_{\rm lung}$	$V_{\rm c}$	$V_{ m b}$	$V_{ m alv}$	$\frac{V_{\mathrm{alv}}}{V_{\mathrm{b}}}$
		(mL)	(mL)	(mL)	(mL)	
Weibel	inspi.	3002	48.73	58.77	2863.5	
	expir.	4759	50.51	94.09	4583.4	
	ΔV	1757	1.78	35.32	1719.9	48.7
Hansen &	inspi.	2696.5	49.1	51.9	2564.5	
Ampaya	expir.	3856.7	50.5	74.9	3700.3	

1160.2

5563.88

 ΔV

total

Yeh & Schum

Table 3.1: Volume of the airway and airspace compartment, regarding the geometrical structure models of Weibel, Hansen & Ampaya, and Yeh & Schum. $V_{\text{lung}} = \text{total lung volume}, V_{\text{c}} = \text{volume of the central bronchi}, V_{\text{b}} = \text{volume of the peripheral bronchi}, and <math>V_{\text{alv}} = \text{alveolar volume}.$

the peripheral bronchi and alveoli compartments expand proportionally to lung volume. For healthy adults, the fraction $V_{\rm alv}/V_{\rm b}$ can be considered as constant under quasi-static conditions, when air flow in system is close to zero:

1.4

64.98

$$\frac{V_{\text{alv}}}{V_{\text{b}}} = \text{const} \quad >> 1. \tag{3.1}$$

23

162.23

This fraction can change dramatically in high dynamic processes such as during forced expiration maneuvers, where the peripheral bronchi above the equal pressure point (EPP) collapse partly. The concept of EPP, introduced by Mead in 1967 [131], explains the existence of a limited maximum flow during the forced expiration maneuver.

The airway and airspace compliances can be derived for pressure and lung volume changes, e.g. during spontaneous breathing. As shown in Table 3.1, Weibel and Hansen & Ampaya proposed the following relation between the static compliances of the central, peripheral, and alveolar compartments C_c , C_b , $C_{\rm alv}$:

$$C_{\rm c}/C_{\rm alv} = \Delta V_{\rm c}/\Delta V_{\rm alv} \approx 0.001 \approx 0,$$
 (3.2)

$$C_{\rm alv}/C_{\rm b} = \Delta V_{\rm alv}/\Delta V_{\rm b} \approx 30 - 50. \tag{3.3}$$

Independent from the works of Weibel and Hansen & Ampaya, Vogel and Smidt proposed the values $C_{\rm alv}=0.2$ and $C_{\rm b}=0.004\,{\rm cmH_2O/L/s}$ for normal healthy subjects [210]. This results in the same fraction $C_{\rm alv}/C_{\rm b}\approx 50$ as reported in the Weibel and Hansen & Ampaya models.

It seems that the fraction $C_{\rm alv}/C_{\rm b}$ has not gained much attention in recent lung researches. However, as shown in later chapters of this work, this fraction

plays a key role in the simplification of model structure and hence, the interpretation of the measurement data obtained with the interrupter and forced oscillation techniques. Model-based detail analysis will be discussed in later chapters.

Flow pattern and flow-dependent resistance

The air velocity in the lungs depends on the geometry of the lungs as well as the applied pressure gradient which creates the air flow. In most situations, gas in the lungs can be considered as Newtonian fluid (incompressible, constant density), unless a high thoracic pressure is created by the muscles while the mouth is closed. The value of the Reynold number determines if the flow is in laminar, transitional, or turbulent regime. Details on flow patterns are explained in Appendix A.2.

Figure 3.3 depicts the Reynold number against the generation number for normal (0.1 L/s) and heavy (1.667 L/m) breathing, as reported in [38]. The normal breathing rate of 0.1 L/s is calculated by twelve breathings of 0.5 L in one minute. According to this diagram, the flow in all airways is laminar during normal breathing. During heavy exercise, while flow in the peripheral airways remains laminar, flow in the central bronchi becomes transitional and turbulent .

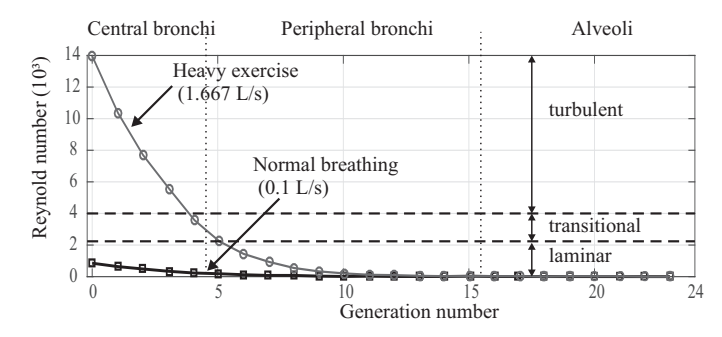


Figure 3.3: Reynold number of flow in the bronchial tree. Redrawn from [38].

A more detailed diagram was reported by Pedley et al. in [161], where airways resistances were predicted as a function of airway generation regarding the Weibel model (Fig. 3.4). The diagram proposed a flow-independent resistance for small airways (N \geq 10), and a flow-dependent resistance for large airways (N \leq 6) at high flow. The middle airway generations (7–10) belongs to a transitional regime: more airways become flow-dependent when the flow

becomes higher. For simplification, the flow-dependent fraction of the middle airways will be considered as a part of the central compartment.

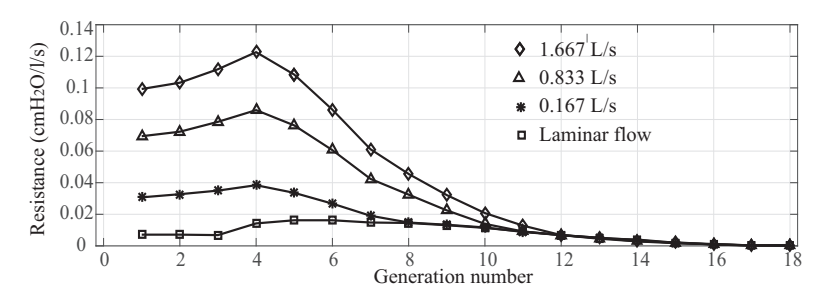


Figure 3.4: Predicted airway resistance as a function of airway generation at different flows. Reproduced and redrawn from [161].

In total, the central compartment consists of upper airways (mouth or nasal passage, glottis, larynx) and the first 5 generations of the bronchial tree. They have rigid wall ($C_c \approx 0$), thus are considered to be volume-independent. The central resistance R_c is given as follow:

$$\Delta P = R_{c}\dot{V} = K_{c,1}\dot{V} + K_{c,2}\dot{V}^{2}$$

$$R_{c} = K_{c,1} + K_{c,2}\dot{V},$$
(3.4)

where $K_{\rm c,1}$ and $K_{\rm c,2}$ are the laminar and turbulent coefficients. Liu [114] estimated these parameters in four healthy subjects and reported average values for $K_{\rm c,1}=0.345\,{\rm cm}H_2{\rm O/L/s}$ and $K_{\rm c,2}=0.325\,{\rm cm}H_2{\rm O/L^2/s}$.

Volume-dependent peripheral resistance

Considering the peripheral bronchi as a cylinder which can constrict and dilate uniformly, its resistance can be determined by the Hagen-Poiseuille equation of fluid dynamics for laminar flow:

$$R_{\rm p} = \frac{8\mu L}{\pi r^4} \,,\tag{3.5}$$

where $R_{\rm p}$ is the peripheral resistance, μ the dynamic viscosity, L the length and r the radius of the tube. In their models, Liu et al., Athanasiades et al., and Lu et al. proposed a proportional relation $R_{\rm p} \sim V_{\rm p}^{-2}$ regarding $V_{\rm p}^2 \sim r^4$ [4,114,117], with $V_{\rm p}$ the volume of the peripheral airways. Although this consideration is useful to describe turbulent flow during forced expiratory maneuvers, it is incorrect for laminar flow. Indeed, since L does not remain constant when

lung volume increases, $R_{\rm p} \sim L r^{-4}$ and $V_{\rm b} \sim L r^2$ occur, which leads to the relation $R_{\rm p} \sim V_{\rm p}^{-1}$. Widdicombe et al. derived a general term for the peripheral resistance [224]:

$$R_{\rm p} = \frac{K_{\rm p,b}}{V_{\rm b}},$$
 (3.6)

where $K_{\rm p,b}$ [cmH₂Os] is a positive constant and estimated to be 0.0014 cmH₂O .min or 0.084 cmH₂Os [224]. If the relation $V_{\rm alv}/V_{\rm b} \approx {\rm const}$ remains, eq. (3.6) can be rewritten as:

$$R_{\rm p} = \frac{K_{\rm p,b}}{V_{\rm b}} = \frac{K_{\rm p}}{V_{\rm lung}},$$
 (3.7)

where $K_{\rm p}$ is another positive constant. For $K_{\rm p,b}=0.084\,{\rm cmH_2O\,s}$ and $V_{\rm lung}/V_{\rm b}\approx 50$ (Weibel), $K_{\rm p}$ can be estimated as $K_{\rm p}=0.084\cdot 50=4.2\,{\rm cmH_2O\,s}$.

Briscoe and Dubois studied the relation between total airway resistance $R_{\rm aw}$ and lung volume in 26 subjects of all ages [23] including 585 measurements with a body plethysmograph. They found that $R_{\rm aw}$ ranges from $2.9V_{\rm lung}^{-1}$ to $7.7V_{\rm lung}^{-1}$ in these subjects. They also reported a linear relation between airway conduction $G_{\rm aw} = 1/R_{\rm aw}$ and lung volume, which leads to the concept of a constant specific airway conductance, as introduced in Chapter 2:

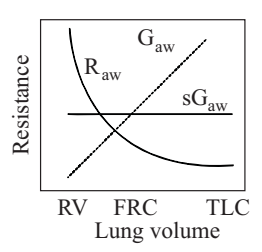


Figure 3.5: Relationship between airway conductance G_{aw} , specific airway conductance G_{aw} , airway resistance R_{aw} , and lung volume, as can be found in literature. RV = residual volume. FRC = functional residual capacity. Redrawn from [94,98].

$$G_{\text{aw}} = 1/R_{\text{aw}} = KV_{\text{lung}}, \quad sG_{\text{aw}} = G_{\text{aw}}/V_{\text{lung}} = K = \text{const.}$$
 (3.8)

The finding of Briscoe and Dubois (Fig. 3.5) is generally accepted and can be found in many textbooks of physiology.

However, the subdivision of the airways into the central and peripheral compartment conflicts with the diagram in Fig. 3.5. The central compartment, especially the upper airways, consist of rigid tubes, and are therefore volume-independent. There is a need to investigate the exact contribution of the central compartment in the airway resistance-volume characteristics. Considering

eq. (3.4) and (3.7), the airway conductance G_{aw} can be rewritten as:

$$G_{\text{aw}} = \frac{1}{R_{\text{aw}}} = \frac{1}{R_{\text{c}} + R_{\text{p}}} = \frac{1}{R_{\text{c}} + \frac{K_{\text{p}}}{V_{\text{corr}}}}$$
 (3.9)

As a plausibility test, we reconstruct the data published by Bricose and Dubois in one subject (named J.Z.) [23] and perform Least Squares regression for two mathematical models eq. (3.8) and (3.9). The results, illustrated in blue and red in Fig. 3.6, are K=4.7899 with the squared 2-norm of the residual $\sum e^2=0.642$ in the original model and $R_{\rm c}=0.1275$, $K_{\rm p}=4.4515$, and $\sum e^2=0.6211$ in the compartmentalized model. Similarly, the new conductance-volume curve differs slightly from the linear original one with a smaller residual error (0.0746) against the original model (0.0936). The black lines in Fig. 3.6 depict the resistance and conductance simulated with $R_{\rm c}=0.345$ (reported in [4]) and $K_{\rm p}=4.2$ (as calculated above). Though the values come from different independent reports, its form and dimension fit the measured data (Fig. 3.6).

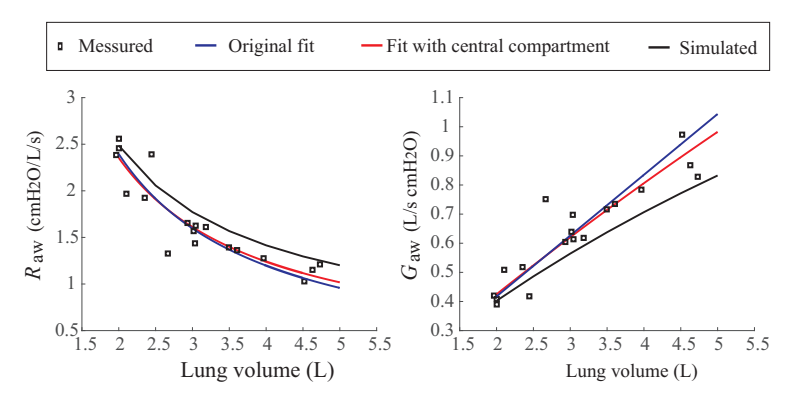


Figure 3.6: Resistance, conductance, and specific conductance against lung volume. Least-squares regressions were performed for the original model of Briscoe and Dubois [23], and our model considering the central airway resistance.

This example demonstrates that the subdivision of airway resistance into a volume-independent, central resistance and a volume-dependent, peripheral resistance is not only more physiological, but can also provide a better fit on experimental data. Hence, the assumption of a linear relationship between $G_{\rm aw}$ and $V_{\rm lung}$ should be replaced by the model shown in eq. (3.9), especially in cases of upper airway obstruction. More investigations on larger data should be taken to confirm this hypothesis.

Static pressure-volume relationship of the peripheral bronchi

In 1988, Gunst and Stropp [66] investigated the pressure-volume (PV) relationship measured in separated canine bronchi segments. This PV curve consists of three phases: collapse, normal (linear), and over-distension (Fig.3.7). Such a behavior can be modeled with a tangent hyperbolic (tanh) or a logarithmic (ln) function:

$$V_{\rm b} = V_0 + 1/\lambda \cdot \tanh(c \cdot P_{\rm tr,b} + P_0) \tag{3.10}$$

or
$$V_{\rm b} = 1/\lambda \cdot \ln(c \cdot P_{\rm tr,b} + P_0) + V_0,$$
 (3.11)

where $V_{\rm b}$ is the bronchial volume and $P_{\rm tr,b}$ the transmural pressure. The parameters V_0 , P_0 , c and λ can be used to adjust the form of the PV curve.

Figure 3.7 shows a fit of the tanh function to the data from [66]. This curve outlines the dependencies of the bronchial volume on the pressure gradient between the intra-thoracic and bronchial pressures. During the collapsed and overextension phases, a large change in the pressure gradient results in a small change in the bronchial volume.

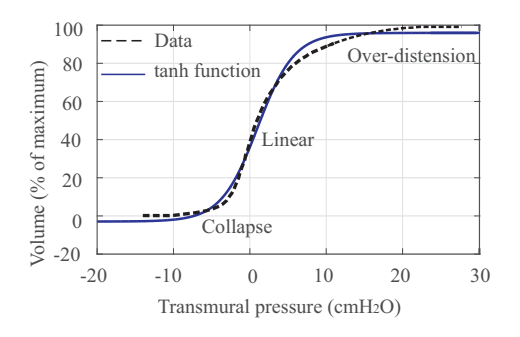


Figure 3.7: Pressure-volume relationship of the peripheral bronchi. Data taken from [66]

Model structure of airways and airspace

The model structure for air

flow in the airways and airspace is illustrated in Fig. 3.8. Entering the peripheral bronchi, the air flow is divided into two components: one passes through the bronchi and reaches the alveoli, and one expands the bronchi. The volume and flow relations are given as:

$$V_{\text{lung}}(t) = V_{\text{c}}(t) + V_{\text{b}}(t) + V_{\text{alv}}(t) \rightarrow \dot{V}_{\text{lung}}(t) = \dot{V}_{\text{b}}(t) + \dot{V}_{\text{alv}}(t)$$
 (3.12)

Eq. (3.12) states a parallel structure between $V_{\rm b}$ and a series of $R_{\rm p}$ and $C_{\rm alv}$, which is known as the Mead's parallel structure [128, 130]. The bronchi and alveoli compliances separate the material inside from the material outside. While air flow corresponds to the left side of the compliances ($C_{\rm b}$ and $C_{\rm alv}$) in Fig. 3.8, bronchi and alveoli are tethered to the surrounding interstitium which, in our model, is assumed to be homogeneous for bronchi and alveoli.

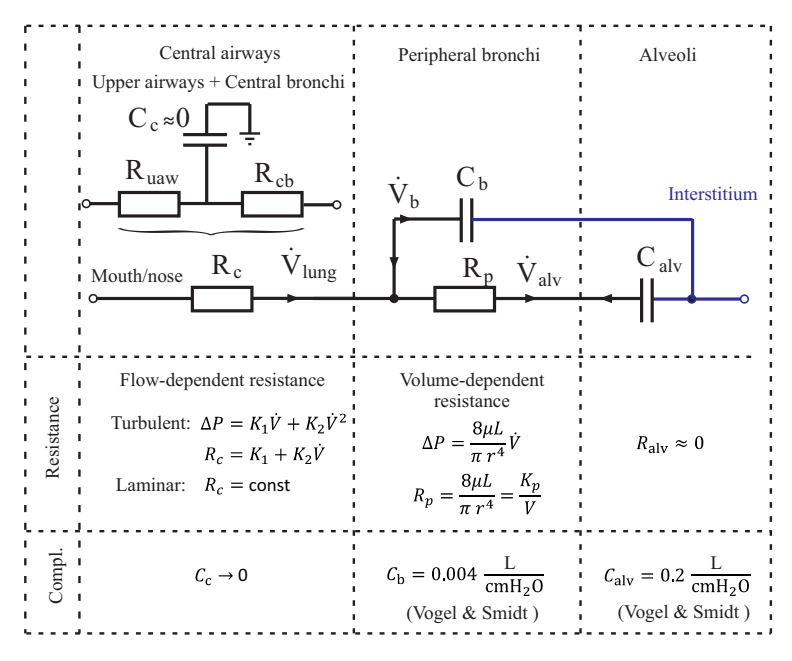


Figure 3.8: Model structure of airways and airspaces and their main components.

3.1.2 Tissue and chest wall

The respiratory system consists of three components: the gas (airways and airspace), the tissue enclosing the airways and airspace, and the chest wall enclosing the lungs (Fig 3.1). The change in volume of one part is equal to that of the other parts [127]:

$$\dot{V}_{cw}(t) = \dot{V}_{ti}(t) = \dot{V}_{lung}(t) = \dot{V}_{b}(t) + \dot{V}_{alv}(t).$$
 (3.13)

Eq. (3.13) indicates a serial structure among airways/airspace, tissue, and chest wall.

Separation of alveoli and interstitial tissue

One of the earliest investigation on the (quasi)-static relation of alveoli and interstitial tissue was carried out by von Neergaard [214]. He compared expiratory pressure-volume curves of air-filled and liquid-filled lungs and empha-

sized the importance of surface tension in the air-liquid interface. However, the role of surfactant on the reduction of the surface tension was not clear at that point. In 1954, Ted Radford reported that the surface area, which was calculated morphometrically, was about one order higher than the expected value, i.e. the surface tension at the alveolar wall was much lower than estimated by von Neergaard. One year later, Pattle published a paper in *Nature* stating the existence of "extracts" from the lungs which could reduce the surface tension [158, 159].

Figure 3.9 illustrates an inflationdeflation loop measured from a single, excised cat lung [172]. While the pressure-volume loop of the salinefilled lung (i.e. only tissue) is mostly linear without any significant difference between inflation and deflation, the air-filled lung exhibits the typical lung hysteresis. From residual volume, an opening pressure of about 9cmH₂O was required to open the airways. Cyclic closing and reopening of the lungs should be prevented in protective ventilation. The use of small tidal volume and inspiratoryexpiratory pressure gradient on an adequate PEEP is recommended by the Open Lung concept, introduced by Lachmann in 1992 [103].

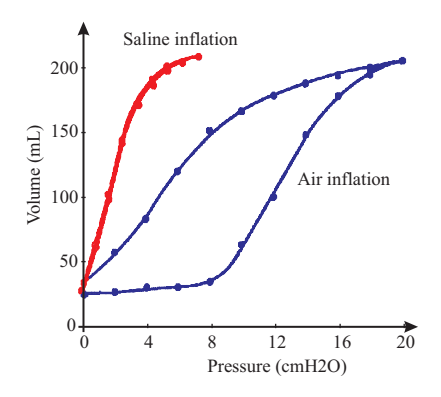


Figure 3.9: Inflation-deflation pressure-volume loop measured from a single cat lung, reproduced and redrawn from [172]. A pressure at about $9\,\mathrm{cm}\,\mathrm{H}_2\mathrm{O}$ was required to open the airways.

Although a separation of tissue elastance and alveolar surface tension is reasonable to describe the quasi-static behavior of the lungs, recent models in literature consider the elasticity of the lungs as one compartment [4,111,114,117,169,204]. In these models, the bronchial compliance is directly connected to the pleural pressure, which is unphysiological, since the bronchi are surrounded by the interstitial tissue. These arguments lead to a novel serial structure of bronchial/alveoli and lung tissue, as shown in Fig. 3.10.

As mentioned above, the PV characteristics of lung tissue without alveolar impact can be experimentally determined by filling the alveoli with isotonic saline. By reducing the surfactant concentration and thus the surface tension, lung compliance increases threefold [68,177] from 0.2 L/cmH₂O [68,114] to 0.6 L/cmH₂O. This component, representing the elasticity of the elastic tissue must be as high or larger than this value.

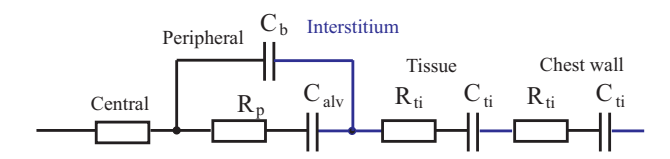


Figure 3.10: The serial structure airways/airspaces-tissue-chest wall.

Alveolar compliance

Although the mechanical behavior of alveoli surface tension has been investigated by multiple research groups [95, 103, 140, 151, 201, 228], it is not yet completely understood [27]. In their works, Yuta [228] and Sundaresan et al. [201] assumed that the main cause of lung volume change during spontaneous breathing is the recruitment of alveoli, not the expansion of the opened alveoli. In our approach, the alveoli charac-

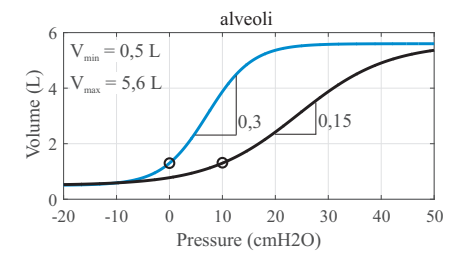


Figure 3.11: Pressure-volume characteristics of the alveoli [142].

teristics are considered as one non-linear component, which models the system behavior of both recruiting and expending alveoli. The PV characteristics of lung alveoli can be described by the following hyperbolic function:

$$V_{\text{alv}}(t) = V_0 + \frac{1}{\lambda} \cdot \tanh(\mathbf{c} \cdot P_{\text{tr,alv}}(t) + P_0), \tag{3.14}$$

where $V_{\rm alv}(t)$ and $P_{\rm tr,alv}(t)$ are the alveolar volume and transmural pressure, respectively. The parameters V_0 , λ , c and P_0 can be determined by maximum and minimum lung volume, as well as maximum alveoli compliance.

Fig. 3.11 depicts the alveolar characteristics. The upper line represents the alveolar compliance curve, and the lower one the compliance of diseased lungs, such as in edematous patients [32, 228]. The black circles in Fig. 3.11 illustrate residual lung volume (RV = 1.3 L [68]). The minimal volume of 0.5 L corresponds to the state when the lungs are separated from the thorax and are completely collapsed. This approach does not yield any contradiction with the balloon-like theory or the recruitment model [228]. It should be noted that the

alveolar hysteresis, as well as surface tension reduction regarding surfactant is not in the focus of this work. A simplification is made by applying a tanhfunction to describe the alveolar pressure-volume relationship. This can be extended in future works by replacing this characteristics with a more complex approach, without affecting other model compartments such as tissue, airways, and chest wall.

Tissue and chest wall visco-elastic resistance

The total respiratory resistance can be divided into airway and visco-elastic resistances by means of measurements via body plethysmography and the forced oscillation technique. The visco-elastic resistance, which accounts for less than 43% of the total resistance [54], is a combination of lung and chest wall (including thoracic and abdominal) tissue damping. Ferris et al. performed measurements on test subjects using needles introduced to the trachea, the alveoli, and the pleural surface to separate these components of the resistance [51]. They reported that the chest wall resistance, which is linear up to flow rates of 2 L/s, accounts for 10-19% of the total resistance during nasal breathing and less than 19% during mouth breathing. They also found a low, insignificant pulmonary tissue resistance, as shown in Fig. 3.12. Hence, $R_{\rm ti}\approx 0$ is considered in our model.

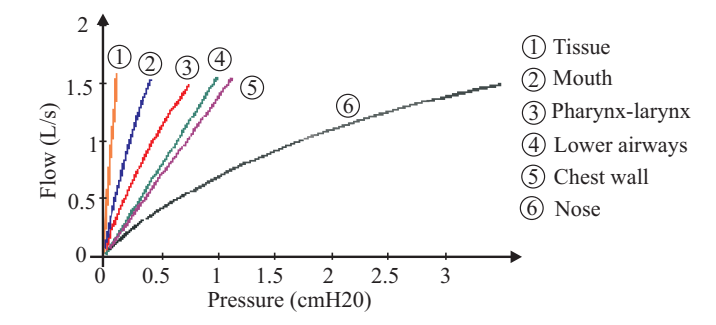


Figure 3.12: Flow-pressure relationship of respiratory segments, reproduced and redrawn from [51]. A high slope describes a low air flow resistance.

Lung-chest wall quasi-static interactions and the pleural space

In 1946, Rahn et al. introduced the pressure-volume diagram of the thorax and the lung [173], as shown in Chapter 2. The chest wall compliance C_{cw}

provides the elasticity of the components surrounding the lungs, i.e. thorax and diaphragm. According to Athanasiades et al. [4], the non-linear pressure-volume curve of $C_{\rm cw}$ is sigmoidal and can be modeled by

$$P_{\rm tr,cw}(t) = A_{\rm cw} - B_{\rm cw} \cdot \log(\frac{\rm TLC - RV}{V_{\rm cw}(t) - \rm RV} - 0.999).$$
 (3.15)

The chest wall compliance C_{cw} is given as follow:

$$C_{\text{cw}}(t) = \frac{\text{TLC} - \text{RV}}{\text{B}_{\text{cw}}} \cdot \frac{\exp(\frac{A_{\text{cw}} - P_{\text{tr,cw}}(t)}{\text{B}_{\text{cw}}})}{[\exp(\frac{A_{\text{cw}} - P_{\text{tr,cw}}(t)}{\text{B}_{\text{cw}}}) + 0.999]^2}.$$
 (3.16)

TLC is the total lung capacity, RV is the lung residual volume, A_{cw} and B_{cw} are constants. Applying parameters given in [4] will result in a maximum chest wall compliance of $0.3 \text{ L/cmH}_2\text{O}$, which is comparable with the average value of approx. $0.2 \text{ L/cmH}_2\text{O}$ given in literature [68, 96, 173].

The parameter A_{cw} from [4] causes a pressure drop over the chest wall $P_{cw} = 0\,\mathrm{cm}H_2\mathrm{O}$ and a pleural pressure $P_{\mathrm{pl}} = 0\,\mathrm{cm}H_2\mathrm{O}$ at normal filling volume of the lungs. In normal condition of 3 L lung volume, a negative pleural pressure $P_{\mathrm{pl}} \approx -5\,\mathrm{cm}H_2\mathrm{O}$ occurs [68]. In other words, the lungs are stretched and the chest wall is shrunk at FRC. Models which use two compliances in series need to be extended to present this negative pleural pressure. One solution is the introduction of the extended pleural pressure source P_{PE} , which incorporates the pre-stress of the chest walls and lung tissue. If P_{PE} is set to $10\,\mathrm{cm}H_2\mathrm{O}$, the pressure gradient between chest wall and lung tissue will be around this physiological value [96]. This pleural-extended model succeeds in not only presenting the well-known PV characteristics of the chest (Fig. 3.14), but also a negative pleural pressure of $P_{\mathrm{pl}} \approx -5\,\mathrm{cm}H_2\mathrm{O}$.

It should be noted that P_{PE} does not present any physiological pressure source within the pleural space, but rather the preload of lung and chest wall at FRC. Another, equivalent way to model the negative pleural pressure is to initialize the lungs and chest wall with a starting volume and modify the pressure-volume relationship with a shift in that volume.

3.2 The two-degree-of-freedom model

The degree of freedom (DOF) of a mechanical system is the number of independent variables which are needed to describe that system entirely. The configuration of the respiratory system as a series of the airways/airspace, the tissue, and the thorax can be expressed in terms of one single variable, the volume. In this consideration, the respiratory system has one DOF. The bronchial-alveolar parallel-structure gives the system another DOF. The overall structure of the 2-DOF model is illustrated in Fig. 3.13. $R_{\rm p}, C_{\rm b}, C_{\rm alv}$, and $C_{\rm cw}$ are non-linear components.

The 2-DOF model is especially useful for simulating lung mechanics during spontaneous breathing and mechanical ventilation, where the respiratory rate does not exceed 1 Hz (60 cycles per minute). High frequency components of the respiratory system such as inertance, upper shunt compliance (cheek vibration) are insignificant in this frequency range.

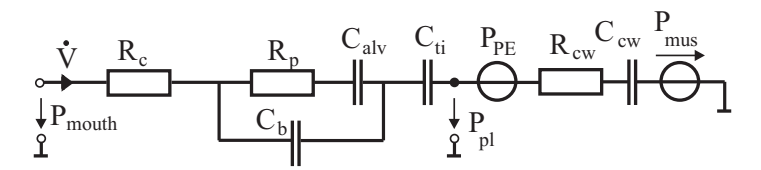


Figure 3.13: The two-degree-of-freedom lung model for low (physiological) frequencies. $R_{\rm p}, C_{\rm b}, C_{\rm alv}$, and $C_{\rm cw}$ are non-linear components.

3.2.1 Parametrization and implementation

For a healthy human during spontaneous breathing, parameter values may be obtained from literature by the following considerations:

- A constant central resistance $R_c = 1 \,\mathrm{cm} H_2 \mathrm{OL}^{-1} \,\mathrm{s}$ is assumed, which is approximately 25% of the airway resistance [68].
- The peripheral resistance R_p is given by eq. (3.7). The cumulative volume of the peripheral airways is estimated to be about 50 mL. At this volume, peripheral resistance is approx. 75% of the airway resistance [68].
- The pressure-volume characteristics of the bronchi and alveoli are given in eq. (3.11) and eq. (3.14). Parameters are given in Tables 3.2 and 3.3.
- Lung tissue compliance is assumed to be constant $C_{\rm ti} = 1\,{\rm L/cmH_2O}$.
- The extended pleural pressure is modeled as constant $P_{\rm PE}=10\,{\rm cm}H_2{\rm O}.$

The total respiratory compliance is given as:

$$\begin{split} \frac{1}{C_{\text{total}}} &= \frac{1}{C_{\text{lung}}} + \frac{1}{C_{\text{cw}}} \\ &= \frac{1}{C_{\text{tissue}}} + \frac{1}{C_{\text{b}} + C_{\text{alv}}} + \frac{1}{C_{\text{cw}}}, \end{split}$$

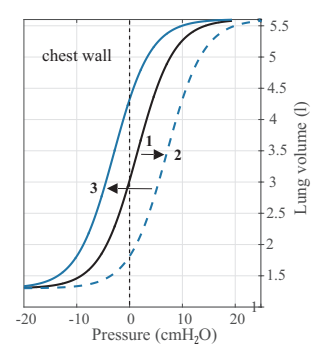


Figure 3.14: Implemented chest wall compliance according to [4]: (1) is the original curve; (2) is the curve after adaption of A_{cw} , and (3) after adaption of P_{PE} . P_{pl} is negative at lung volume < 4.25 L [142].

The maximum value of $C_{\rm total}$ is equal to 0.23 L/cmH₂O in our model.

With the introduction of P_{PE} , A_{cw} needed to be adapted to achieve the original chest compliance curve (Fig. 3.14). The parameters of the chest wall and pleural space are given in Table 3.4.

Respiratory muscles

Consisting of the diaphragm and the intercostal muscles, the respiratory muscles provide the pressure gradient to inflate and deflate the lungs. In the proposed model, the pressure source is connected to the chest wall $C_{\rm cw}$ on one side and to the atmosphere at the body surface on the other side. The alignment of the pressure source in the circuit can be chosen corresponding to a negative or positive $P_{\rm mus}$. With the alignment shown in Fig. 3.13, $P_{\rm mus}$ becomes more negative during inspiration, causing a fall in pleural pressure which drives air into the alveoli and enlarge the thorax cavity. Since the pleural pressure $P_{\rm pl}$ has been shown to have an exponential form in healthy subjects [96], $P_{\rm mus}$ is also likely to have an exponential form.

The implementation of $P_{\rm mus}$ is illustrated in Fig. 3.15. A periodic rectangular pulse generator and a resistance-compliance (RC) network (Voigt model of visco-elastic behavior) is used to generate the signal.

Resistance		Compliance		
	Value	Parameter	Value	
V_1	0.05	V_0	-0.0872	
R_1	3	P_0	7.4414	
V_{\min}	0.005	λ	18.3776	
		Popen	5	

Table 3.2: Parameters of the collapsible airways

Table 3.3: Parameters of the alveoli compartment.

Parameter	Value	Unit
V_0	3.05	L
λ	0.3922	L^{-1}
c	0.1176	-
P_0	-0.8409	$\rm cm H_2 O$

Table 3.4: Parameters of the chest wall and pleural space.

Parameter	Value	Unit
TLC	5.6	L
RV	1.3	L
Acw	7	$\rm cmH_2O$
B_{cw}	3.5	$\rm cm H_2 O$
P_{PE}	10	$\rm cmH_2O$

3.2.2 Simulation results

Dynamic and static behaviors of the respiratory system

To demonstrate the behavior of the respiratory system during spontaneous breathing, a simulation is performed with a respiratory rate of $0.2 \,\mathrm{Hz}$ (12 breaths/min) and inspiration time of 2s. The amplitude of P_{mus} is set to $5 \,\mathrm{cmH_2O}$. Figure 3.16 illustrates the simulative results including lung volume, alveolar, interstitium, and pleural pressure.

During inspiration, pleural and alveolar pressures decreases below $P_{\rm atm}$, so that air enters the lungs and loads the compliances. At the end-inspiratory phase, minimal pressures occurs equal to $P_{\rm int} = -7.1~{\rm cmH_2O}$ in the interstitium and $P_{\rm pl} = -8.3~{\rm cmH_2O}$ in the pleural space. FRC is 2.5 L, and tidal volume

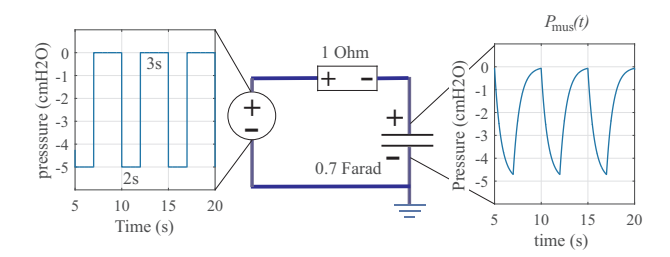


Figure 3.15: The respiratory muscles P_{mus} during spontaneous breathing, generated by a pulse generator and a RC network [142].

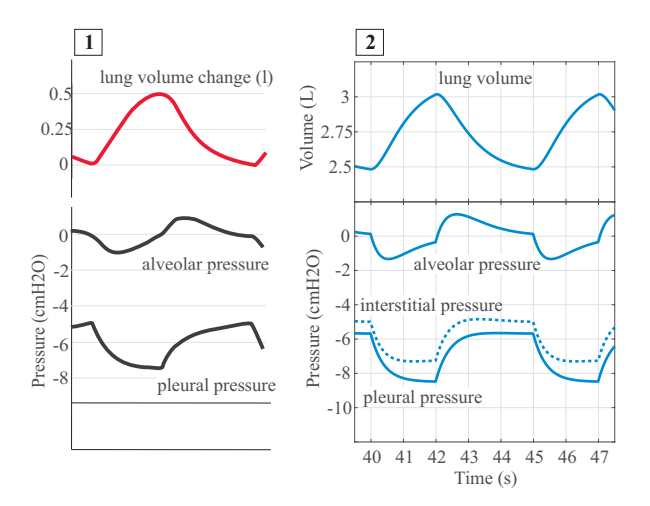


Figure 3.16: Respiratory pressures and volumes during spontaneous breathing [142]. (1): Literature values, reproduced from [68], (2) Simulation results with a functional residual capacity of 2.5 L.

 $V_{\rm T}$ is 500 mL. At end-expiration ($t\approx45~s$), the pleural pressure is $P_{\rm pl}=-5.74~{\rm cmH_2O}$, the interstitial pressure $P_{\rm int}=-4.94~{\rm cmH_2O}$, and the alveolar pressure is slightly positive $P_{\rm alv}=0.015~{\rm cmH_2O}$. All values and dynamics described in [68] can be simulated successfully.

Static pressure-volume relationship during mechanical ventilation

During mechanical ventilation, the monitoring of lung mechanics via PV characteristics is important, since lung over-stretching can occur if airway pressure exceeds $30\,\mathrm{cmH_2O}$ [17]. For simulation purposes, a model of the mechanical ventilator is constructed, which can provide pressure-controlled or volume-controlled ventilation modes. Incremental increases of PEEP and PIP are applied to investigate the dynamic response of lung mechanics to PEEP. The respiratory muscles are deactivated as soon as mechanical ventilation starts. The total respiratory compliance C_{total} was calculated as the quotient of the tidal volume V_{T} and the overall pressure drop [111]:

$$C_{\text{total}} = \frac{V_{\text{T}}}{\text{PIP} - \text{PEEP}}.$$
 (3.17)

Analogously, lung compliance is the quotient of $V_{\rm T}$ and the pressure drop over the lung, which was measured continuously during the simulation.

Figure 3.17, top three diagrams present the results including alveolar and pleural pressure, lung volume, and lung and total compliance. Fig. 3.17, bottom panel presents the simulated static PV characteristics of lungs and chest wall compared to literature data reconstructed from [96]. At FRC, the pressure of lungs and thorax are opposite and equal, which results in a zero overall pressure.

 $P_{\rm pl}$ becomes positive at high ventilation pressures $P_{\rm ven}>15\,{\rm cmH_2O}$. Total compliance decreases from $0.124~{\rm L/cmH_2O}$ at PEEP= 0 to $0.03~{\rm L/cmH_2O}$ at PEEP= 25 cmH₂O due to the implementation of non-linear compartments. As a result of this stiffness change, tidal volume falls from 1.241 L (PEEP=0) to $0.272~{\rm L}$ (PEEP=25). The mean pressure and volume of each PEEP setting fit exactly in the static PV-relationship of lung and thorax. The operating point of the system moves upwards from A (PEEP=0) to F (PEEP=25) regarding the increasing PEEP. Simulation results demonstrate the ability of the model to quantify the non-linear change in tidal volume and compliance during a PEEP-trial.

3.2.3 The linearized respiratory model

Linearization and parametrization

Applying the model for spontaneous breathing with normal tidal volume, the non-linear behavior in pressure-volume or pressure-flow relationships can be replaced by linear resistances and compliances. The result of this process is the linearized model. For simplification, we keep the same notation for the linear model as used in the non-linear one. In high dynamic measurement techniques

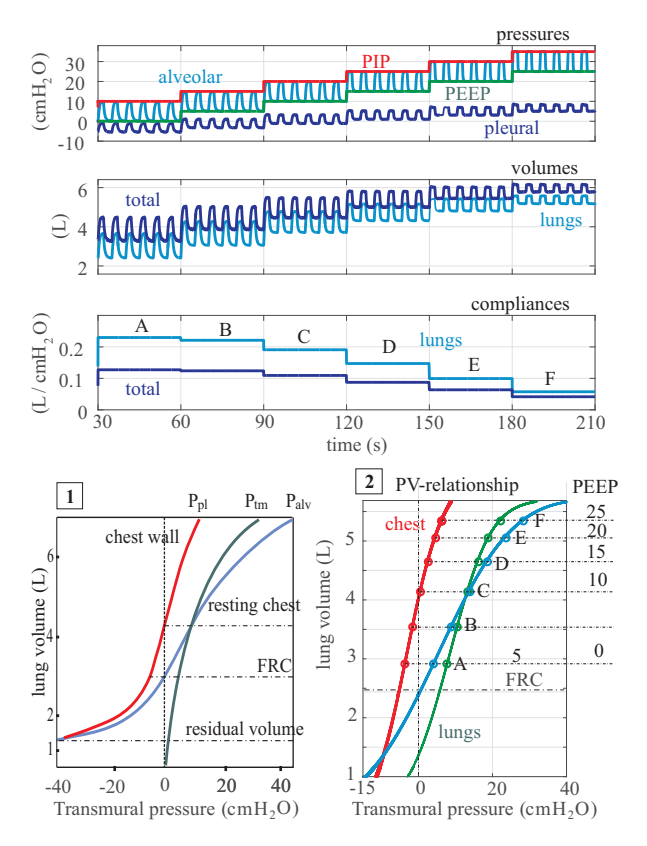


Figure 3.17: Top three diagrams: ventilation pressures, lung volumes and compliance during a PEEP trial. PEEP was incrementally increased from 0 to 25 cmH₂O, PIP was set equal to PEEP +10 cmH₂O. Bottom graph: Static pressure-volume loop of lung and chest wall. (1): Literature values, reproduced from [96], (2): Simulation results. A-F mark the operating points of the system for each set of PEEP and PIP [142].

such as interrupter or forced oscillation technique, the system inertance I and upper airway compliance (cheek vibration) $C_{\rm mouth}$ need to be considered. The new linear model is illustrated in Fig. 3.18.

Typical parameter values of the linear model are:

•
$$C_{\text{cw}} = 0.3$$
; $R_{\text{cw}} = 1$

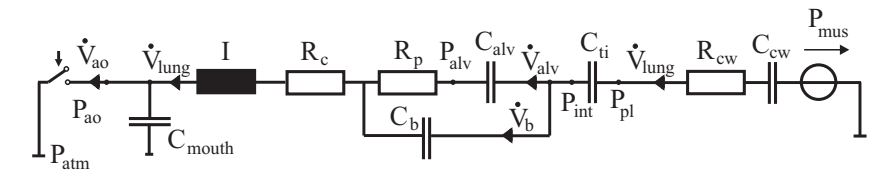


Figure 3.18: The linear lung model with inertance and upper shunt compliance.

- $C_{\text{ti}} = 1$; $C_{\text{alv}} = 0.2$; $C_{\text{b}} = 0.004$
- $R_p = 2$; $R_c = 0.15$; I = 0.01.
- C_{mouth} is between 0.0001667 (cheek supported and 0.001 (cheek unsupported)).
- The overall resistance and compliance of the system are

$$R_{\rm rs} = R_{\rm c} + R_{\rm c} + R_{\rm cw} = 0.35$$
 $C_{\rm lung} = (C_{\rm alv} + C_{\rm b})||C_{\rm ti} = 0.1667$
 $C_{\rm rs} = C_{\rm lung}||C_{\rm chest} = 0.1$
(3.18)

Resistances, inertance, and compliances are given in $cmH_2O/L/s$, $cmH_2O/L/s^2$, and L/cmH_2O , respectively. Values are taken by linearizing the non-linear model as well as from literature [10, 210].

Alteration of model parameters under pathological conditions

Model parameters alter under pathological conditions. The following alterations, which correspond to clinically relevant diagnoses, are of interest [210]:

- Central obstruction: increase in central resistance $R_c = 5$ (grade 1); $R_c = 10$ (grade 2).
- Peripheral obstruction: increase in peripheral resistance, main cause of asthma and COPD, $R_{\rm p}=5$ (grade 1); $R_{\rm p}=10$ (grade 2).
- Pulmonary restriction: reduction of alveolar or tissue compliance $C_{\rm alv}=0.02;\,C_{\rm ti}=0.01.$
- Thoracic restriction: reduction of thoracic compliance $C_{\text{cw}} = 0.03$.

- Bronchial sclerosis: decrease in bronchial compliance $C_b = 0.002 0.008$.
- Non-obstructive emphysema (over-extension): increase in $C_{\rm alv}$ and decrease in $C_{\rm b};\,C_{\rm alv}/C_{\rm b}\gg 50.$
- Obstructive emphysema (non-obstructive emphysema and obstruction): $C_{\rm alv}/C_{\rm b}\gg 50$ and $R_{\rm p}=5$.

Resistances, inertance, and compliances are given in $cmH_2O/L/s$, $cmH_2O/L/s^2$, and L/cmH_2O , respectively.

3.3 Model application: analysis of the interrupter technique

This section analyses the behavior of the respiratory system in the time domain aiming to reevaluate the interrupter technique. As introduced in section 2.2, this technique provides the resistance based on the assumption that the pressure at airway opening $P_{\rm ao}$ equilibrates the alveolar pressure $P_{\rm alv}$ directly after an occlusion. According to Marshall and Dubois [123], the interrupter method measures the total resistance of the whole respiratory system, including airways, lungs, and chest wall. In the original researches of Bates and Sly [10,12,14,18,188], which are the basics of the ATS/ERS official statement [19], the authors introduced a computer model of two compartments using the Otis parallel structure. By setting inhomogeneous airway resistances for each lung ($R_1 = 3R_2$), they suggested that the pendelluft between two lungs is the main cause of the second rise in $P_{\rm ao}$ after an occlusion. Since these models contain only airways without any consideration of lung tissue, chest wall, and respiratory muscles, their explanation on $P_{\rm diff}$ seems to be incomplete.

In fact, there is another, widely accepted opinion, that the second rise in $P_{\rm ao}$ is caused by the respiratory muscles [163]. During the occlusion, these muscles continue their activities, since the duration is short enough not to cause any nervous response. Hence, the interrupter technique is also used in mechanical ventilation to measure the pressure generated by respiratory muscles in ventilated patients [115, 116, 163]. The airway occlusion pressure $P_{0.1}$ measured during the first 100 ms after the occlusion has been reported to play an important role in patient weaning [85, 180].

In this section, we extend our 2-DOF model to describe the system dynamics during interrupter measurements. The aim of this section is to clarify the role of the respiratory muscles and the pendelluft phenomenon in the second rise in $P_{\rm ao}$.

3.3.1 Model behavior during an interruption

The equations of motion of the linear system (Fig. 3.18) are given as:

$$P_{\text{mus}}(t) - P_{\text{ao}}(t) = P_{\text{tr,cw}}(t) + R_{\text{cw}}\dot{V}_{\text{lung}}(t) + P_{\text{tr,ti}}(t) + P_{\text{tr,alv}}(t) + R_{\text{p}}\dot{V}_{\text{alv}}(t) + R_{\text{c}}\dot{V}_{\text{lung}}(t) + I\ddot{V}_{\text{lung}}(t)$$
(3.19)

$$P_{\text{tr b}}(t) = P_{\text{tr alv}}(t) + \dot{V}_{\text{alv}}(t)R_{\text{p}} \tag{3.20}$$

$$P_{\text{tr.mouth}}(t) = P_{\text{ao}}(t). \tag{3.21}$$

 $P_{\rm tr,b}$ and $P_{\rm tr,mouth}$ are the transmural pressure over the compliance $C_{\rm b}$ and $C_{\rm mouth}.$

Let t_s be the closing time, t_s^- the moment shortly before and t_s^+ the moment shortly after closing. The pressures over compliances and the respiratory muscles do not change during the closing process, i.e.:

$$P_{\text{mus}}(t_{s}^{-}) = P_{\text{mus}}(t_{s}^{+})$$

$$P_{\text{tr,cw}}(t_{s}^{-}) = P_{\text{tr,cw}}(t_{s}^{+})$$

$$P_{\text{tr,ti}}(t_{s}^{-}) = P_{\text{tr,ti}}(t_{s}^{+})$$

$$P_{\text{tr,alv}}(t_{s}^{-}) = P_{\text{tr,alv}}(t_{s}^{+}).$$
(3.22)

Applying eq. (3.19) for $t = t_s^-$ and $t = t_s^+$ and subtracting them from each other leads to:

$$P_{\text{ao}}(t_{\text{s}}^{-}) - P_{\text{ao}}(t_{\text{s}}^{+}) = (R_{\text{cw}} + R_{\text{c}})(\dot{V}_{\text{lung}}(t_{\text{s}}^{+}) - \dot{V}_{\text{lung}}(t_{\text{s}}^{-})) + + R_{\text{p}}(\dot{V}_{\text{alv}}(t_{\text{s}}^{+}) - \dot{V}_{\text{alv}}(t_{\text{s}}^{-}) + I(d(\dot{V}_{\text{lung}}(t_{\text{s}}^{+}) - \dot{V}_{\text{lung}}(t_{\text{s}}^{-}))/dt)$$
(3.23)

Let $\Delta P_{\rm ao} = P_{\rm ao}(t_{\rm s}^-) - P_{\rm ao}(t_{\rm s}^+)$ and $\Delta \dot{V}_{\rm lung} = \dot{V}_{\rm lung}(t_{\rm s}^+) - \dot{V}_{\rm lung}(t_{\rm s}^-)$ be the flow and pressure gradients before and after the closing of the interrupter. The bronchial volume $\dot{V}_{\rm b}$ is small compared to that of the lung $\dot{V}_{\rm lung}$ (eq. (3.3) and eq. (3.1)), i.e. the alveolar and total volume can be considered to be equal: $\dot{V}_{\rm alv} = \dot{V}_{\rm lung} - \dot{V}_{\rm b} \approx \dot{V}_{\rm lung}$. Eq. (3.23) becomes:

$$\Delta P_{\text{ao}} = (R_{\text{c}} + R_{\text{p}} + R_{\text{cw}}) \Delta \dot{V}_{\text{alv}} + I(d(\Delta \dot{V}_{\text{alv}})/dt)$$
(3.24)

The first term describes the resistive behavior between the pressure and flow drops before and after an occlusion. The second term $I(d(\Delta V_{\rm lung,s})/dt)$ corresponds to a Dirac-impulse in $\Delta P_{\rm ao,s}$ at $t=t_{\rm s}$ caused by the inertance I. Neglecting the second term and considering that the flow at the airway opening becomes zero directly after shutting (perfect valve closing, $\dot{V}_{\rm alv}(t_{\rm s}^-)=0$, $\Delta \dot{V}_{\rm alv}=\dot{V}_{\rm alv}(t_{\rm s}^+)$), eq. (3.24) becomes:

$$\Delta P_{\text{ao}} = (R_{\text{c}} + R_{\text{p}} + R_{\text{cw}})\dot{V}_{\text{alv}}(t_{\text{s}}^{+}) = (R_{\text{c}} + R_{\text{p}} + R_{\text{cw}})\dot{V}_{\text{ao}}(t_{\text{s}}^{+}). \tag{3.25}$$

Comparing eq. (3.25) with eq. (2.11) shown in Chapter 2:

$$R_{\rm int} = \frac{\Delta P_{\rm ao}}{\dot{V}_{\rm ao}},$$

the relationship of the interrupter resistance R_{int} and other resistance components can be derived as:

$$R_{\rm int} = R_{\rm c} + R_{\rm p} + R_{\rm cw} \tag{3.26}$$

Eq. (3.24) shows that the interrupter resistance, calculated by the quotient of the pressure gradient over flow drop immediately before and after closing of the interrupter, is the sum of airway resistance and chest wall tissue resistance. The chest wall component $R_{\rm cw}$ includes approx. 30-40% of the total resistance, thus contributes a significant fraction to the total resistance. During bronchial challenge or bronchodilator test, the chest wall component is less affected than the airway resistance. This explains why $R_{\rm int}$ is less sensitive than the specific airway resistance sRaw measured with the body plethysmography during diagnostics of airway obstruction, since sRaw contains only airway resistance without any visco-elastic damping components [97]. We should keep this point in mind when performing the interrupter technique.

To analyze the cause of the second rise in $\Delta P_{\rm ao,s}$, a random time instant t between closing and reopening $t_{\rm s} < t < t_{\rm r}$ is considered. During this period, all flows in the system remain zero ($\Delta \dot{V}_{\rm lung} = \Delta \dot{V}_{\rm alv} = 0$), thus eq. (3.19) becomes

$$P_{\text{mus}}(t) - P_{\text{ao}}(t) = P_{\text{tr,cw}}(t) + P_{\text{tr,ti}}(t) + P_{\text{tr,alv}}(t)$$
 (3.27)

Since all flows are zero, the volume of the chest wall, tissue, airway and airspace compartments remain unchanged, and so do the transmural pressures $P_{\rm tr,cw}$, $P_{\rm tr,ti}$, and $P_{\rm tr,alv}$, i.e.:

$$P_{\text{mus}}(t) - P_{\text{ao}}(t) = \text{const} \quad \text{for} \quad t_{\text{s}} < t < t_{\text{r}}$$
(3.28)

Eq. (3.28) indicates that the second rise in $P_{ao}(t)$ is equal to the change in $P_{mus}(t)$ during the closing period. This shows that the respiratory muscles play a mayor role in the second rise and can not be ignored in the model, as referenced in the ATS/ERS document [10, 188].

3.3.2 Simulation-based analysis of the interrupter technique

Eq. (3.24) and (3.26) present the mathematical background of the ideal interrupter technique. In real measurements, several disturbing factors caused by the system inertance, the imperfect closing process of the shutter, the upper airway (cheek) compliance, the bronchial compliance, and the pendelluft between left and right lung occur. Matlab SimscapeTM provides a sophisticated tool to investigate the influences of these disturbances.

Effect of the respiratory muscles

First, we demonstrate an ideal interruption, in which the inertance, mouth and bronchial compliances are set to zero. An interruption during inspiration is realized at $t=t_{\rm S}=17.4~\rm s$ for $0.2~\rm s$ by an ideal switch-element in SimscapeTM. The closing and releasing processes are also assumed to be ideal. Simulation results for spontaneous breathing are shown in Fig. 3.19. In the left graphic, $P_{\rm mus}$ is set to normal spontaneous breathing pressure as shown in Section 3.2. In the right graphic, $P_{\rm mus}$ remains constant while the shutter is closed. This holding corresponds to the Hering-Breuer Inflation Reflex in infants and young children (see Section 2.2.4). Note that in infants, an expiration starts directly after a HBIR inspiratory pause, which is not considered in the simulation.

In the left graphic, flow and pressure change abruptly after closing the valve at $t=17.4~\rm s$. The pressure exhibits two rises: one jump direct at the moment of closing and one ramp between 17.4 s and 17.6 s. As a contrast, the right graphic, simulating a constant $P_{\rm mus}$ during interruption, does not exhibit any ramp in $P_{\rm ao}$ after the first jump. This pressure remains unchanged for constant $P_{\rm mus}$.

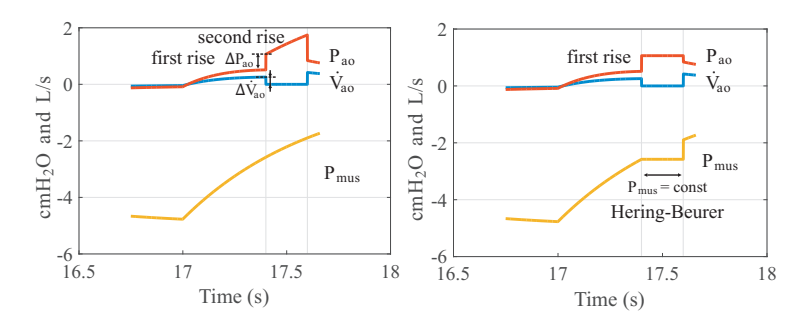


Figure 3.19: Flow and pressure at airway opening, as well as respiratory muscles $P_{\rm mus}$ during an ideal interrupter. Shutter is closed at 17.4 s and released at 17.6 s. Left: normal $P_{\rm mus}$. Right: $P_{\rm mus}$ is hold as constant while the shutter is closed.

The interrupter (total) resistance can be computed as the ratio $\Delta P_{\rm ao}/\Delta \dot{V}_{\rm ao}$ marked in the left graphic. The simulation results demonstrate that the second rise in $P_{\rm ao}$ is directly related to the change in the respiratory muscles $P_{\rm mus}$. While the first rise is believed to related to the airway resistance and the second rise to the tissue resistance in some literatures, as reviewed in [101], our model-based analysis and simulation results strongly support another physiological explanation: the interrupter resistance, which causes the first rise, consists of

airways and tissue/chest wall damping, while the second rise is caused primarily by the respiratory muscles.

Effect of disturbances

Pressure and flow measured at airway opening are affected by several disturbance factors: inertance, bronchial and upper airways, and imperfect valve closing. These effects can be demonstrated by adding disturbing components to the model. The simulation results are depicted in Fig. 3.20.

- Figure 3.20 (A) presents the effect of the inertance I (eq.(3.24)) as a
 Dirac-impulse, appearing directly after valve closing.
- The effect of the bronchial compliance C_b can be analyzed considering V

 > 0 (compared to eq. (3.23)). This models the distention of the bronchi
 right after closing the valve. A charging process occurs between alveolar
 and bronchial compartments right after closing the valve with the time
 constant τ_b given as:

$$\tau_{\rm b} = R_{\rm p} \cdot \frac{C_{\rm b} \cdot C_{\rm alv}}{C_{\rm b} + C_{\rm alv}} \tag{3.29}$$

 $\tau_{\rm b}$ has a typical value at $2 \cdot \frac{0.20.004}{0.204} = 0.0078$ s. This value is ten times smaller than the normal duration of an interruption (100 ms). Figure 3.20 (B) displays the charging process caused by $C_{\rm b}$. The small time constant makes this disturbance relatively insignificant to the measurement.

 Similar to the bronchi, the upper airway (cheek) is also distended during the valve closing process. Its time constant is related to resistances and compliances of the entire system C_{mouth}:

$$\tau_{\text{mouth}} = (R_{\text{c}} + R_{\text{p}} + R_{\text{cw}}) \cdot \frac{1}{\frac{1}{C_{\text{cw}}} + \frac{1}{C_{\text{ti}}} + \frac{1}{C_{\text{alv}}} + \frac{1}{C_{\text{mouth}}}}.$$

$$\approx R_{\text{int}} \cdot C_{\text{mouth}}, \quad \text{since} \quad C_{\text{mouth}} \ll C_{\text{alv}}, C_{\text{ti}}, C_{\text{cw}}(3.30)$$

The typical value of $\tau_{\rm mouth}$ is estimated to be around 3.1 ms for small $C_{\rm mouth}=0.001$ (with supported cheek) and 28.6 ms for large $C_{\rm mouth}=0.01$ (without supported cheek). Although a small cheek compliance is insignificant for the measurement of pressure, as shown in Fig. 3.20 (C), an unsupported cheek can cause a delay in the result, as displayed in Fig. 3.20 (D). In contrast to the bronchi, the effect of the cheek compliance on the results can vary among measurements due to the execution of the test and the cooperation of the patient.

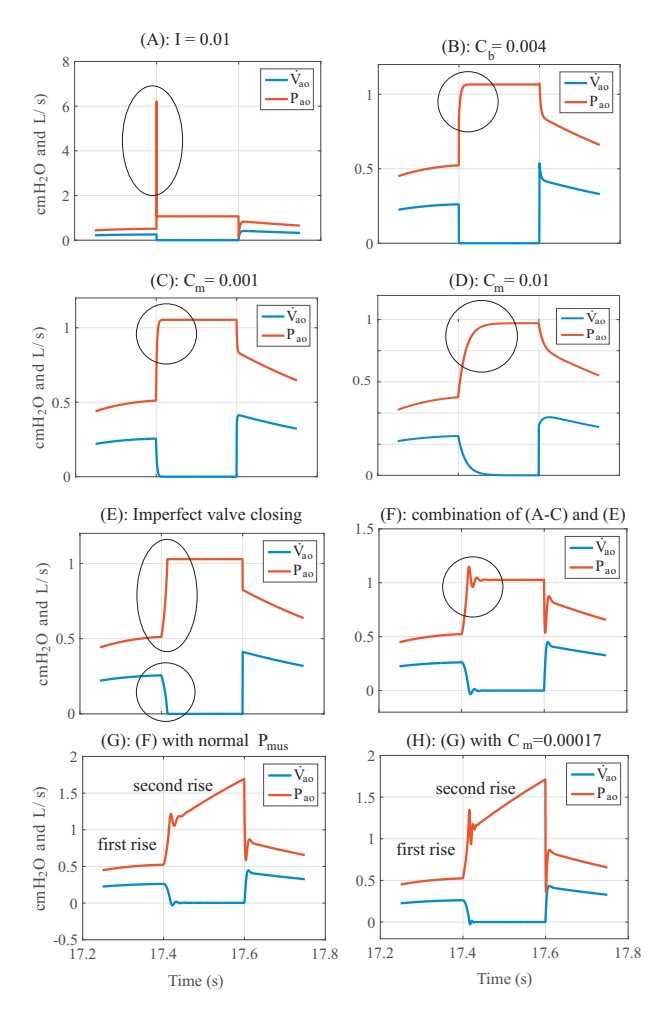


Figure 3.20: Simulated flow and pressure demonstrating the effect of different disturbances in the interrupter technique. (A-F) Holding of $P_{\rm mus}$ during interruption duration. (G-H) normal $P_{\rm mus}$. (A) Bronchial compliance $C_{\rm b}=0.004$. (B) Inertance I=0.01. (C) Mouth compliance $C_{\rm mouth}=0.001$. (D) Mouth compliance $C_{\rm mouth}=0.01$. (E) Imperfect closing of the valve. (F): combination of (A-C) and (E). (G): (F) with $P_{\rm mus}$. (H): (G) with $C_{\rm m}=0.00017$.

- The shutting of a valve is a dynamic process on it own, which depends on the construction and manufacturing of the valve. To demonstrate the effect of the valve on the measurement, we replace the ideal switch by a conductance that falls linearly from 10³ to 10⁻¹⁰ within 15 ms, as reported in [10]. The result is illustrated in Fig. 3.20 (E). The 12 ms period can be observed in the simulated flow and pressure, which does not exhibit a typical exponential charging curve. Its form depends on the change of the conductance (or resistance) during the valve closing. The opening of the valve is demonstrated as ideal without any delay.
- The combination of all introduced disturbances are displayed in Fig. 3.20 (F), (G), and (H). In Fig. 3.20 (G) and (H), the respiratory muscles are reactivated. All pressure responses exhibit dynamic behavior which can be observed in literature [65, 101]. The plotted curve has the form of a DT₂ response describing a system consisting of one inertance and two compliances.

3.3.3 Pendelluft and the Otis parallel model structure

The Otis-parallel structure is based on the consideration of the lungs as a bifurcation of two RC-pathways connected in parallel [157]. This representation of the lungs, referred to as the "bifurcation model", focuses on the pulmonary compartment differences to explain the frequency behavior of the parameters and even the asynchronous ventilation between the lungs [157]. Bates and Sly [10,188] applied this model to the interrupter technique and proposed the effect of pendelluft¹ as the main reason for the second rise in airway pressure. However, they did not consider the influence of the chest wall and the respiratory muscles.

We extend our linear model by the Otis-parallel structure to the model shown in Fig. 3.21. The model has two branches, each one consists of one resistance and one compliance. During the interruption period, if there is a pressure gradient between the two compliance C_1 and C_2 , there will be a redistribution process of air between the two compartments with the time constant τ_{pendel} :

$$\tau_{\text{pendel}} = (R_1 + R_2) \cdot \frac{C_1 \cdot C_2}{C_1 + C_2}$$
(3.31)

Let $R_1 = 1, R_2 = 3 \, \text{cmH}_2 \, \text{O/L/s}$ and $C_1 = C_2 = 0.05 \, \text{L/cmH}_2 \, \text{O}$ as used in [10], τ_{pendel} can be calculated to $(1+3) \cdot (0.05*0.05)/0.1 = 0.1 \, \text{s}$. This time is large

¹The German word "Pendelluft" refers to the movement of air back and forth between the lungs. It is thought to increase the respiratory dead zone and cause ventilation inhomogeneity between the lungs.

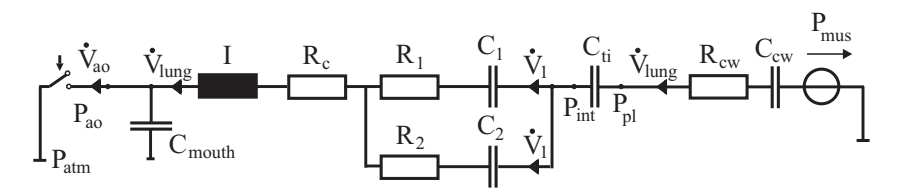


Figure 3.21: The linear lung model with the Otis-parallel structure.

enough to have an influence on the pressure change during the interruption time, as illustrated in Fig. 3.22 (I). If the resistance distribution is inhomogeneous, but the time constants are equal, for example $R_1=1, R_2=3\,\mathrm{cmH_2O/L/s}$ and $C_1=0.075, C_2=0.025\,\mathrm{L/cmH_2O};\ \tau_1=\tau_2=75\,\mathrm{ms},$ the second rise caused by the pendelluft disappears (simulation 3.22 (J)).

Adding I, $C_{\rm mouth}$, and $P_{\rm mus}$ to the model results in more realistic simulation results (Fig. 3.22 (K) and (L)). It is obvious that the impact from $P_{\rm mus}$ is likely dominant in the second rise in $P_{\rm ao}$. It should be noted that the inhomogeneity of $R_1/R_2=1:3$ has previously been assumed by the group of Bates [14,188], which may corresponds to a severe obstruction. In healthy adults, no significant inhomogeneity is expected (typical values are 53% to 47%, as reported in [186]). Since the second rise in $P_{\rm ao}$ can always be observed in measurements with the interrupter technique, even in healthy subjects, we do not support the idea of the pendelluft as the main cause of the second rise as mentioned in the ATS/ERS document [19]. In future works, the effects of the pendelluft during the interrupter technique should be further reevaluated in larger studies, possibly in combination with the Electrical Impedance Tomography (see Chapter 6).

3.4 Summary

This chapter presents a novel biophysical (forward) model of respiratory mechanics. Following the object-oriented compartment modeling, we subdivided the system into upper and central airways, peripheral (bronchial) airways, tissue, pleura and chest wall. The model considers significant non-linearities of model components. Simulation results demonstrate the high performance of model responses compared to data from literature. The model can be used to monitor the change of the compliance during mechanical ventilation.

Analyzing respiratory mechanics during spontaneous breathing, model linearization should be applied for simplification. We investigate the system responses of the linear model to reevaluate physiological interpretation of the

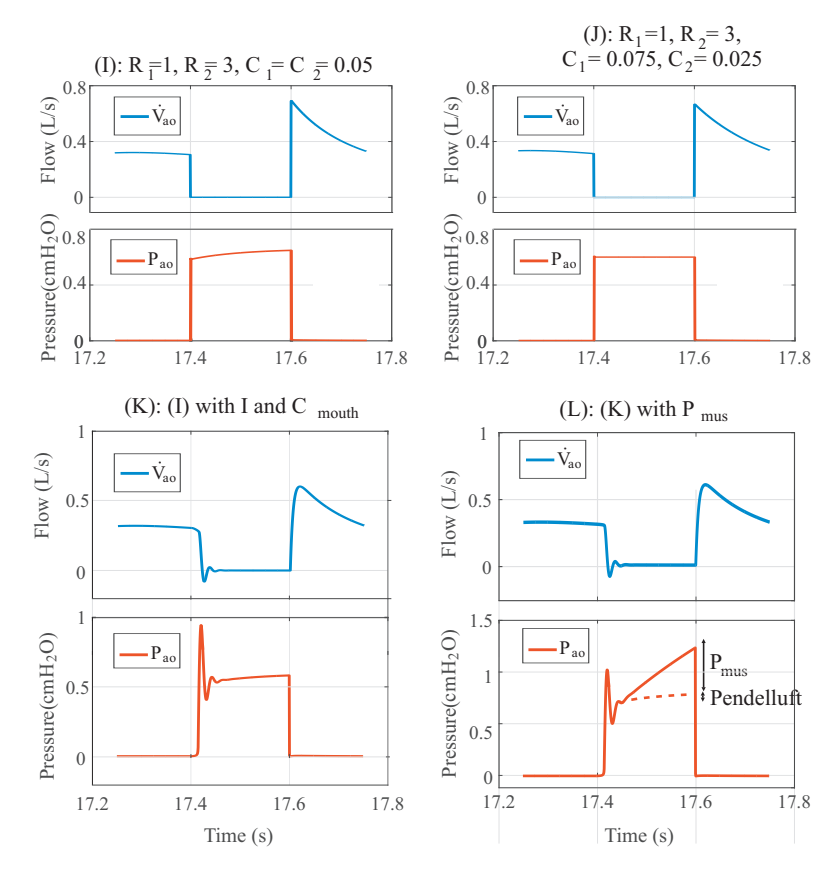


Figure 3.22: Simulated flow and pressure demonstrating the effect of the pendelluft in the interrupter technique. (I-K) Holding of $P_{\rm mus}$ during interruption duration. (I) different time constants between two compartments. (J) same time constants in both compartment. (K) I with inertance and cheek compliance. (L) I with $P_{\rm mus}$.

interrupter technique. The interrupter resistance $R_{\rm int}$ is composed by the airways and visco-elastic (tissue and chest-wall) resistances. The second rise in $P_{\rm ao}$ is mainly caused by the respiratory muscles $P_{\rm mus}$ in adults and children. There is a need for a deeper investigation on effects of the pendelluft during the tests.

4 Model-based parameter estimation with the forced oscillation technique (FOT)

Look at situations from all angels, and you will become more open.

Dalai Lama XIV

This chapter focuses on the dynamic response of the respiratory system in the frequency domain. As introduced in Chapter 2.2, the forced oscillation technique (FOT) measures the respiratory impedance $Z(j\omega)$ over a range of frequencies. Although FOT has a high potential use in infants, young children, and sleeping patients, clinical use of FOT is still limited. Medical workers usually have trouble interpreting the real and imaginary part of the complex impedance $Z(j\omega)$. Moreover, current physiological interpretation of $Z(j\omega)$ by means of different modeling approaches is controversial, even in the ATS/ERS guidelines [19].

First, this chapter presents a FOT measurement system and the computation of $Z(j\omega)$ in the frequency domain. Second, a discussion on the limitation of the existing models will be given, followed by new approaches and hypotheses for parameter estimation using FOT. Third, the chapter discusses the use of FOT in combination with nasal masks.

4.1 Measurement of respiratory impedance

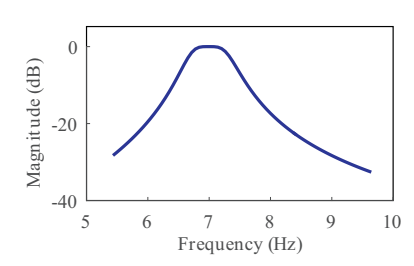
The FOT device used in this research is the Philips Respironics CoughAssist E70 (Philips, Eindhoven, The Netherlands). The function of this device is based on the generation of high frequency oscillations superimposed on a positive pressure, then rapidly shifting to a negative pressure to generate a high expiratory flow rate for secretion clearance. In combination with a pneumotachograph, the CoughAssist functions as a FOT device that generates sinusoidal vibrations. During our FOT measurements on volunteers, the device applied oscillation at an amplitude of $4\,\mathrm{cmH_2O}$ and frequencies between 3 and $20\,\mathrm{Hz}$ superimposed on a positive baseline pressure at $4\,\mathrm{cmH_2O}$. Test subjects were connected to the FOT device through a tube, a bacteria filter, and a mouth piece.

Flow and pressure were recorded at the subject's airway opening with a Hans Rudolph linear Fleisch pneumotachometer (Hans Rudolph, Kansas, USA) at 1 kHz sampling rate. The sensor was heated to $37^{\circ}C$ to prevent condensation on the internal mesh. The signals were sent to a Hans Rudolph Pneumotach Amplifier Series 1110 (Hans Rudolph, Kansas, USA) and converted into ana-

logue voltage signals. A National Instruments USB.X Series Multifunction DAQ (National Instrument, Texas, USA) was used to capture data at 1kHz sampling rate. Data analysis is performed in MATLAB 2015b (The MathWorks Inc., Natick, Massachusetts, USA).

Data analysis in the frequency domain

The calculation of the respiratory impedance $Z(j\omega)$ is performed in the frequency domain. A second-order Butterworth IIR filter with a bandwidth of 0.2 Hz and the center frequency equal to the oscillation frequency is applied on $P_{ao}(t)$ and $V_{ao}(t)$ to separate the oscillation from the spontaneous breathing (Fig. 4.1). To achieve a zero phase shift, the filter is applied forward and backward over the data.



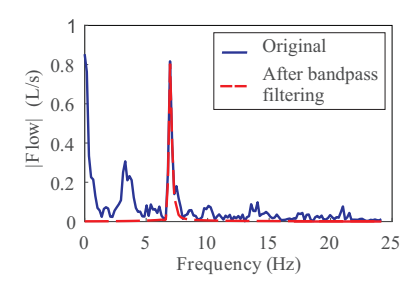


Figure 4.1: Left: Amplitude of the frequency response of the Butterworthbandpass filter second order, $f_{os} = 7 \,\mathrm{Hz}$. Right: fast Fourier transform of the flow amplitude before and after applying the bandpass filtering.

The calculation of $Z(j\omega)$ is possible via two methods: the fast Fourier transform (FFT) and the windowed cosine fitting (WCF).

Fast Fourier transform

The fast Fourier transform (FFT) splits a signal into a sum of cosine waves of different frequencies, amplitudes, and phases. Considering one oscillation frequency $\omega = \omega_{os}$, the amplitude and phase of $Z(j\omega_{os})$ can be determined by the amplitude and phase of the fast Fourier transformed pressure and flow at $\omega = \omega_{\rm os}$:

$$|Z(j\omega)|_{\omega=\omega_{os}} = \frac{|P(j\omega_{os})|}{|\dot{V}(j\omega_{os})|}$$

$$\varphi(j\omega)|_{\omega=\omega_{os}} = \varphi_P(j\omega_{os}) - \varphi_{\dot{V}}(j\omega_{os}).$$
(4.1)

$$\varphi(j\omega)|_{\omega=\omega_{os}} = \varphi_P(j\omega_{os}) - \varphi_{\dot{V}}(j\omega_{os}). \tag{4.2}$$

The complex impedance of the bacteria filter was measured separately and subtracted from $Z(j\omega)$ to achieve accurate values for respiratory impedance.

Alternatively, $Z(j\omega)$ can be calculated by the mean Fourier cross spectrum $S_{P\dot{V}}$ and autosprectrum $S_{\dot{V}\dot{V}}$ of the pressure and flow signals:

$$Z(j\omega)|_{\omega=\omega_{\rm os}} = \frac{S_{P\dot{V}}(j\omega)}{S_{\dot{V}\dot{V}}(j\omega)}|_{\omega=\omega_{\rm os}}$$
(4.3)

Cosine and windowed cosine fitting:

The bandpass-filtered flow and pressure signals comprise only one frequency component:

$$P(t) = A_P \cdot \cos(\omega t + \phi_P)$$

$$\dot{V}(t) = A_{\dot{V}} \cdot \cos(\omega t + \phi_{\dot{V}}),$$

where A, ϕ are amplitude and phase, respectively. Fitting the data with these cosine functions at each oscillation frequency ω_{os} results in amplitude and phase of $Z(j\omega)$.

Cosine fitting:
$$Z_{\rm R}(\omega_{\rm os}) = \Re \{Z(j\omega_{\rm os})\} = \frac{A_P}{A_{\dot{V}}} \cdot \cos(\varphi_P - \varphi_{\dot{V}})|_{\omega = \omega_{\rm os}}$$

$$Z_{\rm X}(\omega_{\rm os}) = \Im \{Z(j\omega_{\rm os})\} = \frac{A_P}{A_{\dot{V}}} \cdot \sin(\varphi_P - \varphi_{\dot{V}})|_{\omega = \omega_{\rm os}}$$

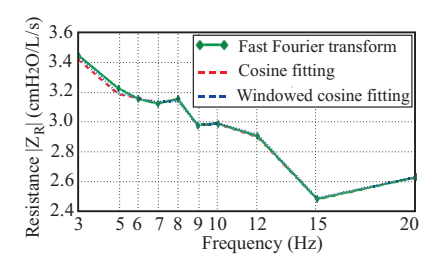
$$(4.4)$$

Performing the cosine fitting for a finite-length window with N data samples of P(t) and $\dot{V}(t)$ and sliding that window over the whole measurement duration, $Z(j\omega)$ can be computed as an function of time [91]. For each N samples of the current sliding window, the amplitudes and phases A_P , $A_{\dot{V}}$, ϕ_P and $\phi_{\dot{V}}$ are determined by applying Least-Squares fitting. The computed impedance is considered to be the value at the middle position of the window (N/2).

Windowed cosine fitting:
$$Z_R(\omega_{os}, t_N + N/2) = A_P/A_{\dot{V}} \cdot \cos(\phi_P - \phi_{\dot{V}})|_{\omega = \omega_{os}}$$
$$Z_X(\omega_{os}, t_N + N/2) = A_P/A_{\dot{V}} \cdot \sin(\phi_P - \phi_{\dot{V}})|_{\omega = \omega_{os}},$$
(4.5)

where t_N is the start position of the window.

An exemplary window size of 0.4s gives N a value of 400 at 1 Hz sampling rate. The WCF method is a combination of the time and frequency domains.



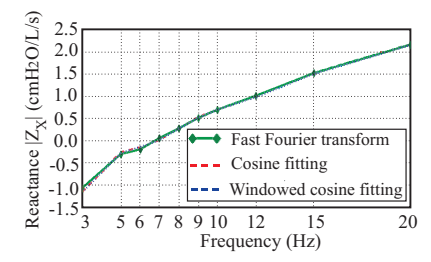


Figure 4.2: Representative resistance and reactance measured on one healthy subject. Calculation of $Z(j\omega)$ with three different methods: fast Fourier transform, cosine fitting and windowed cosine fitting.

Results

Fig. 4.2 shows representative data of the respiratory impedance from one test subject. The resulting reactance shows a positive trend with a resonance frequency at about 7 Hz. The resistance shows a negative frequency gradient from 3.4 to $2.6\,\mathrm{cmH_2O/L/s}$. The different methods provide almost the same values for resistance and reactance.

4.2 Modeling and parameter identification

4.2.1 A survey of lung models used in Forced Oscillation Technique

A physiological interpretation of $Z(j\omega)$ can be made in combination with mathematical (greybox)-modeling and parameter estimation. The simplest model of the respiratory system in oscillometry is the serial RIC-network (Fig. 4.3(F)). The inertance, which can be neglected for respiratory frequencies under 2Hz as in spontaneous breathing and mechanical ventilation, contributes a significant part to $Z(j\omega)$ at higher frequencies:

$$Z_{\rm RIC}(j\omega) = R + j\omega I + \frac{1}{j\omega C}.$$
 (4.6)

The extended-RIC model (Fig. 4.3(G)) has a peripheral resistance $R_{\rm p}$ added in parallel to the compliance C to fit the frequency-dependency of the impedance's real part to experimental data [9, 39, 84, 145]. Physiologically, $R_{\rm p}$ is thought to correspond partially to the airway resistance of the proximal airways. C is thought to be lung compliance [39, 84], $R_{\rm c}$ the central resistance, and I the inertance. However, this common interpretation of C seems to be incorrect

and will be discussed later in this chapter. The total impedance of the model is given as:

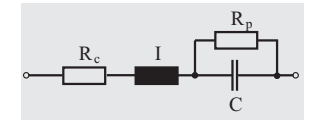
$$Z_{\text{eRIC}}(j\omega) = R + \frac{R_{\text{p}}}{1 + (\omega R_{\text{p}}C)^2} + j\left(\omega I - \frac{\omega R_{\text{p}}^2 C}{1 + (w R_{\text{p}}C)^2}\right)$$
(4.7)

The augmented-RIC model (Fig. 4.3(H)) is an extension of the extended-RIC model complemented by the extrathoracic compliance $C_{\rm e}$. This component presents the upper shunt caused by the cheeks and tongue's movements during the measurement procedure, and is relevant for frequencies above 20 Hz. By having the subjects supporting their cheeks with their hands during the measurements, the influence of $C_{\rm e}$ can be reduced for lower frequencies [210].

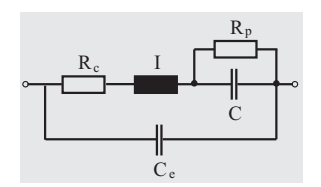
Mead was the first to introduce the parallel structure of a bronchial compliance $C_{\rm e}$ and a series of peripheral resistance $R_{\rm p}$ and lung compliance $C_{\rm l}$ [127,128]. He also assumed a bronchial compliance to be about 1/40 that of the lung parenchyma. Later, an extrathoracic compliance $C_{\rm e}$ and a chest wall component $C_{\rm cw}$ were added into the model. The Mead model with its 7 elements (Fig. 4.3(I)) is very common in parameter estimation with FOT. However, unphysiological values for $C_{\rm l}$ and $C_{\rm cw}$ were reported [39, 40, 84] that have not been completely understood and limit the use of the model in praxis.

The DuBois model (Fig. 4.4(K)) considers a central resistance R_c , an inertance I, an gas compression module C_g in parallel with a tissue compartment of resistance R_{ti} , compliance C_{ti} , and inertance I_{ti} . Although the DuBois' model [43] has a similar parallel structure as the Mead model, they are completely different in physiological interpretation of the parameters.

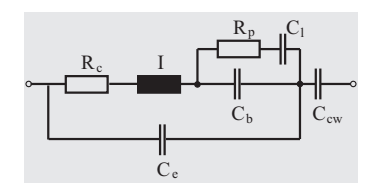




(G): extended RIC



(H): augmented RIC

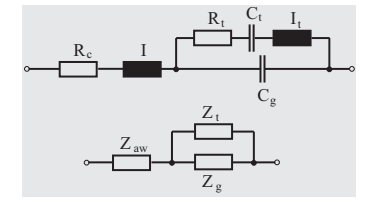


(I): Mead

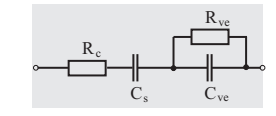
Figure 4.3: Lung models in oscillometry. c = central, p = peripheral, b = bronchial, aw = airway, cw = chest wall, s = static, ve = visco-elastic, e = extra-thoracic, t = tissue, g = gas.

Another model with a serial structure and relatively high biased estimates is the viscoelastic model (Fig. 4.4(J)). It is based on a separation of static components (R_c , C_s) and viscoelastic ones (R_{ve} , C_{ve}) [39]. It is easy to recognize the correspondences between the viscoelastic and the Mead model. Ignoring I, C_e , and C_l , and switching the position of C_{cw} in the Mead model, both become identical. In spite of that, again, both models have different interpretation for C_{cw} , R_p , C_b against R_{ve} , C_s , and C_{ve} .

Researches from the groups of Hantos and Bates [9,11,72] support the idea of a nonlinear constant phase model (Fig. 4.4(L)), which is an extension of the DuBois and viscoelastic models. Based on the tissue characteristics observed in rubber balloon and cat lungs [81], they introduced the constant phase model as a series of airways and tissue compartments. They replaced the tissue part of the DuBois model by a construction of a non-linear, frequency dependent tissue damping G and tissue elastance H. The total respiratory impedance Z is calculated as



(K): DuBoi's



(J): visco elastic



(L): constant phase

Figure 4.4: Lung models in oscillometry. c = central, p = peripheral, b = bronchial, aw = airway, cw = chest wall, s = static, ve = visco-elastic, e = extra-thoracic, t = tissue, g = gas.

$$Z_{\text{constant-phase}} = R_{\text{c}} + j\omega I + \frac{G - jH}{\omega^{\alpha}}$$
 (4.8)

where α is a constant-phase parameter linking G and H through the equation: $\alpha = \frac{2}{\pi} \arctan(\frac{H}{G})$.

Average estimated results obtained from five healthy male adults are shown in Fig. 4.5 and in Table 4.1. R, L, and C are given in cmH₂O/L/s, cmH₂O/L/s², and L/cmH₂O, respectively. While the values of eRLC differ slightly from RLC model, there are no significant differences between eRLC and aRLC.

4.2.2 Model-based analysis

The ATS/ERS recommendations for FOT published in 2003 [155] are focusing on methodology, technical recommendations, and clinical findings regarding the measurement of $Z(j\omega)$. However, they do not include any comments on the underlying physiological models of $Z(j\omega)$. Different study results from Diong et al. [39, 40] and Ionescu [84] lead to similar observations:

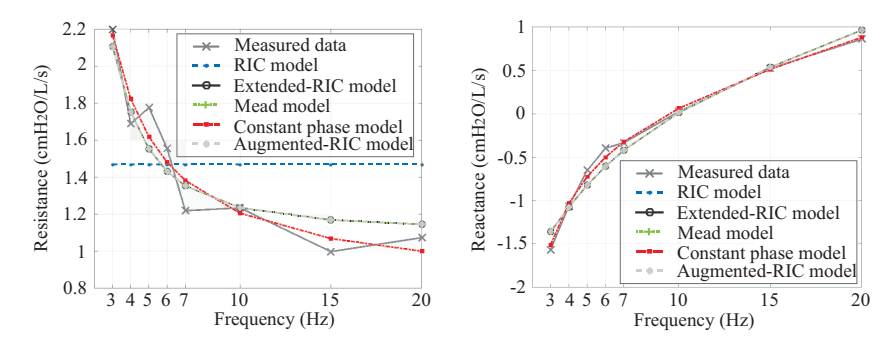


Figure 4.5: Applying parameter estimation on different lung models.

Table 4.1: Parameters for RIC, extended-RIC, and augmented-RIC models. Values are averaged from 5 healthy adults. R, L, and C are given in cmH₂O/L/s, cmH₂O/L/s², and L/cmH₂O, respectively.

	RIC	eRIC	aRIC
R	$1.8464(\pm 0.5978)$	$1.5607(\pm0.6252)$	$1.5607(\pm0.6252)$
I	$0.0131(\pm 0.0049)$	$0.0141(\pm 0.0054)$	$0.0141(\pm 0.0054)$
C	$0.0313(\pm0.0051)$	$0.0253(\pm0.0072)$	$0.0253(\pm0.0072)$
R_p		$3.9444(\pm 1.1611)$	$3.9444(\pm 1.1611)$
$C_e.10^{13}$			$6.3738(\pm 12.779)$
RSS	$0.9701(\pm 0.5096)$	$0.3578(\pm 0.1345)$	$0.3578(\pm 0.1345)$

- 1. Although the 7-element Mead model has the smallest estimation errors, its estimated alveolar and chest wall compliances are unphysiological.
- 2. The estimated compliance in the RIC, eRIC, and aRIC models is one order smaller than normal compliance values known from spontaneous breathing.
- 3. The visco-elastic and the DuBois model have a similar structure with the Mead model, but the physiology is completely different.
- 4. The tissue resistance in the constant phase model alters strongly between healthy and obstructive patients, which is also unexpected.

All these points have not been understood in the current state-of-the-art. In this part, based on the developed model introduced in Chapter 3, we propose physiological hypotheses and mathematical proofs to explain the above mentioned questions.

First simplification: from 9-element model to 7-element Mead models

The 9-element model, as developed in Chapter 3, is illustrated in Fig. 4.6. First

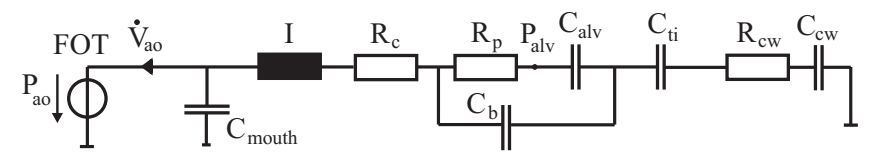


Figure 4.6: The linearized lung model with 9 elements.

neglecting the cheek compliance C_{mouth} , the overall impedance is given as:

$$Z(j\omega) = R_{\rm c} + j\omega I + R_{\rm cw} + \frac{R_{\rm p} - j\left(\omega R_{\rm p}^2 C_{\rm b} + \frac{1}{\omega C_{\rm alv}}\left(\frac{C_{\rm b}}{C_{\rm alv}} + 1\right)\right)}{(\omega R_{\rm p} C_{\rm b})^2 + \left(\frac{C_{\rm b}}{C_{\rm alv}} + 1\right)^2} + \frac{1}{j\omega C_{\rm ti}} + \frac{1}{j\omega C_{\rm cw}}.$$

$$(4.9)$$

Combining the central and chest wall resistances $R_{\rm c+cw} = R_{\rm c} + R_{\rm cw}$, as well as the tissue and chest wall compliances $C_{\rm ti+cw} = \frac{C_{\rm ti}C_{\rm cw}}{C_{\rm ti}+C_{\rm cw}}$, eq. (4.9) becomes:

$$Z(j\omega) = R_{\rm c+cw} + j\omega I + \frac{R_{\rm p} - j\left(\omega R_{\rm p}^2 C_{\rm b} + \frac{1}{\omega C_{\rm alv}}\left(\frac{C_{\rm b}}{C_{\rm alv}} + 1\right)\right)}{(\omega R_{\rm p} C_{\rm b})^2 + \left(\frac{C_{\rm b}}{C_{\rm alv}} + 1\right)^2} + \frac{1}{j\omega C_{\rm ti+cw}}.$$

$$(4.10)$$

Now, adding the cheek compliance $C_{\rm mouth}$, the model structure (4.10) is identical with the model of Mead (Fig. 4.3(K)). In other words, our model is indeed an extension of the Mead model. First, the central resistance as proposed by Mead should contain thorax (and tissue) resistive components $R_{\rm cw}$. Second, his proposed chest wall compliance $C_{\rm cw}$ should comprise the tissue elastance $C_{\rm ti}$ as well.

Second simplification: from 7-element Mead model to extended- and augmented-RIC model

The bronchial compliance $C_{\rm b}$ is much smaller than the alveolar compliance $C_{\rm alv}$ (eq. (3.3)): $\frac{V_{\rm b}}{V_{\rm alv}} (\approx 1/50-1/30)$. Again, considering the impedance without $C_{\rm mouth}, \, Z(j\omega)$ can be further simplified as:

$$Z(j\omega) = R_{\rm c+cw} + j\omega I + \frac{R_{\rm p} - j\left(\omega R_{\rm p}^2 C_{\rm b} + \frac{1}{\omega C_{\rm alv}}\right)\right)}{(\omega R_{\rm p} C_{\rm b})^2 + 1} + \frac{1}{j\omega C_{\rm ti+cw}}, \quad (4.11)$$

with the real part

$$Z_{\rm R}(\omega) = R_{\rm c+cw} + \frac{R_{\rm p}}{(\omega R_{\rm p} C_{\rm b})^2 + 1}$$
 (4.12)

and the imaginary part

$$Z_{\rm X}(\omega) = \omega I - \frac{\omega R_{\rm p}^2 C_{\rm b} + \frac{1}{\omega C_{\rm alv}}}{(\omega R_{\rm p} C_{\rm b})^2 + 1} - \frac{1}{\omega C_{\rm ti+cw}}. \tag{4.13}$$

The imaginary part can be further simplified:

$$Z_{\rm X}(\omega) = \omega I - \frac{\omega^2 R_{\rm p}^2 C_{\rm b} C_{\rm ti+cw} + \frac{C_{\rm ti+cw}}{C_{\rm alv}} - (\omega R_{\rm p} C_{\rm b})^2 - 1}{\omega C_{\rm ti+cw} ((\omega R_{\rm p} C_{\rm b})^2 + 1)}$$

$$\approx \omega I - \frac{\omega^2 R_{\rm p}^2 C_{\rm b} C_{\rm ti+cw} - (\omega R_{\rm p} C_{\rm b})^2}{\omega C_{\rm ti+cw} ((\omega R_{\rm p} C_{\rm b})^2 + 1)}, \quad \text{since } \frac{C_{\rm ti+cw}}{C_{\rm alv}} \approx 1$$

$$\approx \omega I - \frac{\omega^2 R_{\rm p}^2 C_{\rm b} (C_{\rm ti+cw} - C_{\rm b})}{\omega C_{\rm ti+cw} ((\omega R_{\rm p} C_{\rm b})^2 + 1)}$$

$$\approx \omega I - \frac{\omega^2 R_{\rm p}^2 C_{\rm b} C_{\rm ti+cw}}{\omega C_{\rm ti+cw} ((\omega R_{\rm p} C_{\rm b})^2 + 1)}, \quad \text{since } C_{\rm ti+cw} \gg C_{\rm b}$$

$$\approx \omega I - \frac{\omega R_{\rm p}^2 C_{\rm b}}{(\omega R_{\rm p} C_{\rm b})^2 + 1}$$

$$(4.15)$$

The derived real and imaginary parts (eq. (4.12) and (4.15)) are identical with the extended-RIC model in eq. (4.7). Considering the parallel cheek compliance $C_{\rm mouth}$, we get the augmented-RIC model.

This analysis yields two important scientific findings:

• The difference in the dimension (almost 30 -50 times larger) between the "large" compliances (alveolar, tissue, chest wall) and the small bronchial

compliance $C_{\rm b}$ leads to the dominance of $C_{\rm b}$ in the respiratory impedance $Z(j\omega)$. In other words, $Z(j\omega)$ is not sensitive for the measurement of alveolar, tissue, chest wall compliances. As a result, $C_{\rm alv}$ and $C_{\rm cw}$ estimated with the Least-Squares method for the Mead model are unphysiological, as reported in the works of Diong [39] and Ionescu [84]. A detailed sensitivity analysis of the Mead model is given in Appendix A.4.

• The RIC, eRIC and aRIC models are simplifications of the Mead model. The "respiratory compliance" C in these three models corresponds to the bronchial compliance $C = C_{\rm b}$. In other words, the compliance measured by FOT and estimated with these three models is the bronchial compliance $C_{\rm b}$. This explains why the compliance estimated in FOT (as shown in Section 4.2 or reported in [39,84]) yield values which are one order smaller than typical value for lung compliance known from spontaneous breathing and mechanical ventilation.

Physiological explanation of the DuBois, visco-elastic, and constant-phase models

The DuBois model has the Mead model's parallel structure. However, the physiological interpretation of the parameters is different: it comprises a tissue compartment ($R_{\rm ti}$, $I_{\rm ti}$ and $C_{\rm ti}$) instead of the peripheral and alveolar compartment, a parallel gas compression compliance $C_{\rm gas}$ instead of $C_{\rm b}$. In fact, after DuBois introduced this structure in 1956 [43], measurements published by other authors have shown that the influence of gas compression and tissue resistance is rather insignificant in FOT measurements. The gas compression compliance is estimated to be around $1/600\,{\rm L/kPa} = 0.00017\,{\rm L/cmH_{20}}$ [14] in healthy adults, which is at least 20 times smaller than the normal value of $C_{\rm b}$. If this compliance is indeed $C_{\rm b}$, the other parallel branch must be the peripheral and alveolar compartments, since a parallel structure between tissue and bronchi is unphysiological. Moreover, tissue resistance has also reported to be small in several researches (1% [51], 7.41% [129], and 12.77% [31] of the total resistance, several times smaller than the estimated peripheral resistance. Hence, it cannot have a major contribution on the total resistance.

The visco-elastic model also has Mead's parallel structure. Its static compliance $C_{\rm s}$ has exactly the same impact on the impedance as the chest wall compliance $C_{\rm cw}$ in the Mead model, which is not sensitive in FOT measurements (eq. (4.15)). Its viscoelastic components $C_{\rm ve}$ and $R_{\rm ve}$ correspond to $C_{\rm alv}$ and $R_{\rm p}$ in the Mead model. In other words, parameters estimated with the visco-elastic model are identical with those of the Mead model (excluding the inertance I). In my opinion, the visco-elastic model is rather a mathemat-

ical approach than an useful model in respiratory modeling. It does not yield any mathematical or physiological advantages against the Mead model.

The constant-phase model does not have Mead's parallel structure. This model is indeed divided into one frequency-independent (airway) and one frequency-dependent part (tissue). In this model, the lung tissue is the only component which contributes to the frequency-dependency in $Z_{\rm R}(\omega)$. It also ignores the impact of the parallel bronchial compliance to the frequency dependency [128] (which is, in my opinion, the main cause), and the chest wall compartment. As a result, an overestimated tissue resistance is reported in publications using this model (40% of the total resistance [93]). Moreover, scientists who support this model structure have been facing difficulties to convince physiologists of the meaning of G and H, since they do not even have the units of resistance and compliance [8]. When the lungs are challenged with bronchial agonists, G and H invariably increase even though only the airway resistance and no tissue damping should be affected [15]. In fact, the change in G and H during bronchial challenges indicates the contribution of peripheral airway resistance in G and H, which also questions the correctness of this model structure.

4.2.3 Model hierarchy and recommendations

In the ATS/ERS official recommendations 2007 [19], the author stated: "The fact that $R_{\rm rs}$ decreases with increasing frequency and approaches a plateau indicates the presence of parallel pathways. In children, the motion is perhaps the most significant factor [120]. In patients with airway obstruction or induced bronchi-constriction, peripheral inhomogeneity [118, 157, 200] and bronchial compliance [128] represent additional pathways. Elevation of $R_{\rm rs}$ toward lower frequencies, in other words, the contribution of tissue resistance, which has marked negative frequency dependence [189]. In healthy subjects, $R_{\rm rs}$ exhibits increase with frequency above 10 to 15 Hz: this is attributed to multiple mechanisms, such as airway wall compliance, gas compressibility in the central airways, and inertial distortion of the velocity profile [53].".

There are two confusing points in this statement. First, it should be noted that in Marchal et al.'s work [120], the authors performed FOT without cheek supporting in purpose to demonstrate the influence of the upper shunt. In standard FOT measurements, a reduction in $R_{\rm rs}$ was widely observed [100], even when cheek vibration was reduced significantly by cheek supporting. Thus, the check motion is not the most significant factor in children. Second, the document recommends Mead's idea of parallel peripheral airway, but also support the constant-phase model which replaces Mead's structure by a frequency-dependent tissue compartment in series. These two approaches have completely

different structure and physiological interpretation.

Our comprehensive forward non-linear modeling supports the structure of Mead. Figure 4.7 illustrates the relations among the models regarding linearity, model structure, and identifiability. As results of the model-based analysis, we propose several recommendations for parameter identification in FOT:

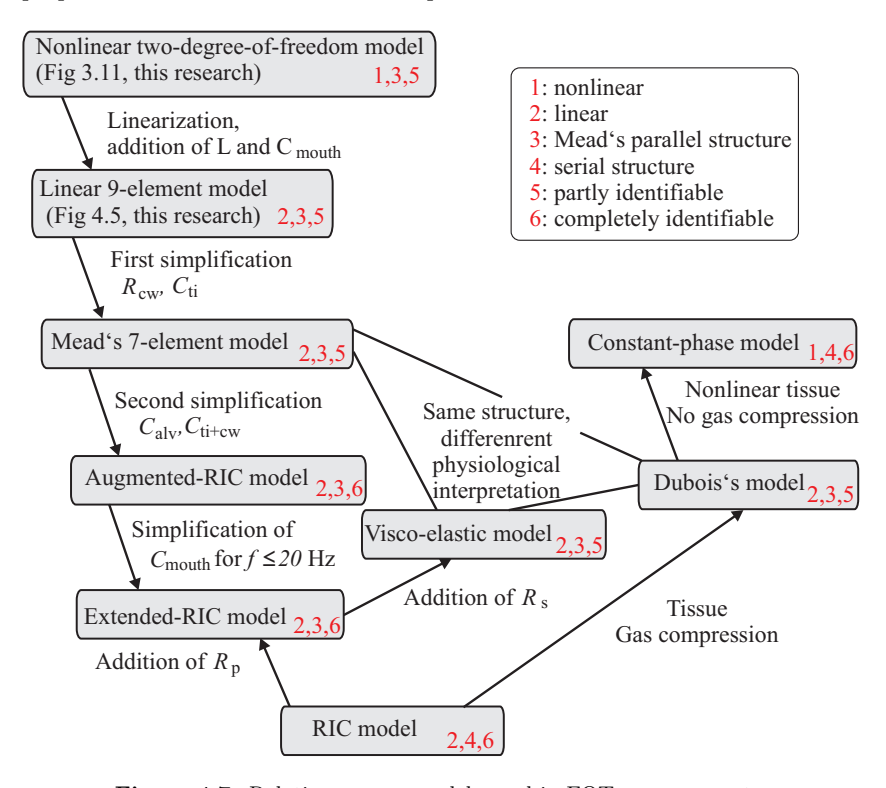


Figure 4.7: Relation among models used in FOT measurements.

- Mead's parallel structure presents the best correspondence to lung physiology. The central resistance of the Mead model may comprise upper airway, lung tissue, and chest wall resistance in series. The chest wall compliance may consist of tissue and chest wall compliances in series.
- 2. The alveolar, chest wall, and tissue compliances cannot be estimated with FOT. There is a leak in sensitivity in the measurement results regarding

these parameters.

- 3. For FOT at frequencies above 3 Hz, the extended-RIC and the augmented RIC models are recommended. These two simplifications of the Mead model are simple, identifiable, and deliver robust estimation results.
- The compliance estimated by the eRIC and aRIC models corresponds to the (peripheral) bronchial compliance, not the total respiratory compliance.

4.3 The volume-dependent FOT

Classic FOT focuses on the frequency-dependency of the respiratory impedance $Z(j\omega)$. However, since $Z(j\omega)$ also depends on lung volume regarding the law of Hagen-Poiseuille, the change of $Z(j\omega)$ over lung volume may provide additional information on lung mechanics. Peslin et al. performed the Forced Oscillation Technique on 54 healthy subjects [164] in 1992. By applying the Rohrer's equation directly on $Z_{\rm R}(j\omega)$ in absence of a model structure and estimating the flow- and volume-dependency of $Z(j\omega)$, they reported an intra-breath (inspiration-expiration) variation of $Z(j\omega)$. Nevertheless, these dependencies have not gained any further attention, since the intra-breath changes are relatively small compared to the frequency-dependency for spontaneous breathing.

4.3.1 Principles of the volume-dependent FOT

In this section, we investigate the volume-dependency of $Z(j\omega)$ over the whole lung volume. By introducing a new measurement protocol, an adapted data analysis, and a novel model-based parameter estimation, we propose a new extension of the classic FOT, which is given the name: volume-dependent FOT (v-FOT). The aims of the extension are to gain a deeper understanding of the physiological nature of $Z(j\omega)$, and to find a more powerful tool to assess respiratory mechanics.

A v-FOT measurement is similar to a classic FOT with the following extensions:

• During the measurements, subjects wear a nose-clip and support their cheeks to minimize the disturbances of the upper airways. After a few cycles of spontaneous breathing, test subjects perform the so-called "slow-flow vital capacity maneuver". From the residual volume level, subjects inhale slowly to total lung capacity, while FOT oscillation is superimposed on the slow inhalation. A healthy subject may breathe in a respiratory volume of about 4-6 L in a time interval of about 5-6 seconds.

- Subjects are asked to perform the deep inspiration three times for each oscillation frequency. The measurement should be repeated at different oscillation frequencies between 3 Hz and 20 Hz.
- Optionally, v-FOT can also be performed during a slow expiration.

The above mentioned Butterworth bandpass filter can be used to extract the frequency component at f_{os} . The windowed cosine fitting method provides the dynamic changes of $Z(j\omega)$ over time. Plotting $Z(j\omega)$ over V provides a new presentation of FOT, namely the impedance-volume (ZV) diagram. Lung volume V forms the ordinate, while $Z_{\rm R}(\omega)$ and $Z_{\rm R}(\omega)$ are the abscissa. Hence, the impedance measured via v-FOT comprises one more dimension: the volume-dependency $Z(j\omega,V)$.

Figure 4.8 displays the measured (solid lines) and estimated ZV diagram obtained on a healthy subject (male, 25 years old, BMI = 22.09). Least-Squares parameter estimations are performed for the extended-RIC and constant-phase models. Data comprise $Z_{\rm R}(j\omega,V)$ and $Z_{\rm X}(j\omega,V)$ at all oscillation frequencies. While the constant-phase model yields a smaller error than the eRIC model, its estimated parameters are unphysiological ($R_{\rm aw} < 0$). In general, no volume-dependency can be estimated by these two models, the residual errors remain large, and the models' behavior differ from the measurement data.

4.3.2 The reduced non-linear model

The linearization of the non-linear model discussed in Chapter 3.2.3 assumes a small change of lung volume, such as in the spontaneous breathing and mechanical ventilation with normal tidal volume. Investigating the lungs over their whole volume, non-linear characteristics of the components should be considered. While the bronchial, alveolar, and chest wall compliances, $C_{\rm b}$, $C_{\rm alv}$, and $C_{\rm cw}$ only become non-linear at extreme lung levels (Fig 3.7 and 3.11), the peripheral resistance is volume-dependent due to Hagen-Poisseuille's law over the whole lung volume. Eq. (3.7) can be rewritten as:

$$R_{\rm p} = \frac{8\mu L}{\pi r^4} = \frac{K_{\rm p}}{V - V_{\rm off}},$$
 (4.16)

where $K_{\rm p}$ is a parameter characterizing $R_{\rm p}$, and $V_{\rm off}$ is a shift in the measured lung volume.

For simplification, we consider only the volume-dependency of R_p in this work. The eRIC and Mead model are extended to the volume-dependent eRIC and Mead models (v-eRIC and v-Mead). The real and imaginary parts of the

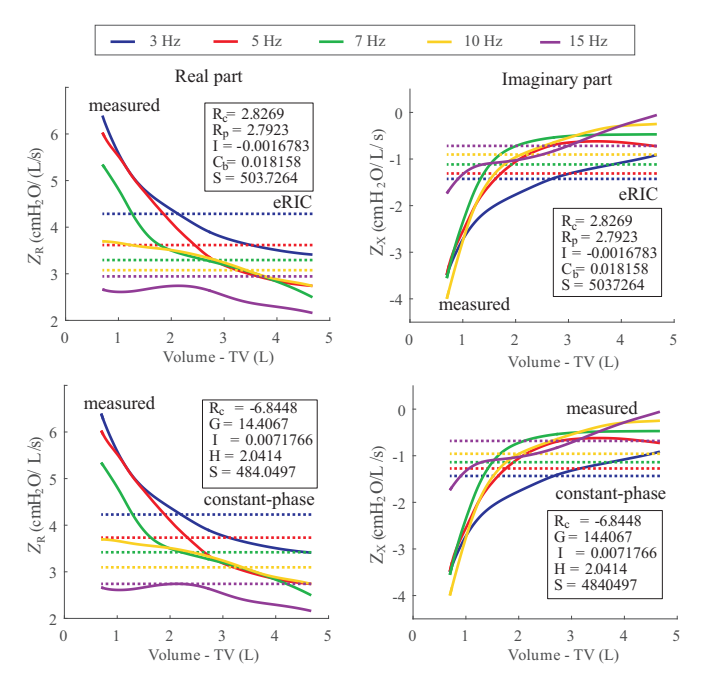


Figure 4.8: Measured (solid lines) and fitted (dashed lines) resistances and reactances measured with vFOT method. Data obtained from a healthy subject (male, 25 years old, BMI = 22.09), computed via Butterworth filtering and windowed cosine fitting method. Least-Squares parameter fitting are performed for the real and imaginary parts for the extended-RIC (eRIC) (top) and the constant-phase models (bottom).

v-Mead model are given as:

$$Z_{R}(\omega, V) = R_{c+cw} + \frac{R_{p}}{(\omega R_{p} C_{b})^{2} + 1}$$

$$= R_{c+cw} + \frac{K_{p}(V - V_{Off})}{(\omega C_{b} K_{p})^{2} + (V - V_{Off})^{2}}$$
(4.17)

$$Z_{\rm X}(\omega, V) = \omega I - \frac{\omega K_{\rm p}^2 C_{\rm b} + \frac{(V - V_{\rm Off})^2}{\omega C_{\rm alv}}}{(\omega C_{\rm b} K_{\rm p})^2 + (V - V_{\rm Off})^2} - \frac{1}{\omega C_{\rm ti+cw}}.$$
 (4.18)

Frequency response of the system for critical frequencies: The frequency responses of $Z_{\mathbf{R}}(\omega, V)$ for $\omega \to 0$ and $\omega \to \infty$ are given as follow:

$$Z_{\rm R}(\omega = 0, V) = R_{\rm c+cw} + \frac{K_{\rm p}}{(V - V_{\rm Off})} = R_{\rm c+cw} + R_{\rm p} = R_{\rm int} \quad (4.19)$$

$$Z_{\rm R}(\omega \to \infty, V) = \lim_{\omega \to \infty} \left(R_{\rm c+cw} + \frac{K_{\rm p}(V - V_{\rm Off})}{(\omega C_{\rm b} K_{\rm p})^2 + (V - V_{\rm Off})^2} \right)$$

$$= R_{\rm c+cw} \quad (4.20)$$

For $\omega \to 0$, $Z_{\rm R}(\omega=0,V)$ is equal to the sum of all resistive components of the respiratory system and equal to the resistance measured via the interrupter technique (Chapter 3.3). For $\omega \to \infty$, the volume-dependency of $Z_{\rm R}(\omega=0,V)$ disappears and $Z_{\rm R}$ comprises only the central and chest wall compartments. The measurement results illustrated in 4.8 confirm our model assumption. While $Z_{\rm R}(\omega=3\,{\rm Hz},V)$ is strongly volume-dependent, this dependency decreases massively at higher frequencies.

These results can be used to augment the general explanation of R5 as the total respiratory resistance and R20 as the central resistance, as commonly known in impulse oscillometry measurements [20,193]. It should also be clarified that both R5 and R20 comprise the chest wall resistance besides the central and peripheral airway resistances, and thus are larger than the total airway resistance $R_{\rm aw}$ measured with the body plethysmography (see Chapter 3.1).

The Mead model assumes a parallel structure between $R_{\rm p}$ and $C_{\rm b}$. Regarding the more sophisticated Weibel model, the respiratory system can be seen as a distributed network of 23 RC-generations (Fig 4.9). Increasing the applied frequency, more and more peripheral bronchi lose their impact on $Z_{\rm R}(\omega=0,V)$. Approximating the 23 RC-generation model by only one RC parallel structure, a subdivision of the peripheral airways into large and small bronchi ($R_{\rm lp}$ and $R_{\rm sp}$) will increase the accuracy of the model's frequency response. The new model is called the v-Mead+ model. Applying the first and second simplification (eq. (4.15) and (4.10)) on the v-Mead+ model results in the v-eRIC+ model (Fig.4.9). The $Z_{\rm R}(\omega=0,V)$ of the v-eRIC+ is given as:

$$Z_{\rm R,\,model}(\omega=0,V) = R_{\rm c+cw} + \frac{K_{\rm lp}}{V(t) - V_{\rm Off}} + \frac{K_{\rm sp}(V(t) - V_{\rm Off})}{(\omega C_{\rm b} K_{\rm p})^2 + (V(t) - V_{\rm Off})^2}$$

$$= R_{\rm c+cw} + \frac{K_{\rm lp}}{V(t) - V_{\rm Off}} + \frac{K_{\rm sp}}{V(t) - V_{\rm Off}}$$

$$= R_{\rm c+cw} + R_{\rm lp} + R_{\rm sp} \qquad (4.21)$$

with
$$R_{
m lp} = \frac{K_{
m lp}}{V(t)-V_{
m Off}}$$
 and $R_{
m sp} = \frac{K_{
m sp}}{V(t)-V_{
m Off}}.$

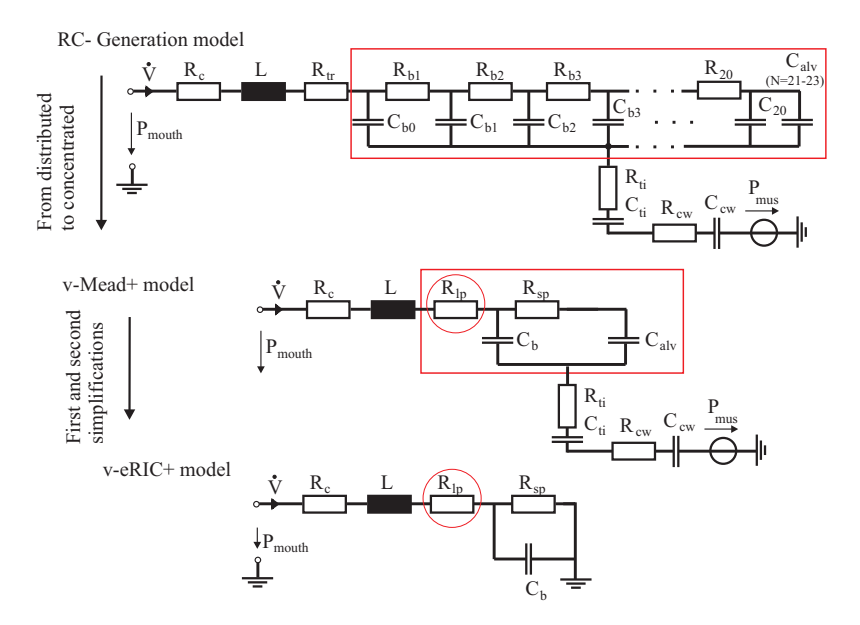


Figure 4.9: Top: the RC-Generation model developed based on the Mead and Weibel models. Bottom: the extended volume-dependent Mead model (v-Mead+) with a large and a small peripheral resistance $R_{\rm lp}$ and $R_{\rm sp}$.

4.3.3 Results of the parameter estimation

Again, we apply the non-linear Least-Squares fitting to estimate the parameter of the v-RIC, v-Mead, and v-RIC+ models. For the v-RIC and Mead model, multi-frequency fitting is performed for $Z_{\rm R}(\omega,V)$ and $Z_{\rm X}(\omega,V)$. Parameter vectors are $\boldsymbol{\theta}_{\rm v-RIC} = (K_{\rm p},R_{\rm c+cw},C_{\rm b},V_{\rm Off},I)^{\rm T} \in \mathbb{R}^{1\times 5}$ and $\boldsymbol{\theta}_{\rm v-Mead} = (K_{\rm p},R_{\rm c+cw},C_{\rm b},V_{\rm Off},I,C_{\rm alv},C_{\rm cw})^{\rm T} \in \mathbb{R}^{1\times 7}$.

For the v-RIC+ model, we performed mono-frequency parameter fitting with $\theta_{\text{v-RIC+}} = (K_{\text{lp}}, K_{\text{sp}}R_{\text{c+cw}}, C_{\text{b}}, V_{\text{Off}})^{\text{T}} \in \mathbb{R}^{1 \times 5}$ only for $Z_{\text{R}}(\omega, V)$ to increase the fitting accuracy, since K_{lp} and K_{sp} can alter by increasing frequencies.

Figure 4.10 displays the results of the parameter estimation with the veRIC, v-Mead, and v-eRIC+ models. Data are obtained from a healthy subject (male, 28 years old, BI = 23.15). The models are able to follow the volume-dependency of $Z_{\rm R}(\omega,V)$ and $Z_{\rm X}(\omega,V)$. All parameters estimated by the veRIC are in physiological ranges. There is no significant different in the residual error between the v-eRIC and v-Mead model. As mentioned above, the "large"

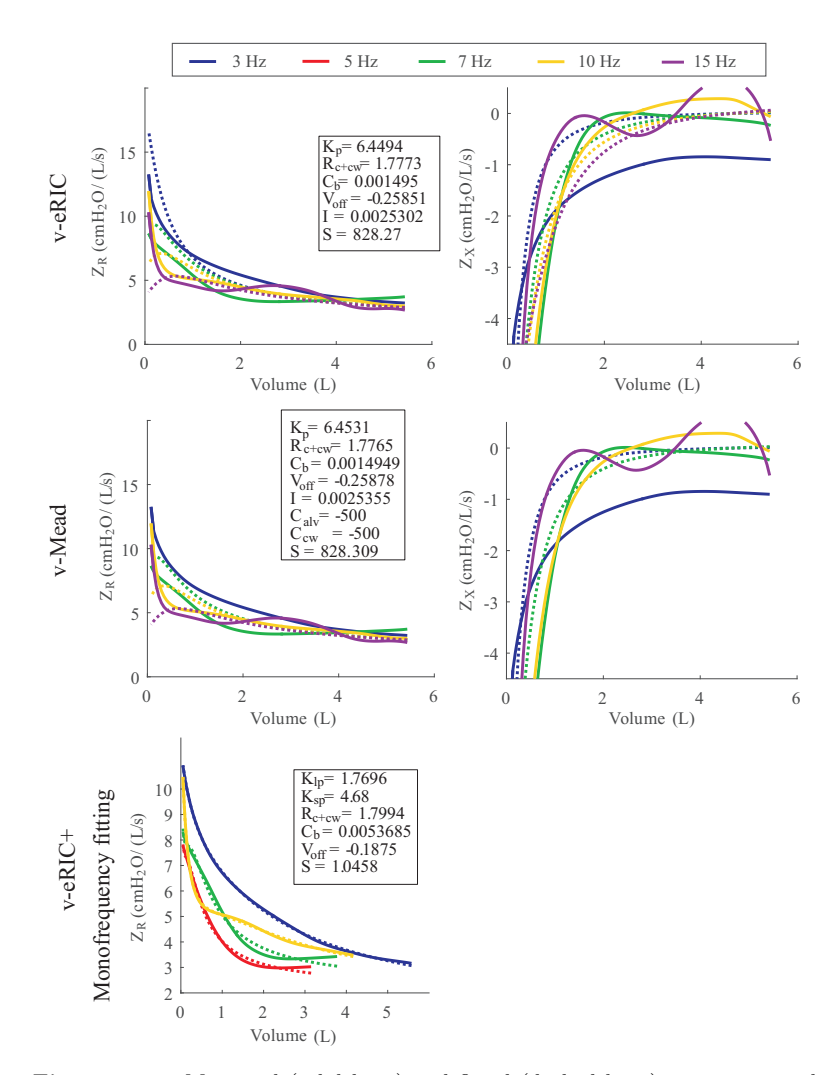


Figure 4.10: Measured (solid lines) and fitted (dashed lines) resistances and reactances. Data obtained from a healthy subject (male, 28 years old, BMI = 23.15). Top and middle panels: Multi-frequency fitting for $Z_{\rm R}(\omega,V)$ and $Z_{\rm X}(\omega,V)$, bottom panel: mono-frequency fitting for $Z_{\rm R}(\omega,V)$ only.

compliances $C_{\rm alv}$ and $C_{\rm cw}$ are estimated to unphysiological values which are at the boundary of the parameter vectors. This corresponds to the sensitivity analysis of the Mead model as shown in Appendix A.4.

The parameter estimation with the v-RIC+ model results in an extremely small residual error S=1.0458. The central resistance $R_{\rm c}$ is almost identical with that in the v-RIC and v-Mead models. All parameters are in physiological ranges.

Table 4.2 presents the average parameters obtained from one subject with mild asthma and five healthy subjects. The large and small peripheral airways at functional residual capacity are computed according to eq. (4.16). The central and chest wall tissue resistance $R_{\rm c+cw}$ is similar in both groups, while higher large and small bronchi resistances $R_{\rm lp,FRC}$ and $R_{\rm sp,FRC}$, respectively, can be observed in the asthmatic volunteer. These results match the physiological expectation of an increase in peripheral bronchi in asthma.

the e-RIC+ model	•			
Parameter	$R_{\mathrm{c+cw}}$	$C_{ m b}$	$R_{ m lp,FRC}$	$R_{\rm sp,FRC}$
Unit	$\rm cmH_2O/L/s$	L/cmH_2O	$\rm cmH_2O/L/s$	$\rm cmH_2O/L/s$
Mild asthmatics (n=1)	1.4	0.01064	0.77	2.78
Healthy subjects (n=5)	1.45	0.00542	0.28	1.5

Table 4.2: Respiratory parameters, measured with vFOT and estimated with the e-RIC+ model.

4.4 The nasal FOT

Since FOT omits the necessity for cooperative maneuvers common in spirometry or body plethysmography procedures, it has a potential application for patients with obstructive sleep apnea (OSA). However, since these patients breathe through their noses during sleep, the effect of the nasal passage and the breathing mask on FOT measurements needs to be considered. Previously, Farré et al. have carried out research using mono-frequency FOT and an esophageal balloon to investigate lung mechanics through a nasal mask [48–50]. This section focuses on the compensation of the undetermined flow leakage caused by using nasal masks and the influence of the nasal passage on multifrequency FOT measurements. To determine the impedance of the nasal passage, test subjects are asked to perform a FOT session with a Philips Respironics ComfortGel Blue nasal mask (Philips Respironics, Pittsburgh, Pennsylva-

nia, USA). Impedance of nasal passage and nasal mask are computed by subtracting the total respiratory impedance (measured via nose) and the lower respiratory impedance (measured via mouth).

Compensation of gas leakage caused by using a nasal mask

The use of a nasal mask causes two different leakage sources: one at the $\rm CO_2$ expiratory valve and one at the contact surface. The masks are fixed on the subject's face through elastic bands around the head. During the measurements, there is another leak around the top of the nose as well as in the cheek region of the subjects (Fig. 4.11). Consequently, the flow entering the respiratory system $\dot{V}_{\rm rs}$ and the flow measured by the pneumotach $\dot{V}_{\rm meas}$ are not the same. The flow and leak components are illustrated in Fig. 4.12. $\dot{V}_{\rm valve}$

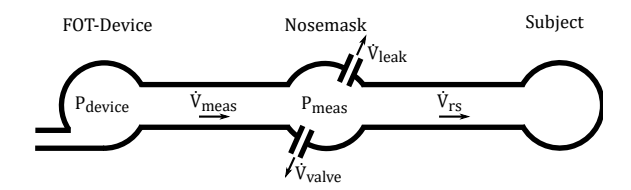


Figure 4.12: Schematic representing the leakage problem caused by using a nasal mask.

is the flow through the expiratory valve and $\dot{V}_{\rm leak}$ the flow leaking out at the mask-face interface. $\dot{V}_{\rm meas}$ can be expressed as

$$\dot{V}_{\text{meas}}(t) = \dot{V}_{\text{rs}}(t) + \dot{V}_{\text{valve}}(t) + \dot{V}_{\text{leak}}(t). \tag{4.23}$$

 $\dot{V}_{\rm leak}$ is a mixture of laminar and turbulent flow. Its pressure-flow relationship is given as the solution of the Rohrer equation (A.8):

$$\dot{V}_{\rm leak}(t) = -\frac{K_1}{2K_2} + \sqrt{(\frac{K_1}{2K_2})^2 + \frac{P_{\rm trans}(t)}{K_2}}, \tag{4.24}$$

where K_1 and K_2 are laminar and turbulent coefficients. To estimate $\dot{V}_{\rm leak}$, the functional residual capacity of the lungs is assumed to be constant during each measurement. If all leakage has been compensated, the integrated lung volume V_{rs} should be zero if the considered period $[T_{\rm Start}, T_{\rm End}]$ is long:

$$\int_{T_{\text{Start}}}^{T_{\text{End}}} \dot{V}_{\text{rs}}(t)dt = 0. \tag{4.25}$$

The parameters K_1 and K_1 have been estimated using non-linear Least Squares parameter estimation. The start value $K_{2,0}$ was estimated by running the Least Squares algorithm only for K_2 assuming K_1 is equal to zero. After finding $K_{2,0} = 500 \,\mathrm{cmH_2O/(L/s)^2}$ and choosing $K_{1,0} = 2 \,\mathrm{cmH_2O/L/s}$, the algorithm was applied again on measurement data.

The corrected volume of a representative measurement is depicted in Fig. 4.13. After the correction of the valve $V_{\text{valve}}(t)$, there is still approximately 1.5L gas inside the lungs, which corresponds to the amount of air leaked out at the mask-face interface. Tab. 4.3 shows the parameters of the leakage compensation. The parameter K_2 of the turbulent flow dominated that of the laminar flow at face-maskinterface.

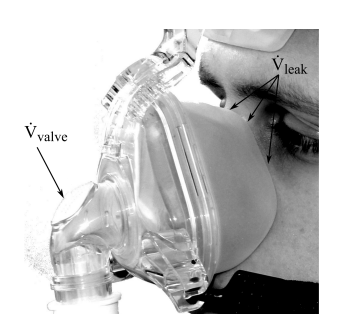


Figure 4.11: Air leaks out at respiratory valve and at mask-face interface [144].

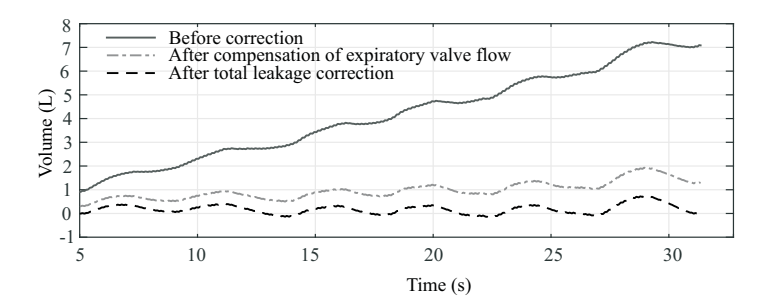


Figure 4.13: One representative result of the leakage compensation: volumes before correction, after compensation of the expiratory valve and after total leakage correction for $T_{\rm End} = 31 \, \text{s} \, [144]$.

Results of the nasal FOT measurements

Applying FOT at patients' mouth and nose in two different measurements demonstrates the effect of the nasal passage and mask on FOT results (see

Frequency	K_1	K_2	RSS
[Hz]	$[cmH_2O/l/s]$	$[\rm cmH_2O/(l/s)^2]$	
5	0.0101	1298.8130	$3.4524 \cdot 10^{-17}$
6	0.0438	2125.8626	$2.1192 \cdot 10^{-21}$
7	0.0102	1306.4878	$4.1273 \cdot 10^{-17}$
8	0.0760	2255.9254	$8.5190 \cdot 10^{-21}$
10	0.0098	695.2472	$5.8974 \cdot 10^{-21}$
15	0.0080	863.1106	$5.1379 \cdot 10^{-20}$

Table 4.3: K_1 and K_2 for compensation of leakage at mask-face interface.

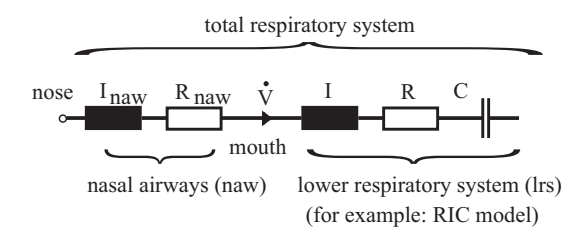


Figure 4.14: Model of the nasal airways and the lower respiratory system.

Fig. 4.15). The average resistance and reactance of the lower (lrs) and total respiratory system for all test subjects are depicted in Fig. 4.15. Both resistances $Z_{\rm R,total}$ and $Z_{\rm R,lrs}$ decreased over frequency. $Z_{\rm X,lrs}$ yields a positive frequency dependence from $-1.159\,{\rm cmH_2O/l/s}$ at 3 Hz to $1.176\,{\rm cmH_2O/l/s}$ at 20 Hz. $Z_{\rm R,total}$ is significantly higher than $Z_{\rm R,lrs}$. Resonance frequency are found to be between 7.5 Hz and 9.5 Hz for the lower respiratory system, which correlates to the results reported by MacLeod and Birch [119]. For the total system, the average resonance frequency decreases to 4 Hz.

Tab. 4.4 displays the values of the nasal (naw) resistance $Z_{\rm R,naw}$ and the ratio $Z_{\rm R,naw}/Z_{\rm R,total}$. $Z_{\rm R,naw}$ is computed by subtracting $Z_{\rm R,total}$ by $Z_{\rm R,lrs}$. The nasal resistance has an average value of $4.096 \pm 2.019 \, {\rm cmH_2O/l/s}$ which corresponds to 66% of the total resistance. Our measurement confirms the results reported in [51] (Fig.3.12) and indicates that the nasal impedance has a large contribution in the total respiratory impedance and cannot be neglected in nasal FOT measurements.

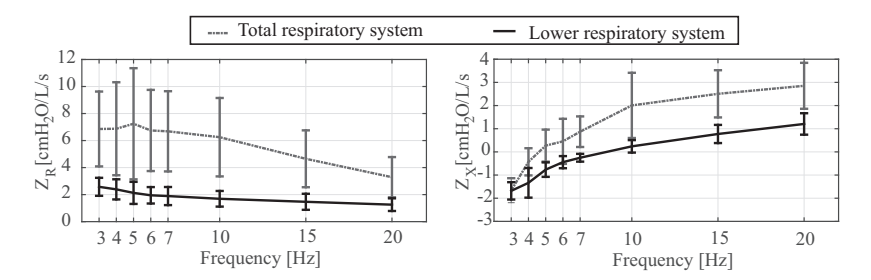


Figure 4.15: Average resistance and reactance of the total and lower respiratory system.

ID	R_{naw}	$R_{\rm naw}/R_{\rm total}$ [%]	$I_{ m naw}$	$I_{\rm naw}/I_{\rm total}[\%]$
1	3.3412	58.58	0.0091	30.33
2	2.7237	65.32	0.0134	52.34
3	2.8278	61.01	0.0178	58.17
4	4.5795	70.44	0.0136	49.64
5	8.5902	73.41	0.0418	78.42
6	2.3394	61.46	0.0118	56.73
7	6.3148	83.58	0.01487	65.22
8	2.0484	57.08	0.01043	53.49
Mean	4.096	66.36	0.0166	55.54
±STD	2.019	7.91	0.00985	12.8

Table 4.4: $R_{\rm naw}$ and proportion of $R_{\rm naw}$ to $R_{\rm rs}$. Resistances are given in cmH₂O/L/s and inertances are given in cmH₂O/L/s².

4.5 Summary

This chapter presents a comprehensive investigation on the respiratory impedance measured via the forced oscillation technique. The windowed cosine fitting method is applied on the bandpass-filtered data to compute the respiratory impedance. The physiological interpretation of the impedance relates to the underlying model structure. The Mead model present the best correspondence to respiratory mechanics. The extended- and augmented-RIC models deliver robust estimation results. The estimated compliance with these two models corresponds to the elasticity of the peripheral bronchi, not the alveoli or tissue.

The volume-dependent FOT is an extension of the classic FOT. It measures the change of the impedance over frequencies and lung volume. The ZV diagram provides additional lung information to assess lung mechanics. It has been show that the extended respiratory models v-eRIC, v-Mead, and v-eRIC+ can be used to describe the volume-dependency of the impedance.

Modeling of cardiopulmonary interactions and cardiogenic congestion

Breathing in, I am aware of my heart.

Breathing out, I smile to my heart.

Thich Nhat Hanh

Cardiopulmonary interactions are indispensable in living beings. Despite many studies on animal and clinical data over the past 50 years, these interactions are only partly understood, especially under pathological conditions or medical treatments. Moreover, there is a lack of computational models which can simulate these interactions quantitatively. This chapter introduces a biophysical forward model of the cardiopulmonary system which focuses on the hemodynamic interactions between the lungs and the heart. First, a cardiovascular model developed in Matlab SimscapeTM is introduced. Second, model validations comparing simulation results with clinical and animal data are discussed. Finally, the model is extended by the lymphatics and the fluid balance system to explain the development of heart failure and cardiogenic congestion.

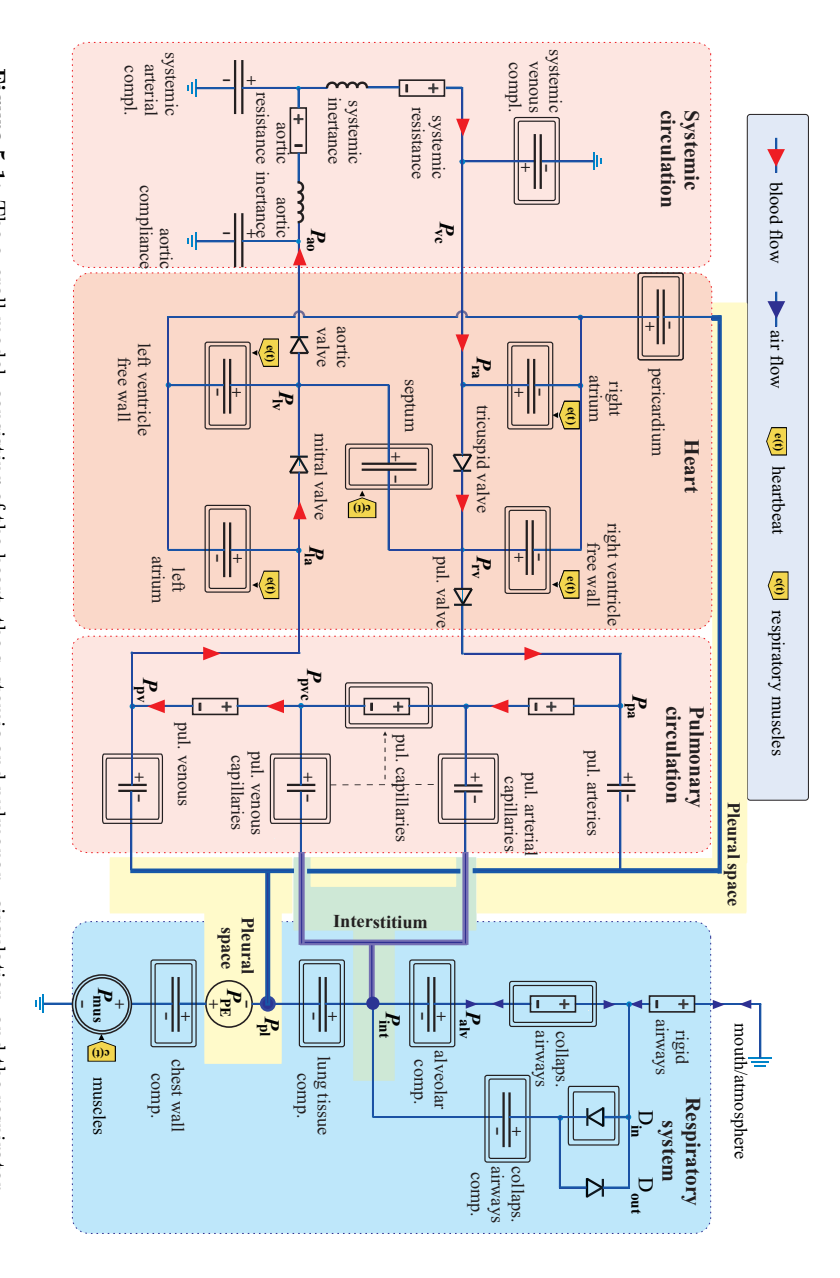
Parts of the chapter were previously published in peer-reviewed journals [142, 150].

5.1 Modeling of heart and circulation

The development of the cardiovascular model is based on the works of Smith et al. [191,192] with several extensions. In the first model extension, the atria will be considered explicitly. Second, non-linear behaviors of the veins and the pulmonary capillaries will be taken into consideration. The comprehensive structure of the cardiovascular model and the overall model is illustrated in Fig 5.1.

5.1.1 Atria, ventricles and heart valves

The heart model consists of left atrium (la), right atrium (ra), left ventricle free wall (lvf), right ventricle free wall (rv), septum (spt), pericardium (pcd) and four heart valves (pulmonary valve $R_{\rm pv}$, bicuspid valve $R_{\rm mt}$, tricuspid valve $R_{\rm tc}$ and aortic valve $R_{\rm av}$). The atria and ventricles are modeled by elastic elements (compliance). Their PV relationships are characterized by the end-diastolic pressure-volume relationship (EDPVR) and end-systolic pressure-volume relationship (ESPVR) [77,153,192]. Let $E_{\rm es}$ be the chamber elastance during systole and $V_{\rm d}$ its filling volume of the ESPVR at zero transmural



system. Flows are distinguished between blood flow (red arrows), air flow (blue arrows). Figure 5.1: The overall model, consisting of the heart, the systemic and pulmonary circulation, and the respiratory

pressure, P_0 the minimal diastolic pressure, λ the curvature of the EDPVR curve, and V_0 atrium volume at zero pressure, then the PV relationships are given as [192]:

$$P_{\rm es} = E_{\rm es} \cdot (V - V_d),\tag{5.1}$$

$$P_{\rm ed} = P_0 \cdot (e^{\lambda(V - V_0)} - 1).$$
 (5.2)

A time-variant driver function e(t) activates either eq. (5.1) or eq. (5.2) to model the transition between the systolic and diastolic pressures:

$$P(V,t) = e(t) \cdot P_{es}(V,t) + (1 - e(t)) \cdot P_{ed}(V,t). \tag{5.3}$$

The driver function e(t) can be modeled as a Gauss distribution for atria, and as a sum of four different Gauss distributions for ventricles and septum. Parameters of e(t) are taken from [153] and given in Appendix A.5. The heart valves are modeled with ideal diodes with transmitting pressures of 10^{-5} cmH₂O, blocking resistances of 10^{5} cmH₂O/L/s, and various transmitting resistances (Table 5.1) [191].

Table 5.1: Transmitting resistances of heart valves $[cmH_2O/L/s]$

	Resistance
Tricuspid	4.0789
Pulmonary	2.7191
Mitral	13.5955
Aortic	6.7977

5.1.2 Septum and pericardium

Septum and pericardium cause ventricular interactions which have a

strong impact on cardiovascular dynamics. Smith et al. [192] separated the ventricles into three free wall components: left ventricle free wall (lvf), septum (spt), and right ventricle free wall (rvf). No component has an influence on the other parts. The septum moves leftward towards the left ventricle during systole and rightward towards the right ventricle during diastole. The ventricular volume is a combination of the septum and ventricular free wall volume. The septum is driven by the same driver function as the left ventricle.

The pericardium is a double-wall sac surrounding four heart chambers and separating them from the pleural space. The pericardium volume is, hence, the sum of ventricular and atrial volumes. In our model, the pericardium is modeled by one compliance; its positive terminal is connected to the pleural space and its negative terminal to the four heart chambers.

5.1.3 Vascular arteries and veins

The vascular system, a network of blood vessels, is modeled by lumped elements regarding its function rather than its anatomical structure [33, 89, 117, 192]. Realistic values of cardiac preload and afterload can be determined by applying the Windkessel model to the systemic and pulmonary circulation [192]. While the aorta and arteries are linearized with parameters adapted from [36], it is necessary to consider the non-linearities of the veins [68, 69, 75, 96, 191, 223, 227, 230]. According to Hainsworth [69] and Rothe [179], the pressure-volume (PV) characteristics of a vessel can be divided into different phases: collapsed, filling, unstressed, distention, and over-distension (Fig. 5.2).

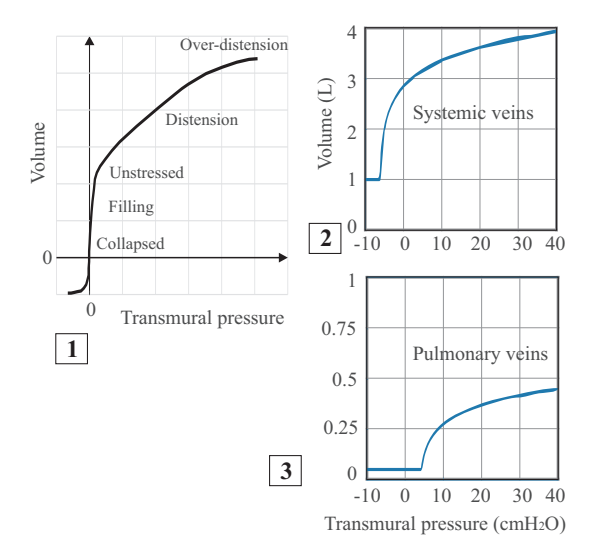


Figure 5.2: (1) Pressure-volume (PV) characteristics of a collapsible tube, reproduced from [69]. (2) PV relation of the systemic veins. (3) PV relation of the pulmonary vein [142].

The nonlinear behavior of the veins can be modeled by the log function

$$V = \frac{1}{\lambda} \cdot \log(P_{\rm tr} + P_0) + V_0, \tag{5.4}$$

including the three parameters P_0 , V_0 and λ . The log function has a high gradient at the beginning which changes quickly to a lower slope after the "unstressed" point. The parameters are obtained for 3 L systemic venous blood

volume and 300 mL pulmonary venous blood volume at normal blood pressures [96]. Figure 5.2 compares the PV characteristics of a separated vessel reported in [69] and the implemented systemic and pulmonary veins.

Unlike the separated vessel, the veins must maintain a nonzero volume even at zero or negative transmural pressure, since they are networks of vessels tethered to the surrounding tissues which prevent them from a total collapse [37,69,179]. The minimum volume of the systemic veins is positive and considered to be 1 L in the model. Under normal conditions, there is around 3 L in the systemic veins under a slightly positive transmural venous pressure.

Pulmonary capillaries

The pulmonary capillaries surround the lung alveoli. Their PV characteristics can be modeled by the hyperbolic function:

$$V_{\rm cap}(t) = V_0 + \frac{1}{\lambda} \cdot \tanh(\mathbf{c} \cdot P_{\rm tr,cap}(t) + P_0). \tag{5.5}$$

The constant parameter V_0 , c, and P_0 are determined based on following considerations [68,96]:

- 1. In a healthy body, the pulmonary capillary transmural pressure is $P_{\rm tr,cap} \approx 15~{\rm cmH_2O}~(=P_{\rm cap}-P_{\rm int}=10-(-5)~{\rm cmH_2O})$, where $P_{\rm cap}$ is the pressure inside the lung capillaries and $P_{\rm int}$ the pressure of the surrounding interstitial pressure.
- 2. At this pressure level, a total blood volume in the pulmonary circulation is approx. 200 mL.
- 3. At normal transmural pressure, the capillaries can be modeled by an ideal compliance with a linear PV relationship. At immoderately low pressure, the capillaries collapse to a minimum volume of approx. $V_{\rm min}=10$ mL. At excessively high pressure, all capillaries are recruited and assumed to reach a maximum volume of 400 mL.

For a detailed description of CPIs and congestion, the pulmonary capillary compliance is subdivided into arterial and venous capillary components. Both together simulate the total PV characteristics shown in Fig. 5.3.

Unlike the peripheral airways, the length of the pulmonary capillaries can be considered to be unchanged during respiratory activities. Thus, according to the law of Poiseuille, flow resistance of the lungs capillaries R(t) is inversely proportional to the square of their volume:

$$R(t) = R_1 \cdot \frac{(V_1 - 0.9V_{\min})^2}{(V(t) - 0.9V_{\min})^2}.$$
 (5.6)

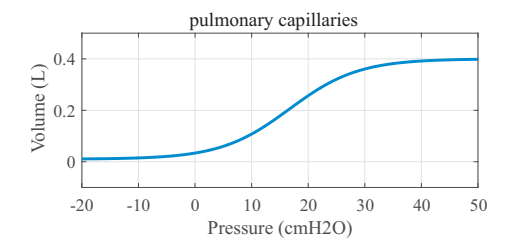


Figure 5.3: PV-characteristics of lung capillaries [142].

 V_{min} is the minimal capillary volume during collapse. V_1 and R_1 are capillary resistance and volume at a normal transmural pressure, respectively. Parameters for the pulmonary capillaries are given in Table 5.2. At a normal filling volume $V=200~\rm mL$, the pulmonary flow resistance is $69.75~\rm cmH_2OL^{-1}$ s, which reaches a maximum value of $R=2.5*10^6~\rm cmH_2OL^{-1}$ s at a collapsing volume of $V=V_{min}=10~\rm mL$.

Table 5.2: Parameters of the pulmonary capillaries.	V_1 ,	V_0 , and	V_{min}	are
given in L, R_1 in cm H_2OL^{-1} s, and λ in L^{-1} . c is a sca	lar.			

Resistance			Compliance		
Parameter	Value	Unit	Parameter Value Unit		
V_1	0.2	L	V_0	0.1025	L
R_1	70.8725	$cmH_2OL^{-1}s$	P_0	-1.3687	cmH ₂ O
V_{\min}	0.005	L	λ	10.256	L^{-1}
			С	0.0821	1

The remaining linear parameters of the systemic and pulmonary circulation are given in Table 5.3. At the beginning of the simulation, each compliance is assigned to an initial volume. Each heart ventricle has an initial volume of 40 mL. The systemic veins are filled with 3.1 L, the systemic arteries and capillaries with 600 mL. On the pulmonary side, initial volume is set to 100 mL for the arteries, 100 mL for the capillaries, and 50 mL for the veins.

5.1.4 Baseline simulation of the cardiovascular system

Baseline simulations were performed to validate the model for a healthy subject. The change in the systemic arterial volume during the initial phase is depicted in Fig. 5.4. At the beginning of each simulation, blood redistributes regarding

Components	Param.	Value	Unit
aortic compliance	C_{ao}	0.000168	$LcmH_2O^{-1}$
syst. arteries compliance	$C_{\rm sys,art}$	0.0011	$LcmH_2O^{-1}$
aortic resistance	Rao	91.78	$cmH_2OL^{-1}s$
syst. resistance	R_{sys}	1359.5	$cmH_2OL^{-1}s$
aortic inertance	L_{ao}	1.1216	$cmH_2OL^{-1}s^2$
syst. inertance	L_{sys}	4894.4	$cmH_2OL^{-1}s^2$
pul. art. resistance	R _{pa}	94.5	$cmH_2OL^{-1}s$
pul. art. compliance	C_{pa}	0.0022	$LcmH_2O^{-1}$
pul. ven. resistance	R_{pv}	31.5	$cmH_2OL^{-1}s$

Table 5.3: Parameters of systemic and pulmonary circulation, from [36, 191].

the ratio between the vessels' compliances. At t = 20 s and t = 25 s, the driver functions of the ventricles and atria are activated, respectively. The operating point of the system, where all compliances have reached their steady-state volume have, is arrived after approx. 40 seconds.

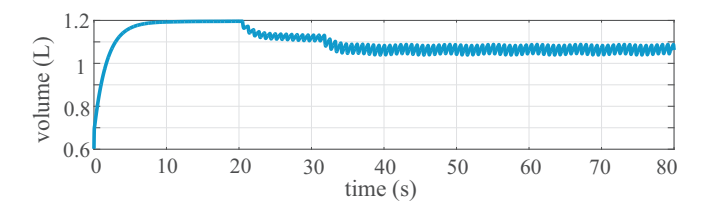


Figure 5.4: Changes in systemic arterial volume during the initial phase of the simulation. From a start value at 0.6 L, the volume reached a stationary value of 1.2 L. After the heart started to pump at t=20 s, the volume stabilized at around 1.05-1.09 L.

Figure 5.5 presents the simulated pressures and volumes during three cardiac cycles in a healthy person. Heart rate is 80 beats per min, stroke volume 72 mL, and cardiac output 5.76 L/min. The aortic pressure rises to 169 cm $\rm H_2O$ (124.3 mm $\rm H_2O$) in systole and falls to 110 cm $\rm H_2O$ (80.9 mm $\rm H_2O$) in diastole.

Table 5.4 compares the simulated blood pressures and cardiac indexes to the standard range of a healthy person [78]. Cardiac and stroke indexes are calculated by assuming a total body surface of $1.73~\mathrm{m}^2$. All simulated values correspond to physiological standard ranges provided in literature. The blood

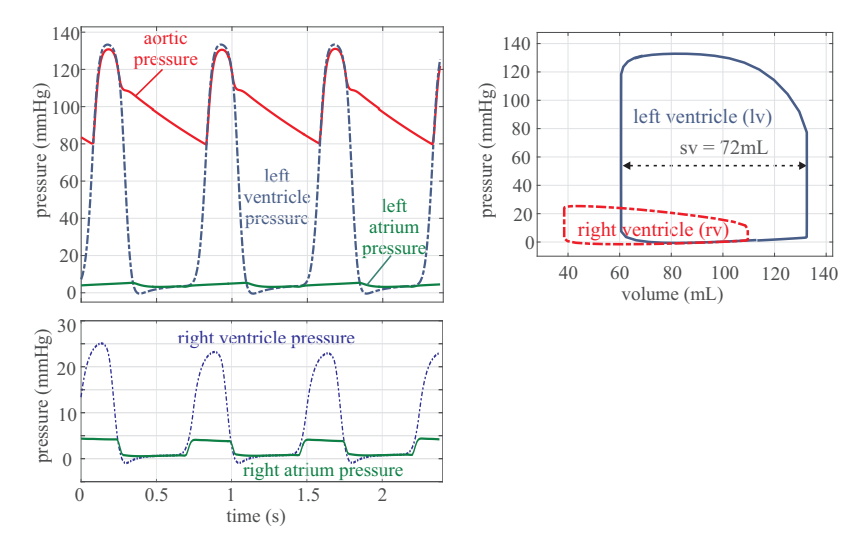


Figure 5.5: Simulative results of the cardiovascular system [142]. Left charts: aortic, left ventricle and atrium pressure over three heart cycles. Right chart: pressure-volume curve of the left and right ventricles.

distribution among different body compartments is depicted in Fig. 5.6.

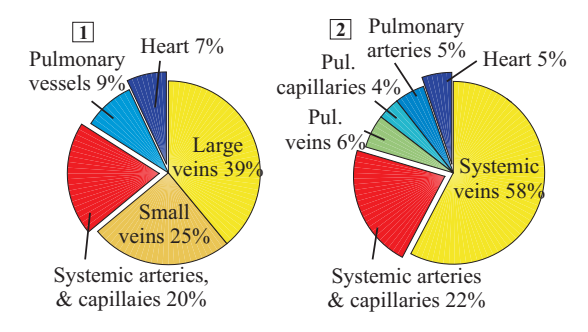


Figure 5.6: Blood volume distribution of the human body. (1) Literature values, reproduced from [68]. (2) Simulation results. Total blood volume is approx. 5~L [142].

Parameter	Model	Standard [78]	Unit
Pressures:			
Left ventricle systolic	124	90 - 140	mmHg
Left ventricle end-diastolic	6	5 - 12	mmHg
Left atrial	3.5 - 5	2 - 12	mmHg
Arterial systolic	122	90 - 140	mmHg
Arterial diastolic	81	60 - 90	mmHg
Right ventricle systolic	25	18 - 30	mmHg
Right ventricle end-diastolic	0.5	-0.5 - 4.5	mmHg
Right atrial mean	0	-2 - 2	mmHg
Pulm. artery systolic	26	13 - 30	mmHg
Pulm. artery diastolic	11	3 - 15	mmHg
Pulm. capillary wedge max	10 – 16	8 - 23	mmHg
Pulm. capillary wedge min	6 – 11	5 - 14	mmHg
Others:			
Cardiac index	3.33	2.5 - 5.3	$L/min/m^2$
Stroke index	41.63	37- 72	mL/beat/m ²

Table 5.4: Baseline simulation results of pressures, cardiac and stroke indexes. The indexes were calculated with a total body surface of 1.73 m². Standard values are given in [78].

5.2 Cardiopulmonary hemodynamic interactions

This section focuses on the mechanical coupling between the respiratory and the circulatory system. The pericardium, pulmonary arteries and veins are surrounded by the pleural pressure $P_{\rm pl}$, while the pulmonary capillaries are surrounded by the interstitial pressure $P_{\rm int}$. The coupling is implemented in Simscape by means of physical connections between the two subsystems. The overall system is presented in Fig. 5.1.

Under normal conditions, the thoracic blood volume (TBV) is about 20% (approx. 1 L) of the total blood volume [68,96]. The chest wall capacity (V_{cw}) from eq. (3.15) has to be adapted, since Athanasiades et al. [4] did not consider TBV in their model and assumed that the maximal chest wall volume was equal to the total lung capacity (TLC). In our model, $V_{cw,max}$ has been adapted to TLC+1 L, the parameter B_{cw} in eq. (3.16) is changed to

$$B_{cw} \approx \frac{V_{max} - RV}{4 \cdot C_{cw,max}} \approx 4.75 \text{ cmH}_2\text{O}.$$
 (5.7)

The new parameters of the chest wall are given in Table 5.5. The initial value

of chest wall volume increases to 2.05 L by taking the TBV into consideration.

om the respiratory to cardiopulmonary system.			
Parameter	RS only	CPS	Unit
A_{cw}	7	7	$\rm cmH_2O$
B_{cw}	3.5	4.75	$\rm cmH_2O$
V_{max}	5.6	6.6	L
RV	1.3	1.3	L
Ppe	10	10	cmH ₂ O

Table 5.5: Adaptation of the chest wall parameter with regard to thoracic blood volume from the respiratory to cardiopulmonary system.

In summary, the comprehensive cardiopulmonary model consists of a 8-element non-linear respiratory model and a cardiovascular model with four heart chambers, hearts valves, a systemic and a pulmonary circulation [142, 148]. The respiratory and the cardiovascular system are coupled at the pleural space and lung interstitium.

5.2.1 Simulation results

The simulation results are compared to clinical data and animal studies reported in literature. Since model parameters can vary among species and individuals, parameter estimation can increase the performance of the model in curve fitting. However, changing randomized parameters via "try and error" in such a large model can lead to parameter "manipulation". For that reason, all parameters are remained unchanged during all simulations. Only the input signal, the respiratory muscles are adapted to generate the required scenarios by changing the pleural pressure during spontaneous breathing and the mouth pressure during mechanical ventilation.

Mueller maneuver

During spontaneous inspiration, a decrease in $P_{\rm pl}$ leads to a shift in blood volume from the systemic to the pulmonary circulation and a fall in a ortic pressure. During inspiration with maximum effort (Mueller maneuver¹), a significant increase in a ortic pressure, transmural left and right ventricular filling

¹During Mueller maneuver, subjects are asked to perform a forced expiratory. After that, an attempt at further inspiration is made with closed mouth and nose, which makes the thoracic pressure maximal subatmospheric. Mueller maneuver can be used in the evaluation of airway obstruction in patients with sleep apnea [194].

pressure during the Mueller maneuver in closed-chest, anesthetized, neurally intact Mongrel dogs was documented by Robotham et al. [175]. Inactivating the respiratory tract due to zero gas flow, and setting the pleural pressure from 0 to $-12~{\rm cmH_2O}$ and back to 0 within a duration of 8 heart beats, the initial condition of the Mueller maneuver occurs.

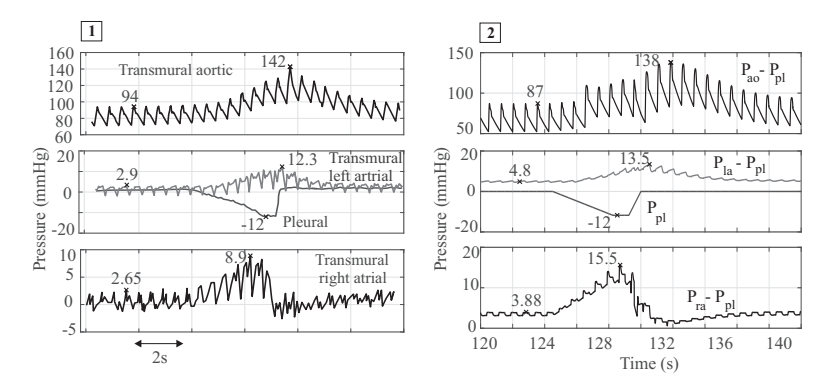


Figure 5.7: Pressure relations during a Mueller maneuver. The pleural pressure, as well as transmural aortic, left and right atrial pressures are depicted. (1) Data measured on a neurally intact Mongrel dog, reproduced from [176]. (2): Model simulation results for a healthy human. The pleural pressure in the model was set from 0 to -12 cm $\rm H_2O$ and back to 0 within 8 heart beats [142].

Figure 5.7 depicts simulation results (2) in comparison with animal data (1). At the second heart beat after the end of the maneuver, the transmural aortic pressure reaches its maximum at 138 mmHg (142 mmHg in animal data). The transmural right atrial pressure rises during the first 5 heart beats, and falls abruptly to a negative value. The transmural left atrial pressure also increases and reaches it maximum about 3 heart beats later than the transmural right atrial pressure. Dynamic behaviors of the model is observed to be similar to animal data.

Pressure relations during ventilation

A ventilator is connected to the cardiopulmonary system to simulate the model's response to mechanical ventilation. Fig 5.8 (1) depicts data from a lung-diseased patient under volume-controlled-ventilation (VCV) published by Jardin et al. [90]. Electrocardiogram (ECG), airway (A), esophageal (E), right atrial (RA), and pulmonary capillary wedge (PCW) pressures were simultaneously recorded. Tidal volume was set to 12 mL/kg (equivalent to 840 mL for a 75 kg

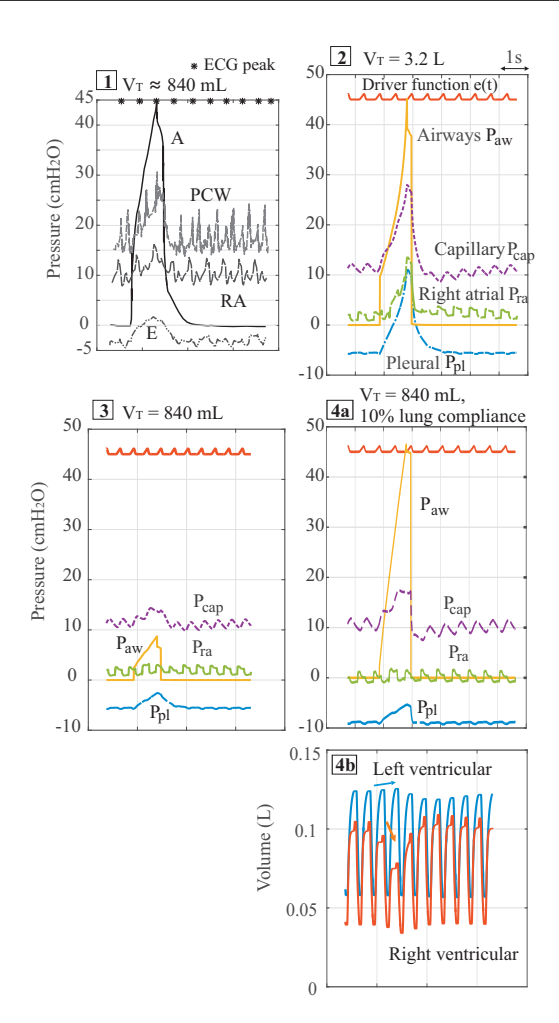


Figure 5.8: Pulmonary and cardiovascular pressures in patients under volume-controlled ventilation (VCV). (1): Data reproduced from [90]. PCW = pulmonary capillary wedge pressure, RA = right atrial pressure, A = airway pressure, E = esophageal pressure. (2,3,4): simulative results: (2) $V_{\rm T} = 3.2$ L (3) $V_{\rm T} = 840$ mL volume. (4a) $V_{\rm T} = 840$ mL and reduction of lung compliance by 90%. (4b) Left and right ventricular volume for simulation (4) [142].

patient). Peak ventilation pressure was 45 cm $\rm H_2O$. Figures 5.8 (2-4) display the simulation data for different tidal volumes. In (2), $V_{\rm T}$ is set to 3.2 L to achieve a peak pressure at 45 cm $\rm H_2O$. Simulation (3) is done for $V_{\rm T}=840$ mL, which results in a peak airway pressure < 10 cm $\rm H_2O$. These results show that such a high ventilation pressure at a low tidal volume does not occur in healthy subjects. The high pressure-volume ratio indicates a dramatic drop in the lung compliance, such as in a severe restrictive pulmonary disease. Reducing the lung compliance (alveolar and tissue compliance) to 10% of the original values, a peak pressure of 45 cm $\rm H_2O$ can be achieved at $V_{\rm T}=840$ mL as shown in 5.8 (4a).

Simulation corresponds to the prediction of a restrictive condition in this pa-Furthermore, Jardin tient. observed that the increase in the pulmonary capillary wedge pressure (PCW) is greater than that in the esophageal pressure, which leads to an increased left ventricular volume; and the increase in right atrial pressure is smaller than that in esophageal pressure, which corresponds to a decrease in right ventricular volume. The pressure relations ($\Delta P_{\rm cap}$ $> \Delta P_{\rm pl} > \Delta P_{\rm ra}$) can be reproduced by the model. Figure 5.8 (4b) displays the change in left and right ventricular volumes during VCV. An increase in left ventricular volume and a decrease in right ventricular volume can be quantitatively observed in the model response.

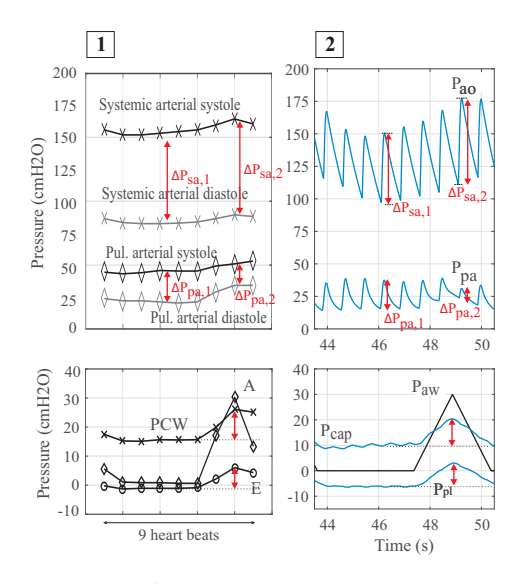


Figure 5.9: Aortic, pulmonary arterial and capillary pressure during a ventilation cycle. (1) Clinical data, reproduced from [90]. (2) Simulative results. Observation: $\Delta P_{\mathrm{sa},1} < \Delta P_{\mathrm{sa},2}$ and $\Delta P_{\mathrm{pa},1} > \Delta P_{\mathrm{pa},2}$ [142].

In the same paper, Jardin et al. performed a beat-to-beat analysis on data from 13 ventilated patients, focusing on the change in systemic and pulmonary arterial pressure during ventilated inhalation (Fig. 5.9 (1)). During the lung inflation, esophageal pressure $P_{\rm pl}$ increased slightly less than PCW. An in-

crease in systemic arterial pressure was reported, where systole was greater than diastole. There was also an increase in the pulmonary arterial pressure, however, change in diastole was greater than in systole. Testing the model with the same scenario, simulation results yield similar behaviors. Figure 5.9 depicts the systole-diastole gradient in systemic and pulmonary arterial pressure, where $\Delta P_{\rm sa,1} < \Delta P_{\rm sa,2}$ and $\Delta P_{\rm pa,1} > \Delta P_{\rm pa,2}$. The model response corresponds to the reported clinical data.

Stroke volume during spontaneous breathing and positive-pressure ventilation

This part compares the change of stroke volume (SV) between spontaneous breathing and positive-pressure ventilation. In anesthetized, intact canines, differential effects of negative (spontaneous inspiration) and positive (positive-pressure inspiration) changes in the intra-thoracic pressure on cardiovascular dynamics were reported [64, 167, 168]. While the left ventricular SV falls with positive pressure inspiration, the right ventricular SV behaved inversely. Fig. 5.10 compares animal data (1) and simulation results (2). The left and right ventricular SV is large in human (50 - 60 mL) comparing to those of a canine (15 - 18 mL). During a positive-pressure inspiration, right ventricular SV first decreases, then increases back to the previous value. This behavior can be observed in animal data and simulation results.

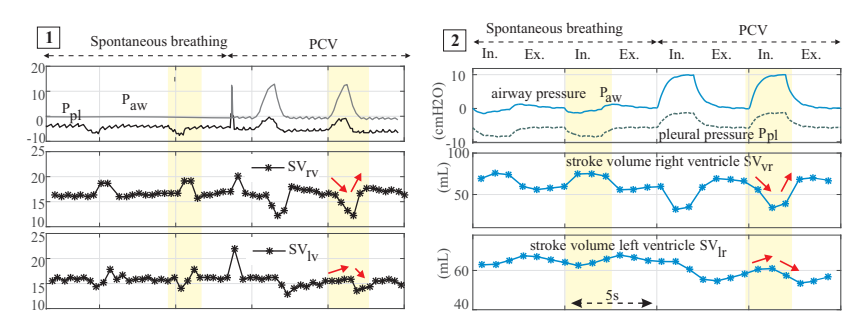


Figure 5.10: Cardiopulmonary interactions during spontaneous breathing and mechanical ventilation. (1) cardiopulmonary interactions observed in animal experiment reported in [64, 168]. (2): model simulation results [142].

Cherpanath et al. introduced a schematic diagram to study CPIs during mechanical ventilation [30] (Fig. 5.11). He qualitatively proposed two causes for the fall of left ventricular SV during positive-pressure ventilation. On the one hand, a higher lung volume causes an increase in the intra-thoracic pressure

(IIP), which reduces venous return and right ventricular preload. On the other hand, a rise in airway pressure leads to an increase in transpulmonary pressure (TPP), followed by an increase in pulmonary vascular resistance and a rise in right ventricular afterload. The diagram is extended quantitatively with model's responses, as shown in Fig. 5.11. The preload is presented by end-diastolic ventricular volume, the afterload by the arterial pressure.

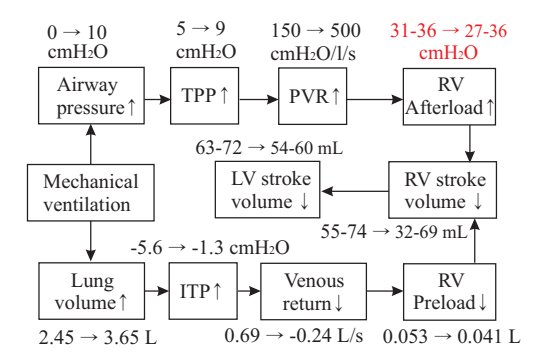


Figure 5.11: Change right and left ventricular stroke volumes under mechanical ventilation. Schema adapted from [30]. Numerical values are from a simulation with pressure-controlled ventilation at PIP=10 cmH₂O [142].

Simulation results confirm the Cherpanath's diagram, with an exception of a variable right ventricular afterload, which does not increase under mechanical ventilation. These results gives an evidence to support the hypothesis, that the changes observed in left and right ventricular SV are primarily caused by the reduction in venous return and right ventricular preload, and less by the change in right ventricular afterload, as proposed in other literatures [64,166].

Effect of PEEP on CPIs

A correlation between PEEP and pleural, transpulmonary, pulmonary arterial, and right atrial pressures was documented by Scharf et al. in anesthetized Mongrel dogs (22–25 kg) [182]. The animals were under VCV ($V_{\rm T}=300-350$ mL (12–14 mL/kg)), PEEP was set to be 0.6, 4.3, 7.7, 11.4, and 16.4 cmH₂O. A comparison between animal data and model response is depicted in Fig. 5.12. Tidal volume $V_{\rm T}$ was set to 12.7 mL/kg (equivalent to 950 mL for a 75 kg healthy human).

Simulation results correlate well with animal data. With increasing PEEP, a rise in lung volume, and further increases in transpulmonary, pleural, pul-

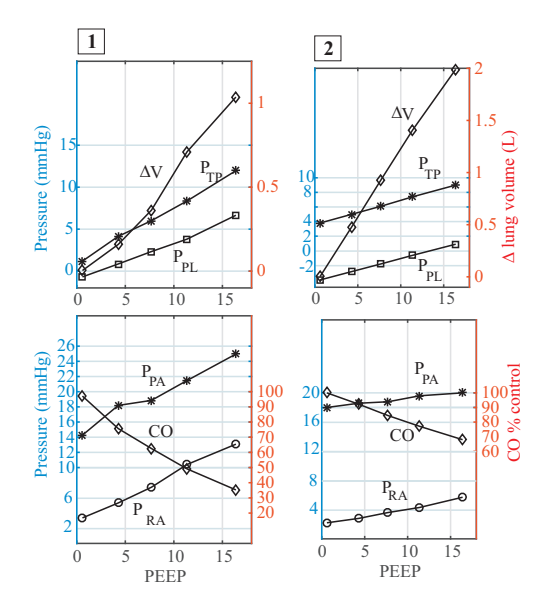


Figure 5.12: Effect of PEEP on lung volume, cardiac output (CO), transpulmonary (TP), pleural (PL), pulmonary arterial (PA), and right atrial (RA) pressures during volume-controlled ventilation. (1) Experimental data in Mongrel dogs, data reproduced from [182], (2) Simulation results [142].

monary arterial, and right atrial pressures can be observed in both data. As PEEP increases from 0.6 to $16.4~\rm cmH_2O$, cardiac output falls to 35% of the original value in dogs and to 65% in simulated human. Note that a better fit between data and model may be achieved by adjusting the parameters of the model. However, this is not the objective of this forward modeling.

5.3 The fluid balance and the lymphatic system

5.3.1 Model development

Modeling of the Starling-equation and the fluid transport

In 1896, Ernest Starling stated that the fluid movement across a vascular barrier would cease when the hydrostatic forces and interstitial osmotic pressures are in balance [197]. This hypothesis, verified by Landis several decades

later [104, 105], is known as the Starling equation:

$$J = K_{\rm f}[(P_{\rm cap} - P_{\rm int}) - \sigma \cdot (P_{\rm osm, cap} - P_{\rm osm, int})]. \tag{5.8}$$

Here, J (in [mol/s]) is the total flux of molecules from the capillaries to the lung interstitium, $K_{\rm f}$ is the permeability of the capillary walls, and σ is the osmotic reflection coefficient for large proteins. $P_{\rm cap}$ and $P_{\rm int}$ are the capillary and interstitial hydrostatic pressures, and $P_{\rm osm,cap}$ and $P_{\rm osm,int}$ are the corresponding colloid osmotic pressures, respectively. Typical parameter values of eq. (5.8) are given in Table 5.6.

Table 5.6. Typical parameters of the Starting equation			
Parameter	Value	Unit	Reference
K_{f}	10^{-6}	$L cm H_2 O^{-1} s^{-1}$	[68] [217] [136]
$P_{\rm cap}$	10	cmH ₂ O	[222] [68]
$P_{ m int}$	-5	$\rm cmH_2O$	[109] [228]
σ	0.75	1	[109] [136]
$P_{ m osm, cap}$	38.07	cmH ₂ O	[68]
$P_{ m osm,int}$	19.04	$\rm cmH_2O$	[68]

Table 5.6: Typical parameters of the Starling equation

In literature, the protein reflection coefficient σ was reported to be between $\sigma=0.7$ [109] and $\sigma=0.8$ [136]. The osmotic pressure depends on the protein concentration in blood. Its typical values are 28 mmHg at artery end and 14 mmHg at venous end of the pulmonary capillaries [68]. The determination of the permeability $K_{\rm f}$ is difficult. In animals experiments, a typical value of $K_{\rm f}=10^{-6}~{\rm LcmH_2O^{-1}\,s^{-1}}$ was estimated by measuring the hydrostatic pressures and the lymphatic flux [68,135,217]. This flux can be easily removed by the lymphatic system under normal conditions. The permeability $K_{\rm f}$ is the product of the hydraulic conductivity K and the filtration surface area $K_{\rm f}$ and the capillaries with a length k0 and a radius k1 relation between k1 and the capillary volume k2 can be derived as

$$K_{\rm f} = K \cdot A = K \cdot 2\pi l = K \cdot 2\sqrt{\pi \cdot l \cdot V_{\rm cap}}.$$
 (5.9)

Then the hydraulic membrane resistance R_{Starling} is given as:

$$R_{\text{Starling}} = \frac{1}{K_{\text{f}}} = \frac{1}{K \cdot 2\sqrt{\pi \cdot l \cdot V_{\text{cap}}}}.$$
 (5.10)

The Starling equation (5.8) yields:

$$J = \frac{1}{R_{\text{Starling}}} [(P_{\text{cap}} - P_{\text{int}}) - \triangle P_{\text{os}}], \tag{5.11}$$

where $\triangle P_{os} = \sigma \cdot (P_{osm,cap} - P_{osm,int})$ is the osmotic pressure gradient between the pulmonary capillaries and the lung interstitium.

Eq. (5.11) states a correlation of the flux through a membrane and the membrane's transmural pressure gradient, similar to Ohm's law for an electrical current. In this work, the filtration is modeled by a current flow through an electrical resistance, as illustrated in Fig. 5.13. Note that ΔP_{os} was implemented as a DC-pressure source and set in series with $R_{Starling}$.

The fluid transport, illustrated in Fig. 5.14, is a continuous process. Fluid flux changes from positive at the arterial capillary end (filtration) to negative at the venous capillary end (re-

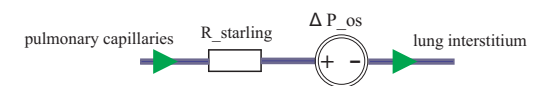


Figure 5.13: Electrical equivalent representation of the Starling equation.

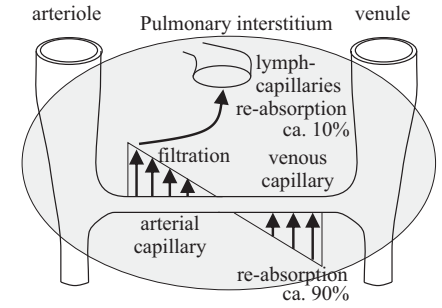


Figure 5.14: Filtration and resorption at capillary endothelial wall, modified from [184].

absorption) due to the pressure relations [184]. In normal conditions, 90% of the flux is reabsorbed at the venous capillaries. The other 10% is removed by the lymphatic system. In our model, the capillary compartment is subdivided into an arterial and a venous part ($R_{\rm cap,art}$ and $R_{\rm cap,ven}$) (see eq. 5.15). The resistances can be derived as

$$R_{\rm Starling,art} = \mathbf{R}_{1,\rm art} \cdot \sqrt{\frac{\mathbf{V}_{1,\rm art}}{V_{\rm cap,art}}}, \quad R_{\rm Starling,ven} = \mathbf{R}_{1,\rm ven} \cdot \sqrt{\frac{\mathbf{V}_{1,\rm ven}}{V_{\rm cap,ven}}}, \ (5.12)$$

where $V_{\rm cap,art}$ and $V_{\rm cap,ven}$ are the volume of the arterial and venous capillaries. $R_{1,\rm art}, \, V_{1,\rm art}, \, R_{1,\rm ven}$ and $V_{1,\rm ven}$ are constant parameters. These parameters, given in Tab. 5.7, were calculated considering following factors:

 The sum of the arterial and venous Starting resistance is equal the total Starling resistance of the capillaries.

$$\begin{split} R_{\text{Starling}} &= R_{\text{Starling,art}} + R_{\text{Starling,ven}} \\ &= R_{1,\text{art}} \cdot \sqrt{\frac{\mathbf{V}_{1,\text{art}}}{V_{\text{cap,art}}}}) + (\mathbf{R}_{1,\text{ven}} \cdot \sqrt{\frac{\mathbf{V}_{1,\text{ven}}}{V_{\text{cap,ven}}}}) \end{split}$$

 Hydraulic conductivity at capillary venous end is 40% higher than one at capillary arterial end [109].

Once the fluid has entered the lung interstitium, it continues moving forward to the peribronchovascular space, where it is absorbed by the lymphatics. The quantitative behavior of extracellular fluid movement in the interstitium is not well understood, as well as any influence of this resistance to the development of pulmonary edema or the absorption over the lymphatics [202]. In this work, the hydraulic resistance for fluid movement within interstitium (see Fig. 5.15) was assumed to be $R_{\rm int}=1000~{\rm cm}H_2{\rm OL}^{-1}{\rm s}$. The large value of $R_{\rm int}$ is considered, since the flow resistance within interstitium can be neglected in comparison to the trans-membrane Starling resistances. Table 5.7 summarizes the parameters of the model.

Parameter	Value	Unit
R _{1,art}	$2.4*10^{6}$	$\mathrm{cmH_2OL}^{-1}\mathrm{s}$
V _{1,art}	0.12	L
R _{1,ven}	$1.7*10^{6}$	$cmH_2OL^{-1}s$
V _{1,ven}	0.08	L
$\triangle P_{osm}$	14.27	cmH ₂ O
$R_{ m int}$	1000	$cmH_2OL^{-1}s$

Table 5.7: Parameters of the implemented Starling equation

A model of the lymphatic system

The lymphatic pump and flow resistance are modeled by a parallel structure of a compliance and a resistance. The fluid flow entering the lymph $I_{\rm in,lym}$ is given as

$$I_{\rm in,lym} = \frac{1}{R_{\rm int}} \cdot (P_{\rm int} - P_{\rm lym}), \tag{5.13}$$

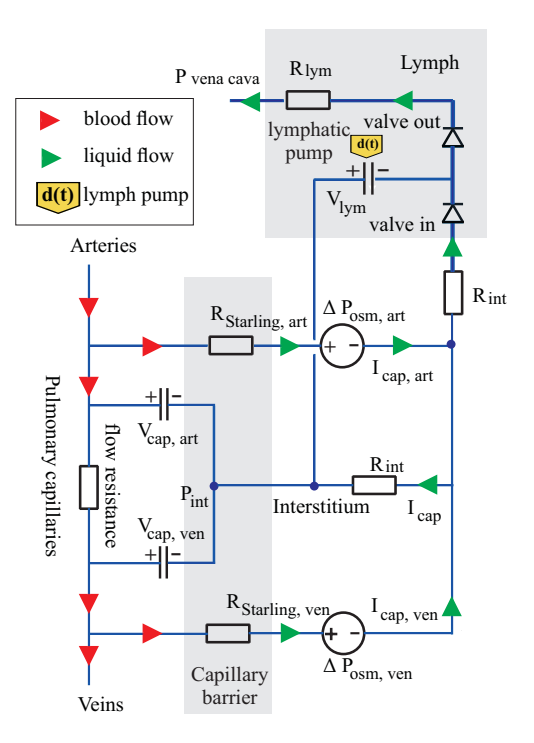


Figure 5.15: The lymphatic system from pulmonary interstitium to vena cava. The Starling equation is implemented at arterial and venous ends of the pulmonary capillaries.

where P_{lym} is the lymphatic pressure. The volume-pressure characteristics of the lymphatic pump is modeled, similarly to the heart pump, with an driver function d(t). d(t) switches the contraction of the lymphatic collector from an active to a passive phase and vice versa:

$$V_{\rm lym} = (1-d(t)) (\frac{\ln(P_{\rm lym} + P_{\rm 0,lym})}{\lambda_{\rm lym}} + \mathbf{V}_{\rm 0,lym}) + d(t) \cdot (\frac{P_{\rm lym}}{E_{\rm es,lym}} + \mathbf{V}_{\rm d,lym}),$$

where $V_{\rm lym}$ is the lymphatic volume. The parameters $\lambda_{\rm lym}$, $P_{\rm 0,lym}$ and $V_{\rm 0,lym}$ define the passive, $E_{\rm es,lym}$ and $V_{\rm d,lym}$ the active phase of the pump (Tab. 5.8).

The driver function d(t) realizes a switch between a diastolic and systolic phase of the lymphatic pump (see Fig. 5.16). While the heart rate is given by

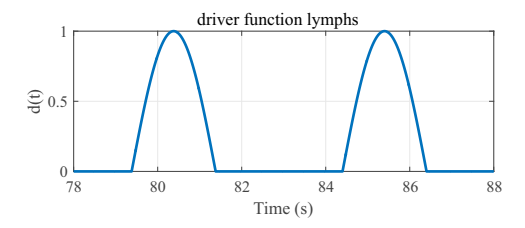


Figure 5.16: Driver function d(t) of the lymphatic pump. A pumping cycle is 2 second long. The maximum frequency of the pump is 12 beat per minute.

the sinus node and thus, volume-independent, the activation of the lymphatic pump depends on its filling volume $V_{\rm liq}$ [184]. There is less known about the regulation of the lymphatic pump [202]. The maximal transport capacity of the lymph within the lungs differs strongly among different references and also varies for specific lung pathologies. It is reported to be higher in chronic heart failure or mechanical damages of the pulmonary capillaries than in hydrostatic edema [68, 202]. In this work, the maximal flow was derived due to the safety factor introduced in [68, 202]. In fact, the lymphatic system is able to remove the extra fluid filtration, which is caused by an increase in the pulmonary venous hydrostatic pressure by 5 mmHg. This elevation causes an extra flux of approx. $6.8*10^{-6}~{\rm L\,s^{-1}}$, according to the Starling-equation. The maximum pump frequency is 12 beat per minute [184], which leads to an amount of $3.4*10^{-5}~{\rm L}$ removed per lymphatic contraction. The pressure-volume behavior of the pump is illustrated in Fig. 5.17.

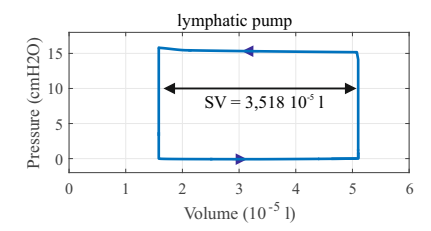


Figure 5.17: PV-curve of the lymph during a contraction

The lymphatic stroke volume is $3.518*10^{-5}$ L. At a pump rate of 12 beats per minute, the maximum possible absorption rate is 25.3 mLh⁻¹ or 607.9 mL

per day.

Parameter	Value	Unit
$R_{ m lym}$	1	$\mathrm{cmH_2OL^{-1}s}$
$V_{ m d,lym}$	0	L
$E_{\rm es,lym}$	10^{6}	$\rm cmH_2OL^{-1}$
$V_{0,\mathrm{lym}}$	$8.731*10^{-5}$	L
$P_{0,lym}$	0.1527	$\rm cmH_2O$
$\lambda_{ m lym}$	50364	L^{-1}
$R_{ m int}$	10^{3}	$\rm cm H_2 O L^{-1} s$
$P_{\rm valve,in}$	10^{-6}	$\rm cmH_2O$
$P_{\rm valve,in}$	10	$\rm cmH_2O$

Table 5.8: Parameters of the lymphatic model

Similar to the structure of the systemic veins, lymphatic flows are unidirectional due to the non-return valves located along the lymphatic vessels. In our model, these valves were modeled by two diodes ($valve\ in$ and $valve\ out$, see Fig. 5.15). The overall model is illustrated in Fig. 5.18. The sophisticated model includes three different hydraulic media: blood flow in the circulation, air flow in the respiration, and fluid flow in the lymphatics. The interstitial pressure $P_{\rm int}$ is connected to all three systems.

5.3.2 Model extension for cardiogenic pulmonary congestion

During pulmonary congestion, the accumulated fluid affects the mechanics of the lungs. Healthy human lungs with a dry weight of 1000 g [5] and a wetdry-relation of $\frac{W}{D} \approx 4~\frac{\rm g}{\rm g_{dry}}$ [109] contain approx. 800 mL fluid in the intra-and extracellular spaces. A acute pulmonary edema occurs by an increase of interstitial fluid increases by 25 to 35% (+ 200 bis 300 mL) [21,109,202].

The lung tissue during congestion

As the interstitial pressure $P_{\rm int}$ rises, the fluid amount within the lung tissue also increases. The maximal fluid volume is reached when (1) lung tissue is not able to capture more fluid and (2) bronchial and alveolar edema occur [109]. In our model, the lung tissue compliance is extended to depend on the fluid

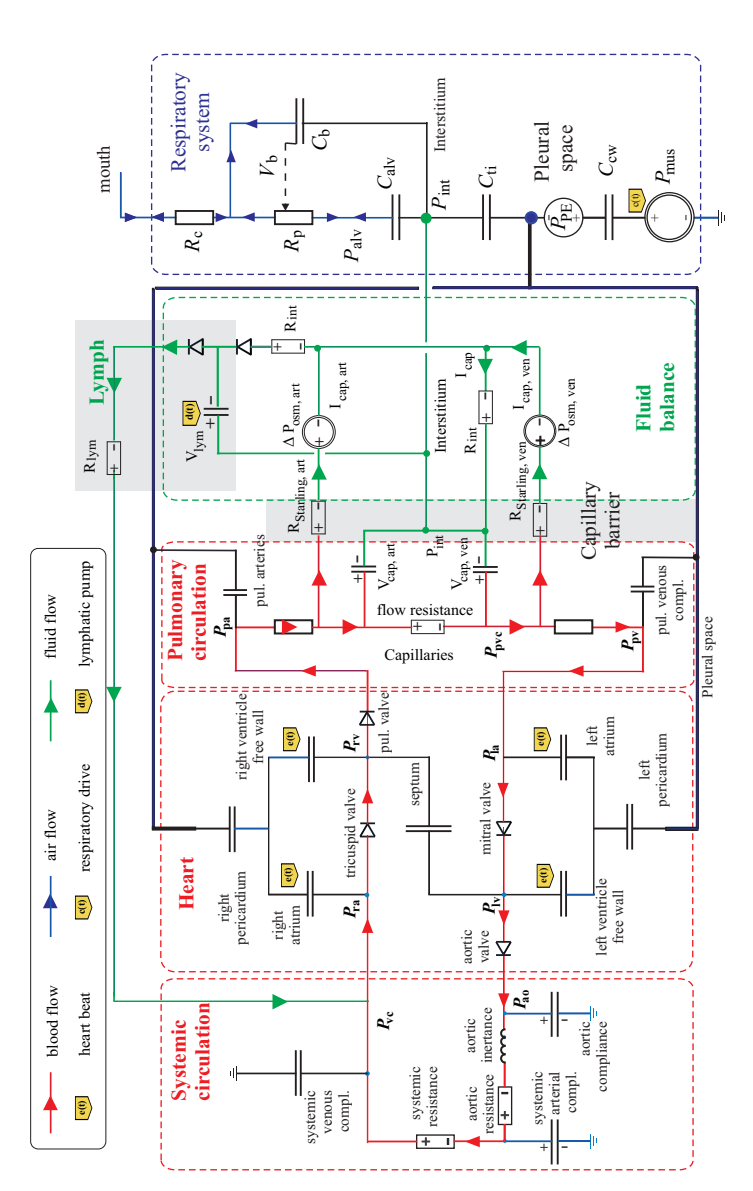


Figure 5.18: The overall model, consisting of the heart, the systemic and pulmonary circulation, the respiratory system, and the fluid balance. Flows are distinguished between blood flow (red arrows), air flow (blue arrows) and fluid flow (green arrows).

amount accumulated in the lung interstitium:

$$\Delta P_{\rm tr,ti} = \frac{1}{C_{\rm ti}} \cdot V_{\rm lung} + P_{\rm safe} \cdot (1 - e^{-20 \cdot V_{\rm liq}}), \tag{5.14}$$

where $V_{\rm liq}$ presents the extra-fluid amount inside the lung interstitium. $P_{\rm safe}$ is the maximum pressure gradient caused by the change in tissue elasticity. $P_{\rm tr,ti}$ presents the transmural pressure of the lung interstitium and equals the difference between the pleural and interstitial pressure $(P_{\rm tr,ti} = P_{\rm pl} - P_{\rm int})$. $P_{\rm safe}$ is determined to be 9.5 cmH₂O due to the maximum rise in interstitial pressure $\triangle P_{\rm int} = 6.8$ cmH₂O. Fig. 5.19 illustrates the influence of $V_{\rm liq}$ on the PV characteristics of the tissue component.

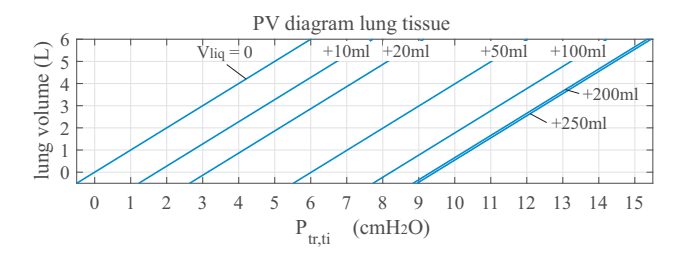


Figure 5.19: The shift of the PV characteristics of the tissue component regarding the interstitial liquid amount $V_{\rm liq}$ during the development of pulmonary congestion.

The osmotic pressure during congestion

The critical venous pressure at which fluid starts to accumulate in interstitium is defined as the safety factor in pulmonary edema [68]. A rise in the pulmonary venous pressure by 13.6 cmH₂O (10 mmHg) is critical before an alveolar edema occurs [68, 202]. Note that the safety factor of 13.6 cmH₂O is without a consideration of the osmotic pressure, which can be up to 50% of the total safety factor (20 mmHg) [68, 109]. Indeed, as the fluid amount accumulated in the lung interstitium rises, the protein concentration and the interstitial osmotic pressure $P_{\rm osm,int}$ decrease, which leads to a reduction of the fluid filtration regarding the Starling equation. To compensate the safety factor difference, a reduction of the osmotic gradient $\triangle P_{\rm osm,int} = 13.6$ cmH₂O/ $\sigma \approx 18.1$ cmH₂O is considered. This corresponds to a reduction of almost 100% of the osmotic pressure ($P_{\rm osm,int} = 19$ cmH₂O).

In this work, a polynomial function of second order was used to model the dependency of the osmotic pressure on the filtration rate [202]:

$$P_{\text{osm,int}} = P_{\text{osm,int,0}} \cdot \left(1 - \sqrt{\frac{V_{\text{liq}}}{V_{\text{liq,max}}}}\right). \tag{5.15}$$

 $P_{\rm osm,int,0} = 19~\rm cmH_2O~presents~the~constant~osmotic~pressure~without~extra~fluid~filtration,~V_{\rm liq,max}~is~the~critical~fluid~amount~(V_{\rm liq,max} = 250~\rm mL).$

The alveolar and bronchial flooding

In later stages of pulmonary congestion, the distal bronchi and alveoli are filled with fluid and collapse due to a reduction of surface tension [21,109]. The pressure-volume characteristics of edematous bronchi and alveoli are characterized by an increase in the threshold opening pressure (TOP) and a reduction of the compliance due to decreased surfactant concentration [21,32,32,228]. Animal trials predict a change of TOP up to 20 cmH₂O [111]. In the model, the change in the pressure-volume relationship of the alveoli and bronchi during pulmonary edema is considered to be dependent on the fluid amount accumulated in interstitial space $V_{\rm liq}$. If $V_{\rm liq}$ exceeds 250 mL, an edema occurs in the alveoli and peripheral bronchi (see Fig. 5.20). The alveolar TOP increases by $\Delta P_{\rm TOP} = 10~{\rm cmH_2O}$ and the maximum alveoli compliance $C_{\rm alv,max}$ decreases by half of its value, from 0.3 to 0.15 LcmH₂O⁻¹. The parameter λ of the peripheral bronchi (eq. (3.11)) increases from 18.38 to 36.76 L⁻¹.

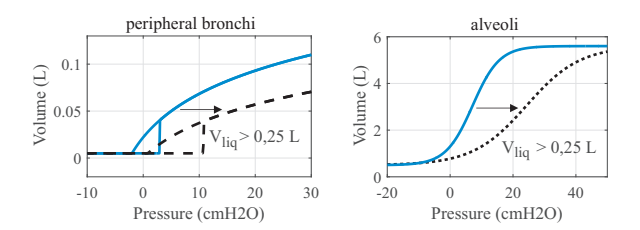


Figure 5.20: Alteration in the PV characteristics of the peripheral bronchi and the alveoli during edema. If the interstitial fluid amount exceeds a critical value $V_{\rm liq} > 250$ mL, their PV curves shift to the right, TOP increases and compliances fall

When a bronchial airway collapses, the fluid film surrounding the inner wall of the bronchi causes the bronchi to stick together. To reverse this process, i.e. to open the bronchi, a higher pressure is necessary to overcome the surface tension of the new fluid layer [28,170]. Chen et al. [28] estimated the opening pressure $P_{\rm open}$ at 5 cm H_2O at different levels of $P_{\rm pl}$. In our model, the closing and re-opening of the bronchi has been implemented by connecting the compliance $C_{\rm b}$ in series with two diodes $D_{\rm in}$ and $D_{\rm out}$ (an electrical form of hydraulic valve). A positive flow through $D_{\rm in}$ increases the bronchial volume $V_{\rm b}$ and vice versa. If $V_{\rm b}$ drops below a threshold value, the opening pressure (breakdown voltage of an electrical diode) of $D_{\rm in}$ increases (Fig. 5.20, dashed line).

5.4 Simulation results

5.4.1 Fluid filtration through the capillary walls

Healthy subjects Figure 5.21 shows the simulation results of the fluid filtration for a healthy subject. While the osmotic pressure is constant at $\Delta P_{osm} = 14.28$ cmH₂O, the transmural hydrostatic pressure is larger than ΔP_{osm} at the arterial end $(P_{\text{cap,art}} - P_{\text{int}})$ ΔP_{osm}). This positive pressure gradient results in a positive fluid filtration from the capillaries into the interstitium $I_{\text{cap,art}} \approx 2.2 * 10^{-6}$ L/s. At the venous end, the process is inverse; the transmural hydrostatic pressure is below the osmotic gradient, which results in a negative flux $I_{\text{cap,ven}} \approx -10^{-6}$ L/s. About half of the fluid filtration from the arterial capillaries is reabsorbed by the venous part, which results in

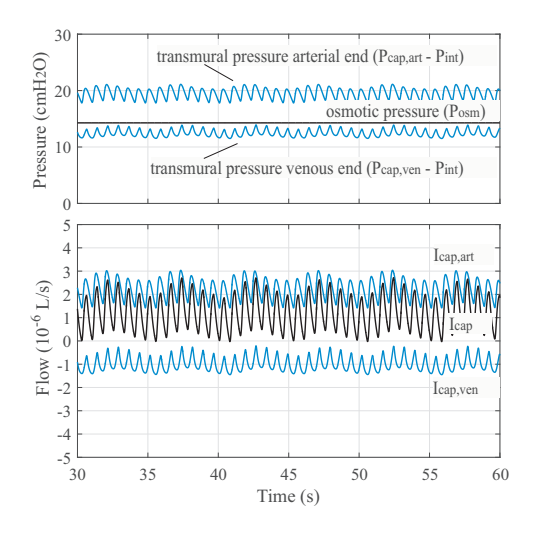


Figure 5.21: Filtration and absorption of fluid from capillaries to interstitium. Fluid is filtrated at artery capillary end and absorbed at venous capillary end. The net flux is approx. $1.2*10^{-6}$ L/s.

a net flux of $I_{\rm cap} \approx 1.2 * 10^{-6}$ L/s. Although the model's re-absorption rate of approx. 50% is below the 90% rate reported in literature [68,184], the net flux

of $1.2*10^{-6}$ L/s conforms the works of Miserocchi [135] and Wangensteen [217]. These authors reported a daily fluid amount of 103.7 mL fluid filtration from the pulmonary capillaries to the interstitial space.

Heart failure Cardiogenic failure leads to an elevated pressure in pulmonary circulation and a rise in fluid filtration. The simulation of a left ventricular dysfunction can be performed by reducing the elasticity of the left ventricle $E_{\rm es,lvf}$. Figure 5.22 presents the pressure and volume changes during a simulated sudden heart failure, where $E_{\rm es,lvf}$ falls to 20% of it maximal value.

The transmural pressure at the arterial end rises from approx. 19.5 to $26.7~\rm cm H_2O$, the filtrated flow increases by $3.8*10^{-6}$ to $6.0*10^{-6}$ L/s. At the venous end of the capillaries, the transmural pressure increases to $25.09~\rm cm H_2O$, and therefore to values larger than the average osmotic gradient. For healthy subjects, the absorption process at venous end becomes an additional filtration process due to the ele-

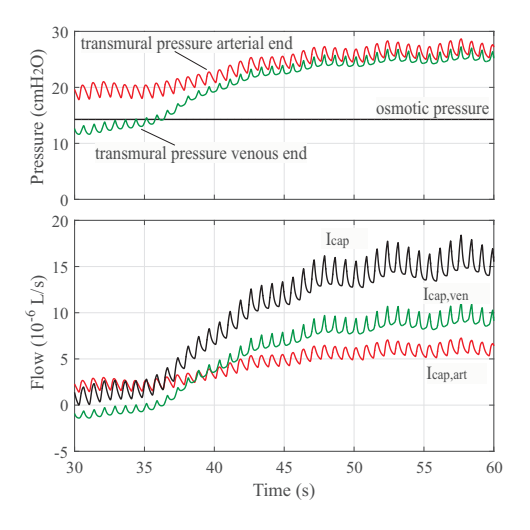


Figure 5.22: Change in capillary pressure and blood flow in heart failure. Blood flow becomes positive at the venous capillary end. There is an additional fluid filtration to the interstitial instead of re-absorption. Regarding the high permeability of the capillaries at the venous end, the venous flux exceeds the flux at the arterial capillary end. The total flux increases from $1.25*10^{-6}$ L/s to $15*10^{-6}$ L/s.

vated hydrostatic pressure. The amount of fluid filtrated at the venous end even exceeds the amount at the artery end, which correlates to the observation of Lenfant et al. [109]. The reason for this high filtration is the high permeability of the capillaries at the venous end [109]. The net flux is $I_{\rm cap} \approx 15*10^{-6}$ L/s, which results in 1296 mL within 24 hours.

5.4.2 Lymphatic absorption

To demonstrate the lymphatic response to the change in pulmonary blood pressure, simulations has been performed for different grades of heart failure. The ventricle's elasticity $E_{\rm es,lvf}$ has been reduced to 35% at $t_1=100$ s and to 20% at $t_1=200$ s, as shown in Fig. 5.23.

As a result of heart failure, the pulmonary venous pressure increases by 7.67 cmH_2O after t_1 and again by $7.26 \text{ cmH}_2\text{O} \text{ after } t_2.$ gradient of the volume curve $V_{\rm cap}$ corresponds to a positive fluid filtration from the capillaries to lung interstitium. The first pressure elevation after t_1 does not cause a fluid accumulation in interstitial space due to an adaption of the lymphatic system by increasing the pump frequency. While the pump is activated only once between t = 50 s and 100 s, its rate rises to approx. 0.18 Hz after t_1 .

After t_2 , the lymphatic pump rate rises to 0.2 Hz and achieves its maximum capac-

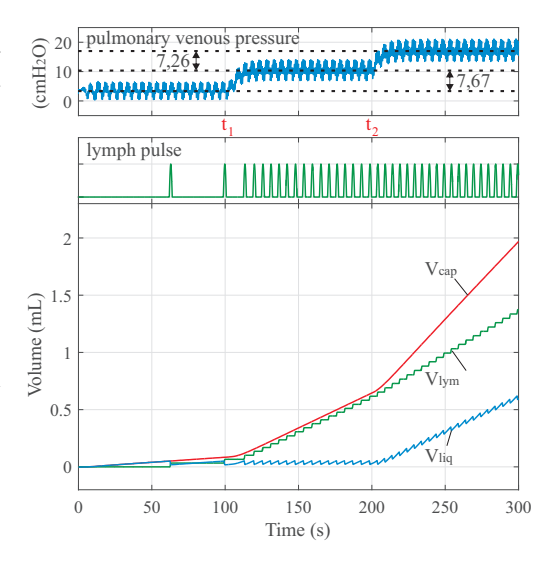


Figure 5.23: Filtration volume at different levels of the pulmonary venous pressure.

ity. However, the pump is not able to remove all the fluid filtration. The simulation yield a safety factor of 7.67 cmH₂O. This safety factor is slightly above literature values (6.8 cmH₂O). After t_2 , a positive change in edematous fluid by 0.4 mLmin⁻¹ is predicted by the model. The simulation results shows that fluid filtration can be removed back to the systemic circulation via the lymphatic system, as long as the safety factor regarding the pulmonary pressure is maintained.

5.4.3 Cardiogenic pulmonary congestion and CPAP treatment

This part demonstrates the model behavior in the development of cardiogenic pulmonary congestion and the effect of CPAP treatment via a long time simulation (for over 90 hours). A heart failure with reduced $E_{\rm es,lvf}$ to 10% of the normal value [83] was modeled at t=12 hours which directly causes an increase in the pulmonary blood pressures, and later, a lung congestion. A CPAP treatment was started at t=60 hours to demonstrate the effect of the therapy in lung congestion. Simulation results are displayed in Fig. 5.24, 5.26, and 5.25.

By reducing the elastance of the left ventricle to 10% of the normal value, the venous pressure rose by 25 cmH₂O and as result, the cardiac stroke volume fell from 5.8 to 2.2 L/min. The intrathoracic blood volume (ITBV) increased by 400 mL to 1.05 L. The extra tissue liquid $V_{\rm liq}$ rose from 0 to 221 mL within 12 hours, but is still below the critical volume of 250 mL (Fig. 5.24). Since hormonal and neural regulation is not considered in the model, cardiac output remained at a low level. The average interstitial pressure $P_{\rm int}$ increased from -6.5 cmH₂O at the beginning of the simulation to -0.5 cmH₂O 12 hours after the heart failure.

In the respiratory system, the pleural pressure $P_{\rm pl}$ fell from $-7.5~{\rm cmH_2O}$ to $-10.5~{\rm cmH_2O}$. The transmural pressure over lung tissue $P_{\rm tr,ti}$ rose from 1 to 10 cmH₂O. Implementing the same respiratory muscles activity for the whole simulation, tidal volume fell from 0.5 L by almost 60% to 0.23 L. The static PV characteristics of the respiratory system moved rightward due to the change in the lung compliance (Fig. 5.26). The total compliance of the system was 25% smaller at point 2 (pulmonary congestion) than in point 1 (healthy). The lung volume at FRC also fell by 1.1 L to 1.5 L.

The reduction of the lung volume during pulmonary congestion depends on two factors. First, the extra interstitial fluid reduces the tissue compliance $C_{\rm ti}$ and make the lungs "stiffer" (Fig. 5.19). Second, a rise in total thoracic blood volume suppresses the lungs and make it harder to expand. Since the chest wall and the lung compliances are approx. the same, a rise by 400 mL in ITBV results in a decrease of 200 mL in lung volume and an increase of 200 mL in chest wall volume (Fig. 5.25). In reality, an adaption of the respiratory muscles is required to maintain a normal lung volume and gas exchange, which increases the work of breathing and makes breathing heavier for patients with congestive diseases.

At t = 60 h, a CPAP therapy with a PEEP of 10 cmH₂O has been started. PEEP had an immediate effect on the respiratory system: lung volume came back to its normal value of 2.5 L at FRC. The tidal volume normalized at 500 mL. The PEEP compensates the transmural pressure $P_{\rm tissue}$, which increased due to the fluid filtration into the interstitium. The pleural pressure also returned back to its normal value and the system moved back to its normal operating point (point 3). $V_{\rm liq}$ fell from 221 mL to 3 mL within 12 hours. ITBV fell by 150 mL, the pulmonary blood pressure decreased by 7 cmH₂O.

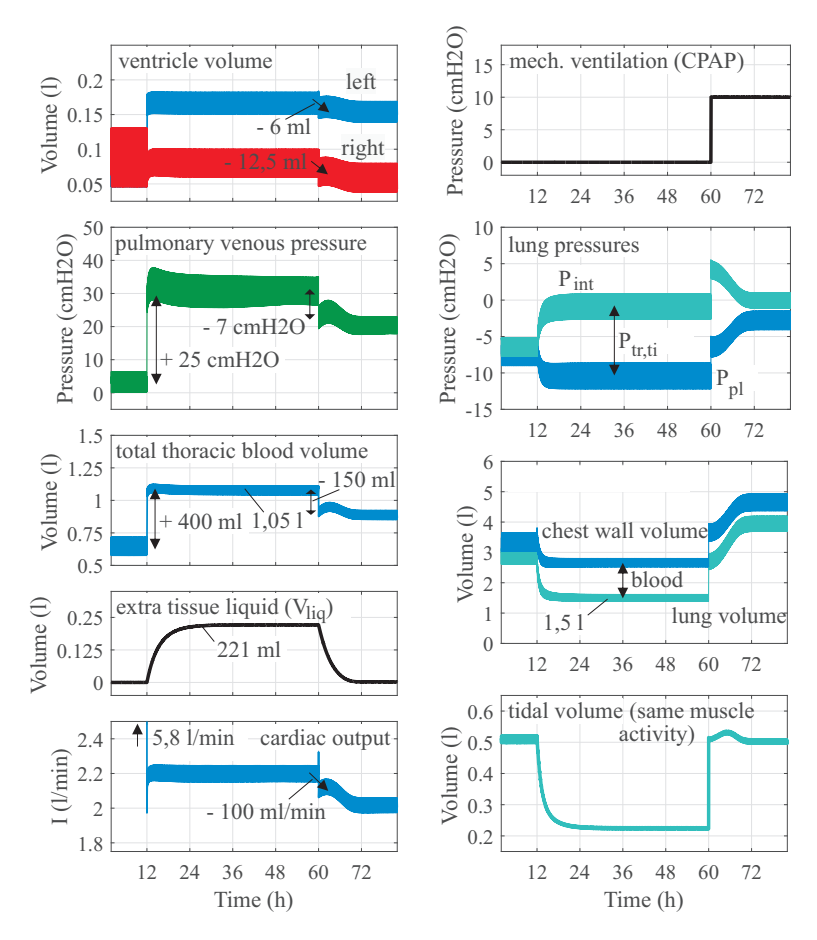


Figure 5.24: Simulation result of lung congestion. At t=12 h, heart failure is stimulated by reducing left ventricle elasticity to $10\,\%$ of the original value. Pulmonary blood volume and pressures increases, while cardiac output falls. After 60 hours (2 days after occurrence of heart failure), a treatment with CPAP therapy (PEEP = $10~\text{cmH}_2\text{O}$) is initiated simulatively.

The simulation predicts that the use of CPAP leads to an immediate normalization of ventilation. The rise in the pleural and interstitial pressures via CPAP "presses" the fluid out of interstitium and reduces ITBV.

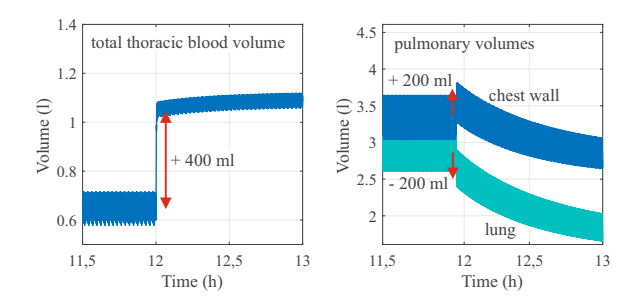


Figure 5.25: Change in ITBV, lung and thorax volume during pulmonary congestion. The change at t=12 h relates to the shift in ITBV. The slower change after t=12 h relates to the change in lung tissue compliance regarding the fluid accumulation in interstitium.

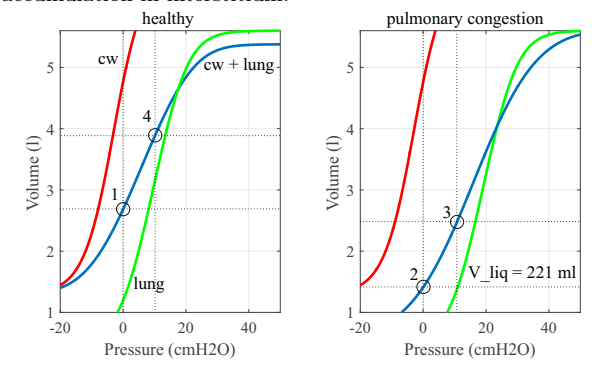


Figure 5.26: Static PV-characteristics of the respiratory system. Four operation points are marked during the simulation. Point 1: healthy, during the first 12 hours. Point 2: At t=36 h, 24 hours under pulmonary congestion. Point 3: short after started CPAP therapy with PEEP= 10 cmH₂O. Point 4: after 12 hours of CPAP therapy.

While the use of CPAP obviously improves the respiration, it has a negative impact on the cardiac output, as expected. While a left heart failure already reduces the preload of the right ventricle, the use of CPAP increases the intra thoracic pressures and the afterload of the right ventricle, which causes a further reduction in the cardiac output. In the simulation, cardiac output fell from 2.2 per minute to 2 liter per min during the use of CPAP 5.24.

5.5 Discussion and summary

This chapter introduces a comprehensive model of the hemodynamic interaction between the lungs and the cardiovascular system. The overall model includes more than 30 elements. Simulation speed was 30 times faster than real time (on a PC with Intel Core i7-4770 CPU). The object-oriented modeling language Simscape has the advantage that bi-directional interactions between subsystems can be implemented via physical connections. Similar to chapter 3, the model introduced non-linear behaviors of the components.

To our knowledge, this model is the first to focus on the non-linear functionality of the lung mechanics with respect to static and dynamic behavior of the compliances. The interconnections between the lungs and heart present the most complex object-oriented approach in the state-of-the-art. Baseline simulations and simulation with different testing scenarios (Mueller maneuver, PCV, VCV) have demonstrated the accuracy of the model response compared to clinical data and animal experiments.

Other novel works introduced in this chapter are the lymphatic model and the fluid balance system. Simulation results have demonstrated the physiological development of cardiogenic pulmonary congestion as the result of a ventricular dysfunction. By simulation, the filtration and re-absorption of the lymphatic fluid from the pulmonary capillaries to lung interstitium have been shown to correlate with the elevation of the pulmonary blood pressure. CPAP treatment has been demonstrated to affect the accumulated fluid and the lung mechanics instantaneously, but may have a negative impact on the cardiac output.

The model has a high potential for application. First, it should be use as a demonstrator for educational and training purposes. It can help physicians and biomedical engineers to understand the complex physiology of the lung mechanics and cardiopulmonary interactions. Second, the model can be used for further investigation on other cardiopulmonary diseases, such as pneumothorax, cardiac tamponade, nightly fluid shift and peripheral edema, fluid responsiveness, or ventilator-induced lung injuries. It should also be expanded to capture the physiology of atelectasis, in order to model lung mechanics and cardiopulmonary interactions during ARDS.

6 Assessment of global and regional ventilation using Electrical Impedance Tomography (EIT)

Boredom is only for people who do not know themselves or the wonders of life. Tom Brown Jr.

The existing pulmonary function tests spirometry, oscillometry, body plethysmography, and breath washout technique are restricted to functional and global information [199,212]. Yet, regional information is beneficial to assess heterogeneous changes in lung and to improve treatment in pathologies. Currently, the chest x-ray is used to detect regional morphologic alterations with limited validity, while a low-dose high resolution computed tomography is the gold standard for evaluation of parenchymatous changes [45]. These techniques, however, expose patients to harmful ionizing radiation that increases the risk of radiation-related diseases, particularly by repeated examinations for longitudinal monitoring. Magnetic resonance imaging (MRI) of the lung has become a relevant diagnostic procedure, but the spatial resolution is still limited for evaluation of early pulmonary diseases. The hyperpolarized He-magnetic resonance imaging, a combination of morphological and functional MRI, is limited to selected centers without providing routine diagnostics [171].

Since electrical impedance tomography (EIT) can provide regional information of lung ventilation, it has a promising applicability in regional pulmonary function. The linearity between the EIT-derived global impedance index and lung volume allows the determination of gas flow in different parts of the lungs, for instant, the left and right lung, or the four quadrants left dorsal, right dorsal, left ventral, right ventral of the lungs. Figure 6.1 illustrates the separation of gas distribution between the left and right lung by means of EIT. This

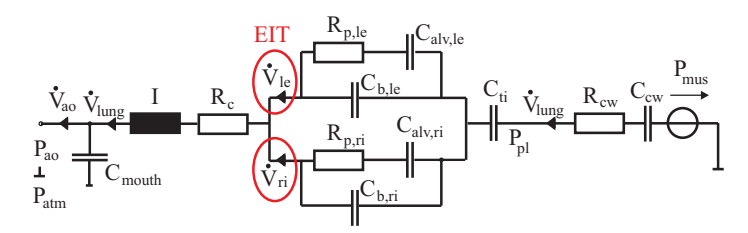


Figure 6.1: A respiratory model with extended structure of left and right lungs. Electrical impedance tomography provides regional ventilation $\dot{V}_{\rm le}$ and $\dot{V}_{\rm ri}$ of the left and right lung.

chapter demonstrates the use of EIT in lung function testing based on measurement results obtained in different human studies. The first section focuses on EIT measurements during the Tiffeneau-test demonstrating its discriminative power for healthy and asthmatic patients. The second section introduces a novel measurement modality by combining EIT and the Forced Oscillation Technique (FOT).

6.1 Diagnosis of pulmonary function with EIT during forced expiratory maneuvers

Simultaneous EIT measurements during forced expiratory maneuvers (Tiffeneautest) have been investigated by different research groups [107,108,165,212,213,229]. These authors aimed to assess pulmonary function by analyzing the global impedance index measured with EIT. However, an important requirement for the use of EIT during forced expiratory maneuvers, the linearity between EIT impedance changes and gas volume at maximum lung volume level, has not been reported before. This section investigates the linearity between EIT and spirometric data during forced expiratory maneuvers in healthy adults and pediatric patients with obstructive diseases.

6.1.1 Study design

Study on healthy adults Seven lung-healthy volunteer adults (1 female, 6 male, aged from 21 to 55 years) were asked to follow three breathing sequences illustrated in Figure 6.2. Each sequence included an apnea phase with 10 s breath holding, a synchronizing phase with five normal breaths and a test phase. There were three different types of test:

- Test 1: Slow breathing with increasing effort. Beginning with a small tidal volume, subjects were animated to achieve maximum and minimum lung volume after 4 to 6 breath cycles by increasing the tidal volume after each breath. The respiratory rate should remain low.
- Test 2: Slow breathing with maximum effort. Subjects conducted five normal breaths, followed by ten breaths at maximum lung level.
- Test 3 (Tiffeneau-test): Forced expiration maneuver according to ATS/ERS guidelines [133]. Subjects performed forced expiration from total lung capacity to the residual volume under vigorous exhalation.

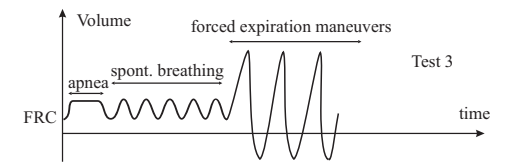


Figure 6.2: Sequence of test 3 (forced expiration maneuver): apnea, tidal respiration, and three forced breathing maneuvers according to ATS / ERS recommendation to perform spirometry, modified from [147].

Study on pediatric asthmatics and controls The data analyzed in this work was recorded by Dr. med. Sylvia Lehmann in the clinical study no. CIV-14-03-011942 (no. of Ethics Committee approval EK088) at the University Hospital Aachen between June 2014 and January 2015. The study was designed as a prospective observational study, in which healthy children and those with obstructive lung diseases were examined during lung function testing, including positive bronchospasmolysis (BSL) in accordance with the ATS/ERS guidelines [19,133]. This work focuses on data obtained from n=58 asthmatic and 58 age-matched lung healthy children. The n=58 asthmatic patients were 11.86 ± 3.13 years old in average, with a mean BMI of 20.89 ± 4.73 , which are close to those of the healthy controls (age 12.12 ± 2.90 years old, BMI 19.04 ± 4.35).

Data acquisition and data processing Respiratory flow $\dot{V}(t)$ was captured by a MasterScreen Body (Care Fusion Inc., Hoechberg, Germany) with a flow sensor of Fleisch type. In the volunteer study on adults, raw data of flow and volume were exported for further signal processing. In the clinical study on the children, lung function parameters were provided by the MasterLab device with automatic selection of the best forced expiration maneuver from three displaying loops. Parameters are: forced vital capacity (FVC), forced expiratory volume in 1 second (FEV₁), forced expiratory volume in 0.5 second (FEV_{0.5}), and maximum expiratory flow at 25, 50, and 75 % of FVC (MEF₇₅, MEF₅₀, and MEF₂₅), respectively.

EIT data were acquired with a PulmoVista 500 (Dräger Medical GmbH, Lübeck, Germany) with the attached electrode belts. To generate an EIT frame, the device applied an alternating current (IEC 60601-1-2, $80-130\,\mathrm{kHz}$, automatic adjusted current amplitude) to the body. 16 consecutive current injections at 13 adjacent electrode pairs resulted in 208 voltages during each cycle, reduced to 104 linearly independent values due to reciprocity. The device can generate a frame rate of 50 frames per second. Data were converted to

MATLAB file format for later analysis. An integrated finite-element-method-based, linearized Newton-Raphson reconstruction algorithm for ellipsoid EIT images was used to reconstruct 32×32 -pixel-images at every measured time instance. Each pixel $\Delta z(k,t)$ represents the relative impedance change compared to a reference (baseline). Let t be the time instance and k the position $(1 \le k \le 1024)$, the global impedance index $\Delta Z_{\rm EIT}(t)$ is defined as the sum of the pixels $\Delta Z_{\rm EIT}(t) = \sum_{k=1}^{1024} \Delta z(k,t)$. Tomograms were divided into four 16x16-pixel quadrants [107]. Further data analysis required a selection of one forced breathing cycle and the computation of the maximum impedance change during forced expiration FVC_{EIT} [AU], as well as the impedance changes in the first 1s and 0.5s, FEV_{1,EIT}, and FEV_{0.1,EIT}. To generate the conventional form of a classic flow volume (FV) loop, $d\Delta Z_{\rm EIT}(t)/dt$ was plotted over $\Delta Z_{\rm EIT}(t)$ after being mirrored and shifted to the origin.

Scaling EIT-data At lower lung volume changes, a strong correlation of EIT data and lung volume in dogs was documented already back in 1997 by Adler et al. [2], which was confirmed by e.g. Marquis et al. in humans for diverse anthropometric parameters and body positions [122]. This relation can be written as:

$$V_{\text{spiro}}(t) = a * \Delta Z_{\text{global}}(t) + b, \tag{6.1}$$

where a represents the scaling factor from EIT arbitrary unit [AU] to liter [L] and b is an offset. These coefficients were calculated differently in the two data set regarding disposability of the data. Since raw data of flow and volume were available in the volunteer study, a and b were calculated by the least squares (LS) method minimizing the error

$$E(a,b) = \sum_{n=1}^{N} (V_{ao}(t) - a\Delta Z_{EIT}(t) - b)^{2},$$
(6.2)

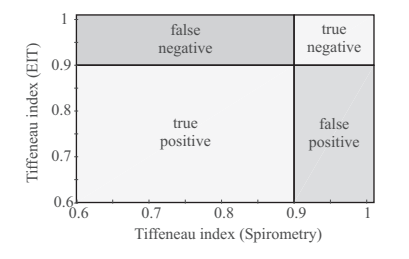
where N is the number of data points belonging to the first five spontaneous breathing cycles (synchronous phase). In the pediatric study, a was calculated regarding FVC_{spiro} [L] and FVC_{EIT} [AU]:

$$a = FVC_{spiro}/FVC_{EIT}$$
 (6.3)

With respect to a, EIT-derived lung function parameters were scaled from [AU] and [AU/s] to [L] and [L/s]. Note that a and b differ among the measurements and do not yield any physiological relevance.

Statistical analysis Statistics was performed in Matlab 2015b to demonstrate the correlation between both measurement modalities. For the volunteer study, the algorithm searches maximal and minimal peaks of the scaled EIT signals, calculates the EIT-derived tidal volume and correlates them with spirometric data. Pearson's test with Bland-Altman and box-whiskey-plot were applied on the data. A p-value < 0.05 was considered statistically significant.

For the pediatric children, a spirometry test result was considered positive in terms of asthma if the Tiffeneau-index (TI) FEV₁/FVC was reduced (TI < 90% for children < 12 years old and TI < 80% for children \leq 12 years old), and the bronchodilator test was positive ($\Delta {\rm FEV_1} > 12\%$). A binary classification test was performed for the TI and the bronchodilator results considering the spirometry as gold standard, as shown in Fig. 6.3.



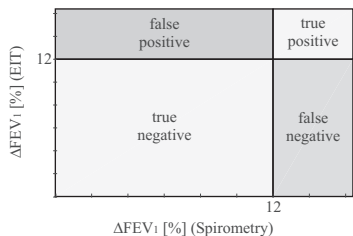


Figure 6.3: Binary classification test for the Tiffeneau index and the bronchodilator result measured by EIT on asthmatic and control children compared with the standard spirometry. Inclusion criteria: TI < 90% for children under 12 years old and < 80% for children between 12 and 18 years old; positive bronchodilator test ($\Delta FEV_1 > 12\%$) [143].

6.1.2 Linearity between EIT and spirometry in healthy adults

For illustration, selected volume and flow data are illustrated in Fig. 6.4(a) (test 1 and 2 from subject 1) and Fig. 6.4(c) (test 3 from subjects 2 and 3), where spiromtric data is presented in blue lines and EIT data in red dash-lines. Though the parameter a and b were calculated on data of the first five spontaneous breathing, $V_{ao}(t)$ and $V_{EIT}(t)$ correlate accurately for lung volumes during breathing with increasing and maximum effort, as well as during forced expiration maneuvers. At the beginning of the forced expiration, where the lungs are at maximum inspiratory levels, a small deviation in volume can be observed.

Figure 6.4 (b and d) show the correlation and Bland-Altman plots for spirometric and EIT data of test 1 and 2 (b) and test 3 (d) from seven lung healthy

adults. The results yield high correlations (r=0.993, p<0.001) and a low Bland-Altman mean bias (0.243) between EIT and spirometry during test 1 and 2. In test 3, also a high correlation (r=0.998, p<0.001) can be observed; however, the mean bias (0.323) is slightly higher than in test 1 and 2. Figure 6.5 presents the correlation and Bland-Altman plots for the lung function parameter FEV₁ (a), Tiffeneau-index FEV₁/FVC (b), and flow parameter PEF, MEF₂₅, MEF₂₀ and MEF₇₅ (c). Again, high correlations can be observed in all parameters: r=0.81, p<0.001, MEAN -0.074 for FEV₁; r=0.8491, p<0.001, MEAN -0.07216 for FEV₁/FVC, and r=0.965, p<0.001 for flow parameters.

In some of our measurements, an inaccuracy of the peak flow during the forced expiration maneuvers was observed. Two exemplary FV loops from subjects 3 and 4 with calculated parameters are depicted in Fig. 6.5 (d). While the EIT and spirometric FV loop from subject 4 shows a high fit, there is a drift in the FV loops from subject 3. This indicates a good, but imperfect linearity, especially at the beginning of the forced expiration. This moderately lower linearity adjusts towards the end of expiration.

6.1.3 Linearity between EIT and spirometry in pediatric patients with asthma

Correlation in lung function parameters Figure 6.6 displays box-whiskey box plots and correlation values EIT and spirometry in pediatric patients with asthma. The mean spirometric value of FVC was 2.48 ± 0.93 L in the controls and 2.37 ± 0.92 L $(2.42 \pm 0.93$ L) in the asthmatics before (after) BSL. A strong correlation was found in FEV₁ and FEV_{0.5} (all p-values < 0.05, all r-values > 0.9). MEF₇₅, MEF₅₅, and MEF₂₅ values also correlated well with p-values < 0.05 and r-values ranging from 0.673 to 0.805). Similar to data of heathy adults, small deviations were found at the higher flows (MEF₇₅). Mean MEF_{75} were 4.62 ± 1.61 L/s in spirometry for the controls, slightly above in EIT $(6.16 \pm 2.77 \text{ L/s})$, with an r-value of 0.673. At lower flows, a better correlation between EIT and spirometry was documented (r = 0.792 for MEF₅₀ and r= 0.805 for MEF₂₅). Similar correlations were found in data of the asthmatic, as demonstrated in the Bland-Altman analysis shown in Fig. 6.7. Table A.5 depicts the mean values and standard deviation (SD) of lung function parameters measured by spirometry and EIT on 58 asthmatics before and after BSL, as well as 58 age-matched healthy controls.

We speculate that the reason for the nonlinearity at the beginning of the forced expiration could be attributable to two aspects. First, the PulmoVista 500 was originally designed for monitoring of patients undergoing mechanical ventilation in an intensive care unit. The normal tidal volume is significantly

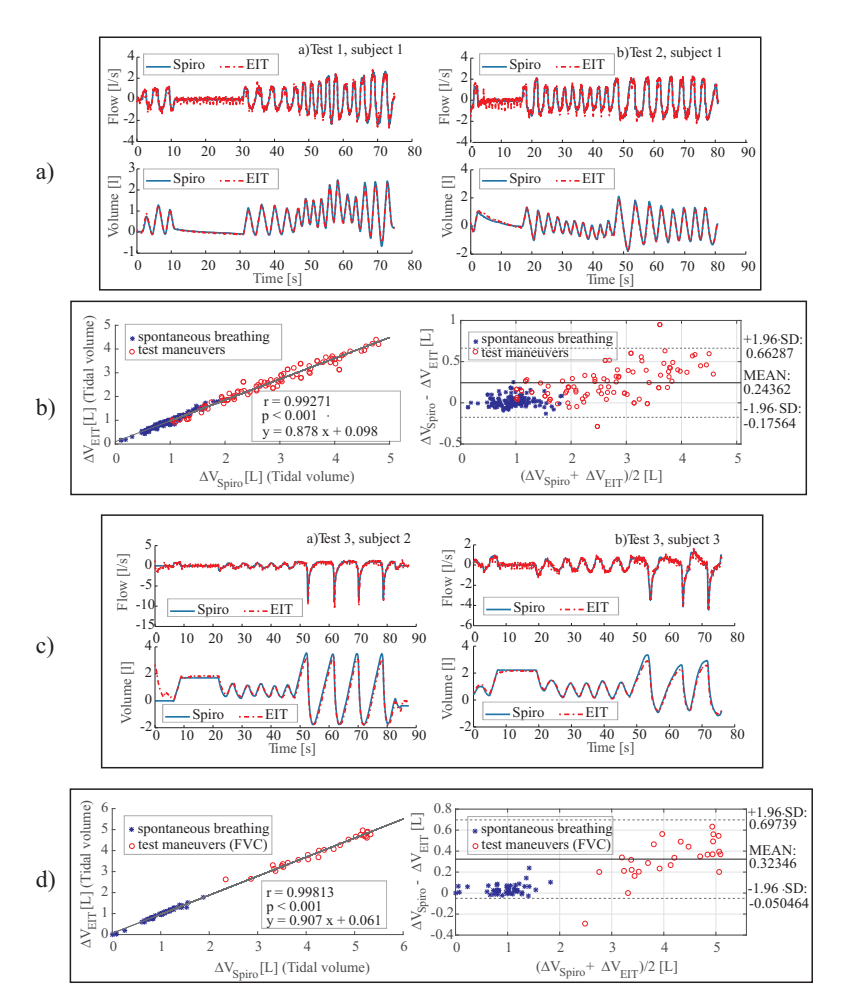


Figure 6.4: Correlation between spirometric and scaled EIT data measured on healthy adults. a) Breathing with increasing (test 1) and maximum effort (test 2) from subject 1. b) Correlation and Bland-Altman plots for different tidal volume from seven lung healthy adults. c) Forced expiration maneuvers (test 3) from subjects 2 and 3. d) Correlation and Bland-Altman plots for forced vital capacity (test 3). Modified from [147].

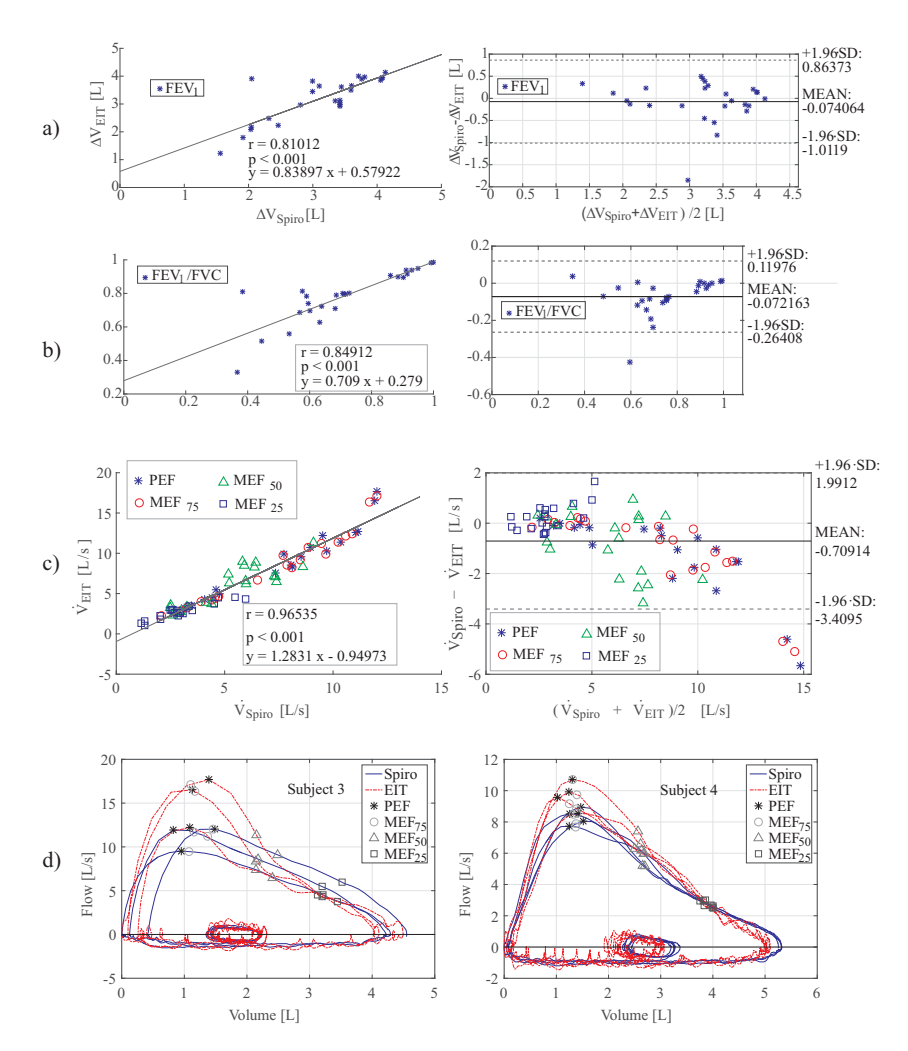


Figure 6.5: Bland-Altman analysis of FEV_1 (a), Tiffeneau-index FEV_1/FVC (b), and flow parameter (c) for spirometry and scaled EIT data. (d): Flow-volume loops and the spirometric parameters, measured from healthy adults 3 and 4. Modified from [147]

smaller and the process is slower than during a forced expiration maneuver. Since the reconstruction matrix used in the present study is based on a linear approach developed for normal tidal volumes, a more precise reconstruction algorithm might increase the accuracy of the EIT signals. Other nonlinear aspects such as the change in thorax circumference, the position of the electrodes, and the position of the tissue and respiratory muscles may be considered in this approach. Second, during a forced expiration maneuver, the respiratory muscles contract maximal, the intra-thoracic pressure increases rapidly. As a result, the venous return is reduced and the cardiac output is increased instantaneously. The reduction in the intra-thoracic blood volume causes a further disturbance in the measured EIT signals. More experiment should be set up to clarify these hypotheses.

The use of Tiffeneau-index and positive BSL in discriminating asthma In asthmatic patients, all lung function parameters increased after BSL. FVC increased from 2.37 ± 0.92 to 2.42 ± 0.93 , and FEV₁ from 2.16 ± 0.83 (2.24 ± 0.85 by EIT) to 2.29 ± 0.86 (2.36 ± 0.89 by EIT). This resulted in a positive bronchodilator index Δ FEV₁[%] = 7.44 ± 12.94 (4.79 ± 12.93 by EIT). Positive effects of BSL on the asthmatic patients were also documented in MEF₇₅, MEF₅₀, and MEF₂₅.

The results of the binary classification tests on the Tiffeneau-index and the bronchodilator index are presented in Fig. 6.8, considering spirometry as the gold standard. For the Tiffeneau-index, the data were split into two groups, i. e. children over and below 12 years of age regarding the different criteria for pathological asthma [1]. The binary classification test yields high sensitivity in ΔFEV_1 (86.67%) and low sensitivity in TI (25% and 35.29%). High specificities (> 93%), high positive predictive value ($\leq 75\%$) and high negative predictive value (> 80%) can be observed in all three criteria. No significant differences between the two groups of age is documented.

Since the FV loops of the asthmatics exhibit typical concave forms [133], a graphical comparison of these loops in the asthmatics and controls is clinically useful. However, since a large number of our pediatric patients were under medical treatment and hence, exhibited normal pulmonary function values, a graphical comparison of n=58 would not demonstrate the discriminative power of EIT between healthy and asthmatic FV loops. A better comparison will be between n=10 patients (3 under 12 years old and 7 over 12 years old) who had confirmed pathological asthma (reduced TI index and positive bronchodilator test) with selected age-matched controls. Figure 6.9 illustrates the mean FV loops of these 10 patients (divided into two groups of different ages) and the controls in the same diagrams.

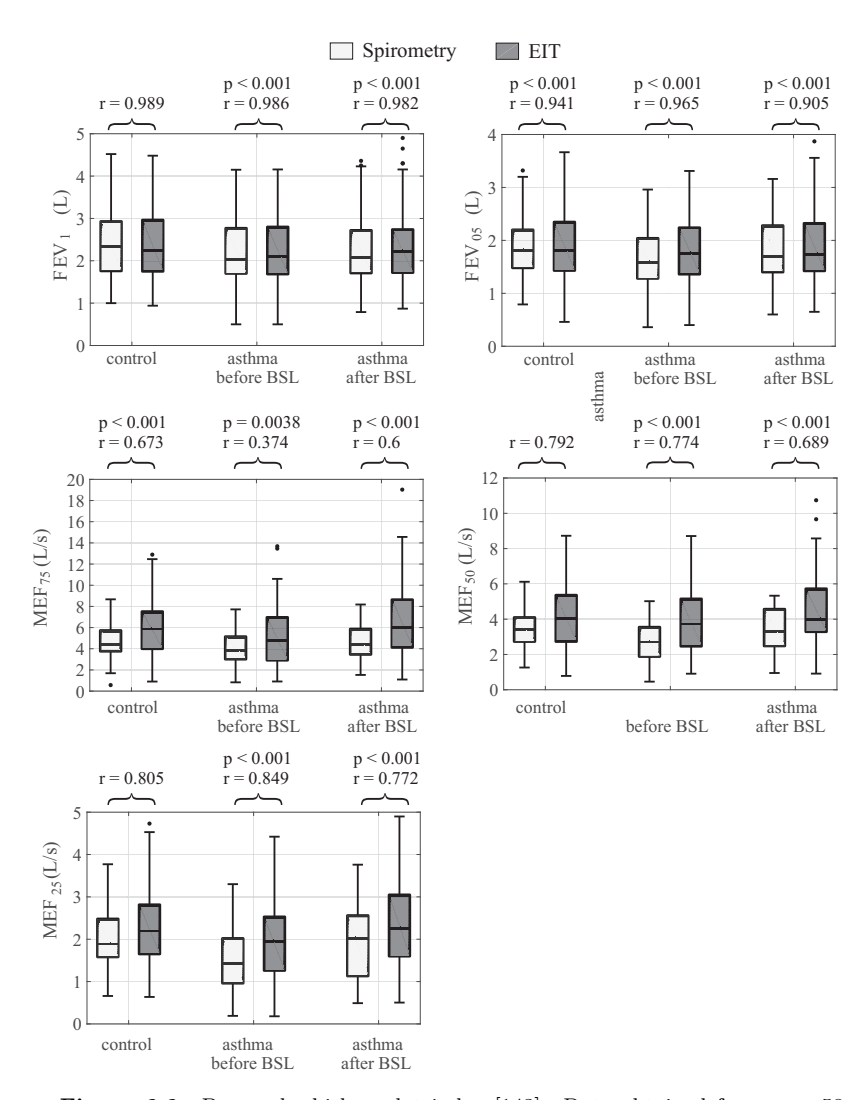


Figure 6.6: Box and whiskey plot index [143]. Data obtained from n=58 controls and n=58 asthmatics before and after BSL.

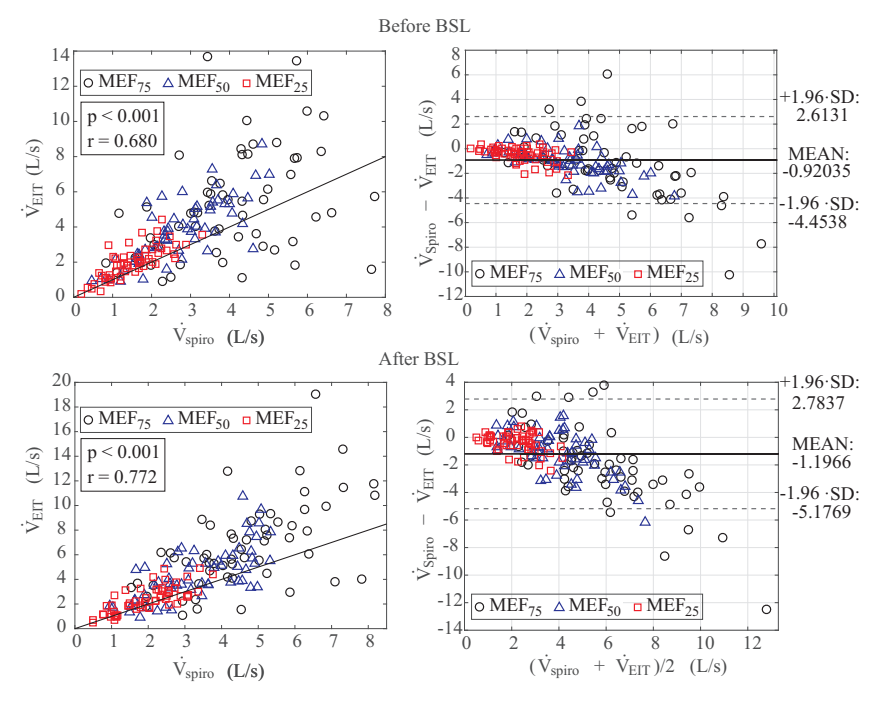


Figure 6.7: Bland-Altman plot. Data obtained from n=58 controls and n=58 asthmatics before and after BSL.

6.1.4 Regional EIT-derived flow volume (FV) loop

An EIT scan displays a 32x32-pixel image at one time instance. To investigate regional characteristics, each tomogram was divided into four quadrants, i.e. right dorsal (RiDo), right ventral (RiVe), left dorsal (LeDo), and left ventral (LeVe) with 16x16 pixels each. By summing up the temporal impedance change of the pixel for each quadrant, regional impedance indexes can be calculated, e. g. $\Delta Z_{\rm RiDo} = \sum_{i \in {\rm RiDo}\Delta Z_i(t)}$ [107]. Figure 6.10 illustrate global and regional FV loops of three representative asthmatic patient (I-III). The deviation between the spirometric and EIT-derived global FV loops at maximal flow can be observed. The regional FV loops confirm positive BSL. The effect of BSL is inhomogeneous among the lung quadrants: Larger positive bronchodilator occurs in left dorsal and right ventral lung quadrants.

It should be noted that there is no existing reference for the regional lung

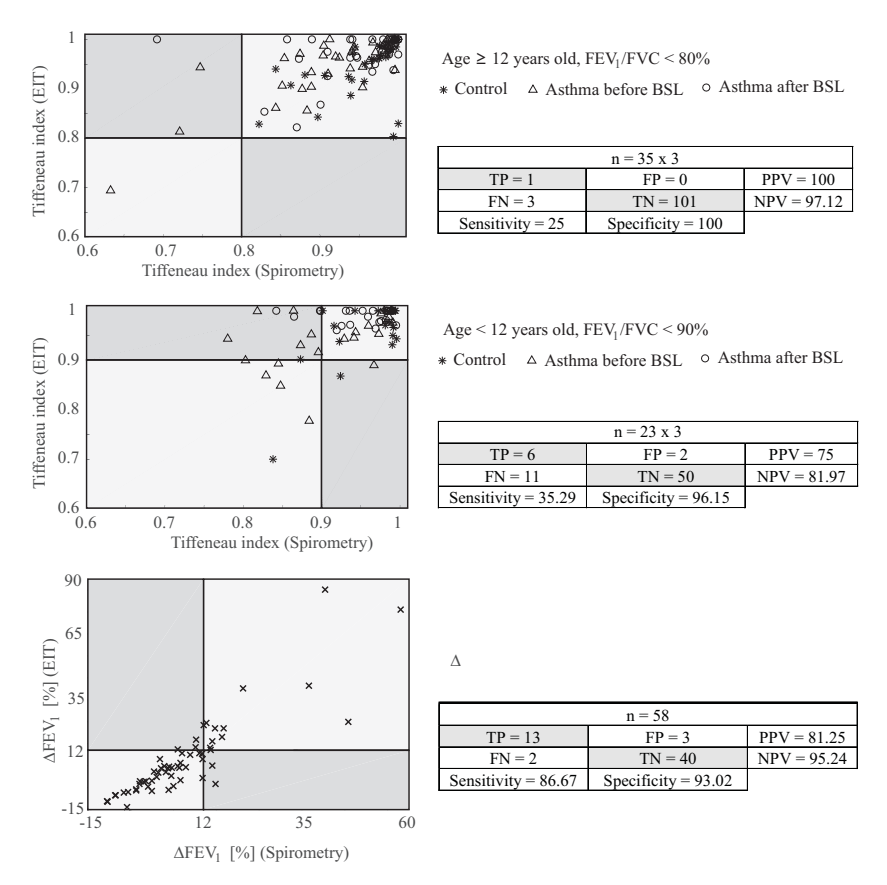


Figure 6.8: Binary classification test for TI and bronchodilator index [143]. Top: FEV₁/FVC < 80% for n = 35 x 3 children \leq 12 years old (control, asthma before and after BSL). Center: FEV₁/FVC < 90% for n = 23 x 3 children < 12 years old (control, asthma before and after BSL). Bottom: Δ FEV₁[%] > 12 for n = 58 asthmatic children. TP = true positive, FP = false positive, TN = true negative, FN = false negative, PPV = positive predictive value, NPV = negative predictive value.

function for this group of children. Non-invasive radiological technique, e. g. hyper-polarized He-magnetic resonance imaging, was not performed due to non-availability and ethical reasons. Thus, quantitative evaluation and interpretation of the results depicted in Fig.6.10 is difficult. However, our re-

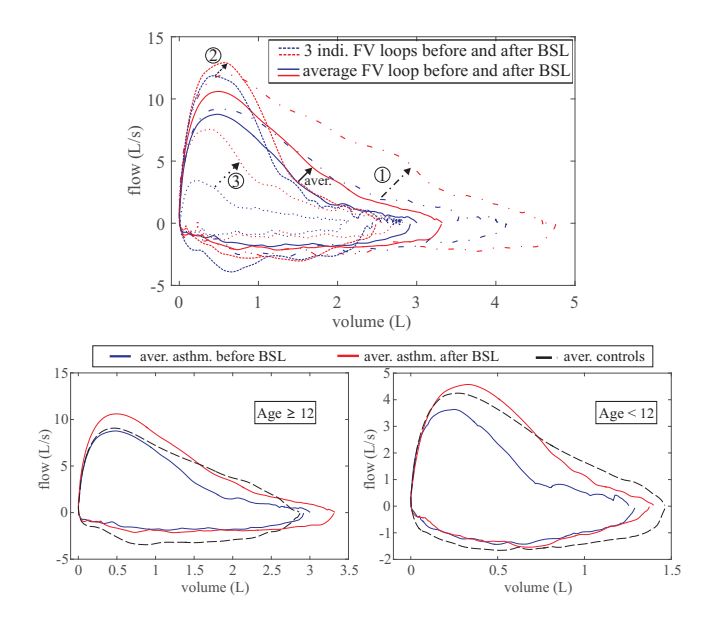


Figure 6.9: Top: three individual FV loops before and after BSL. An increase in FVC after BSL can be observed in all individual FV loops. Bottom: average FV loops lung healthy controls (black, dotted), asthmatics before (blue, drawn) and after (red, drawn) BSL [143]. Selection criteria for asthmatics: left: n = 3 \leq 12 years of age, TI < 0.8, $\Delta {\rm FEV}_1 >$ 12% , right: n = 7 < 12 years of age, TI < 0.9, $\Delta {\rm FEV}_1 >$ 12%.

sults demonstrate the usability of EIT to monitor not just regional ventilation changes in diagnostic procedure, but also to determine efficacy of local drug effects for therapy.

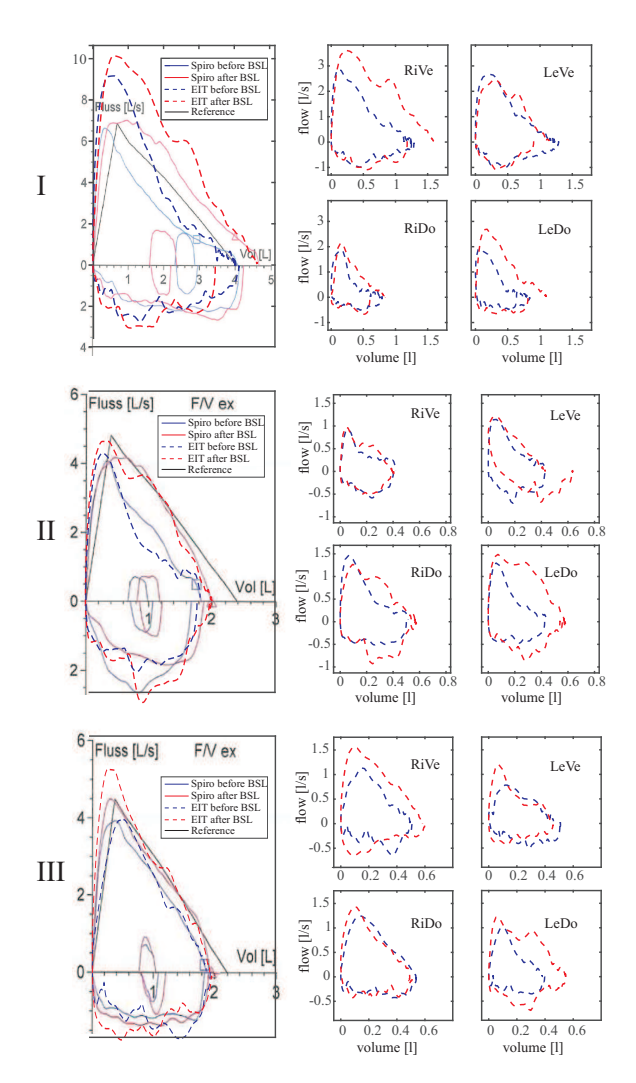


Figure 6.10: Spirometric and EIT-derived FV loop of one representative asthmatic patient. Left: global FV loops, right: regional FV loops obtained from EIT images for right ventral (RiVe), left ventral (LeVe), right dorsal (RiDo), and left dorsal (LeDo) quadrant of the lung. [143].

6.2 Introduction of oscillatory Electrical Impedance Tomography (oEIT)

The use of EIT in the Tiffeneau-Test for regional lung functions is not suited for infants, young children, and patients with serve lung damages, since the forced expiration maneuvers requires strong patients' cooperation. In this section, we investigate a new measurement modality to assess regional lung mechanics by combining EIT and FOT. The new technique is named oscillatory electrical impedance tomography (oEIT).

The measurement system of oEIT, illustrated in Fig. 6.11, consists of an FOT device, a flow and pressure sensor system, and an EIT device. The FOT measurements were performed as described in Chapter 4. Simultaneously, EIT frames were generated with the PulmoVista 500. Measurements were performed on n=5 healthy volunteers (four male, one female, age between 23 and 55). Subjects were asked to perform an apnea for 10s, followed by normal breathing.

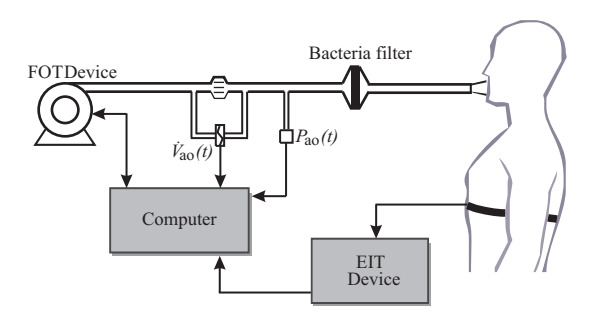


Figure 6.11: The oEIT measurement system [149].

6.2.1 Visibility of FOT frequencies in EIT signal

 $\Delta Z_{\rm eit}(t,5\,{\rm Hz})$ and its derivative $d\Delta Z_{\rm eit(t,5\,Hz)}/dt$ on a exemplary measurement at $f_{\rm os}=5\,{\rm Hz}$ are depicted in Fig. 6.12. In the apnea phase, $\Delta Z_{\rm eit}(t,5\,{\rm Hz})$ remains unchanged except of small cyclic perturbations at heart rate. The 5 Hz-oscillations are visible in the derivative $d\Delta Z_{\rm eit}(t,5\,{\rm Hz})/dt$. The results indicate the visibility of the FOT frequency in the EIT response.

Fig. 6.13 presents a representative magnitude of the Fourier transforms computed for $\dot{V}_{\rm oEIT}(t)$ measured with EIT. $\dot{V}_{\rm oEIT}$ contains three groups of

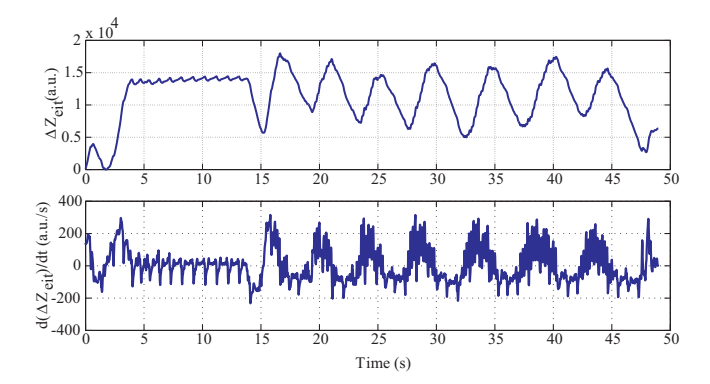


Figure 6.12: oEIT impedance signal and its time derivative measured from subject ID2 at 5 Hz. Values are given in EIT arbitrary units [a.u.] [149].

frequency components: spontaneous breathing (SB) at approximately 0.5 Hz, heart/cardiac activity (H1, H2, H3) and oscillation (O1 , O2). H2 and H3 are harmonics of H1, which has the highest peak at approximately 1.4 Hz. Similarly, O1 is maximal at the oscillation frequency 5 Hz, while a smaller peak at the second harmonics O2 can be observed at 10 Hz. In contrast, only the components of spontaneous breathing (SP) and oscillation (O1 and O2) can be observed in the FFT of $P_{\rm ao}$ and $\dot{V}_{\rm ao}$. They are, as expected, free of the blood irrigation influence caused by cardiac activity.

The linear coefficient $E_{\rm os}(f_{\rm os})$ is defined as the ratio between the FFT oscillation peak in oEIT and pneumotachograph signal, scaled by that ratio during spontaneous breathing:

$$E_{\rm os}(f_{\rm os}) = \left| \frac{FFT(\dot{V})_{\rm oEIT}(f_{\rm os})}{FFT(\dot{V})_{\rm ao}(f_{\rm os})} \right| \cdot \left| \frac{FFT(\dot{V})_{\rm ao}(f_{\rm SB})}{FFT(\dot{V})_{\rm oEIT}(f_{\rm SB})} \right|.$$

with $f_{\rm SB}$ the peak frequency of the spontaneous breathing. $E_{\rm os}=0$ means that no oscillation can be recorded by EIT, while $E_{\rm os}=1$ implies that the entire oscillatory signals have reached the lungs and can be captured by oEIT.

Figure 6.14 shows the values of $E_{\rm os}(f_{\rm os})$ in percent for all measurements. A general trend of $E_{\rm os}(f_{\rm os})$ with higher values at low frequency, a maximal value between 3-6 Hz and a drop after 10 Hz can be observed.

6.2.2 The band-pass filtered oEIT signal

Regional information provided by oEIT can be presented in the form of a spatial 2D image. A restrictive band-pass filter at f_{os} was applied to every pixel

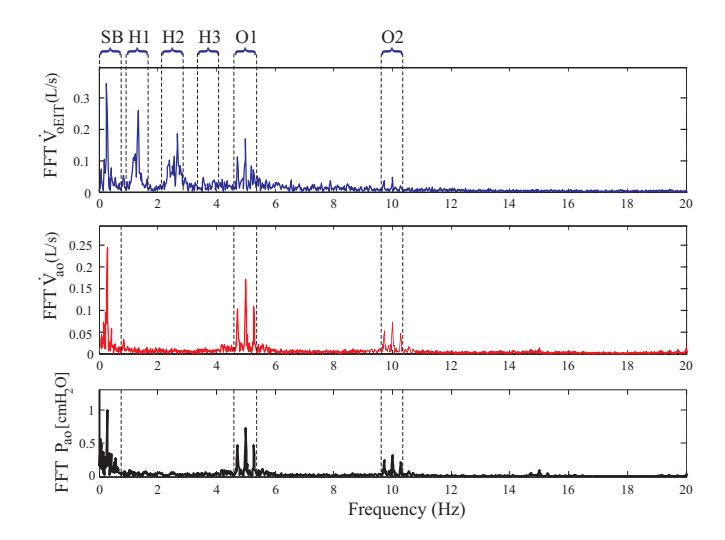


Figure 6.13: Fast Fourier transform of \dot{V}_{oEIT} , \dot{V}_{ao} and P_{ao} . $f_{\text{os}} = 5$ Hz [149]. Components: SB = spontaneous breathing, H = heart, O = oscillation.

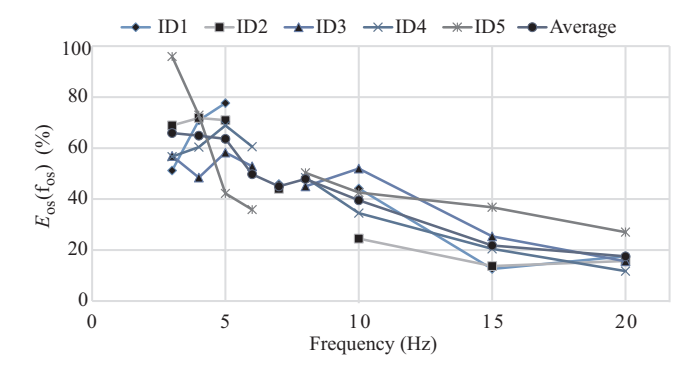


Figure 6.14: The coefficient $E_{os}(f_{os})$ in percent [149].

 $\Delta z_{\rm oEIT}(i,j,f_{\rm os})$ to exclude any cardiac or spontaneous breathing activity. The band-pass filtered oEIT images have the same orientation of unfiltered EIT images (Fig. 6.15). Fig. 6.15 also depicts three random consecutive oscillatory cycles for bandpass-filtered oEIT volume and flow. The signals consist of sinusoidal oscillation with a period of $T_{\rm os}=0.2$ s. Each period includes 10

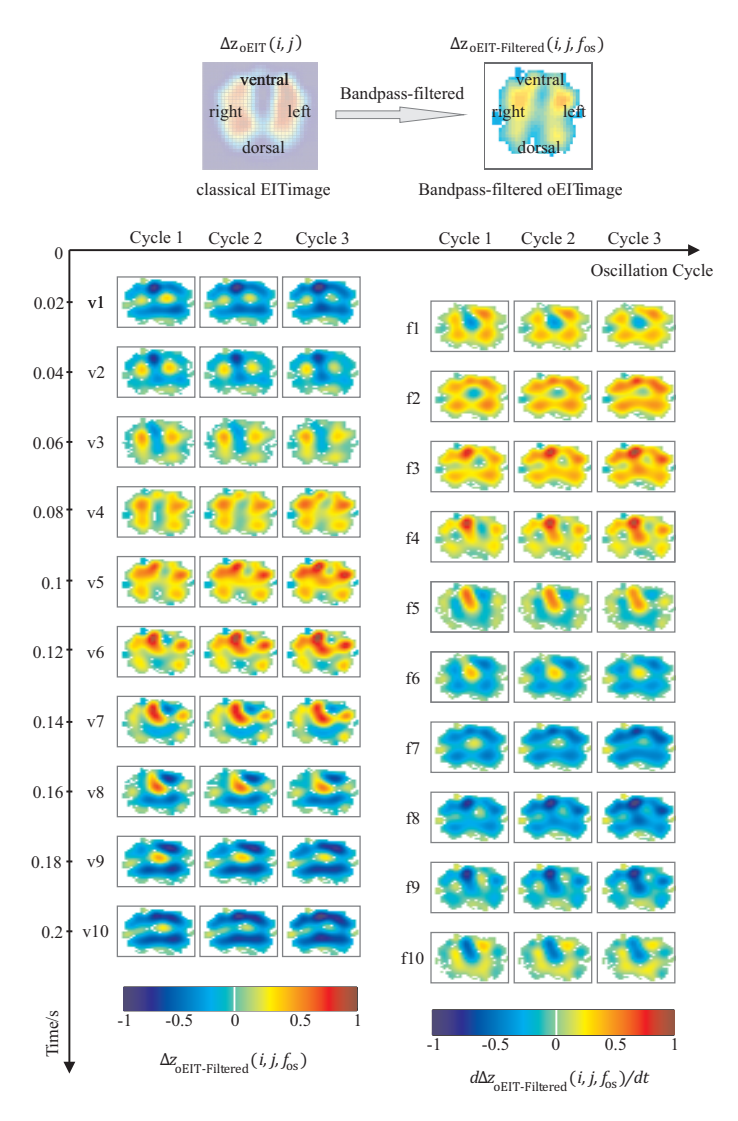


Figure 6.15: Top: Orientation of the band-pass filtered oEIT images. Bottom: oEIT volume (left) and flow (right) during three oscillatory cycles. From [149]

images numbered from 1 to 10. $\Delta z_{\text{oEIT}}(i,j,f_{\text{os}})$ are shown on the left side (v1-v10) and the derivative $d\Delta z_{\text{oEIT}}(i,j,f_{\text{os}})/dt$ on the right side (f1-f10), where $f_i = v_{i+1} - v_i, i = 1..10$. Each oscillatory cycle starts at low lung volume (v1), reaches the maximum after 5 sampling times (v5-v6), and ends at minimal lung volume (v10). Pixels with impedance almost equal to zero were set to white to separate the lung and non-lung regions.

Regarding the results, we hypothesize several properties of the band-pass filtered oEIT signal:

- Band-pass filtered oEIT images have repeating patterns in several consecutive oscillatory cycles. The images v1-v10 do not alter significantly among three oscillation cycles.
- Absolute value of band-pass filtered oEIT flows is $\frac{f_{os}}{2}$ -periodic. The images f1, f2, f3, f4, f5 are almost equal to f6, f7, f8, f9 and f10, respectively, with a sign conversion.
- Ventilation appears to be stronger in ventral than dorsal lung regions. In Fig. 6.15, ventral ventilation is stronger in oEIT volume and flow images (see v2, v3, v4, f2, f3, f4,...). The effect of the sinusoidal perturbation might be considered as small amplitude mechanical ventilation which causes a stronger gas distribution in the ventral regions [152].
- A band-pass filtered oEIT cycle is observed to consist of a homogeneous and an inhomogeneous phase. Each positive or negative half cycle could be divided into a homogeneous phase (images f1, f2) and an inhomogeneous phase (images f3-f5). After f3, the oEIT volume becomes left-right inhomogeneous. The positive oEIT flows concentrates in an oval region-shaped region, while flows in other regions have already become negative.

6.3 Summary

There has been an increasing interests in the use of EIT for global and regional lung function diagnostics. Strict correlation of EIT impedance change and thoracic air content has been reported in the literature for normal tidal breathing. Our studies on healthy subjects and asthmatic pediatric patients investigate this correlation for the forced expiratory maneuvers. Results show a strict linearity between global EIT and spirometric data in all parameters (FEV $_1$,FEV $_0$,MEF $_{50}$,MEF $_{50}$,MEF $_{50}$,MEF $_{50}$). The EIT-derived Tiffenenau index and the bronchodilator test index have a high potential in assessing asthma in pediatric patients. The EIT-derived mean FV loops of the asthmatic children yield typical concave shapes with improvement of the FV loops before and after

BSL. Regional lung function may be illustrated by regional FV loops obtained by EIT for different lung regions. Further studies on regional pulmonary functions with EIT are needed to validate the findings, since no established gold standard for regional lung function exists.

Another method for regional pulmonary diagnostics is the novel combination oEIT between EIT and FOT. Measurements on healthy subjects show the visibility of FOT frequencies in the Fourier transform of the global EIT index. Optimal oEIT frequencies are between 4Hz and 10Hz. The band-pass filtered oEIT signal demonstrates the dynamic behavior of different lung regions and might become a future tool in regional pulmonary function.

7

The journey is what brings us happiness not the destination.

Dan Millman

This book has accompanied us on a long journey throughout the complex physical nature of lung mechanics and a wide range of comprehensive mathematical descriptions and measurement methodologies. Following the goals defined at the beginning, various facets are comprised in this research. Starting with a nonlinear lumped modeling approach, the thesis continues applying model-based analysis to reevaluate existing pulmonary testing methods and to develop novel, innovative advances in respiratory measurements. Sophisticated models of the lung-heart interactions including the lymphatics and the interstitial fluid filtration contributes to a better understanding in the systematic development of cardiopulmonary diseases.

Throughout this work, miscellaneous scientific contributions have been achieved. Some of them are in the center of scientific discussions in the current state-of-the-art. Reviewing the chapters of this book, some answers can be proposed for the discussions:

1. Are object-oriented programming languages useful for modeling of complex physiological systems?

Yes, definitely.

The use of object-oriented modeling language (OOML) in simulation of technical systems is not a new approach. In 2008, Mathworks released the first Simscape version in their R2008a+ product. Object-oriented applications in the fields of biophysical and medical systems came later and are still moderate. Only a few publications can be found which use OOML to model biophysical systems: Brunberg 2009 (Dymola) [24], Barnea 2010 (Matlab Simpower) [7], de Canete 2013 (Simscape) [36], Heinke 2015 (Dymola) [77]. The models introduced in this research are the most comprehensive OOML model of the cardiorespiratory mechanics so far. The OOML SimscapeTM exhibits the following significant advantages over more "traditional" modeling tools (Fortran, C++, Matlab SimulinkTM):

The graphical implementation of complex model structure in OOML is intuitive for developers. In text-based programming language, the engineer has to deal with a great amount of equations which explodes for complex systems. More detailed comparisons between the causal (text-based, signal-oriented) and acausal modeling (OOML) are discussed in [36,99]. In OOML, the implementation of constitutive and

phenomenological equations are "decentralized", i.e. coupled with a graphical component, and no explicit implementation of balance equations is needed. The meaning of the components in a graphical model is directly understandable.

- OOML can connect subsystems bi-directionally as in the real physical world. This was demonstrated with the interconnection between the respiratory and cardiovascular system in our model. While cardiopulmonary models published by other authors consider an unidirectional between these systems, i.e. the changes in cardiovascular blood pressures and volume regarding in- and expiration [3,89,117], our model describes the interactions in both directions, for example the development of cardiogenic pulmonary congestion.
- 2. Are nonlinear multi-compartment models of lung mechanics recommended for off-line or even real-time applications in respiratory care? Yes, perhaps.

In most applications in respiratory care, the respiratory system are approximated by a simple resistance-compliance model [111]. This simplification has become a standard description in all physiological and medical textbooks [68, 96]. However, this model structure is too simple to adequately present the highly non-linear mechanics of the lungs. It is obvious that with only two parameter $R_{\rm rs}$ and $C_{\rm rc}$, descriptions of pathological conditions are very limited.

The respiratory model introduced in Chapter 3 has demonstrated its ability to model more complex nonlinear behaviors of the lungs. The compartmentalization ensures an equivalent between mathematical description and physiological interpretation. It should be noted that the developed model demonstrates the first use of OOML in analysis and evaluation of respiratory mechanics, as shown for the interrupter technique in Chapter 3.

Multi-compartment modeling yields more possibilities in interpretation of measurement data regarding physiological equivalent and possible disturbances. Furthermore, since the simulation in $Simscape^{TM}$ is more than ten times faster than in real-time, model-based online monitoring and decision support can be considered as potential applications of the model in future research.

3. Is there a clear physiological and physical coherence between the respiratory parameters measured with different pulmonary testing method, such as body plethysmography, interrupter, and forced oscillation technique?

With high probability.

In the current state-of-the-art, the coherence between the parameter obtained with the body plethysmography $(R_{\rm aw})$, the interrupter technique $(R_{\rm int})$, and the forced oscillation technique at different frequencies (R5, R20, $Z(j\omega)$) is not clearly addressed. Clinical studies showed correlation among the value of these parameter in presence of pathologies, however, did not focus on the underlying physiology. The model-based analysis discussed in Chapter 3 and Chapter 4 proposes clear correspondences between the compartments and the measurement techniques. The interrupter resistance $R_{\rm int}$ comprises the airway resistance $R_{\rm aw}$ and chest wall damping $R_{\rm cw}$.

4. Does model-based parameter identification provide additional diagnostic information beside the respiratory impedance measured with FOT? And if yes, which models should be used? Yes and no.

Recently, an interesting discussion on the use of the respiratory impedance $Z(j\omega)$ in pulmonary function testing and lung monitoring has been carried out by world leading scientists in lung mechanics [8]. The main discussion was between Bates, who supported the use of $Z(i\omega)$ in relation with the constant-phase model and Mitzner, who questioned the contribution of $Z(j\omega)$ in clinical praxis. The discussion indicated that the interpretation of G and H in the constant-phase model estimated with $Z(i\omega)$ is not persuasive to describe the changes in lung mechanics during pathological conditions. Unfortunately, Mitzner and Bates focused their discussion only on the constant-phase model (which they considered as the newest, most advanced model) and did not consider the Mead model. Our model-based analysis with the step-by-step model simplification has pointed out, that the RIC, eRIC, aRIC, and visco-elastic models are simplification of the Mead model. Indeed, the Mead model presents the best correspondence to lung physiology, while the constant-phase and DuBois's models overestimate the influence of lung tissue damping.

The results of this research support the use of the eRIC model for normal FOT, aRIC model for FOT including frequencies above 20 Hz, and the v-eRIC+ model for volume-dependent FOT measurements.

5. Is the object-oriented cardiopulmonary model able to reproduce the system behaviors physiologically during various scenarios from spontaneous breathing to mechanical ventilation?

Yes, it is.

The object-oriented model of the cardiopulmonary interactions was val-

idated for spontaneous breathing, the Mueller maneuver, and different mechanical ventilation modes. In most cases, model behaviors correlate well with clinical and animal data. It should be noted again that model parameters remained constant during all simulation, i.e no parameter estimation and adaption was performed to fit the data.

The model does not include the cardiac and respiratory regulation, thus, is almost completely passive in its current form. All of the components except the driver functions are passive elements (resistance, compliance, diodes, inertance). Simulation results have suggested that the passive intrathoracic pressure as a mechanical coupling between the cardiovascular and respiratory system has an important role in cardiopulmonary interactions.

6. Are the lymphatics and the fluid balance system successfully modeled? Likely.

There is a lack of understanding the physiological functionality of the lymphatics, and also a lack on animal and clinical data of the lymphs. As a first pilot simulative study, a comprehensive extension of the model was considered. The respiratory system was coupled with the cardiovascular system over the lymphatics. Simulation results have demonstrated the expected behaviors of the lymph, the fluid filtration and re-absorption during the development of cardiogenic edema and the effect of CPAP therapy. Similar simulations can be used to design future clinical study for a better understanding of the lymphatics and thoracic fluid balance.

7. How much potential does Electrical Impedance Tomography have as a future tool for online monitoring and assessing of global and regional lung mechanics?

Very high potential.

Existing lung function methods are restricted to global information. By contrast, the Electrical Impedance Tomography provides a non-invasive tool to assess regional dynamic functionality of lung mechanics. This research presents the novel use of the EIT-derived flow-volume loop in diagnosing of asthma in pediatric patients. Linearity between EIT and spirometry was reported in adults and children with a slight deviation at the maximum flow. This research also proposed a novel combination between EIT and FOT and demonstrates the visibility of high frequency components in the EIT signal. Combination between EIT and other measurement modalities such as body plethysmography and interrupter technique, as well as a large clinical study for oEIT should be considered in future researches.

A Appendix

A.1 Non-linear parameter identification using Least Squares fitting

Least Squares is a standard method in regression analysis to estimate the solution of overdetermined equation systems. It minimizes the sum of the squares of the residuals between data and model. The sum of the squares error S is given as:

$$S = \sum_{i=1}^{n} r_i^2 = \sum_{i=1}^{n} (y_i - f(x_i, \boldsymbol{\theta}))^2 = \|\boldsymbol{y} - \boldsymbol{f}\|_2^2.$$
 (A.1)

 r_i is the error between data y_i and model $f(x_i, \theta)$ for the i-th model equation. The vectors $\mathbf{y} \in \mathbb{R}^n$, $\mathbf{f} \in \mathbb{R}^n$ and $\mathbf{\theta} \in \mathbb{R}^m$ present the measurement data, the model outputs, and the parameters. The Least Squares method is generally a minimization problem $\min_{\mathbf{\theta}} \|\mathbf{y} - \mathbf{f}\|_2^2$.

For parameter estimation of lung mechanics in the frequency domain, a nonlinear Least-Squares fitting can be applied. The estimation problem can be written as:

$$\min_{\boldsymbol{\theta}} \| \boldsymbol{Z}_{\text{meas}} - \boldsymbol{Z}_{\text{model}} \|_{2}^{2} = \min_{\boldsymbol{\theta}} \left\| \left(\begin{array}{c} \boldsymbol{Z}_{\text{R, meas}} - \boldsymbol{Z}_{\text{R, model}} \\ \boldsymbol{Z}_{\text{X, meas}} - \boldsymbol{Z}_{\text{X, model}} \end{array} \right) \right\|_{2}^{2} \tag{A.2}$$

$$= \min_{\boldsymbol{\theta}} \left\| \left(\begin{array}{c} \boldsymbol{Z}_{\text{R, meas}}(\omega_{1}, \boldsymbol{\theta}) - \boldsymbol{Z}_{\text{R, model}}(\omega_{1}, \boldsymbol{\theta}) \\ \vdots \\ \boldsymbol{Z}_{\text{R, meas}}(\omega_{n}, \boldsymbol{\theta}) - \boldsymbol{Z}_{\text{R, model}}(\omega_{n}, \boldsymbol{\theta}) \\ \boldsymbol{Z}_{\text{X, meas}}(\omega_{1}, \boldsymbol{\theta}) - \boldsymbol{Z}_{\text{X, model}}(\omega_{1}, \boldsymbol{\theta}) \\ \vdots \\ \boldsymbol{Z}_{\text{X, meas}}(\omega_{n}, \boldsymbol{\theta}) - \boldsymbol{Z}_{\text{X, model}}(\omega_{n}, \boldsymbol{\theta}) \end{array} \right) \right\|_{2}^{2}$$

with the impedance vectors \mathbf{Z}_{meas} , $\mathbf{Z}_{\text{model}} \in \mathbb{C}^{m \times (2n)}$, the resistive impedance vector $\mathbf{Z}_{\text{R, meas}}$, $\mathbf{Z}_{\text{R, model}} \in \mathbb{R}^{m \times n}$, and the reactance vectors $\mathbf{Z}_{\text{X, meas}}$, $\mathbf{Z}_{\text{X, model}} \in \mathbb{R}^{m \times n}$. m is the number of data points, and n is the number of the measured FOT frequencies ω .

A non-linear fitting can be performed with the Matlab function *lsqnonlin*, which is based on an upper and a lower limit of the parameters to be identified on a trust-region-method [34]. The numerical solution for minimizing the error by the trust region method is not a global but a local minimum. The non-linear function to be minimized is approximated by a quadratic function. Because of

the trust region method, this approximation only takes place locally near the iterations of the parameter vector. Hence, for the identification of respiratory parameters, the choice of initial values of the parameter vector is an important issue.

A.2 Reynold number, flow patterns, and Hagen-Poiseuille's law

In 1883, Reynolds examined patterns of flow by injecting ink into a water stream through a pipe [185]. He found that flow could be described by two different categories depending on its velocity: laminar and turbulent flow. This classification is not only valid for fluids, but air flow can be divided into laminar and turbulent flow as well. An important figure in characterizing flow is the dimensionless Reynolds number Re, which is calculated as follows:

$$Re = \frac{vd}{\nu} = \frac{\dot{V}d}{A\nu},\tag{A.3}$$

where d is diameter and A is cross-sectional Area of a circular pipe. Re is dependent on the properties of the passed pipe, the physical properties of the fluid and the flow rate. If the shape of the pipe and the flowing fluid are known, Re is linearly dependent on the flow rate and thus, can be employed as a classification figure for flow regimes.

Laminar flow is characterized by a regular, ordered flow pattern [185]. Fig. A.1(a) illustrates the laminar airflow in the main direction of flow with a parabolic velocity profile. Laminar flow is found for low flow rates and for Re \leq 2100 in circular pipes. For laminar flow, pressure is connected to flow in a linear relationship:

$$\Delta P(t) = K \dot{V}(t) = \frac{8\mu L}{\pi r^4} \dot{V}(t) \,, \tag{A.4} \label{eq:deltaP}$$

where K is a constant [70], which, for circular tubes, can be expressed by physical properties of the fluid (or gas) and the length L and the radius r of the tube. This relation is known as Hagen-Poiseuille's law [87]. K corresponds to the laminar flow resistance of a pipe:

$$R_{\text{laminar}} = \frac{8\mu L}{\pi r^4} \,. \tag{A.5}$$

For increasing flow rates, air (or fluid) movements become turbulent. Fig. A.1(b) shows the flow pattern for turbulent flow. The regular flow patterns are abandoned by the addition of random fluctuations superimposed on the velocity

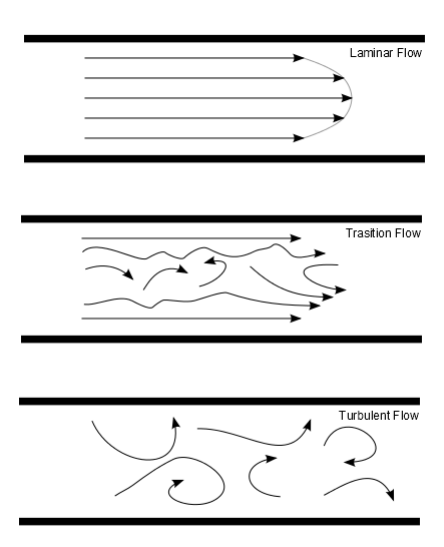


Figure A.1: Patterns for different flow regimes.

component in direction of flow [185] and air moves chaotically. The irregular movement of flow causes additional friction and the pressure-flow relationship becomes non-linear:

$$\Delta P(t) = K \dot{V}^{\alpha}(t), \qquad \alpha \in [1.75; 2], \tag{A.6}$$

where K is a constant, [70]. In a circular pipe, turbulent flow is associated with Re $\succeq 4000$ [185].

Laminar flow does not change to turbulent flow abruptly and for $2100 \leq \text{Re} \leq 4000$ flow transfers through a transition regime [185], in which both laminar and turbulent flow attributes are found. The pressure-flow relationship in the transition regime can be described by the Rohrer equation, which is defined as follows:

$$\Delta P(t) = K_1 \dot{V}(t) + K_2 \dot{V}^2(t),$$
 (A.7)

where K_1 and K_2 are constants. Turbulent flow resistance of a pipe is flow-dependent:

$$R_{\text{turbulent}} = K_1 + K_2 \dot{V}. \tag{A.8}$$

A.3 Respiratory modeling

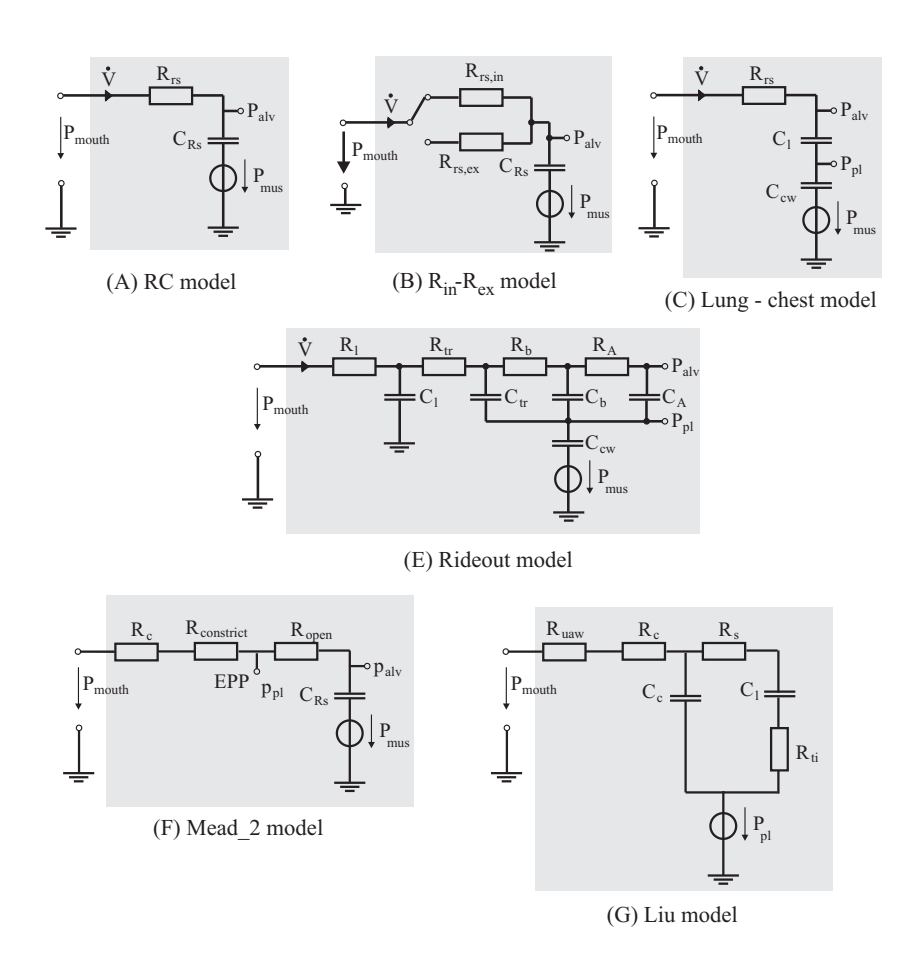


Figure A.2: Lung models used in mechanical ventilation (A-D), or in spirometry for description of flow limitation (E-F).

Table A.1: Anatomical model of the human bronchial tree according to Weibel, N = generation number; $N_{\rm b} =$ number of tubes, L = length of tube, d = diameter of tube, S = total cross-sectional area, $V_{\rm b} =$ total volume of tubes, $\sum V_{\rm b} =$ cumulative tube volume of all generations up to N, $V_{\rm alv} =$ alveolar volume, V = total volume, $\sum V =$ cumulative total volume [38].

ative total	volume	[38].								
N	$N_{ m T}$	T	p	S	$V_{ m b}$	$\sum V_{ m b}$	$V_{ m alv}$	Λ	\sum_{V}	
	cm	cm	cm	$^{ m cm}^2$	cm^3	cm^3	$^{\mathrm{cm}_{3}}$	cm^3	cm^3	
0	1	12	1.8	2.54	30.54	30.5	0	30.54	30.54	
П	2	4.76	1.22	2.34	11.13	41.7	0	11.13	41.67	
2	4	1.9	0.83	2.16	4.11	45.8	0	4.11	45.78	
3	∞	0.65	0.479	1.44	0.94	46.7	0	0.94	46.72	
4	16	1.085	0.385	1.86	2.02	48.7	0	2.02	48.74	
ಬ	32	0.915	0.299	2.25	2.06	50.8	0	2.06	50.8	
9	64	0.769	0.239	2.88	2.21	53.0	0	2.21	53.01	
7	128	0.65	0.197	3.88	2.52	55.5	0	2.52	55.53	
∞	256	0.547	0.159	5.08	2.78	58.3	0	2.78	58.31	
6	512	0.462	0.132	6.97	3.22	61.5	0	3.22	61.53	
10	1024	0.393	0.111	6.6	3.9	65.4	0	3.9	65.43	
11	2048	0.333	0.093	14	4.65	70.1	0	4.65	70.08	
12	4096	0.282	0.081	21.2	5.98	76.1	0	5.98	26.06	
13	8192	0.231	0.02	31.6	7.29	83.4	0	7.29	83.35	
14	16384	0.197	0.063	51.5	10.12	93.5	0	10.12	93.47	
15	32768	0.171	0.056	85	14	107.5	0	14	107.47	
16	65536	0.141	0.051	135	19.09	126.6	0	19.09	126.56	
17	131072	0.121	0.046	219	26.43	153.0	3.9	30.33	156.89	
18	262144	0.1	0.043	376	37.6	190.6	13.1	50.7	207.59	
19	524288	0.085	0.04	664	56.23	246.8	39.4	95.63	303.22	
20	1048576	0.071	0.038	1218	86.4	333.2	138	224.4	527.62	
21	2097152	90.0	0.037	2225	133.1	466.3	273	406.1	933.72	
22	4194304	0.02	0.035	4045	204	670.3	551	755	1688.72	
23	8388608	0.043	0.035	8091	345.7	1016.0	938	1283.7	2972.42	

A.4 Sensitivity analysis of the Mead's model

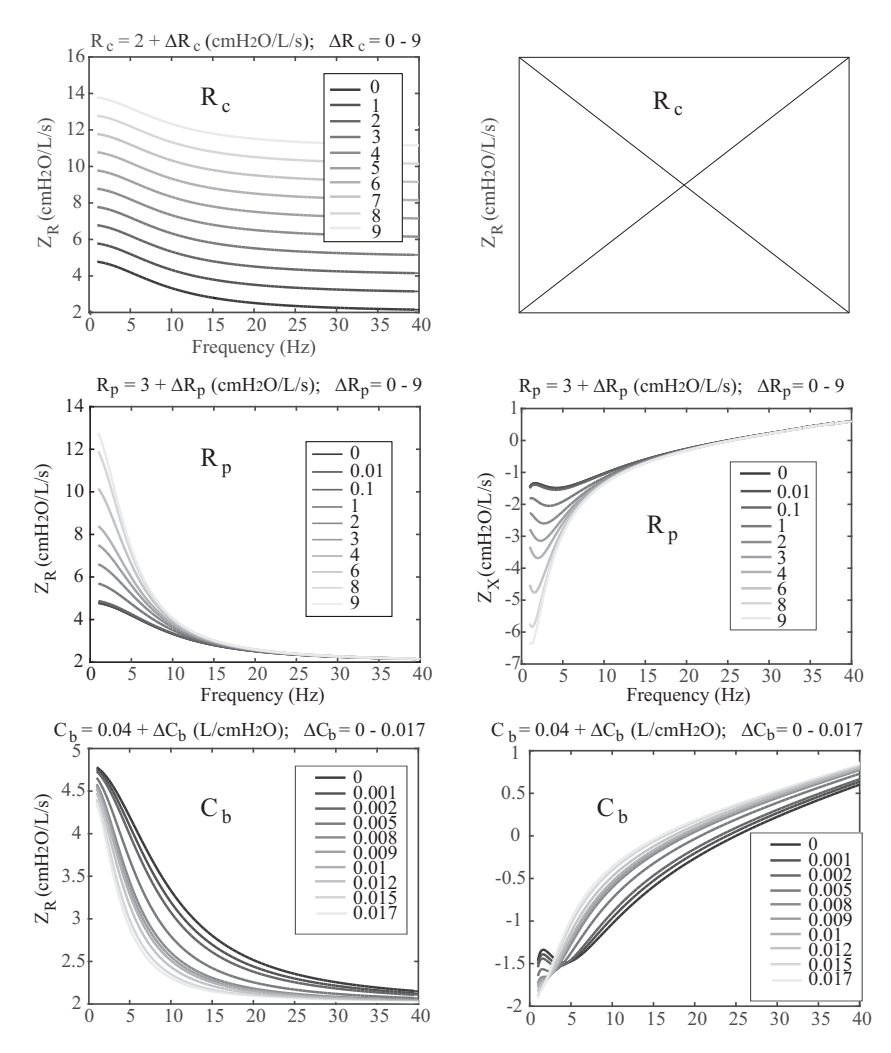


Figure A.3: Sensitivity analysis of the parameter $R_{\rm c}$, $R_{\rm p}$, and $C_{\rm b}$ of the Mead's model.

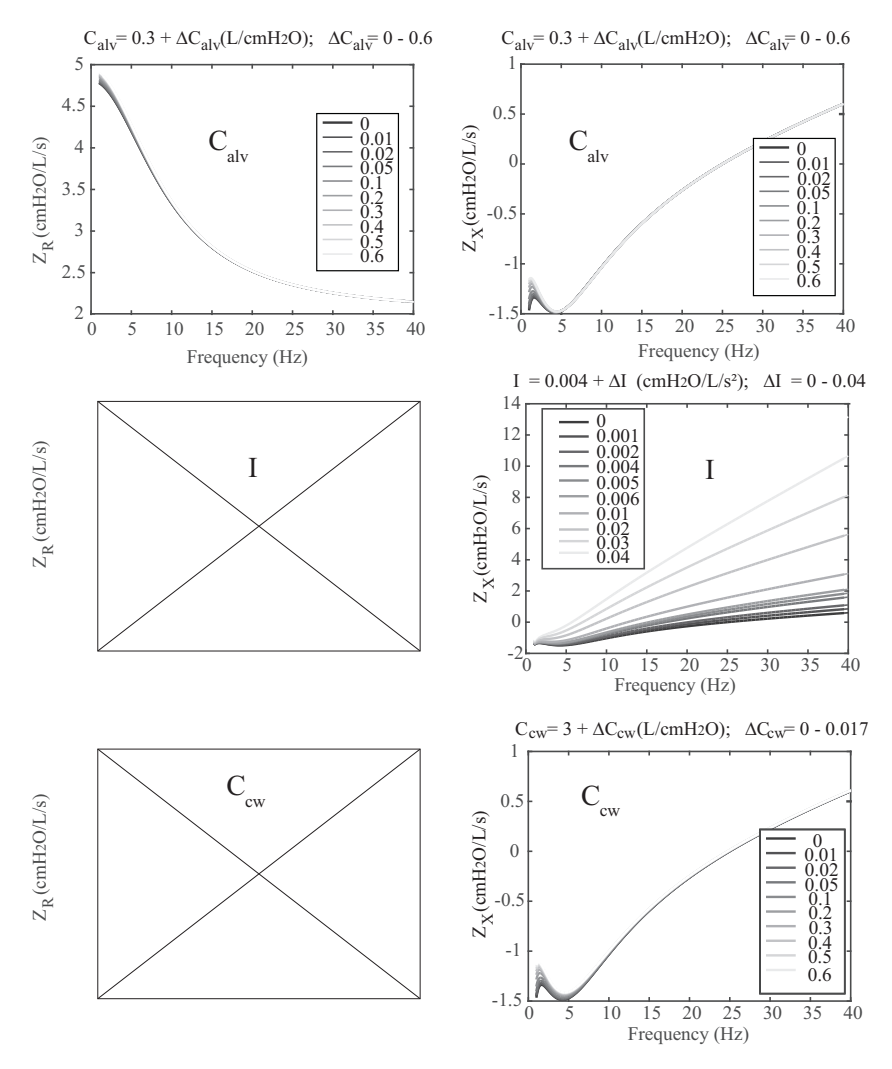


Figure A.4: Sensitivity analysis of the parameter $C_{\rm alv}$, I, and $C_{\rm cw}$ of the Mead's model.

A.5 Parameter of the cardiovascular model

A.5.1 Heart

Driver functions of atria, ventricles and septum:

$$e_{\text{la,ra}}(t) = A_{\text{a}} \cdot e^{-\frac{0.5}{B_{\text{a}}^2} \cdot (\frac{HR}{80})^2 \cdot (t - C_{\text{a}} \cdot \frac{80}{HR})^2}$$

$$e_{\text{lvf,rvf}}(t) = \sum_{i=1}^4 A_i \cdot e^{-\frac{0.5}{B_i^2} \cdot (\frac{HR}{80})^2 \cdot (t - C_i \cdot \frac{80}{HR})^2} + D$$

$$e_{\text{sept}}(t) = e_{\text{lvf}}(t)$$
(A.9)

 $A,\,B,\,$ and C are the Gaussian magnitude, width, and delay, respectively [153]. HR is the heart rate. D is a baseline/offset which prevents the ventricular pressure from reaching negative values. D is equal 0.02 for the left and 0.07 for the right ventricle.

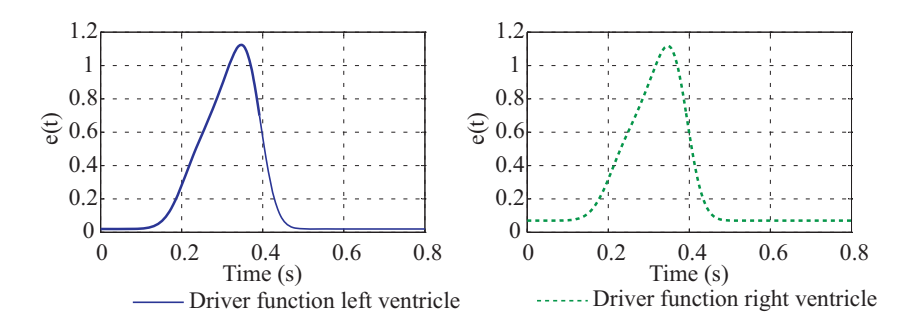


Figure A.5: Left and right ventricular driver functions.

Param.	Units	i = 1	i = 2	i = 3	i = 4
$A_{\mathrm{v},i}$	_	0.43	0.36	0.5	0.55
$B_{\mathrm{v},i}$	\mathbf{s}	0.045	0.035	0.037	0.036
$C_{\mathrm{v},i}$	\mathbf{s}	0.175	0.23	0.275	0.3
$A_{\rm a}$	_	0.9	_	_	_
$B_{\mathbf{a}}$	\mathbf{s}	0.018	_	_	_
$C_{\mathbf{a}}$	\mathbf{s}	0.065	_	_	_

ESPVR and EDPVR of four heart chambers and septum:

$$\begin{aligned} P_{\text{es}} &= E_{\text{es}} \cdot (V - V_d) \\ P_{\text{ed}} &= P_0 \cdot (e^{\lambda(V - V_0)} - 1) \\ P(V, t) &= e(t) \cdot P_{\text{es}}(V) + (1 - e_t t)) \cdot P_{\text{ed}}(V) \end{aligned}$$

Pressure-volume relationship of the pericardium:

$$P_{\text{pcd}}(t) = P_{0,\text{pcd}}(e^{\lambda_{\text{pcd}}(V_{\text{pcd}}(t) - V_{0,\text{pcd}})} - 1)$$

Volume balance equations:

та	ble A.2: P	'aramet	ers of t	ne near	t model.
Param.	P_0	V_0	$V_{\rm d}$	λ	E_{es}
Units	$\rm cmH_2O$	mL	mL	L^{-1}	$\rm cm H_2 O L^{-1}$
la	1.1236	0	20	60	294.27
ra	1.1236	0	20	50	217.53
lvf	0.0926	20	15	33	3573.7
rvf	0.211	20	5	23	895.5
sept.	1.5096	2	2	435	66303
peri.	0.068	260	_	30	_

Table A.2: Parameters of the heart model.

$$\begin{aligned} V_{lvf} &= V_{lv} - V_{spt} \\ V_{rvf} &= V_{rv} + V_{spt} \\ V_{lv} &= V_{lvf} + V_{spt} \\ V_{rv} &= V_{rvf} - V_{spt} \\ V_{pcd}(t) &= V_{la}(t) + V_{lv}(t) + V_{ra}(t) + V_{rv}(t) \end{aligned}$$

A.5.2 Pulmonary and systemic circulation

Veins

Normal veins:

$$V = \frac{1}{\lambda} \cdot \log(P_{\text{tm}} + P_0) + V_0 \tag{A.10}$$

Collapsed veins:

$$if V \le V_{clp}$$

$$\begin{split} V &= 0.2 \cdot V_{\rm clp} \cdot \tanh(\frac{5}{V_{\rm clp} \cdot \lambda \cdot (P_{\rm clp} + P_0)} \cdot (P - P_{\rm clp})) + V_{\rm clp} \\ P_{\rm clp} &= e^{\lambda (V_{\rm clp} - V_0)} - P_0 \\ \text{where } V_{\rm clp} \text{ is a threshold volume of collapsed veins.} \end{split}$$

Table A.3: Parameters of the veins.

Param.	P_0	V_0	$V_{\rm clp}$	λ
Units	$\rm cmH_2O$	L	L	L^{-1}
Syst. veins	6.328	1.8456	1.25	1.8361
Pulm. veins	-3.567	0.0895	0.0625	10

Pulmonary capillaries

Pulmonary capillaries compliance:

$$V = V_0 + \frac{1}{\lambda} \cdot \tanh(\mathbf{c} \cdot P_{tm} + P_0) \tag{A.11}$$

Pulmonary capillaries resistance:

$$R = R_1 \cdot \frac{(V_1 - 0.9V_{\min})^2}{(V_t - 0.9V_{\min})^2}$$
(A.12)

Parameters of the pulmonary capillaries are given in Table 5.2. The systemic capillaries are included in the systemic arteries.

Arteries

The pressure-volume characteristics of pulmonary and systemic arteries:

$$V - V_{\rm d} = P_{\rm tm} \cdot C \tag{A.13}$$

Table A.4: Parameters of the arteries.

Param.	С	V_{d}
Units	L/cmH_2O	L
Syst. arteries	0.0011	0.6
Pulm. arteries	0.0022	0.1

A.6 Exemplary Simscape code of a model component

The following Simscape code presents the non-linear resistance of the peripheral airways. A component belongs to a domain (in this case electrical branch) and contains parameters, inputs, outputs, and equations. It should be distinguished between algebraic (with '=') and physical equations (with '==').

```
component R_vessel < foundation.electrical.branch</pre>
% non-linear colapsible resistance
        = { 1, 'Ohm' };
R.1
V1
        = { 0.1, 'A*s' };
                            % V1
        = { 0.05, 'A*s' }; % Vmin
Vmin
end
inputs
        = { 1, 'A*s' };
Vol
                            % Volume
end
outputs
Rout
        = { 1, 'Ohm' };
                            % R_out
end
equations
let
R.
          R1*(V1-0.9*Vmin)/(Vol-0.9*Vmin);
in
v
        == R*i;
Rout
        == R;
end
end
end
```

A.7 Spirometric and EIT-derived parameters

	S	pirometric para	meters (pneumo	otachography)		
	Healthy	controls	Asthma b	efore BSL	Asthma a	after BSL
		Mean % ref.		Mean % ref.		Mean % ref.
	$Mean \pm SD$	pred. \pm SD	$Mean \pm SD$	pred. \pm SD	$Mean \pm SD$	pred. \pm SD
FVC [L]	2.48 ± 0.93	78 ± 15.9	2.37 ± 0.92	77.3 ± 15	2.42 ± 0.93	79.7 ± 14.7
FEV_1 [L]	2.38 ± 0.87	90.3 ± 13.7	2.16 ± 0.83	83.7 ± 16.9	2.29 ± 0.86	88.9 ± 16
$FEV_{0.5}$ [L/s]	1.86 ± 0.63	93.1 ± 16.9	1.64 ± 0.61	83.7 ± 20.5	1.80 ± 0.63	92.7 ± 19.9
$MEF_{75}[L/s]$	4.62 ± 1.61	93.4 ± 18.9	4.03 ± 1.6	80.1 ± 23.3	4.63 ± 1.67	92.1 ± 21.1
MEF_{50} [L/s]	3.5 ± 1.18	98 ± 21.6	2.75 ± 1.09	77.4 ± 23.3	3.37 ± 1.24	95.0 ± 24.6
MEF_{25} [L/s]	2.02 ± 0.77	109.3 ± 28.7	1.52 ± 0.67	82.7 ± 28.5	1.95 ± 0.81	106.3 ± 32.4
FEV ₁ /FVC [%]	95.97 ± 4.56	115.2 ± 12.5	91.36 ± 7.62	108.8 ± 9.72	94.89 ± 5.68	112.6 ± 6.9
ΔFEV_1	-	-	-	-	7.44 ± 12.94	_

	EIT-derived spirometry parameters								
	Healthy	controls	Asthma b	efore BSL	Asthma a	after BSL			
	$Mean \pm SD$	-	$Mean \pm SD$	-	$Mean \pm SD$	-			
FVC [L]	2.48 ± 0.93	=	2.38 ± 0.92	-	2.42 ± 0.93	-			
FEV_1 [L]	2.36 ± 0.87	-	2.24 ± 0.85	-	2.36 ± 0.89	-			
$FEV_{0.5}$ [L/s]	1.90 ± 0.73	-	1.79 ± 0.69	-	1.90 ± 0.73	-			
MEF_{75} [L/s]	6.16 ± 2.77	-	5.24 ± 2.98	-	6.68 ± 3.51	-			
MEF_{50} [L/s]	4.23 ± 1.89	-	3.84 ± 1.78	-	4.52 ± 2.17	-			
$MEF_{25}[L/s]$	2.25 ± 0.97	-	1.99 ± 0.92	-	2.34 ± 1.07	-			
$ \text{FEV}_1/\text{FVC} [\%] $	95.28 ± 5.93	-	94.22 ± 5.99	-	97.73 ± 3.67	-			
ΔFEV_1	-	-	-	-	4.79 ± 12.93	-			

Table A.5: Mean values \pm SD of lung function parameters, measured by spirometry and EIT on 58 asthmatics before and after BSL, as well as 58 age-matched healthy controls [143].

B Publications

Peer-reviewed Journal Articles

- C. Ngo, S. Leonhardt, T. Zhang, B. Misgeld, T. Vollmer, K. Tenbrock, and S. Lehmann: "Linearity of electrical impedance tomography during maximum effort breathing and forced expiration maneuvers". *Physiolog*ical Measurement, 38(1),77, 2016.
- S. Lehmann, S. Leonhardt, C. Ngo, L. Bergmann, I. Ayed, S. Schrading, and K. Tenbrock: "Global and regional lung function in cystic fibrosis measured by electrical impedance tomography". *Pediatric Pulmonology*, 51(11),1191–1199, 2016.
- C. Ngo, K. Krüger, T. Vollmer, S. Winter, B. Penzlin, S. Lehmann, S. Leonhardt, and B. Misgeld: "Effects of the nasal passage on forced oscillation lung function measurements". Biomedical Engineering/Biomedizinische Technik, 62(6),635–642, 2017.
- C. Ngo, S. Spagnesi, C. Munoz, S. Lehmann, T. Vollmer, B. Misgeld, and S. Leonhardt: "Assessing regional lung mechanics by combining electrical impedance tomography and forced oscillation technique". Biomedical Engineering/ Biomedizinische Technik, 63(6), 673–681, 2018.
- C. Ngo, F. Dippel, S. Leonhardt, K. Tenbrock, and S. Lehnmann: "Flow-volume loops measured with electrical impedance tomography in pediatric patients with asthma". *Pediatric Pulmonology*, 53(5), 636–644, 2018.
- S. Lehmann, S. Leonhardt, C. Ngo, L. Bergmann, S. Schrading, K. Heimann, N. Wagner, and K. Tenbrock: "Electrical impedance tomography as possible guidance for individual positioning of patients with multiple lung injury". The Clinical Respiratory Journal, 12(1),68-75, 2018.
- C. Ngo, S. Dahlmanns, T. Vollmer, B. Misgeld, and S. Leonhardt: "An object-oriented computational model to study cardiopulmonary hemodynamic interactions in humans". Computer Methods and Programs in Biomedicine, 159,167–183, 2018.
- 8. C. Ngo, S. Dahlmanns, T. Vollmer, B. Misgeld, and S. Leonhardt: "Object-oriented modeling of thoracic fluid balance to study cardiogenic

- pulmonary congestion in humans". $Computer\ Methods\ and\ Programs\ in\ Biomedicine,$ In review.
- C. Ngo, and S. Leonhardt: "A model-based analysis to re-evaluate the first and second rises in the rapid interrupter technique measurements". *Journal of Applied Physiology*, In review.

Peer-reviewed Conference Proceedings

- C. Ngo, B. Misgeld, T. Vollmer, S. Winter, and S. Leonhardt: "Linear affine lung mechanics model with emphasis on pleural dynamics".
 Biomedizinische Technik, 59(S1),807–810. 48. DGBMT Jahrestagung,
 Hannover, Germany, Oct. 8.–10., 2014.
- S. Lehmann, S. Leonhardt, C. Ngo, S. Schrading, N. Wagner, K. Tenbrock: "Regionale Lungenfunktionsdiagnostik mittels Elektrischer Impedanz Tomographie bei Patienten mit Cystischer Fibrose". 18. Deutsche Mukoviszidose Tagung 2015). Würzburg, Germany, Nov. 19.–21., 2015.
- 3. S. Lehmann, S. Leonhardt, C. Ngo, N. Wagner, and K. Tenbrock: "Ventilations-Monitoring mittels Elektrischer Impedanztomographie in unterschiedlichen Positionen bei einer lobektomierten Patientin mit cystischer Fibrose". 37. Jahrestagung der Gesellschaft für Pädiatrische Pneumologie e.V.. Basel, Switzerland, March 5.–7., 2015.
- C. Ngo, A. Kube, K. Krüger, T. Vollmer, S. Winter, S. Leonhardt, and B. Misgeld: "Identification of respiratory parameters in frequency and time domain with Forced Oscillation Technique". The 9th IFAC Symposium on Biological and Medical Systems, IFAC-PapersOnLine 48.20 (2015): 177-182. Berlin, Germany, Aug. 31.—Sep 2., 2015.
- C. Ngo, R. Schlözer, T. Vollmer, S. Winter, B. Misgeld and S. Leonhardt: "A simulative model approach of cardiopulmonary interaction". World Congress on Medical Physics and Biomedical Engineering, Springer, Cham, 2015 S. 1679–1682. Toronto, Canada, June 7–12, 2015.
- C. Ngo, S. Dahlmanns, T. Vollmer, B. Misgeld and S. Leonhardt: "Die objektorientiere Umgebung Matlap Simscape zur Modellierung physiologischer Systeme". Workshop AUTOMED 2016. Wismar, Germany, Sept. 21–23, 2016.
- C. Ngo, S. Briones Herranz, B. Misgeld, T. Vollmer, and S. Leonhardt: "
 An object-oriented model of the cardiopulmonary system with emphasis

- on the gravity effect". The 38th Annual International Conference of the IEEE Engineering in Medicine and Biology Society (EMBC 2014), 2737-2740. Orlando, Florida, USA, Aug. 16 18, 2016.
- 8. C. Ngo, C. Munoz, and S. Leonhardt: "Combination of Electrical Impedance Tomography and Forced Oscillation Technique: a new pulmonary diagnostics tool?". 18th International Conference on Biomedical Applications of Electrical Impedance Tomography. Hanover, New Hampshire, USA, June 21.–24, 2017.

Supervised Student Theses

- 1. R. Schlözer: Modeling of the human cardiopulmonary system for lung congestion and edema. Diploma thesis, 2014.
- 2. A. Kube: Model-based analysis of respiratory mechanics for patients with pulmonary congestion. Bachelor thesis, 2014.
- 3. A. Barham: Modeling of respiratory muscles for multi-compartment lung models. Bachelor thesis, 2014.
- 4. F. Dippel: Model-based analysis of the respiratory activity in spontaneous breathing and forced pulmonary function tests with Electrical-Impedance-Tomography. Bachelor thesis, 2015.
- 5. K. Krüger: Compensation of the nasal influence on the respiratory system using a nose mask in Forced Oscillation Technique. Bachelor thesis, 2015.
- S. Briones Herranz: Modeling the ventilation-perfusion mismatch of the cardiopulmonary system in Matlab Simscape. Master thesis, 2015.
- 7. S. Spagnesi: Investigation the frequency-dependence of respiratory parameters and the effect of pendelluft using Electrical-Impedance-Tomography. Master thesis, 2015.
- 8. S. Dahlmanns: Modeling of the human cardiopulmonary system for the simulation of lung edema. Master thesis, 2015.
- 9. C. Munoz: Signal processing in oscillatory electrical impedance tomography for regional lung function diagnostics. Bachelor thesis, 2016.
- 10. P. Ackermann: Model-based analysis of lung mechanics in spontaneous breathing and oscillation techniques. Bachelor thesis, 2016.

- 11. H. Malik: Extension of an object-oriented model of the human cardiopulmonary system with respect to the systemic vascular bed and the effect of gravity. Bachelor thesis, 2016.
- 12. R. Herges: Sensitivity analysis of a mathematical model of the human respiratory system. Bachelor thesis, 2017.
- 13. F. Dippel: Nonlinear modeling and robust identification of respiratory mechanics. Master thesis, 2017.

Bibliography

- [1] Global initiative for asthma. Global strategy for asthma management and prevention, 2018. Available from: wwww.ginaasthma.com.
- [2] A. Adler, R. Amyot, R. Guardo, J. Bates, and Y. Berthiaume. Monitoring changes in lung air and liquid volumes with electrical impedance tomography. *Journal of Applied Physiology*, 83(5):1762–1767, 1997.
- [3] A. Albanese, L. Cheng, M. Ursino, and N. Chbat. An integrated mathematical model of the human cardiopulmonary system: model development. American journal of physiology. Heart and circulatory physiology, 310(7):H899–921, 2016.
- [4] A. Athanasiades, F. Ghorbel, J. Clark Jr, S. Niranjan, J. Olansen, J. Zwischenberger, and A. Bidani. Energy analysis of a nonlinear model of the normal human lung. *Journal of Biological Systems*, 08(02):115–139, 2000.
- [5] G. Baldi, G. Luna, and A. Antonio. Lung water assessment by lung ultrasonography in intensive care: a pilot study. *Intensive care medicine*, 39(1):74–84, 2013.
- [6] D. Barber, B. Brown, and I. Freeston. Imaging spatial distributions of resistivity using applied potential tomography—apt. In *Information Processing in Medical Imaging*, pages 446–462. Springer, 1984.
- [7] O. Barnea. Open source programming of cardiovascular pressure-flow dynamics using simpower toolbox in matlab and simulink. *The Open Pacing, Electrophysiology & Therapy Journal*, 3:55–59, 2010.
- [8] J. Bates. Point:counterpoint: Lung impedance measurements are/are not more useful than simpler measurements of lung function in animal models of pulmonary disease. *Journal of Applied Physiology*, 103(5):1900–1901, 2007.
- [9] J. Bates. Lung mechanics: an inverse modeling approach. Cambridge University Press, 2009.
- [10] J. Bates, P. Baconnier, and J. Milic-Emili. A theoretical analysis of interrupter technique for measuring respiratory mechanics. *Journal of Applied Physiology*, 64(5):2204–2214, 1988.

- [11] J. Bates, C. Irvin, R. Farré, and Z. Hantos. Oscillation mechanics of the respiratory system. Comprehensive Physiology, 1(3):1233, 2011.
- [12] J. Bates, A. Rossi, and J. Milic-Emili. Analysis of the behavior of the respiratory system with constant inspiratory flow. *Journal of Applied Physiology*, 58(6):1840–1848, 1985.
- [13] J. Bates, G. Schmalisch, D. Filbrun, and J. Stocks. Tidal breath analysis for infant pulmonary function testing. ers/ats task force on standards for infant respiratory function testing. european respiratory society/american thoracic society. *European Respiratory Journal*, 16(6):1180–1192, 2000.
- [14] J. Bates, P. Sly, T. Kochi, and J. Martin. The effect of a proximal compliance on interrupter measurements of resistance. *Respiration physiology*, 70(1):301–312, 1987.
- [15] J. Bates and B. Suki. Assessment of peripheral lung mechanics. Respiratory physiology & neurobiology, 163(1):54-63, 2008.
- [16] J. Batzel, M. Bachar, and F. Kappel. Mathematical modeling and validation in physiology: applications to the cardiovascular and respiratory systems, volume 2064. Springer, 2012.
- [17] A. Bersten. Measurement of overinflation by multiple linear regression analysis in patients with acute lung injury. *European Respiratory Journal*, 12(3):526–532, 1998.
- [18] N. Beydon. Interrupter resistance: what's feasible? Paediatric respiratory reviews, 7:S5–S7, 2006.
- [19] N. Beydon, S. Davis, E. Lombardi, J. Allen, H. Arets, P. Aurora, H. Bisgaard, G. Davis, F. Ducharme, and H. Eigen. An official american thoracic society/european respiratory society statement: pulmonary function testing in preschool children. *American journal of respiratory and critical care medicine*, 175(12):1304–1345, 2007.
- [20] S. Bickel, J. Popler, B. Lesnick, and N. Eid. Impulse oscillometry: interpretation and practical applications. CHEST Journal, 146(3):841–847, 2014.
- [21] J. Biondi, R. Hines, P. Barash, C. Baker, M. Matthay, and R. Matthay. The adult respiratory distress syndrome. The Yale journal of biology and medicine, 59(6):575, 1986.

- [22] L. Borcea. Electrical impedance tomography. Inverse problems, 18(6):R99, 2002.
- [23] W. Briscoe and A. DuBois. The relationship between airway resistance, airway conductance and lung volume in subjects of different age and body size. *Journal of Clinical Investigation*, 37(9):1279, 1958.
- [24] A. Brunberg, S. Heinke, J. Spillner, R. Autschbach, D. Abel, and S. Leonhardt. Modeling and simulation of the cardiovascular system: a review of applications, methods, and potentials/Modellierung und Simulation des Herz-Kreislauf-Systems: ein Überblick zu Anwendungen, Methoden und Perspektiven. *Biomedical Engineering*, 54(5):233–244, 2009.
- [25] A. S. Buist, M. A. McBurnie, W. M. Vollmer, S. Gillespie, P. Burney, D. M. Mannino, A. M. Menezes, S. D. Sullivan, T. A. Lee, K. B. Weiss, et al. International variation in the prevalence of copd (the bold study): a population-based prevalence study. *The Lancet*, 370(9589):741–750, 2007.
- [26] D. Chalut, F. Ducharme, and G. Davis. The preschool respiratory assessment measure (pram): a responsive index of acute asthma severity. *The Journal of pediatrics*, 137(6):762–768, 2000.
- [27] S. Chang, N. Kwon, J. Kim, Y. Kohmura, T. Ishikawa, C. Rhee, J. Je, and A. Tsuda. Synchrotron x-ray imaging of pulmonary alveoli in respiration in live intact mice. *Scientific reports*, 5:8760, 2015.
- [28] Z. Chen, Y. Song, Z. Hu, S. Zhang, and Y. Chen. An estimation of mechanical stress on alveolar walls during repetitive alveolar reopening and closure. *Journal of applied physiology (Bethesda, Md. : 1985)*, 119(3):190–201, 2015.
- [29] L. Cheng, A. Albanese, M. Ursino, and N. Chbat. An integrated mathematical model of the human cardiopulmonary system: model validation under hypercapnia and hypoxia. American journal of physiology. Heart and circulatory physiology, 310(7):H922-37, 2016.
- [30] T. Cherpanath, W. Lagrand, M. Schultz, and A. Groeneveld. Cardiopulmonary interactions during mechanical ventilation in critically ill patients. Netherlands heart journal: monthly journal of the Netherlands Society of Cardiology and the Netherlands Heart Foundation, 21(4):166– 172, 2013.

- [31] S. Chiang, J. Green, W. Wang, Y. Yang, G. Shiao, and S. King. Measurements of components of resistance to breathing. *Chest*, 96(2):307–311, 1989.
- [32] Y. S. Chiew, T. Desaive, B. Lambermont, N. Janssen, G. M. Shaw, C. Schranz, K. Möller, and J. G. Chase. Physiological relevance of a minimal model in healthy pigs lung. *IFAC Proceedings Volumes*, 45(18):444– 449, 2012.
- [33] D. Chung, S. Niranjan, J. Clark Jr, A. Bidani, W. Johnston, J. Zwischenberger, and D. Traber. A dynamic model of ventricular interaction and pericardial influence. *American Journal of Physiology*, 272(6):2942–2962, 1997.
- [34] T. Coleman and Y. Li. An interior trust region approach for nonlinear minimization subject to bounds. SIAM Journal on optimization, 6(2):418–445, 1996.
- [35] C.-P. Criée, X. Baur, D. Berdel, D. Bösch, M. Gappa, P. Haidl, K. Husemann, R. Jörres, H.-J. Kabitz, P. Kardos, et al. Leitlinie zur spirometrie. Pneumologie, 69(03):147–164, 2015.
- [36] J. de Canete, P. del Saz-Orozco, D. Moreno-Boza, and E. Duran-Venegas. Object-oriented modeling and simulation of the closed loop cardiovascular system by using simscape. *Computers in biology and medicine*, 43(4):323–333, 2013.
- [37] F. de Freitas, E. Faraco, D. de Azevedo, J. Zaduchliver, and I. Lewin. Behavior of normal pulmonary circulation during changes of total blood volume in man. *Journal of Clinical Investigation*, 44(3):366, 1965.
- [38] F. de Jongh. Ventilation modelling of the human lung. PhD thesis, Delft University of Technology/ Faculty of Aerospace Engineering, Delft, 1995.
- [39] B. Diong, H. Nazeran, P. Nava, and M. Goldman. Modeling human respiratory impedance. *IEEE Engineering in Medicine and Biology Magazine*, 26(1):48–55, 2007.
- [40] B. Diong, A. Rajagiri, M. Goldman, and H. Nazeran. The augmented ric model of the human respiratory system. *Medical and Biological En*gineering and Computing, 47(4):395–404, 2009.

- [41] A. DuBois, S. Botelho, G. Bedell, R. Marshall, and J. Comroe Jr. A rapid plethysmographic method for measuring thoracic gas volume: a comparison with a nitrogen washout method for measuring functional residual capacity in normal subjects. *Journal of Clinical Investigation*, 35(3):322, 1956.
- [42] A. DuBois, S. Botelho, and J. Comroe Jr. A new method for measuring airway resistance in man using a body plethysmograph: values in normal subjects and in patients with respiratory disease. *Journal of Clinical Investigation*, 35(3):327, 1956.
- [43] A. DuBois, A. Brody, D. Lewis, and B. Burgess. Oscillation mechanics of lungs and chest in man. *Journal of Applied Physiology*, 8:587–594, 1956.
- [44] F. Ducharme and G. Davis. Measurement of respiratory resistance in the emergency department: feasibility in young children with acute asthma. *Chest*, 111(6):1519–1525, 1997.
- [45] M. Eichinger, D. Optazaite, A. Kopp-Schneider, C. Hintze, J. Biederer, A. Niemann, M. Mall, M. Wielpütz, H. Kauczor, and M. Puderbach. Morphologic and functional scoring of cystic fibrosis lung disease using mri. European journal of radiology, 81(6):1321–1329, 2012.
- [46] H. Elmqvist and S. Mattsson. Modelica-the next generation modeling language-an international design effort. In *Proceedings of first world* congress of system simulation, pages 1–3, 1997.
- [47] S. England. Current techniques for assessing pulmonary function in the newborn and infant: advantages and limitations. *Pediatric pulmonology*, 4(1):48–53, 1988.
- [48] R. Farré, E. Gavela, M. Rotger, M. Ferrer, J. Roca, and D. Navajas. Noninvasive assessment of respiratory resistance in severe chronic respiratory patients with nasal cpap. *European Respiratory Journal*, 15(2):314–319, 2000.
- [49] R. Farré, J. Montserrat, and D. Navajas. Noninvasive monitoring of respiratory mechanics during sleep. European Respiratory Journal, 24(6):1052–1060, 2004.
- [50] R. Farré, J. Montserrat, and D. Navajas. Assessment of upper airway mechanics during sleep. Respiratory Physiology and Neurobioogy, 163(1-3):74-81, 2008.

- [51] B. Ferris, J. Mead, and L. Opie. Partitioning of respiratory flow resistance in man. *Journal of Applied Physiology*, 19(4):653–658, 1964.
- [52] W. Findeisen. Über das Absetzen kleiner, in der Luft suspendierter Teilchen in der menschlichen Lunge bei der Atmung. Pflüger's Archiv für die gesamte Physiologie des Menschen und der Tiere, 236(1):367– 379, 1935.
- [53] K. Finucane, S. Dawson, P. Phelan, and J. Mead. Resistance of intrathoracic airways of healthy subjects during periodic flow. *Journal of applied physiology*, 38(3):517–530, 1975.
- [54] A. Fisher, A. DuBois, and R. Hyde. Evaluation of the forced oscillation technique for the determination of resistance to breathing. *Journal of Clinical Investigation*, 47(9):2045, 1968.
- [55] M. Fletcher, C. Dezateux, and J. Stocks. Respiratory compliance in infants—a preliminary evaluation of the multiple interrupter technique. *Pediatric pulmonology*, 14(2):118–125, 1992.
- [56] O. Frank. The basic shape of the arterial pulse. first treatise: Mathematical analysis. *Journal of Molecular and Cellular Cardiology*, 22:255–277, 1990.
- [57] I. Frerichs. Electrical impedance tomography (eit) in applications related to lung and ventilation: a review of experimental and clinical activities. *Physiological measurement*, 21(2):R1, 2000.
- [58] I. Frerichs, W. Golisch, G. Hahn, K. Michael, H. Burchardi, and G. Hellige. Heterogeneous distribution of pulmonary ventilation in intensive care patients detected by functional electrical impedance tomography. *Journal of Intensive Care Medicine*, 13(4):168–173, 1998.
- [59] U. Frey, J. Stocks, A. Coates, P. Sly, and J. Bates. Specifications for equipment used for infant pulmonary function testing. ers/ats task force on standards for infant respiratory function testing. european respiratory society/american thoracic society. European Respiratory Journal, 16(4):731-740, 2000.
- [60] U. Frey, J. Stocks, P. Sly, and J. Bates. Specification for signal processing and data handling used for infant pulmonary function testing. ers/ats task force on standards for infant respiratory function testing. european respiratory society/american thoracic society. European Respiratory Journal, 16(5):1016–1022, 2000.

- [61] M. Gappa, A. Colin, I. Goetz, and J. Stocks. Passive respiratory mechanics: the occlusion techniques. *European Respiratory Journal*, 17(1):141–148, 2001.
- [62] M. Goldman, H. Smith, and W. Ulmer. Whole-body plethysmography. European Respiratory Monograph, 31:15, 2005.
- [63] M. D. Goldman. Clinical application of forced oscillation. Pulmonary pharmacology and therapeutics, 14(5):341–350, 2001.
- [64] H. Gomez and M. R. Pinsky. Effect of mechanical ventilation on heartlung interactions. In *Principles and Practice of Mechanical Ventilation*, pages 821–849. McGraw-Hill New York, 2013.
- [65] S. Gottfried, B. Higgs, A. Rossi, F. Carli, P. Mengeot, P. Calverly, L. Zocchi, and J. Milic-Emili. Interrupter technique for measurement of respiratory mechanics in anesthetized humans. *Journal of Applied Physiology*, 59(2):647–652, 1985.
- [66] S. Gunst and J. Stropp. Pressure-volume and length-stress relationships in canine bronchi in vitro. *Journal of Applied Physiology*, 64(6):2522– 2531, 1988.
- [67] A. Guyton, T. Coleman, and H. Granger. Circulation: overall regulation. Annual review of physiology, 34(1):13-44, 1972.
- [68] A. Guyton and J. Hall. Textbook of medical physiology. Elsevier Saunders, Philadelphia, 11 edition, 2006.
- [69] R. Hainsworth. Vascular capacitance: its control and importance. In Reviews of Physiology, Biochemistry and Pharmacology, Volume 105, pages 101–173. Springer, 1986.
- [70] L. Hamilton. Nasal airway resistance: its measurement and regulation. The Physiologist, 22(3):43, 1979.
- [71] J. Hansen and E. Ampaya. Human air space shapes, sizes, areas and volumes. *Journal of Applied Physiology*, 38(6):990–995, 1975.
- [72] Hantos Z., Daroczy B., Suku B., Nagy S., and Fredberg J.J. Input impedance and peripheral inhomogenity of dog lungs. *The American Physiological Society*, 72:168–178., 1992.

- [73] N. Harris, A. Suggett, D. Barber, and B. Brown. Applied potential tomography: a new technique for monitoring pulmonary function. *Clinical Physics and Physiological Measurement*, 9(4A):79, 1988.
- [74] Harris, RS. Pressure-volume curves of the respiratory system. RESPI-RATORY CARE, 50(1):78–99, 2005.
- [75] K. Hayashi, H. Handa, S. Nagasawa, A. Okumura, and K. Moritake. Stiffness and elastic behavior of human intracranial and extracranial arteries. *Journal of biomechanics*, 13(2):181–184, 1980.
- [76] S. Heinke. Hard-und Software-Simulation des herzinsuffizienten Kreislaufs zur Entwicklung von Herzunterstützungssystemen. Shaker, 2014.
- [77] S. Heinke, C. Pereira, S. Leonhardt, and M. Walter. Modeling a healthy and a person with heart failure conditions using the object-oriented modeling environment dymola. *Medical & Biological Engineering & Computing*, 53(10):1049–1068, 2015.
- [78] T. Heldt. Computational models of cardiovascular response to orthostatic stress. PhD thesis, Massachusetts Institute of Technology, 2004.
- [79] J. Hellinckx, K. De Boeck, and M. Demedts. No paradoxical bronchodilator response with forced oscillation technique in children with cystic fibrosis. *Chest*, 113(1):55–59, 1998.
- [80] R. Henderson and J. Webster. An impedance camera for spatially specific measurements of the thorax. Biomedical Engineering, IEEE Transactions on, 25(3):250–254, 1978.
- [81] J. Hildebrandt. Comparison of mathematical models for cat lung and viscoelastic balloon derived by laplace transform methods from pressure volume data. The Bulletin of Mathematical Biophysics, 31(4):651–667, 1969.
- [82] D. Holder and A. Temple. Effectiveness of the sheffield eit system in distinguishing patients with pulmonary pathology from a series of normal subjects. *Clinical and physiological applications of electrical impedance tomography*, pages 277–298, 1993.
- [83] A. Hummel, K. Empen, M. Dörr, and S. Felix. Akute und akut dekompensierte chronische Herzinsuffizienz. *Deutsches Ärzteblatt*, 112(17):298–310, 2015.

- [84] C. Ionescu and R. De Keyser. Parametric models for characterizing respiratory input impedance. *Journal of medical engineering & technology*, 32(4):315–324, 2008.
- [85] G. A. Iotti, J. X. Brunner, A. Braschi, T. Laubscher, M. C. Olivei, A. Palo, C. Galbusera, and A. Comelli. Closed-loop control of airway occlusion pressure at 0.1 second (p sub 0.1) applied to pressure-support ventilation: Algorithm and application in intubated patients. *Critical* care medicine, 24(5):771–779, 1996.
- [86] R. Isermann. Mechatronic systems: fundamentals. Springer Science & Business Media, 2007.
- [87] M. Ismail, A. Comerford, and W. Wall. Coupled and reduced dimensional modeling of respiratory mechanics during spontaneous breathing. International Journal for Numerical Methods in Biomedical Engineering, 29(11):1285–1305, 2013.
- [88] A. Jackson, H. Milhorn Jr, and J. Norman. A reevaluation of the interrupter technique for airway resistance measurement. *Journal of Applied Physiology*, 36(2):264–268, 1974.
- [89] J. Jallon, E. Abdulhay, P. Calabrese, P. Baconnier, and P. Gumery. A model of mechanical interactions between heart and lungs. *Philosophical Transactions of the Royal Society A: Mathematical, Physical and Engineering Sciences*, 367(1908):4741–4757, 2009.
- [90] F. Jardin, J. Farcot, P. Gueret, J. Prost, Y. Ozier, and J. Bourdarias. Cyclic changes in arterial pulse during respiratory support. *Circulation*, 68(2):266–274, 1983.
- [91] J. Jiang and Y. Zhang. A revisit to block and recursive least squares for parameter estimation. Computers & Electrical Engineering, 30(5):403– 416, 2004.
- [92] R. M. Kacmarek. The mechanical ventilator: past, present, and future. Respiratory care, 56(8):1170–1180, 2011.
- [93] D. Kaczka, E. Ingenito, B. Suki, and K. Lutchen. Partitioning airway and lung tissue resistances in humans: effects of bronchoconstriction. *Journal* of Applied Physiology, 82(5):1531–1541, 1997.
- [94] D. Kaminsky. What does airway resistance tell us about lung function? Respiratory care, 57(1):85–99, 2012.

- [95] H. Kitaoka, G. Nieman, Y. Fujino, D. Carney, J. DiRocco, and I. Kawase. A 4-dimensional model of the alveolar structure. The journal of physiological sciences: JPS, 57(3):175–185, 2007.
- [96] R. Klinke and S. Silbernagl. Lehrbuch der Physiologie. Thieme, 4 edition, 2003.
- [97] B. Klug and H. Bisgaard. Measurement of lung function in awake 2–4-year-old asthmatic children during methacholine challenge and acute asthma: A comparison of the impulse oscillation technique, the interrupter technique, and transcutaneous measurement of oxygen versus whole-body plethysmography. Pediatric pulmonology, 21(5):290–300, 1996.
- [98] B. Koeppen and B. Stanton. Berne and Levy Physiology E-Book. Elsevier Health Sciences, 2017.
- [99] J. Kofránek, M. Mateják, P. Privitzer, and M. Tribula. Causal or acausal modeling: labour for humans or labour for machines. *Technical Comput*ing Prague, pages 1–16, 2008.
- [100] H. Komarow, I. Myles, A. Uzzaman, and D. Metcalfe. Impulse oscillometry in the evaluation of diseases of the airways in children. *Annals of Allergy, Asthma & Immunology*, 106(3):191–199, 2011.
- [101] E. Kooi, S. Schokker, T. Van Der Molen, and E. Duiverman. Airway resistance measurements in pre-school children with asthmatic symptoms: the interrupter technique. *Respiratory medicine*, 100(6):955–964, 2006.
- [102] P. Kunst, A. V. Noordegraaf, O. Hoekstra, P. Postmus, and P. De Vries. Ventilation and perfusion imaging by electrical impedance tomography: a comparison with radionuclide scanning. *Physiological measurement*, 19(4):481, 1998.
- [103] B. Lachmann. Open up the lung and keep the lung open. *Intensive care medicine*, 18(6):319–321, 1992.
- [104] E. Landis and J. Gibbon Jr. The effects of temperature and of tissue pressure on the movement of fluid through the human capillary wall. Journal of Clinical Investigation, 12(1):105, 1933.
- [105] E. Landis, L. Jonas, M. Angevine, and W. Erb. The passage of fluid and protein through the human capillary wall during venous congestion. *Journal of Clinical Investigation*, 11(4):717, 1932.

- [106] R. Laniado-Laborín. Smoking and chronic obstructive pulmonary disease (copd). parallel epidemics of the 21st century. *International journal of environmental research and public health*, 6(1):209–224, 2009.
- [107] S. Lehmann, S. Leonhardt, C. Ngo, L. Bergmann, I. Ayed, S. Schrading, and K. Tenbrock. Global and regional lung function in cystic fibrosis measured by electrical impedance tomography. *Pediatric pulmonology*, 51(11):1191–1199, 2016.
- [108] S. Lehmann, S. Leonhardt, C. Ngo, L. Bergmann, S. Schrading, K. Heimann, N. Wagner, and K. Tenbrock. Electrical impedance tomography as possible guidance for individual positioning of patients with multiple lung injury. *The clinical respiratory journal*, 12(1):68–75, 2018.
- [109] C. Lenfant, editor. Pulmonary Edema: Lung Biology in Health and Disease. Marcel Dekker Inc, 116 edition, 1998.
- [110] S. Leonhardt. Automatisierte Lungenfunktionsdiagnose bei spontanatmenden Säuglingen. Shaker, 2000.
- [111] S. Leonhardt, S. Böhm, and B. Lachmann. Optimierung der Beatmung beim akuten Lungenversagen durch Identifikation physiologischer Kenngrößen. Automatisierungstechnik, 46(11), 1998.
- [112] S. Leonhardt and B. Lachmann. Electrical impedance tomography: the holy grail of ventilation and perfusion monitoring? *Intensive care medicine*, 38(12):1917–1929, 2012.
- [113] S. Leonhardt and M. Walter. Medizintechnische Systeme: Physiologische Grundlagen, Gerätetechnik und automatisierte Therapieführung. Springer-Verlag, 2016.
- [114] C. Liu, S. Niranjan, J. Clark Jr, K. San, J. Zwischenberger, and A. Bidani. Airway mechanics, gas exchange, and blood flow in a nonlinear model of the normal human lung. *Journal of applied physiology*, 84(4):1447–1469, 1998.
- [115] K. Lopez-Navas. Adaptive Regulation of Ventilation Parameters. PhD thesis, University of Lübeck, 2013.
- [116] K. Lopez-Navas, S. Brandt, M. Strutz, H. Gehring, and U. Wenkebach. Non-invasive determination of respiratory effort in spontaneous breathing and support ventilation: a validation study with healthy volunteers. Biomedical Engineering/Biomedizinische Technik, 59(4):335–341, 2014.

- [117] K. Lu, J. Clark Jr, F. Ghorbel, D. Ware, and A. Bidani. A human cardiopulmonary system model applied to the analysis of the valsalva maneuver. American Journal of Physiology-Heart and Circulatory Physiology, 281(6):H2661–H2679, 2001.
- [118] K. Lutchen and H. Gillis. Relationship between heterogeneous changes in airway morphometry and lung resistance and elastance. *Journal of Applied Physiology*, 83(4):1192–1201, 1997.
- [119] D. MacLeod and M. Birch. Respiratory impedance measurements: forced oscillation methods. Medical and Biological Engineering and Computing, 39(5):505–516, 2001.
- [120] F. Marchal, P. Hauouzi, R. Peslin, C. Duvivier, and C. Gallina. Machinal properties of the upper airway wall in children and their influence on respiratory impedance measurements. *Pediatric pulmonology*, 13(1):28– 33, 1992.
- [121] J. Marini. Mechanical ventilation: past lessons and the near future. Critical care, 17(1):S1, 2013.
- [122] F. Marquis, N. Coulombe, R. Costa, H. Gagnon, R. Guardo, and Y. Skrobik. Electrical impedance tomography's correlation to lung volume is not influenced by anthropometric parameters. *Journal of clinical monitoring and computing*, 20(3):201–207, 2006.
- [123] R. Marshall and A. DuBois. The measurement of the viscous resistance of the lung tissues in normal man. Clinical science (London, England: 1979), 15(1):161, 1956.
- [124] J. Masip, A. Betbesé, J. Páez, F. Vecilla, R. Cañizares, J. Padró, M. Paz, J. de Otero, and J. Ballús. Non-invasive pressure support ventilation versus conventional oxygen therapy in acute cardiogenic pulmonary oedema: a randomised trial. *The Lancet*, 356(9248):2126–2132, 2000.
- [125] A. Mattu, J. Martinez, and B. Kelly. Modern management of cardiogenic pulmonary edema. *Emergency Medicine Clinics*, 23(4):1105–1125, 2005.
- [126] J. Mead. Volume displacement body plethysmograph for respiratory measurements in human subjects. *Journal of Applied Physiology*, 15(4):736–740, 1960.
- [127] J. Mead. Mechanical properties of lungs. The American Physiological Society, 41(2):281–330, 1961.

- [128] J. Mead. Contribution of compliance of airways to frequency-dependent behavior of lungs. *Journal of Applied Physiology*, 26(5):670–673, 1969.
- [129] J. Mead and E. Agostoni. Dynamics of breathing. Handbook of Physiology. Respiration, 1:411–427, 1964.
- [130] J. Mead, I. Lindgren, and E. Gaensler. The mechanical properties of the lungs in emphysema. *Journal of Clinical Investigation*, 34(7 Pt 1):1005, 1955.
- [131] J. Mead, J. Turner, P. Macklem, and J. Little. Significance of the relationship between lung recoil and maximum expiratory flow. *Journal of Applied Physiology*, 22(1):95–108, 1967.
- [132] M. Miller, R. Crapo, J. Hankinson, V. Brusasco, F. Burgos, R. Casaburi, A. Coates, P. Enright, C. van der Grinten, P. Gustafsson, et al. General considerations for lung function testing. *European Respiratory Journal*, 26(1):153–161, 2005.
- [133] M. Miller, J. Hankinson, V. Brusasco, F. Burgos, R. Casaburi, A. Coates, R. Crapo, P. Enright, C. van der Grinten, P. Gustafsson, R. Jensen, D. Johnson, N. MacIntyre, R. McKay, D. Navajas, O. Pedersen, R. Pellegrino, G. Viegi, and J. Wanger. Standardisation of spirometry. The European respiratory journal, 26(2):319–338, 2005.
- [134] E. Mireles-Cabodevila, U. Hatipoğlu, and R. Chatburn. A rational framework for selecting modes of ventilation. *Respiratory Care*, 58(2):348–366, 2013.
- [135] G. Miserocchi. Physiology and pathophysiology of pleural fluid turnover. European Respiratory Journal, 10(1):219–225, 1997.
- [136] G. Miserocchi, D. Negrini, M. Del Fabbro, and D. Venturoli. Pulmonary interstitial pressure in intact in situ lung: transition to interstitial edema. *Journal of Applied Physiology*, 74(3):1171–1177, 1993.
- [137] M. Morris, P. Gustafsson, R. Tepper, M. Gappa, and J. Stocks. The bias flow nitrogen washout technique for measuring the functional residual capacity in infants. *European Respiratory Journal*, 17(3):529–536, 2001.
- [138] P. E. Morrow. Lymphatic drainage of the lung in dust clearance. Annals of the New York Academy of Sciences, 200(1):46–65, 1972.

- [139] C. Mottram. Ruppel's Manual of Pulmonary Function Testing 10: Ruppel's Manual of Pulmonary Function Testing. Elsevier Health Sciences, 2013.
- [140] E. Namati, J. Thiesse, J. d. Ryk, and G. McLennan. Alveolar dynamics during respiration: are the pores of kohn a pathway to recruitment? American journal of respiratory cell and molecular biology, 38(5):572– 578, 2008.
- [141] T. G. A. Network. The global asthma report 2014. Auckland, New Zealand, 769, 2014.
- [142] C. Ngo, S. Dahlmanns, T. Vollmer, B. Misgeld, and S. Leonhardt. An object-oriented computational model to study cardiopulmonary hemodynamic interactions in humans. Computer methods and programs in biomedicine, 159:167–183, 2018.
- [143] C. Ngo, F. Dippel, K. Tenbrock, S. Leonhardt, and S. Lehmann. Flow-volume loops measured with electrical impedance tomography in pediatric patients with asthma. *Pediatric Pulmonology*, 53(5):636–644, 2018.
- [144] C. Ngo, K. Krüger, T. Vollmer, S. Winter, B. Penzlin, S. Lehmann, S. Leonhardt, and B. Misgeld. Effects of the nasal passage on forced oscillation lung function measurements. *Biomedical Engineer-ing/Biomedizinische Technik*, 62(6):635–642, 2017.
- [145] C. Ngo, A. Kube, K. Krüger, T. Vollmer, S. Winter, S. Leonhardt, and B. Misgeld. Identification of respiratory parameters in frequency and time domain with forced oscillation technique. In The International Federation of Automatic Control, editor, 9th IFAC Symposium on Biological and Medical Systems, pages 177–182, 2015.
- [146] C. Ngo and S. Leonhardt. A model-based analysis to re-evaluate the first and second rises in the rapid interrupter technique measurements. 2019.
- [147] C. Ngo, S. Leonhardt, T. Zhang, M. Lüken, B. Misgeld, T. Vollmer, K. Tenbrock, and S. Lehmann. Linearity of electrical impedance tomography during maximum effort breathing and forced expiration maneuvers. *Physiological measurement*, 38(1):77, 2016.
- [148] C. Ngo, R. Schlözer, T. Vollmer, S. Winter, B. Misgeld, and S. Leonhardt. A simulative model approach of cardiopulmonary interaction. In World Congress on Medical Physics and Biomedical Engineering, June 7-12, 2015, Toronto, Canada, pages 1679–1682, 2015.

- [149] C. Ngo, S. Spagnesi, C. Munoz, S. Lehmann, T. Vollmer, B. Misgeld, and S. Leonhardt. Assessing regional lung mechanics by combining electrical impedance tomography and forced oscillation technique. *Biomedical Engineering/Biomedizinische Technik*, 63(6):673–681, 2018.
- [150] C. D. S. Ngo, T. Vollmer, B. Misgeld, and S. Leonhardt. Object-oriented modeling of thoracic fluid balance to study cardiogenic pulmonary congestion in humans. *Computer Methods and Programs in Biomedicine*, In review, 2019.
- [151] G. Nieman. Amelia earhart, alveolar mechanics, and other great mysteries. Journal of applied physiology (Bethesda, Md. : 1985), 112(6):935–936, 2012.
- [152] W. Oczenski. Atmen Atemhilfen: Atemphysiologie und Beatmungstechnik. Georg Thieme Verlag, 9 edition, 2012.
- [153] J. Olansen, J. Clark, D. Khoury, F. Ghorbel, and A. Bidani. A closed-loop model of the canine cardiovascular system that includes ventricular interaction. *Computers and biomedical research*, 33(4):260–295, 2000.
- [154] A. Olinsky, A. Bryan, and M. Bryan. A simple method of measuring total respiratory system compliance in newborn infants. South African medical journal, 50(5):128–130, 1976.
- [155] E. Oostveen, D. MacLeod, H. Lorino, R. Farre, Z. Hantos, K. Desager, and F. Marchal. The forced oscillation technique in clinical practice: methodology, recommendations and future developments. *European Respiratory Journal*, 22(6):1026–1041, 2003.
- [156] A. Otis, W. Fenn, and H. Rahn. Mechanics of breathing in man. *Journal of Applied Physiology*, 2(11):592–607, 1950.
- [157] A. Otis, C. McKerrow, J. Mead, M. McIlroy, N. Selverstone, and E. Radford. Mechanial factors in distribution of pulmonary ventilation. *J Appl Physiol*, 8:427–443, 1956.
- [158] R. Pattle. Properties, function, and origin of the alveolar lining layer. Nature, 175:1125–1126, 1955.
- [159] R. Pattle. Properties, function, and origin of the alveolar lining layer. Proceedings of the Royal Society of London B: Biological Sciences, 148(931):217–240, 1958.

- [160] R. Pauwels, A. Buist, P. Calverley, C. Jenkins, and S. Hurd. Global strategy for the diagnosis, management, and prevention of chronic obstructive pulmonary disease: Nhlbi/who global initiative for chronic obstructive lung disease (gold) workshop summary. American journal of respiratory and critical care medicine, 163(5):1256–1276, 2001.
- [161] T. Pedley, R. Schroter, and M. Sudlow. The prediction of pressure drop and variation of resistance within the human bronchial airways. *Respi*ration physiology, 9(3):387–405, 1970.
- [162] R. Pellegrino, G. Viegi, V. Brusasco, R. Crapo, F. Burgos, R. Casaburi, A. Coates, C. van der Grinten, P. Gustafsson, J. Hankinson, et al. Interpretative strategies for lung function tests. *European Respiratory Journal*, 26(5):948–968, 2005.
- [163] A. Pesenti, P. Pelosi, G. Foti, L. D'Andrea, and N. Rossi. An interrupter technique for measuring respiratory mechanics and the pressure generated by respiratory muscles during partial ventilatory support. *Chest*, 102(3):918–923, 1992.
- [164] R. Peslin, Y. Ying, C. Gallina, and C. Duvivier. Within-breath variations of forced oscillation resistance in healthy subjects. *European Respiratory Journal*, 5(1):86–92, 1992.
- [165] R. Pikkemaat, K. Tenbrock, S. Lehmann, and S. Leonhardt. Electrical impedance tomography: New diagnostic possibilities using regional time constant maps. Applied Cardiopulmonary Pathophysiology, 16:212–225, 2012.
- [166] M. Pinsky. The hemodynamic consequences of mechanical ventilation: an evolving story. *Intensive care medicine*, 23(5):493–503, 1997.
- [167] M. Pinsky. Cardiovascular issues in respiratory care. CHEST Journal, 128(5 Suppl 2):592S-597S, 2005.
- [168] M. R. Pinsky, G. Matuschak, and M. Klain. Determinants of cardiac augmentation by elevations in intrathoracic pressure. *Journal of Applied Physiology*, 58(4):1189–1198, 1985.
- [169] A. Pomprapa, D. Schwaiberger, B. Lachmann, and S. Leonhardt. A mathematical model for carbon dioxide elimination: an insight for tuning mechanical ventilation. *European Journal of Applied Physiology*, 114(1):165–175, 2014.

- [170] H. Prange. Laplace's law and the alveolus: A misconception of anatomy and a misapplication of physics. AJP: Advances in Physiology Education, 27(1):34–40, 2003.
- [171] M. Puderbach, M. Eichinger, J. Haeselbarth, S. Ley, A. Kopp-Schneider, S. Tuengerthal, A. Schmaehl, C. Fink, C. Plathow, M. Wiebel, et al. Assessment of morphological mri for pulmonary changes in cystic fibrosis (cf) patients: comparison to thin-section ct and chest x-ray. *Investigative radiology*, 42(10):715-724, 2007.
- [172] E. Radford. Recent studies of mechanical properties of mammalian lungs. Tissue Elasticity, pages 177–190, 1957.
- [173] H. Rahn, A. B. Otis, L. E. Chadwick, and W. O. Fenn. The pressure-volume diagram of the thorax and lung. American Journal of Physiology-Legacy Content, 146(2):161–178, 1946.
- [174] V. Rideout. Mathematical and computer modeling of physiological systems. Prentice Hall advanced reference series. Physical and life sciences. Prentice Hall, Englewood Cliffs and N.J, 1991.
- [175] J. Robotham, W. Lixfeld, L. Holland, D. MacGregor, A. Bryan, and J. Rabson. Effects of respiration on cardiac performance. *Journal of Applied Physiology*, 44(5):703–709, 1978.
- [176] J. Robotham, J. Rabson, S. Permutt, and B. Bromberger-Barnea. Left ventricular hemodynamics during respiration. *Journal of Applied Physi*ology, 47(6):1295–1303, 1979.
- [177] J. Rodarte. Respiratory-Circulatory Interactions in Health and Disease. Lung biology in health and disease. Mercel Dekker, New York, 2001.
- [178] F. Rohrer. Der Strömungswiderstand in den menschlichen Atemwegen und der Einfluss der unregelmaessigen Verzweigung des Bronchialsystems auf den Atmungsverlauf in verschiedenen Lungenbezirken. Pfuegers Arch.ges. Physiol., 162(5):221–232, 1915.
- [179] C. F. Rothe. Venous system: physiology of the capacitance vessels. Comprehensive Physiology, pages 397–452, 1983.
- [180] C. Sassoon, T. Te, C. Mahutte, and R. Light. Airway occlusion pressure: An important indicator for successful weaning in patients with chronic obstructive pulmonary disease 1–3. *American Review of Respiratory Disease*, 135(1):107–113, 1987.

- [181] N. Saxena. Restrictive lung disease. In The Perioperative Medicine Consult Handbook, pages 199–202. Springer, 2015.
- [182] S. Scharf, P. Caldini, and R. Ingram. Cardiovascular effects of increasing airway pressure in the dog. American Journal of Physiology-Heart and Circulatory Physiology, 232(1):H35–H43, 1977.
- [183] R. Schlegelmilch and R. Kramme. Pulmonary function testing. In Springer Handbook of Medical Technology, pages 95–117. Springer, 2011.
- [184] M. Schnüke, E. Schulte, and U. Schumacher. Prometheus Lernatlas der Anatomie: Allgemeine Anatomie und Bewegungssystem: 4., überarbeitete und erweiterte Auflage. Georg Thieme Verlag, Stuttgart, 4 edition, 2014.
- [185] W. Schröder. Fluidmechanik. Aachener Beiträge zur Strömungsmechanik, Band 7. Wissenschaftsverlag Mainz in Aachen, 3. korrigierte auflage edition, 2010.
- [186] R. Serrano, B. de Lema, O. Casas, T. Feixas, N. Calaf, V. Camacho, I. Carrió, P. Casan, J. Sanchis, and P. Riu. Use of electrical impedance tomography (eit) for the assessment of unilateral pulmonary function. *Physiological measurement*, 23(1):211, 2002.
- [187] R. Shayan, M. Achen, and S. Stacker. Lymphatic vessels in cancer metastasis: bridging the gaps. *Carcinogenesis*, 27(9):1729–1738, 2006.
- [188] P. Sly and J. Bates. Computer analysis of physical factors affecting the use of the interrupter technique in infants. *Pediatric pulmonology*, 4(4):219–224, 1988.
- [189] P. Sly, M. Hayden, F. Peták, and Z. Hantos. Measurement of low-frequency respiratory impedance in infants. *American journal of respiratory and critical care medicine*, 154(1):161–166, 1996.
- [190] P. Sly, R. Tepper, M. Henschen, M. Gappa, and J. Stocks. Tidal forced expirations. *European Respiratory Journal*, 16(4):741–748, 2000.
- [191] B. Smith, S. Andreassen, G. Shaw, P. Jensen, S. Rees, and J. Chase. Simulation of cardiovascular system diseases by including the autonomic nervous system into a minimal model. *Computer methods and programs* in biomedicine, 86(2):153–160, 2007.
- [192] B. Smith, J. Chase, R. Nokes, G. Shaw, and G. Wake. Minimal haemodynamic system model including ventricular interaction and valve dynamics. *Medical Engineering & Physics*, 26(2):131–139, 2004.

- [193] H. Smith, P. Reinhold, and M. Goldman. Forced oscillation technique and impulse oscillometry. *European Respiratory Monograph*, 31:72–105, 2005.
- [194] M. C. M. Soares, A. C. R. Sallum, M. T. M. Gonçalves, F. L. M. Haddad, and L. C. Gregório. Use of muller's maneuver in the evaluation of patients with sleep apnea-literature review. *Brazilian journal of otorhinolaryngology*, 75(3):463–466, 2009.
- [195] L. Solymar, P.-H. Aronsson, and R. Sixt. The forced oscillation technique in children with respiratory disease. *Pediatric pulmonology*, 1(5):256–261, 1985.
- [196] E. Spriggs. John hutchinson, the inventor of the spirometer-his north country background, life in london, and scientific achievements. *Medical history*, 21(4):357, 1977.
- [197] E. Starling. On the absorption of fluids from the connective tissue spaces. The Journal of physiology, 19(4):312–326, 1896.
- [198] J. Stocks, S. Godfrey, C. Beardsmore, E. Bar-Yishay, R. Castile, et al. Plethysmographic measurements of lung volume and airway resistance. *European Respiratory Journal*, 17(2):302–312, 2001.
- [199] P. Subbarao, C. Milla, P. Aurora, J. Davies, S. Davis, G. Hall, S. Heltshe, P. Latzin, A. Lindblad, J. Pittman, et al. Multiple-breath washout as a lung function test in cystic fibrosis. a cystic fibrosis foundation workshop report. Annals of the American Thoracic Society, 12(6):932–939, 2015.
- [200] B. Suki, H. Yuan, Q. Zhang, and K. Lutchen. Partitioning of lung tissue response and inhomogeneous airway constriction at the airway opening. *Journal of Applied Physiology*, 82(4):1349–1359, 1997.
- [201] A. Sundaresan, T. Yuta, C. Hann, J. Chase, and G. Shaw. A minimal model of lung mechanics and model-based markers for optimizing ventilator treatment in ards patients. *Computer methods and programs in biomedicine*, 95(2):166–180, 2009.
- [202] A. Taylor. The lymphatic edema safety factor: the role of edema dependent lymphatic factors (edlf). Lymphology, 23(3):111–123, 1990.
- [203] E. Teschner, M. Imhoff, and S. Leonhardt. Electrical impedance tomography: The realization of regional ventilation monitoring. *Dräger Medical GmbH*, 2015.

- [204] S. Thibault, L. Heyer, G. Benchetrit, and P. Baconnier. Ventilatory support: A dynamical systems approach. Acta Biotheoretica, 50(4):269– 279, 2002.
- [205] F. Thien. Measuring and imaging small airways dysfunction in asthma. Asia Pacific Allergy, 3(4):224, 2013.
- [206] J. Tomashefski and C. Farver. Anatomy and histology of the lung. Dail and Hammar's Pulmonary Pathology, pages 20–48, 2008.
- [207] I. Trindade, A. Gomes, A. Sampaio-Teixeira, and S. Trindade. Adult nasal volumes assessed by acoustic rhinometry. *Brazilian journal of otorhinolaryngology*, 73(1):32–39, 2007.
- [208] M. Valentinuzzi and R. Johnston. Spirometry: A historical gallery up to 1905 [retrospectroscope]. IEEE pulse, 5(1):73-76, 2014.
- [209] J. Van Noord, J. Smeets, J. Clement, K. Van de Woestijne, and M. Demedts. Assessment of reversibility of airflow obstruction. American journal of respiratory and critical care medicine, 150(2):551–554, 1994.
- [210] J. Vogel and U. Smidt. Impuls-Oszillometrie: Analyse der Atemmechanik in Ambulanz und Klinik, Epidemiologie und experimenteller Forschung. Pmi-Verl.-Gruppe, Frankfurt am Main and Moskau and Sennwald and Wien, 1994.
- [211] C. Vogelmeier, G. Criner, F. Martinez, A. Anzueto, P. Barnes, J. Bourbeau, B. Celli, R. Chen, M. Decramer, L. Fabbri, et al. Global strategy for the diagnosis, management and prevention of chronic obstructive lung disease 2017 report. *Respirology*, 22(3):575–601, 2017.
- [212] B. Vogt, C. Falkenberg, N. Weiler, and I. Frerichs. Pulmonary function testing in children and infants. *Physiological measurement*, 35(3):R59–90, 2014.
- [213] B. Vogt, S. Pulletz, G. Elke, Z. Zhao, P. Zabel, N. Weiler, and I. Frerichs. Spatial and temporal heterogeneity of regional lung ventilation determined by electrical impedance tomography during pulmonary function testing. *Journal of Applied Physiology*, 113(7):1154–1161, 2012.
- [214] K. von Neergaard. Neue Auffassungen über einen Grundbegriff der Atemmechanik. Zeitschrift für die gesamte experimentelle Medizin, 66(1):373– 394, 1929.

- [215] K. von Neergaard and K. Wirz. Die Messung der Strömungswiderstände in den Atemwegen des Menschen, insbesondere bei Asthma und Emphysem. Z Klin Med, 105(5):1–82, 1927.
- [216] C. Wang. A brief history of respiratory deposition modeling. *Aerosol science and technology: History and reviews*, pages 391–409, 2011.
- [217] D. Wangensteen, E. Lysaker, and P. Savaryn. Pulmonary capillary filtration and reflection coefficients in the adult rabbit. *Microvascular Re*search, 14:81–97, 1976.
- [218] J. Wanger, J. Clausen, A. Coates, O. Pedersen, V. Brusasco, F. Burgos, R. Casaburi, R. Crapo, P. Enright, C. Van Der Grinten, et al. Standardisation of the measurement of lung volumes. *European Respiratory Journal*, 26(3):511–522, 2005.
- [219] E. Weibel. Geometry and dimensions of airways of conductive and transitory zones. Springer Berlin Heidelberg, 1963.
- [220] E. Weibel. Morphometry of the human lung. Academic Press, New York, 1963.
- [221] J. West. Challenges in teaching the mechanics of breathing to medical and graduate students. Advances in physiology education, 32(3):177–184, 2008.
- [222] J. West. Respiratory physiology: the essentials. Lippincott Williams & Wilkins, 2012.
- [223] N. Westerhof, J. Lankhaar, and B. Westerhof. The arterial windkessel. Medical & Biological Engineering & Computing, 47(2):131–141, 2009.
- [224] J. Widdicombe and J. Nadel. Airway volume, airway resistance, and work and force of breathing: theory. *Journal of applied physiology*, 18(5):863– 868, 1963.
- [225] E. Widmaier, H. Raff, and K. Strang. Vander's human physiology, volume 5. McGraw-Hill New York, NY, 2006.
- [226] H. Yeh and G. Schum. Models of human lung airways and their application to inhaled particle deposition. Bulletin of mathematical biology, 42(3):461–480, 1980.
- [227] F. C. Yin and C.-T. Ting. Compliance changes in physiological and pathological states. *Journal of Hypertension*, 10(6):S31–3, 1992.

- [228] T. Yuta. Minimal Model of Lung Mechanics for Optimising Ventilator Therapy in Critical Care: A thesis presented for the degree of Doctor of Philosophy in Mechanical Engineering. University of Canterbury, Christchurch, New Zealand, 2007.
- [229] Z. Zhao, R. Fischer, I. Frerichs, U. Müller-Lisse, and K. Möller. Regional ventilation in cystic fibrosis measured by electrical impedance tomography. *Journal of Cystic Fibrosis*, 11(5):412–418, 2012.
- [230] Y. Zheng and J. Mayhew. A time-invariant visco-elastic windkessel model relating blood flow and blood volume. *NeuroImage*, 47(4):1371–1380, 2009.